Optimisation of Natural Laminar Flow Aerofoils and Wings for Robustness to Critical Transition Amplification Factor

Jed Hollom

Department of Mechanical Engineering
The University of Sheffield
United Kingdom

Supervisor: Professor N. Qin

A thesis submitted for the degree of
Doctor of Philosophy.

September 2018

Abstract

This thesis investigates the use of robust design and optimisation methods to improve natural laminar flow (NLF) aerofoil and wing robustness to variations both in operating conditions and uncertainty in surface and flow quality.

NLF is a promising method for aircraft drag reduction but has high sensitivity to operating conditions, flow quality and surface finish. Existing research on this topic has looked to improve NLF designs at a range of operating conditions, but uncertainty in surface and flow quality has not been considered. In this work, surface and flow quality are represented by the critical transition amplification factor, or N-factor, from the e^N transition model.

A probabilistic distribution and quantification method for uncertainty in critical N-factor is first selected. This is then used to assess NLF aerofoil performance with uncertainty in critical N-factor. Transition location sensitivity to critical N-factor is found to be linked to transition location sensitivity to lift coefficient; and drag robustness is found to be closely related to transition location robustness.

Robust optimisation is then used to design NLF aerofoils that are insensitive to uncertainty in critical N-factor. This is found to be effective; however, the robustness at off-design flight conditions deteriorates as a result. Many designs with no laminar flow are also generated. These are inherently robust to critical N-factor uncertainty but of no practical use.

A method is then developed that enables the coupling of multi-point and robust optimisation without an increase in computational costs. This uses the N-factor envelope from e^N stability analysis to predict transition locations over the critical N-factor range. Multi-point robust optimisation of NLF aerofoils with critical N-factor uncertainty is then carried out. This is able to produce NLF aerofoils with good robustness to critical N-factor uncertainty over a range of lift coefficients and Mach numbers. This envelope sampling method is then extended to account for three-dimensional flows and is used to optimise swept and tapered wing sections for NLF with uncertainty in critical N-factor.

Overall, this work demonstrates that robust design and optimisation method are well suited to the design of NLF aerofoils and wings. Furthermore, it shows that the N-factor envelope from e^N stability analysis can be used to reduce the dimensionality of robust NLF design, making it no more computationally expensive than current multi-point optimisation problems. It therefore makes an original contribution to the field of NLF design and optimisation.

Acknowledgements

I would first like to thank my supervisor, Professor Ning Qin, for giving me the opportunity to undertake this PhD. Through it, I have been able to expand my knowledge, develop as a person and make many long-lasting friendships.

I would also like to thank Murray Cross for facilitating the link between my PhD and Airbus Commercial Aircraft. This work would not have been possible and would not have been as relevant without the connection to Airbus that Murray provided.

I would like to thank Dr. Stephen Rolston for providing me with the opportunity to spend time at Airbus Group Innovations (AGI) in Bristol. I also appreciate Stephen allowing me to repeatedly extend my stay and for accepting my short notice requests to visit.

I am incredibly grateful to Dr. James Alderman for his advice, support and guidance during my time at AGI and for the remainder of my PhD. James has been instrumental in the development of this work and I greatly enjoyed our discussions on this and many other topics.

I would also like to thank everyone in the Aeromechanics and Acoustics team at AGI for the warm and friendly working environment they created. It was both a pleasure to spend time there and the most productive period of my studies.

I would like to thank my family for their love and kindness, and the opportunities they have provided me with. I would particularly like to thank them, and Elena Paci, for their support towards the end of my PhD, which carried me through to the finish. I could not have done this without them.

Finally, I would like to thank my peers in the University of Sheffield engineering department and my friends in Sheffield, for making the last few years some of the best.

Contents

Nomenclature

Acronyms/Abbreviations

CF	Crossflow
CFD	Computational Fluid Dynamics
HLFC	Hybrid Laminar Flow Control
LFC	Laminar Flow Control
NLF	Natural Laminar Flow
TS	Tollmien-Schlichting
VII	Viscous-Inviscid Interaction

Greek

δ	Boundary Layer Thickness
δ^*	Boundary layer Displacement
$\Delta_{z_{te}}$	Trailing Edge Thickness
η	Crowding Number
γ	Vorticity Strength
Λ	Sweep Angle
ω	Frequency
ψ	Stream Function
σ	Source Strength
θ	Momentum Thickness
ε	Ellipticity

ξ	Stream-wise coordinate

Roman

C_d	Drag Coefficient
C_{df}	Skin Friction Drag Coefficient
C_{dp}	Pressure Drag Coefficient
C_{dv}	Viscous Drag Coefficient
C_{dw}	Wave Drag Coefficient
C_l	Lift Coefficient
N_{step}	Critical N-factor Sample Spacing
A_r	Class Shape Transformation Coefficients
$C(u)$	Class Function
C_τ	Shear Stress Coefficient
C_E	Dissipation/Entrainment Coefficient
C_m	Moment Coefficient
$F_\mu(N)$	Mean Output
$F_\sigma(N)$	Output Standard Deviation
H	Shape Factor
H^*	Kinetic Energy Shape Factor
H_k	Kinematic Shape Factor
H_ρ	Density Shape Factor
h_{rms}	Surface Roughness height (Root Mean Square)
k_m	Multi-point Sample Number
k_r	Robust Sample Number
M	Mach Number
M_{2D}	Two-dimensional Mach Number
n	Bernstein Polynomial Power

n_1/n_2	Class Function Exponents
N_σ	Critical N-factor Standard Deviation
N_i	Ideal Critical N-factor
n_i/n_t	Current/Total Generation Number
N_{dv}	Number of Design Variables
N_{pop}	Population Size
$P(N)$	Probability Density Function
r	Normal Leading Edge Radius
Re	Reynolds Number
Re_θ	Reynolds number (Momentum Thickness)
$S(u)$	Shape Function
S_{ref}	Wing Area
Tr	Transition Location
Tu	Turbulent Intensity
u	Chord Length Position
W	Summation of Weights
z_o/z_p	Original/Perturbation z coordinate

Subscripts

0	Initial
δ	Boundary Layer Thickness
ac	Aircraft
cf	Crossflow
cr	Critical
l	Lower Surface
le	Leading Edge
max	Maximum

te	Trailing Edge
ts	Tollmien-Schlichting
u	Upper Surface
e	Boundary Layer Edge
EQ	Equilibrium flow

Chapter 1

Introduction

Within the commercial aviation industry, there is a constant demand for reduced fuel consumption. This is required to meet the stringent environmental targets set by aviation authorities, as well as to reduce running costs for airline operators. Such environmental targets are outlined by the European Commission who specify a 75 percent reduction in CO_2 and 90 percent reduction in NO_x per passenger kilometre by the year 2050 [1].

Throughout aviation history, advancements in aircraft design, engine technology and fuel composition have all resulted in improved aircraft performance. Modern commercial aircraft are highly efficient as a result. However, as the basic configuration of aircraft has remained largely unchanged, each additional design effort produces a diminishing return on improved aircraft efficiency. For this reason, development of new aerodynamic configurations and the exploitation of more complex flow phenomena is required for a step change in aircraft performance to be found.

Drag on a transonic commercial transport aircraft can be broken down into individual components as shown in figure 1.1. Parasite and lift-induced drag make up approximately 94 percent of the total aircraft drag [2, 3]. Lift-induced drag occurs when the lift generated by the wing has a component opposite to the direction of flight. This occurs when a difference in pressure causes flow at the wing-tip to move from the pressure to suction surface, leading to a vortex downstream of the wing-tip and down-wash over the wing itself. This down-wash induces a change in the local angle of flow over the wing, and so the angle at which lift is generated.

Parasite drag is experienced when an objective moves through a viscous fluid and can be split into skin friction and form drag components. Skin friction accounts for 96 percent of parasite drag, and is the loss of energy due to shear stresses within the boundary layer that forms as a result of flow viscosity. As all wetted areas contribute to this, the fuselage and wing are the largest sources and collectively account for 74 percent of skin friction on an aircraft. Form drag is also due to the formation of the boundary layer, which changes how oncoming flow interacts with the aircraft. Thickening of the boundary layer increases the effective thickness of an aerodynamic body, causing a change in pressure distribution and an increase in drag. This is referred to as form drag. As modern aircraft are highly streamlined, form drag is a small component of parasite drag, contributing only 4 percent.

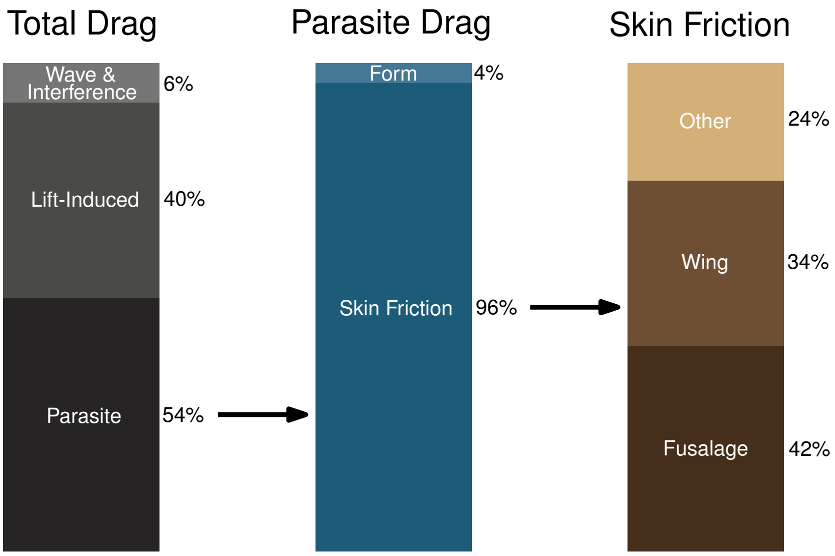

Figure 1.1: *Drag breakdown for a typical commercial transport aircraft (data taken from [3])*

The other drag sources accounting for approximately 8 percent of total aircraft drag are wave drag and interference drag. Interference drag occurs when flow from different aerodynamic surfaces mix such that the combined drag is larger than the sum of the individual components. This can occur at junctions between components, where two components are close or if one is behind another [4]. For commercial aircraft, key sources of interference drag are at the intersections between fuselage, wing, pylon and engine. Drag from these sources can, however, be avoided by the inclusion of fairing between components and with careful design, a reduction in drag can instead be obtained [2].

Wave drag is the result of entropy loss through shock waves that can form when there is supersonic flow over an aircraft. This can become a significant component of total drag if strong shock-waves are allowed to form on aerodynamic surfaces such as the wing. Wave drag can, however, be avoided through the use of increased wing sweep, supercritical aerofoil design [5] and shock control methods [6].

There has been extensive research on the reduction of skin friction as it is a significant source of drag. Two approaches to this are possible: turbulent drag reduction and the extension of laminar flow [2, 7]. Turbulent drag reduction attempts to reduce skin friction by modifying turbulent flow features. This has wide applicability as the majority of flow over modern commercial aircraft is turbulent. Such methods include synthetic jets, riblets and large eddy breakup devices [8]. The alternative approach is extension of laminar flow by delaying its transition from laminar to turbulent. As laminar flow can have as much as 90 percent less skin friction drag than turbulent flow [9], and as most flow over modern aircraft is turbulent, there is potential for substantial drag reductions.

Transition from laminar to turbulent flow is due to the growth of small disturbances within the boundary layer flow. If unstable, these instabilities will increase in magnitude until they result in the breakdown of laminarity [10]. Methods available for reducing instability growth are Laminar Flow Control (LFC), Natural Laminar Flow (NLF) or Hybrid Laminar Flow Control (HLFC).

LFC is the active and continuous modification of the boundary layer through surface cooling or suction [11]; as altering the temperature or velocity profile through the boundary layer is found to have a strong effect on flow stability. LFC is typically associated with boundary layer suction as this has seen more extensive research [9]. NLF makes use of the strong effect pressure gradient has on flow stability. An aerodynamic surface can be designed in such a way as to create the required pressure gradient to dampen boundary layer instabilities. This is considered a passive approach as the pressure gradient is induced naturally during flight.

The choice of LFC or NLF depends on the application and flow conditions being experienced. LFC is able to provide instability damping where NLF is not effective. Such areas include aircraft fuselage, highly swept wings [11], wings with large chord length and when at high transonic speeds. Where effective, NLF is preferable to LFC as it requires no additional suction or cooling components which increase aircraft weight, manufacturing complexity and cost [2]. Running of a LFC system also requires power which, when siphoned from the propulsion system, reduces aircraft performance. Due to the drawbacks seen with both approaches, a combined Hybrid Laminar Flow Control (HLFC) approach has seen much research. This entails the use of NLF with LFC only where it is not possible to suppress the growth of boundary layer instabilities passively, such as towards the leading edge of highly swept wings. Combining LFC and NLF reduces the suction requirements and complexity of the LFC suction system but also allows for effective instability suppression where not possible with NLF alone. Further developments in LFC and HLFC make use of passive suction, routing the suction chambers to a location on the aircraft with low pressure.

Several major research efforts involving wind tunnel and flight testing of NLF and HLFC have been carried out in Europe. Flight testing of a NLF glove and wind tunnel testing of a half-scale model was carried out by DLR in the late 1980s as part of the national German laminar flow technology programme [12]. This led to the flight test of a second NLF wing glove as part of the European Laminar Flow Investigation (ELFIN) program which began in the early 1990s [13]. Airbus, in partnership with DLR and ONERA, carried out design, wind tunnel and flight testing of HLFC applied to the fin of an A320 test aircraft. This was undertaken in the 1990s and done as part of the Laminar Fin Program [14]. The most recent flight tests were carried out by Airbus in 2017 as part of the Breakthrough Laminar Aircraft Demonstrator in Europe (BLADE) programme, under the European Clean-sky 1 project [15]. This involved the testing of an A340 with NLF outboard wing sections, shown in figure 1.2.

Although LFC and HLFC are effective in obtaining extended laminar flow where not possible with NLF, it is still desirable to avoid suction-based systems entirely if possible. Therefore, aircraft designs exploiting NLF while having low sweep and reduced Mach number have been proposed. Novel aircraft configurations such as those with strut-braced wings also have excellent potential for NLF [17].

While NLF has seen extensive research, laminar flow is often not considered during the design of, and not obtained on, most commercial transport aircraft. One of the main reasons for this is that transition occurs through a number of complex instability mechanisms and is often sensitive to small changes in aerodynamic shape, surface and flow quality and the

Figure 1.2: *Airbus BLADE NLF wing section (Photo: P. Pigeyre / Master Films. Copyright: Airbus) [16].*

chosen flight conditions [18]. As a result, obtaining extended laminar flow during flight is challenging. Maintaining extended laminar flow over a wide range of operating conditions and at varying surface and flow quality is even harder. For NLF to become viable on modern commercial aircraft, it must be made robust to the factors effecting transition. This requires design at both on and off-design conditions, with consideration for uncertainty in many other input variables.

Research in recent years has, however, indicated that optimisation and robust design methods may be effective at tackling these issues [19–21]. Thanks to increasing computational power, more complex optimisation problems can now be considers. Increasing the dimensionality of the design problem, considering multiple design objectives and possible input uncertainties should each help to produce NLF aerofoils and wings with a more consistent performance over a wider range of conditions.

1.1 Thesis Aim

The aim of this work is to investigate the use of robust design and optimisation methods applied to NLF aerofoil and wing design. The goal of this research is to identify means of improving aircraft performance by reducing drag via the extension of NLF while also reducing performance sensitivity to changes in operating conditions, flow and surface quality. This is pursued as a lack of robustness to these factors is one of the issues currently limiting the wide-spread use of NLF as a drag reduction method.

Chapter 2 introduces the fields of flow transition, transition modelling and NLF design. Chapter 3 following this provides some background knowledge on optimisation and robust design, and the current state-of-the-art in applying these methods to the development of NLF aerofoils and wings. The current limitations to the practical use of NLF on modern commercial aircraft are then assessed and the specific objective of this study outlined.

Chapter 2

Natural Laminar Flow

2.1 Flow Transition

At its fundamental level, flow transition is a result of environmental disturbances entering the boundary layer. These can originate from turbulence within the freestream flow or interaction of the flow with surface roughness and irregularities through a process known as receptivity [22]. Flow stability is determined by the growth or decay of these disturbances over time, through space or a combination of both [7]. A flow is stable if disturbances decay while an unstable flow results in disturbance growth. Disturbance growth results in the formation of regular oscillations within the boundary layer, referred to as instability waves. The shape and behaviour of each instability wave depends on the amplitude, frequency and phase of the initial flow disturbance [23]. A wide range of disturbance characteristics are possible and result in several different paths to transition. These are shown in figure 2.1.

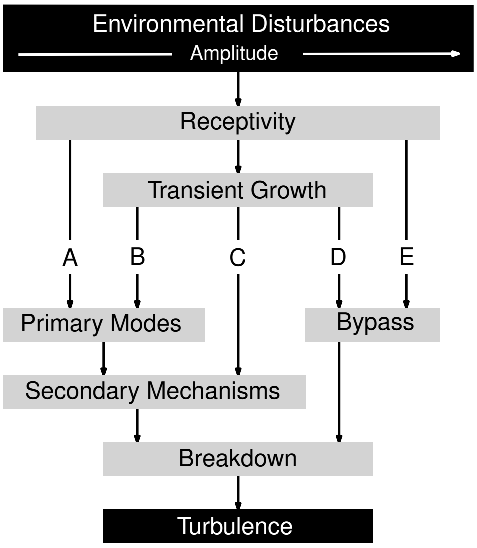

Figure 2.1: *Possible paths to transition [24].*

For small disturbance amplitudes, path A is taken. The growth of boundary layer instabilities is linear and occurs slowly over a large distance. These are referred to as primary instabilities. The continued amplification of primary instabilities results in the creation of secondary instabilities which lead to a rapid breakdown of the flow and the onset of transition [25]. This path to transition is sometimes referred to as 'Natural Transition' [26]. An alternative path to transition occurs when environmental disturbances are large. The development of primary and secondary instabilities is skipped as turbulent flow features form directly within the laminar boundary layer and result in breakdown of the flow. This is path E, known as bypass transition.

Natural transition and bypass transition both occur when disturbances with an unstable wavelength enter the boundary layer flow. It is also possible for transition to occur when all disturbance frequencies are stable. This is through a process known as transient growth, where stable disturbances interact and see large amplification before decaying. This growth can result in primary instabilities (path B), secondary instabilities (path C) or may be large enough to trigger bypass transition (path D).

Regardless of the path to transition, eventual destabilization and breakdown of the flow is due to the development of what are referred to as 'Emmon spots' or 'turbulent spots'. Each spot begins with a point-like instability of the laminar flow that grows linearly downstream. Following this is an arrow head shaped region of turbulent flow of smaller scale than the boundary layer height [27]. Breakdown of the flow refers to the initialization and growth of these spots which eventually engulf the entire boundary layer flow.

Natural transition (path A) is of most interest for the development of NLF as disturbance amplitudes are typically small during flight due to low freestream turbulence intensity levels [28, 29]. Primary instabilities are also the easiest to model due to their linear behaviour. As transition occurs quickly after non-linear effects occur, the end of this linear region provides a good approximation of the final transition location. The following sections cover different stages of the natural transition process and some of the properties that flow stability and transition are sensitive to.

2.1.1 Flow Stability

A disturbance wave of a given frequency (ω) at a given Reynolds (Re) number will be in one of three possible states: amplifying, neutral or decaying [30]. Calculating the stability of disturbances with a range of frequencies over a range of Reynolds numbers allows for a neutral stability curve plot to be generated, such as shown in figure 2.2. In both plots, the x axis shows Reynolds number based on boundary layer thickness (Re_δ), the y axis shows frequency based on boundary layer thickness (ω_δ) and the contour lines represent neutral stability, separating the stable and unstable regions.

Disturbances have a fixed frequency moving downstream, as indicated in figure 2.2b by the horizontal dashed line. Disturbances are initially stable but can encounter an unstable region downstream. Disturbances will normally decay in the stable region and amplify in the unstable region. However, if amplification through the unstable region is large, secondary instabilities can develop and amplification will continue even on re-entering the stable region. This will result in a rapid breakdown of the flow to turbulence [30].

Two different forms of the neutral stability curve are typically observed. Figure 2.2a shows a neutral stability curve with an unstable region starting at a low Reynolds number and extending to $Re_\delta \to \infty$. Given that the flow is unstable at both low and high Reynolds numbers, the instability is not dependent on viscosity and so is considered inviscid. Inviscid instability is directly related to the mean boundary layer velocity profile shape. An inflection point within the velocity profile is found to be a sufficient condition for the flow to be unstable [22]. Free-shear flows, such as jets, wakes and separated flows, and wall bounded flows under an adverse pressure gradient are prone to inviscid instability [28, 30].

Figure 2.2b shows the neutral stability curve for a boundary layer flow with viscous instability. In this case, disturbances at all frequencies are damped when Reynolds number is sufficiently large and inertial forces dominate. Thus, viscous forces have a destabilising effect on the flow for a finite Reynolds number range [30]. A flow with viscous instability can be unstable without an inflection point within the boundary layer velocity profile [30]. Wall-bounded flows have viscous instability when incompressible and under neutral or favourable pressure gradient [28, 30].

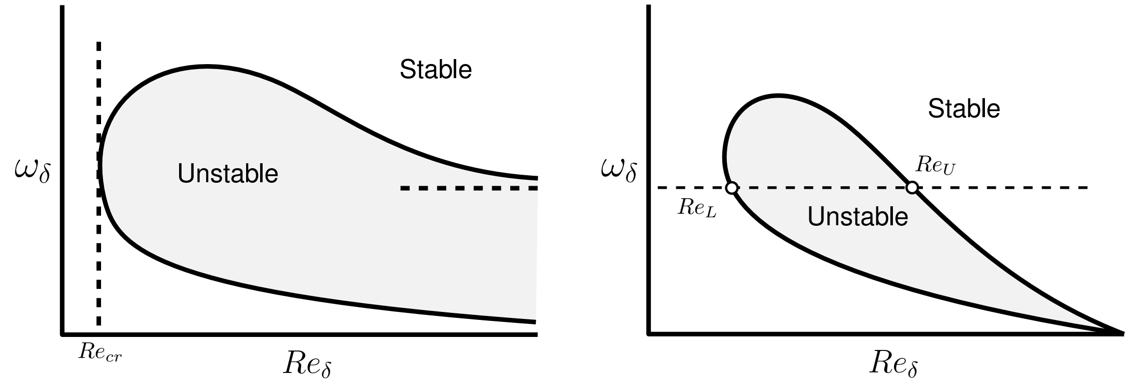

(a) *Inviscid instability* **(b)** *Viscous instability*

Figure 2.2: *Example of neutral stability curves for a two-dimensional flow [30].*

All disturbances are stable and decay below what is referred to as the Critical Reynolds number ($Re_\delta|_{\text{cr}}$). It would be desirable to keep Reynolds number below this critical value as disturbances at all frequencies are stable. However, critical Reynolds number is typically of the order of $Re_\delta|_{\text{cr}} = \mathcal{O}[10^3]$ for wall-bound viscous dominated flows and so this is not possible [28]. A low Reynolds number also causes a boundary layer flow to be less resistant to separation. If this occurs, the resulting free-shear layer is also highly susceptible to inviscid instabilities and can quickly transition [28]. This is an important design consideration for low Reynolds number NLF.

2.1.2 Primary Instabilities

There are several types of primary instability. For transonic flows over swept wings such as those seen on commercial aircraft, the most important primary instability types are Tollmien-Schlichting, crossflow, attachment line and centrifugal [10].

Tollmien-Schlichting (TS) waves are stream-wise viscous instabilities seen as travelling sine waves of vorticity within the boundary layer flow. These are the primary transition mechanism for un-swept wings due to their two-dimensional nature and typically see slow amplification resulting in transition mid-chord [31].

Crossflow (CF) waves are three-dimensional inviscid instabilities found to dominate swept flow transition. The combination of sweep and pressure gradient on a swept wing results in highly curved inviscid streamlines at the boundary layer edge, as shown in figure 2.3. The same effects occur within the boundary layer, but the curvature is greater as the fluid has lower momentum. This difference in curvature is strongest towards the leading and trailing edges [32]. Splitting of the boundary layer velocity profile into components normal and tangential to the inviscid streamline is shown in figure 2.4. The flow normal to the inviscid streamline is referred to as the crossflow component. As this is zero at the boundary layer edge, and zero at the wall due to the no-slip condition, there exists an inflection point within the velocity profile which leads to inviscid instability growth.

Crossflow waves can be stationary or travelling although typically only one type will be dominant within the flow. While travelling waves see larger amplification, stationary modes are found to dominate the transition process at low free-stream turbulent intensity levels seen during flight. This is due to their interaction with surface roughness elements at these conditions [33].

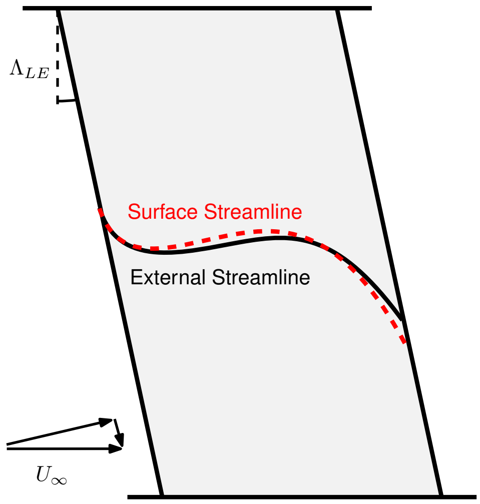

Figure 2.3: *External and surface streamlines over a swept wing.*

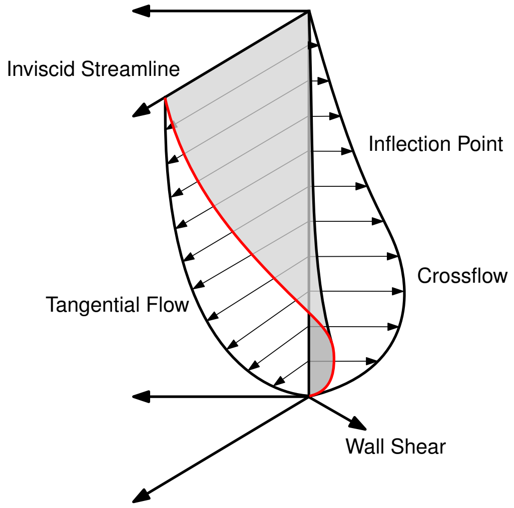

Figure 2.4: *Boundary layer velocity profile with stream-wise and crossflow velocity components [34].*

Attachment line instability and contamination must be avoided should any laminar flow be obtained on a swept wing. Attachment line instability is due to the interaction of acoustic waves with surface roughness, defects and contamination at the leading edge [35]. Attachment line contamination is the propagation of turbulence generated at the wing-root intersection along the wing leading edge. This can occur for wings with leading edge sweep larger than 20° and results in span-wise flow perturbations that trigger early transition [35].

To avoid attachment line transition and contamination, the momentum thickness Reynolds number at the attachment line must be kept below a specific threshold in each case. This can be calculated using equation 2.1 if the leading edge represents a general elliptical shape [32, 35]. Λ_{le} is the leading edge wing sweep, r is the leading edge normal aerofoil radius and ε is the ellipticity. To avoid attachment line transition, Re_θ must be kept below $230 - 240$, while to avoid attachment line contamination from propagating along the leading edge, Re_θ should be kept below $90 - 100$ [35].

$$Re_\theta = 0.404 \left[\frac{U_\infty r \sin^2(\Lambda_{le})}{(1+\varepsilon)\, \nu \cos(\Lambda_{le})} \right]^{\frac{1}{2}} \tag{2.1}$$

Centrifugal instabilities, otherwise known as Gortler instabilities, occur in flows travelling over concave surfaces [28]. This causes the creation of stationary counter-rotating vortices parallel to the stream-wise flow that change the stream-wise velocity profile and leads to the development of secondary instabilities. As concave surfaces are not typically used in locations where laminar flow can be obtained, centrifugal instabilities are usually not an issue [31].

2.1.3 Secondary Instabilities

Large amplification of primary instabilities results in the development of secondary instabilities. These are highly non-linear, of very high frequency [36] and play an important role in transition. Once secondary instabilities appear, rapid development of turbulent spots and breakdown of the laminar flow occurs. This process typically leads to fully turbulent flow 5 percent of the chord length downstream of the initial secondary instability [33]. Visualization of the transition front provides insight into the dominant instability type and secondary instabilities present. Figure 2.5 shows visualisation of the transition front for swept wings under different flow conditions. This is achieved using naphthalene sublimation.

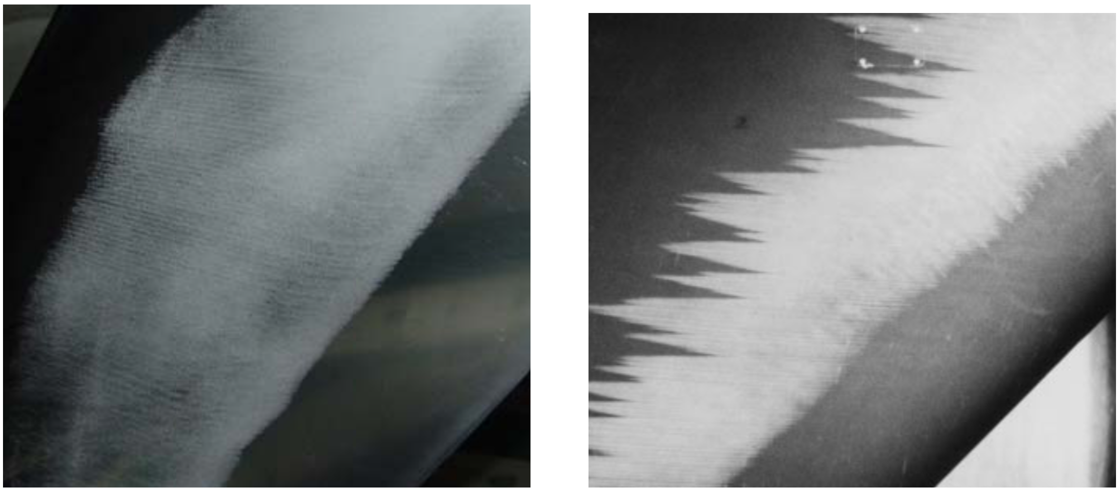

(a) *Tollmien-Schlichting dominated [37]*

(b) *Crossflow dominated [34]*

Figure 2.5: *Naphthalene sublimation visualization of flow transition fronts resulting from different primary instability dominance. Flow in each case is moving from left to right.*

For flows dominated by TS instabilities, secondary instabilities are seen as a series of span-wise peaks and valleys distorting the uniform TS waves. These become more pronounced as the flow develops [25] however the transition front itself is uniform in the span-wise direction, as seen in figure 2.5a. When transition originates from CF instability growth, modulation in the span-wise mean flow results in a velocity profile inflection point and local development of secondary instability [29]. This leads to a local breakdown of the flow and a saw-tooth transition front pattern [33], as shown in figure 2.5b.

2.1.4 Compressible Flow Stability

Increasing Mach number introduces compressibility effects into the boundary layer flow. At subsonic speeds, this does not change the fundamental physics of boundary layer flow stability and incompressible stability theory can be used [7]. The effect of compressibility does, however, become important at higher speeds.

For transonic flows, compressibility has a small stabilizing effect on two-dimensional instability waves, but a large destabilising effect for flows over surface defects [7]. As such, increasing Mach number lowers the amount of instability amplification required for TS induced transition [38]. Compressibility also increases the angle at which instability waves move in relation to the streamline flow, causing instability waves to become increasingly three-dimensional [39]. Crossflow instabilities remain relatively invariant to increasing Mach number up to $M = 1$, and incompressible stability theory still gives acceptable results for the prediction of crossflow amplification [39]. However, due to the difference in amplification predicted for stream-wise instabilities, compressible linear stability theory should be used for transition prediction of transonic flows [40].

2.1.5 Receptivity

Receptivity is the process by which external disturbances enter the boundary layer flow. These can originate from two sources: free-stream turbulence and acoustic noise [41]. Although not a source of disturbance, surface roughness plays a pivotal roll in the receptivity process as the interaction between disturbance sources and roughness elements introduces short scale variations into the boundary layer flow [42]. Flow stability is unaffected by surface roughness below a specific diameter [43] but has a strong effect on stability above this with very large surface roughness levels triggering bypass transition.

Both disturbance sources contribute to the development of Tollmien-Schlichting instability waves. For receptivity to take place, however, the environmental disturbances need to reduce in wavelength. This is achieved at locations where the boundary layer rapidly changes in thickness such as at the leading edge and at surface discontinuities [44]. As such, the initial amplitude of TS instability waves are larger as surface roughness increases or in the presence of two-dimensional surface irregularities such as steps, bumps and gaps [42]. Although both disturbance sources contribute to receptivity, the interaction of acoustic waves with the surface roughness elements is found to have a much stronger effect [44].

Crossflow instabilities can also originate from both disturbance sources, although free-stream turbulence interacting with surface roughness has the stronger effect [26]. Turbulent intensity controls the type of crossflow instability waves that develop within the flow. For low turbulence levels seen in flight, stationary waves dominate the transition process. These are a direct result of the boundary layer flow interacting with surface roughness elements [26]. Figure 2.6 shows experimental results for stationary crossflow amplification at low turbulence levels (0.1% $< Tu <$ 0.3%) such as those seen during flight. The amount of stationary crossflow instability amplification required to trigger transition under these conditions reduces with increasing surface roughness height. Increasing turbulent intensity results in stronger travelling wave amplification within the flow while increasing both turbulent intensity and surface roughness causes interdependent stationary and travelling waves to dominate [26]. The amplification required to trigger transition then becomes invariant to further increases in either property [26].

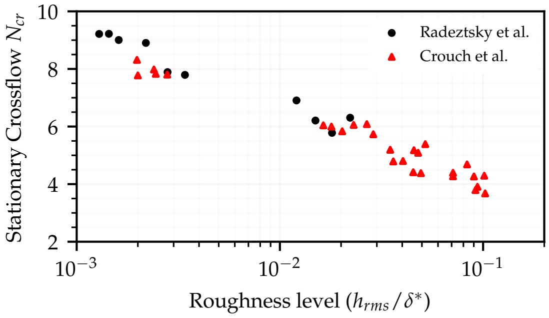

Figure 2.6: *Experimental results from Radeztsky et al. [43] and Crouch et al. [26] showing stationary crossflow critical amplification factor against normalized surface roughness at low freestream turbulent intensity ($Tu = 0.1 - 0.3\%$).*

2.2 Transition Modelling

While there are many models available for simulating turbulent flow in computational fluid dynamics (CFD), there are few for flow transition. This is in part due to the complexity of the transition process [45]. The different paths to transition each require different modelling considerations, and many of the non-linear effects can prove too challenging to solve. There can also be difficulties in combining transition modelling methods with modern flow solvers and optimization algorithms. As transition location is sensitive to changes in geometry shape and flow conditions, accurate modelling of the flow and transition location is crucial. It is therefore desirable to couple transition modelling methods to high fidelity flow solvers, such as those based on Reynolds Averaged Navier-Stokes (RANS) equations. Both flow solver and transition models should also couple well with modern optimization algorithms.

The different approaches available for transition modelling can be categorized as either empirical criteria or physical modelling. Empirical criteria derive some variable from boundary layer properties that can be calibrated against experimental results so that when its value exceeds some limit, transition occurs. Many examples of empirical criteria are given by Arnal [46] with a popular approach linking transition location to momentum thickness Reynolds number Re_θ [47]. These criteria provide a simple and very computationally cheap method for predicting transition with acceptable accuracy, but do not model the actual flow physics behind the transition process.

Physical modelling of the transition process is the most mature and popular approach for transition location prediction [41]. Models of this type are based on stability theory and try to determine transition location based on boundary layer instability growth. This approach is desirable as the fundamental physics behind flow transition are modelled, although the models represents a simplified versions of the real process which is complex.

2.2.1 Linear Stability Theory

Mack [30] provides an excellent derivation of linear stability theory, which will be summarised here. Beginning with the Navier-Stokes equations, flow properties are split into mean and fluctuating components. The mean flow components satisfy the governing equation and are removed, leaving only the fluctuating terms. Quadratic fluctuating terms are also removed as they are considered small, linearising the equations. The parallel flow assumption flow is then made, where span-wise and wall normal base flow velocities are set to zero. These terms are removed from the linearised Navier-Stokes equations. A mathematical representation for the flow disturbance is then selected. This is a sinusoidal wave described by equation 2.2 where r is any flow property and $\hat{r}(y)$ is its amplitude function which, due to the parallel flow assumption, is dependent on y only. The terms α and β are x and z components of the wave-number $\hat{k}$, ω is frequency and t is time.

$$r = \hat{r}(y) \exp\left[i(\alpha x + \beta z - \omega t)\right] \tag{2.2}$$

Equation 2.2 is substituted into the linearised Navier-Stokes equations, producing a set of ordinary differential linear stability equations. For three-dimensional flows, there are 8 equations if compressible or 6 equations if incompressible. For two-dimensional flows, there are 6 equations if compressible while the single fourth order Orr-Sommerfeld differential equation is obtained if incompressible. Boundary conditions for boundary layer flows dictate that the disturbance disappears both at the wall and far from the wall as $y \to \infty$.

A disturbance wave has neutral temporal and spatial stability if α, β and ω are all real. If α or β are complex, the disturbance amplitude will change as it propagates in space while if ω is complex, as it propagates in time. For spatial amplification, the flow disturbance takes the form shown in equation 2.3, where α_i determines disturbance stability in the stream-wise direction and β_i determines disturbance stability in the span-wise direction. The disturbance wave angle is calculated as $\phi = tan^{-1}(\beta_r/\alpha_r)$. This angle is in relation to the x direction and is used to identify the type of instability found. Angles between $0 - 40^\circ$ indicate a TS wave, while angles between $85 - 90^\circ$ indicate a CF wave [41].

$$r = \hat{r}(y) \exp\left[-(\alpha_i x + \beta_i z)\right] \exp\left[i(\alpha_r x + \beta_r z - \omega_r t)\right] \tag{2.3}$$

$$\begin{array}{llll} -\alpha_i < 0 & \text{Stable} & -\beta_i < 0 & \text{Stable} \\ -\alpha_i = 0 & \text{Neutral} & -\beta_i = 0 & \text{Neutral} \\ -\alpha_i > 0 & \text{Unstable} & -\beta_i > 0 & \text{Unstable} \end{array}$$

The linear stability equations can be grouped by terms and written in matrix form such that equation 2.4 is obtained. The matrix F contains the basic flow properties such as mean flow velocities, pressure and additional terms if compressible, along with the disturbance wave properties α, β and ω. The matrix K contains all disturbance amplitude functions and derivatives.

$$FK = 0 \quad \text{where} \quad \begin{array}{l} F(\text{Flow Properties}, \alpha, \beta, \omega) \\ K(\text{Amplitude Functions}) \end{array} \tag{2.4}$$

The linear stability equations now represent an eigenvalue problem where non-zero solutions, referred to as normal modes, exist only if $\det(F) = 0$. Therefore, at a specific stream-wise station and specified ω, only certain α and β values will produce non-zero disturbance amplitudes. Boundary layer flows will have a finite number of discrete solutions at each stream-wise position and ω value. For incompressible subsonic flows where $\beta = 0$, only one of these solutions is found to become unstable and so is referred to as the first mode. For compressible and supersonic flows, additional unstable modes may exist.

2.2.2 e^N Transition Model

Predicting transition locations using linear stability theory is done using the e^N transition model developed by Smith and Gamberoni [48] and Van Ingen [49]. The e^N model uses the fact that transition occurs very soon after a disturbance wave first exhibits non-linear growth with the observation that non-linear growth occurs when a disturbance's amplitude increases by some critical factor from its initial amplitude.

The mathematical relationship used by the e^N transition model is found by manipulating equation 2.5 showing the spatial disturbance wave equation with no span-wise disturbance amplification ($\beta_i = 0$). The wave amplitude function $\hat{r}$ does not depend on x or t and so represents the initial r value (r_0) at the selected y. Dividing the equation by r_0 and taking the natural log of both sides results in equation 2.6. The amplitude of a wave function is represented by its real component, and so the natural log of the initial and final amplitude ratio is shown in equation 2.7.

$$r = \hat{r}(y) \exp\left[-(\alpha_i x)\right] \exp\left[i(\alpha_r x + \beta_r z - \omega_r t)\right] \tag{2.5}$$

$$\ln(r/r_0) = [-\alpha_i x][i(\alpha_r x + \beta_r z - \omega_r t)] \tag{2.6}$$

$$\ln(A/A_0) = -\alpha_i x \tag{2.7}$$

Disturbances within the boundary layer have a fixed frequency but varying α_i as they move downstream. The upper plot in figure 2.7 shows an example neutral stability curve where the horizontal line represents a disturbance wave. As α_i varies along the stream, the natural log of the amplitude ratio is calculated by taking the integral of α_i from $x_0 \rightarrow x$ using equation 2.8. Evaluating $\ln(A/A_0)$ along the stream produces an amplification envelope, shown on the lower plot in figure 2.7. This is done for a wide range of disturbance frequencies, producing a number of amplification envelopes. As transition occurs when a disturbance wave first exceeds some threshold amplification factor, the maximum amplification ratio at each stream-wise position is obtained using equation 2.9. This is referred to as the amplification factor, or N-factor, envelope. The threshold amplification factor is referred to as the critical N-factor.

$$\ln(A/A_0) = -\int_{x_0}^{x} \alpha_i \, dx \tag{2.8}$$

$$N = \max\left(\ln(A/A_0)\right) \tag{2.9}$$

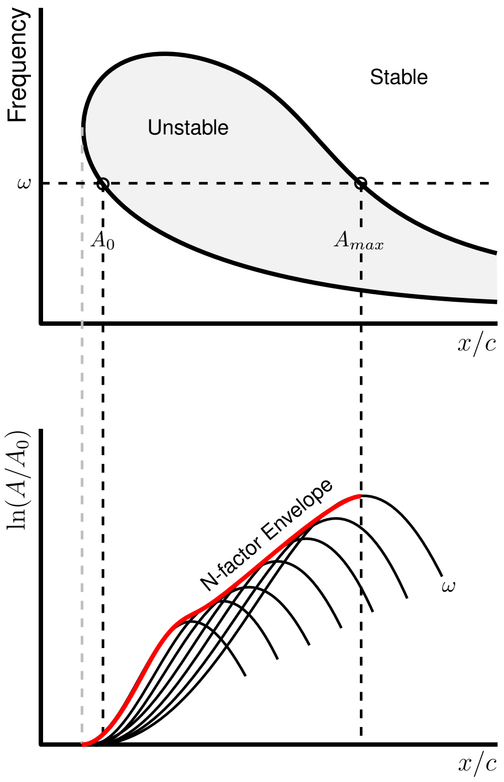

Figure 2.7: *Use of neutral stability plot to generate N-factor envelope for e^N transition model [41].*

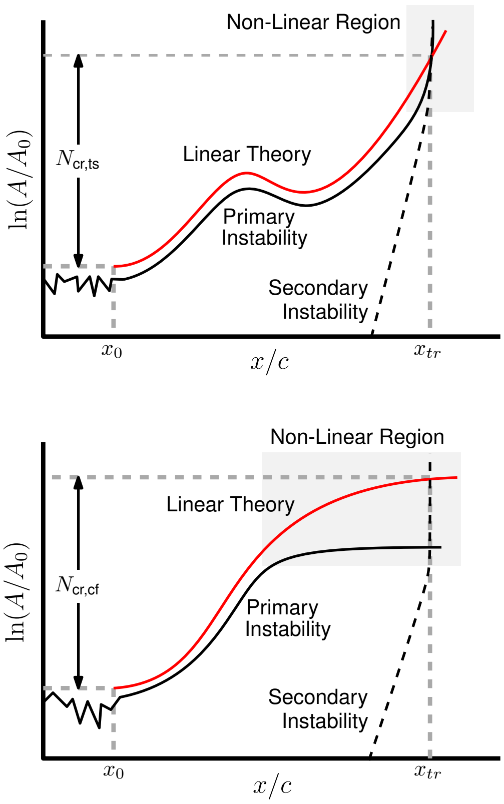

Figure 2.8: *Instability growth and linear modelling for Tollmien-Schlichting and Crossflow instability envelopes [50].*

Importantly, the e^N transition model only makes use of the ratio between the initial and final amplitudes and does not require the actual value of either. This is beneficial as it avoids modelling of the receptivity process which is very complex and still regarded as a ”missing piece” in developing a more thorough amplitude-based transition model [42]. Although the need to model the receptivity process is avoided, the initial amplitude of boundary layer disturbances do play a role in determining transition location. As such, the critical N-factor cannot be calculated and must instead be calibrated against wind tunnel and flight test data obtained at the desired surface roughness, free-stream turbulent intensity levels and, if using compressible theory, Mach number. This ensures that the threshold used for transition modelling is similar to the value found at real flight conditions.

Figure 2.8 shows the section of instability growth that linear stability theory and e^N method attempt to model. Both plots show instability amplitude against chord length for primary and secondary instabilities. The upper plot shows growth of a TS instability wave while the lower plot shows growth of a CF instability wave down-stream. Towards the leading edge, receptivity continuously introduces disturbances into the boundary layer that decay in the stable flow region, resulting in a constant but noisy maximum disturbance amplitude [50]. As the flow moves into the unstable region, maximum disturbance amplitude begins to rise for both instability types. Linear stability theory is able to model this period of growth well but eventually non-linear effects will occur. Accuracy of the linear theory method breaks down here and the eventual development of secondary instability then leads to transition. As can be seen, linear theory is better able to model the growth of TS instability waves compared to CF instabilities due to the smaller non-linear amplification region.

2.2.3 $\mathbf{e^N}$ Analysis of Three-Dimensional Flows

Although the e^N model is limited to analysis of two-dimensional boundary layer slices, it can predict transition for three-dimensional flows. However, this does increase model complexity. For two-dimensional incompressible flows, disturbance will have a wave angle of zero ($\phi = 0$ so $\beta_r = 0$) and see no span-wise amplification ($\beta_i = 0$). For three-dimensional flows, disturbances will have a non-zero wave angle and may see amplification in the span-wise direction. This is also true for compressible flows where wave angle may not be zero even if the flow is two-dimensional [41]. For infinitely-swept and swept-tapered wings, it is often assumed that there is still no amplification in the span-wise direction ($\beta_i = 0$) [41]. However, wave angle needs to be considered in the solution process. Methods for this are the envelope, envelope of envelopes or dual envelope (or $N_{ts} - N_{cr}$) strategies [41].

The envelope approach requires calculation of the amplification rate as a function of wave angle at each chord-wise location, so that the maximum amplification rate and wave-angle can be obtained. The envelope of envelopes approach extends the normal e^N model by analysing many disturbances with different frequencies and also with different wave angles or span-wise wave numbers. Thus amplification envelopes for various angle or wave-numbers can be created, and the maximum amplification envelope from these then found.

The dual envelope method is favoured by the European aerospace industry [41, 51]. The approach separates TS and CF instabilities by wave angle and finds a maximum amplification envelopes for each. Both then have their own critical N-factor threshold. As some interaction between the two instability types occur at high amplifications, a limiting curve is defined [41, 50]. This can take three shapes depending on the strength of the interaction, as shown in figure 2.9. Based on flight test data, a weak interaction type is observed at the speeds and altitudes common for civil transport aircraft [41].

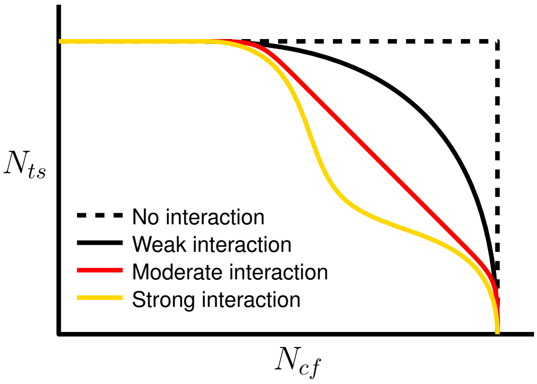

Figure 2.9: *Critical N-factor mixing curves with different instability interaction strengths for the dual envelope e^N transition model (recreated from [41]).*

2.2.4 e^N Model Calibration

The critical N-factor limits used in the e^N transition model require calibration against experimental or ideally flight test data. For three-dimensional flows using the dual envelope method, this requires calibration of both N_{ts} and N_{cf} critical N-factor limits. An example of data available for this purpose comes from two independent NLF glove flight tests carried out using a Fokker 100 aircraft as part of the European Laminar Flow Investigation (ELFIN) program and using the ATTAS aircraft, done as part of the national German laminar flow technology programme [12]. Both flight tests took place over a range of Reynolds numbers, Mach numbers and with NLF gloves at variable sweep angles. A summary of these conditions as presented in table 2.1.

Application of the dual envelope approach to linear stability theory on the recorded pressure distributions at these various conditions allows for the calculation of the N_{ts} and N_{cf} values at transition. These are shown in figure 2.10, calculated using incompressible and compressible linear stability theory. When analysed using incompressible linear stability theory, the results between the two flight tests agree well for both N_{ts} and N_{cf}. When analysed using compressible linear stability theory, results from each flight case differ substantially. While N_{cf} values have decreased slightly at each point for both test cases, N_{ts} values for the Fokker 100 case have reduced much more than for the ATTAS case. This difference is attributed to the higher Mach numbers reached during the Fokker flight tests [51] and highlights the dependence of N_{ts} on Mach number when compressible linear stability theory is used.

Table 2.1: *Aircraft flow condition ranges for the ATTAS and Fokker 100 NLF flight tests [51].*

Aircraft	Reynolds Number	Mach Number	Sweep Angle
ATTAS	$12 - 23 \times 10^6$	$0.33 - 0.67$	$19.5° - 22.4°$
Fokker 100	$12 - 23 \times 10^6$	$0.50 - 0.80$	$17.0° - 24.0°$

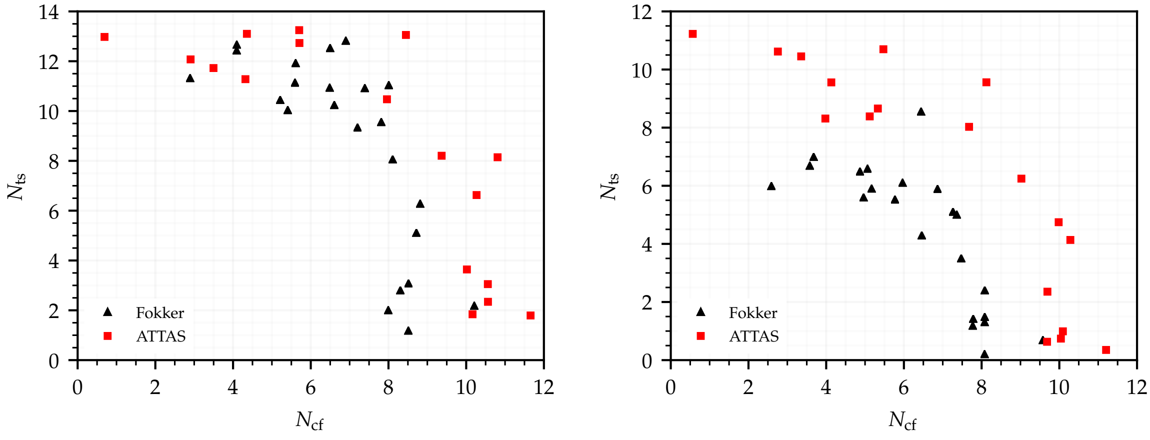

(a) *Incompressible*

(b) *Compressible*

Figure 2.10: *(N_{cf}, N_{ts}) data points calculated using the e^N dual envelope approach with incompressible and compressible linear stability theory from pressure distributions obtained from the Fokker 100 and ATTAS NLF flight tests [51].*

Analysis of the flight test data [38, 51–53] finds that critical N_{cf} is relatively independent to changes in Mach number, Reynolds number and sweep angle for both compressible and incompressible approaches. This can be seen by comparing N_{cf} values between figures 2.10a and 2.10b. N_{ts} appears insensitive to Mach number using incompressible theory but is highly sensitive when analysed with compressible theory. This is again seen in figures 2.10a and 2.10b. Thus, incompressible stability theory is considered to give a more universal critical N-factor value for N_{ts} and N_{cf} regardless of the operating conditions [38, 50].

However, compressible linear stability theory should be used for transonic test cases, and so compressible critical N-factor limits are required. To obtain these, analysis at the chosen flight conditions should first be carried out using incompressible linear stability theory. The values of N_{ts} and N_{cf} can then be altered while carrying out stability analysis using compressible stability theory so as to match the transition locations found from the incompressible method. Critical N-factor values that best accomplish this are then used.

2.2.5 $\mathbf{e^N}$ Model Coupling to Flow Solvers

The main drawback to linear stability theory based transition modelling is the difficulty in coupling it with RANS-based flow solvers and optimisation frameworks. Menter et al. [54] proposed several conditions that transition modelling method should satisfy for easy integration with any RANS-based solver. These included the use of only local mathematical operations and the ability to predict transition locations for three-dimensional simulations.

Both of these conditions are not met by the e^N transition model. The e^N model requires boundary layer velocity profiles at each chord-wise position, which are difficult for a RANS-based solver to obtain. This is because the edge of the boundary layer is difficult to determine, many elements will make up a chord-wise boundary layer slice and grids may be split into different blocks for parallel computing [54]. The e^N model is also only able to model transition on an entire three-dimensional aircraft or wings by performing transition analysis on stacked two-dimensional slices.

Coupling of the e^N transition model with CFD codes is therefore somewhat complex and is outlined in figure 2.11. First, a flow solution with fully turbulent or laminar flow is obtained. A two dimensional streamline slice is then passed to a boundary layer solver which is used to generate velocity and pressure profiles along the chord-length. This is then passed to the stability analysis code which generates critical N-factor envelopes and locates a transition position. Transition is then prescribed at this location in the CFD flow solver and a new flow solution is obtained. The solution from this is again analysed and a transition location found. This process is repeated until the transition location converges to its final value.

Given the complexity of effectively coupling stability based transition models with modern flow solvers, there has been a push for truly local transition modelling methods. This has lead to the development of transport equation models. These can be thought of as an extension to empirical criteria. The general idea is to model transition using a flow property referred to as intermittency γ that dictates the laminarity of the flow, where $\gamma = 0$ is fully laminar and $\gamma = 1$ is fully turbulent. When applied to CFD, this term is used to scale eddy viscosity within the flow [54]. Intermittency is then related only to local flow properties, rather than local boundary layer properties such as used in empirical criteria.

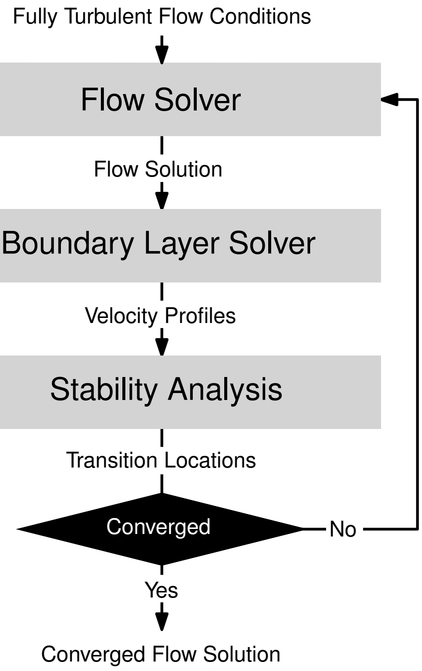

Figure 2.11: *Workflow for CFD solver and linear stability theory transition model coupling.*

The most popular transport equation based approach is the $\gamma - Re_\theta$ model, developed by Menter et al. [47, 55]. This is a two equation transition model for intermittency and transitional momentum thickness Reynolds number. Another transport equation based model has been developed by Coder and Maughmer [56]. This is based on the work of Drela and Giles [57] where amplification factor is related to local flow variables. Transport equation based approaches have seen a large amount of research over the past decade and are implemented in many commercial RANS-based CFD solvers. While the approach is maturing, physical modelling of flow stability has remained the preferred method used within the aerospace industry [15, 41].

2.3 Delaying Transition

The key to the design of NLF aerofoils and wings is the passive prevention of transition. Firstly, efforts must be made to ensure that transition follows the natural path, rather than via bypass or attachment line contamination. Once this is done, passive extension of laminar length is obtained via the tailoring of aerodynamic pressure gradient so as to dampen the growth of primary instabilities within the boundary layer.

The type of pressure gradient required depends on the instability types that dominate the flow transition process. TS instability waves are suppressed via the use of a favourable pressure gradient. This can be used to reduce instability amplification, remove inflection points from within the boundary layer, re-laminarise a turbulent boundary layer and reduce the size of turbulent spots [7, 45, 58, 59]. Favourable pressure gradient is, however, unsuitable for flows dominated by crossflow instabilities, as this causes instability amplification especially towards the leading edge. Instead, a strong leading edge pressure rise followed by a slight adverse pressure gradient is best [60].

These conflicting pressure gradient profiles are shown in figure 2.12. The type of instability dominating the flow transition process is determined by the sweep angle Λ. Three sweep regimes can be defined: TS dominated when $\Lambda < 25°$, TS and CF dominated when $25° < \Lambda < 30°$ and CF dominated when $35° > \Lambda$ [9]. Flows with transition dominated by TS instability waves are found on subsonic aircraft where no sweep angle is needed. For transonic aircraft such as modern commercial transport aircraft, sweep angles within the TS and CF dominated regime are used as this reduces the leading edge normal flow velocities and so wave drag. Sweep angles above 35° are found on supersonic aircraft.

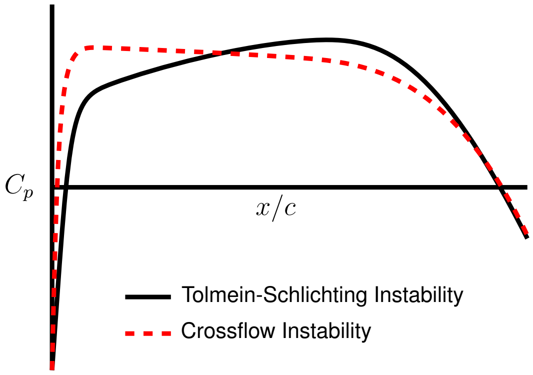

Figure 2.12: *Ideal pressure distributions for Tollmien-Schlichting and Crossflow instability suppression [60].*

2.3.1 Design Considerations for NLF

While NLF is a promising drag reduction method, its practical implementation is difficult to achieve due to the numerous and often conflicting design requirements. For subsonic NLF design, a favourable pressure gradient can be used to suppress TS instability growth which is the only instability type present. This is done by changing aerofoil shape upstream and shifting the point of maximum thickness aft. However, this can produce large pitching moments and thus incur additional trim drag penalties. If too large, this can negate any benefits found from NLF [61]. A balance between NLF and overall performance is also needed as designs with highly delayed transition resemble the Stratford profile [62]. This has a long favourable pressure gradient rooftop and short pressure recovery region with very little skin friction, but experiences rapid separation and aggressive stall characteristics [63].

Transonic NLF design is complex as NLF and supercritical wing design considerations differ. At transonic speeds, wing sweep is required to avoid the formation of strong shocks and so high wave drag. Sweep also helps to delay shock position, which can trigger upstream transition. However, sweep also leads to strong CF instability amplification that can dominate the transition process and is harder to suppress with passive control methods. On highly swept wings, NLF is not possible for this reason.

Increased wing sweep can also lead to attachment line instability and propagation of attachment line contamination, depending on the flight Reynolds number and leading edge radius. A small leading edge radius helps to avoid attachment line instability and contamination and also reduces the region where leading edge CF growth can occur [9]. However, a large radius is preferred for supercritical aerofoil design so as to create flow pre-compression which reduces shock strength and so wave drag. This is obtained by an initial spike in pressure at the leading edge that reflects between the sonic line and aerofoil surface [5]. This initial pressure spike also helps to reduce leading edge CF instability amplification but makes it difficult to obtain a favourable pressure gradient downstream so as to suppress TS instability growth. Additionally, while a favourable pressure gradient is needed, it can lead to very large pressure recovery which at transonic speeds, results in the formation of a strong shock, reducing the effectiveness of the laminar flow extension [2].

2.3.2 Transition Location Robustness

A further limitation to the use of NLF is the high sensitivity of transition location to geometric shape, surface roughness and operating conditions. It is common for NLF aerofoils to be very susceptible to large reductions in laminar length due to leading edge contamination, icing and surface damage [64, 65] as well as steps between panels, rivet bumps and general irregularities in the roughness and machining quality of the aerodynamic surface [9, 18]. Significant contamination can divert the transition process from natural transition and cause secondary instabilities or bypass. Slight changes to surface roughness can cause larger initial disturbance amplitudes via increased receptivity. As such, flight tests of laminar flow designs require highly smoothed single-piece aerodynamic surfaces, avoiding panels and rivets typically used for aircraft manufacturing. As transition is strongly affected by free-stream turbulence and environmental noise, lab-based research is difficult to carry out. Usable transition location estimations are only obtainable using low noise wind tunnels.

Additionally, without consideration for a wide range of operating conditions, NLF designs are often highly point-optimum with poor off-design performance. As transition is influenced by pressure gradient, changes in Mach number, Reynolds number or angle of attack can all result in significant movement of the transition location. This can result in a strong 'drag bucket' shape on an aerofoil's lift/drag polar such as those found with the NACA 6-series aerofoils, designed for extended NLF [66]. Alternatively it may lead to a low drag divergence Mach number such as found with the NLF0215F and NLF0414F [67].

It is also found that aerofoils designed for extended laminar flow often perform worse at fully turbulent conditions than those designed for fully turbulent flow [68]. As such, design of early NLF aerofoils typically involved comparison of laminar and fully turbulent characteristics to ensure performance is maintained if laminarity is lost [65, 69, 70].

2.4 Summary

The complex requirements for effective implementation of NLF, and the high sensitivity of NLF designs to changes in shape and operating conditions, has limited its use on commercial transport aircraft. A key challenge of NLF design is balancing the design practices needed for the extension of laminar flow, and the tradition design methods used for reducing form and wave drag [71]. To further complicate the NLF design process, it is also important that the benefits found with NLF are maintained away from the optimum operating environment by considering both on and off-design conditions. These benefits also need to be made more robust to uncontrollable factors such as surface quality, design shape or environmental conditions.

As the design of NLF aerofoils and wings has complex constraints, requirements and tradeoffs, it is seen as a suitable problem for aerodynamic optimisation. Uncertainty analysis and robust design are also useful tools in the development of robust NLF as NLF aerofoils and wings are often highly sensitive to properties affecting transition location. These topics and their application to NLF design are explored in the next chapter.

Chapter 3

Approaches to Aerodynamic Design

3.1 Aerodynamic Shape Optimisation

In broad terms, optimisation can be described as the selection of some design variables that, coupled with state variables, maximizes or minimizes an objective function subject to constraints [72]. When applied to aerodynamic shape optimisation, state variables are typically flight conditions specified in the flow solver. These include Mach number, Reynolds number, freestream turbulent intensity or lift coefficient. Design variables come from the chosen parametrisation method and describe the aerodynamic shape being optimised [73, 74]. The objective function is then an aerodynamic property output from the flow solver. This can be drag coefficient (Cd), lift coefficient (Cl), endurance (ML/D) or some other performance parameter. Constraints are typically equalities or inequalities applied to geometric sizing or other aerodynamic properties not directly being considered during the optimisation process.

There are two fundamental approaches to performing optimisation. These are one-shot, or direct solution of the optimisation problem, and iterative convergence towards an optimized solution [72]. One-shot approaches involve analytically solving the optimisation problem to directly obtain design variable inputs for the optimum objective function value. This approach is preferable as an exact solution is found quickly with low computational requirements. In practice, however, it is often not possible to solve the optimisation problem due to its complex nature, CFD-based problems being an example of this [72]. Iterative approaches must instead be used for these type of optimisation problems as an optimum design is found instead via a guided trail and error process. This involves taking an initial guess at optimum design variable values that are then used to evaluate the objective function. New values are then selected using the chosen iterative approach and the objective function evaluate again with the hope improved its value. This process is repeated until no further improvements are possible and an optimal design is found.

The most important step in this process is the selection of new design variable values. Methods proposed for this can be categorized into Gradient-based and Gradient-free approaches. Gradient-based approaches determine the direction of search by evaluating the objective function first derivative with respect to the design variables whereas gradient-free methods select new design variables through methods that avoid knowledge of the design space.

Each approach has its benefits and drawbacks. The choice of an optimisation algorithm can be affected by the complexity of the objectives, constraints and limits placed on the design problems. As such, optimisation problems are often described as either single-objective or multi-objective. Furthermore, choosing between a gradient-based and gradient-free approach is influenced by the scope of the optimisation problem being addressed. Design problems are categorised as single-point or multi-point depending on the number of discrete operating conditions considered.

3.1.1 Gradient-Based Optimisation

By using objective function derivatives, gradient-based optimisation algorithms are able to quickly traverse the design space while continuously improving the objective function value. As such, gradient-based methods are fast, efficient and widely used for aerospace optimisation problems [75]. For a gradient-based approach to be suitable for the design problem being addressed, it must be possible to obtain the first and second order derivatives of the objective function, and the design space must have low modality [76].

The first order derivative is required to guide the optimisation while the second order derivative is used to evaluate convergence. Derivatives can be found using either analytical methods, automatic or algorithmic differentiation, complex-step approximation or via finite difference [75]. The modality of the design space dictates the ability of the optimisation algorithm to move towards a global optimum. Due to the gradient dictating search direction, gradient-based approaches are excellent at finding the global optimum for uni-modal problems. They do, however, struggle when multiple modes are present. It may be possible to avoid this issue by restarting the optimisation several times with different design variable values, but escaping the local optima already found remains challenging [76]. As such, gradient-based optimisation is unlikely to find the global optimum case for a high number of modes [75].

This illustrates the potential dependence of gradient-based methods on initial design variable values and prior knowledge of the design space. Modality in CFD-based shaped optimisation at fully turbulent conditions has been studied by a number of authors and is considered to be low. Analysis by Yu et al. [77] found that optimisation of a full wing has a close to uni-modal design space. When transition modelling is included, there is no clear consensus. Robitaille et al. [78] performed gradient-based aerofoil optimisation with free transition and found that a global optimum was not reached, suggesting a multi-modal design space. Youngren [79] performed multi-point aerofoil optimisation with free transition and reported that the design space resembled a minefield with large spikes in gradient that cause huge changes in design and transition location.

3.1.2 Gradient-Free Optimisation

Gradient-free methods do not require objective function derivatives and so are typically easier to implement and avoid both requirements set out for gradient-based optimisation [80]. They are better suited to highly modal design problems as new design variables are selected discretely rather than by moving in a favourable direction through the design space. How new design variables are chosen depends on the specific gradient-free method in use.

A popular gradient-free approach for aerospace applications [77] is the Evolutionary or Genetic Algorithm [81]. By replicating the selection, mating and mutation processes found in natural evolution, this approach allows for a global search of the design space with successive generations combining favourable characteristics until a highly evolved aerofoil design is found. Another approach receiving strong interest is the Particle Swarm algorithm [82] that mimics the behaviour of swarming creatures. An initial population of designs is randomly generated throughout the design space. With each iteration, designs move towards the global optimum value and the best value found by that particular design. The speed of movement is also randomly scaled to allow for better design space exploration.

As well as avoiding any need for prior knowledge of the design space, gradient-free methods do not make use of a starting geometry directly [75]. Instead, many candidate designs are selected by randomly generating design variable values between specified bounds. While an informed selection of these bounds can help to speed up convergence and reduce computational costs substantially, it is not a necessity for undertaking optimisation. This makes gradient-free approaches appealing for optimisation problems where new flow physics or design requirements are put in place [80].

Although gradient-free methods are better at design space exploration, they typically have a much larger computational cost compared to gradient-based approaches. This is due to their slow convergence speed and difficulty in defining appropriate termination conditions [80]. Zingg et al. [80] compared the genetic algorithm against an adjoint gradient-based algorithm and found the gradient-free approach $6-187$ and $24-200$ times more computationally expensive for single point and multi-point optimisation respectively.

Many applications of gradient-free optimisation make use of viscous-inviscid interaction (VII) based flow solvers [83–85] which are computationally cheaper but lower fidelity than RANS-based solvers now widely used. Surrogate models are also used to approximate the design space and reduce the number of computational flow solutions required [84, 86, 87]. Due to these drawbacks, gradient-free optimisation is best for optimisation problems where gradient calculation is difficult or if the gradient is inaccurate due to noise or a highly modal design space [88].

3.1.3 Multi-Objective Optimisation

The simultaneous improvement of multiple objectives is required for many design problems. Examples of this include the reduction of aircraft drag while increasing cruise Mach number, or extending laminar flow over the wing while reducing pitching moment. When objectives are complementary, they are often combined into a single function for optimisation. When objectives are conflicting, multi-objective optimisation is needed. As it is likely no single design will be best, the goal of multi-point optimisation is to obtain a range of designs so that a designer is able to select the desired combination of performance properties [89]. To explore these trade-offs, the selected optimisation method must maintain a diverse set of non-dominated designs as it progresses [89].

Non-dominated designs are defined as having objective function values that no other design can simultaneously improve [85, 89]. These are of interest to a designer as they represent an optimum combination of objectives, whereas for any dominated design, there exists another design with an improved value for all objectives [85]. A group of non-dominated designs is referred to as a Pareto front. While a design may be non-dominated, it may not be on the global Pareto front and so a Pareto front should be suitably explored to ensure no further improvements are possible. Figure 3.1 shows an example of multi-objective optimisation where two objectives f_1 and f_2 have been minimised. Dominated designs, non-dominated designs and the resulting Pareto front are shown.

A diverse range of designs is needed so that the final Pareto front is well defined with many different designs available for selection by the designer. While obtaining a diverse set of designs, consideration must also be given to how much of a trade-off between objectives is acceptable. Pursuit of the optimum for one objective may produce designs that are of no use to a designer given the poor value of the trade-off objective. Designs of this type are non-dominated and on the Pareto front, but represent wasted computational resources given their lack of value as viable designs. The non-dominated designs at the upper left and lower right of the Pareto front in figure 3.1 may represent such designs given the strong trade-off seen with the other objective in each case.

Gradient-based methods can struggle with multi-objective design problems, as objectives must be combined into a single weighted sum. This results in only a small section of the Pareto front being explored for a chosen set of weights, and prevents any exploration of non-convex regions [90]. Better exploration can be achieved by scaling the weights but non-convex areas remain hidden [80]. Figure 3.2 shows this for a two-objective minimisation problem, where weights w_1 and w_2 are selected to obtain the weighted sum k. Designs are obtained above the non-convex region when w_1/w_2 is small, and below the non-convex region when w_1/w_2 is large, but never within the non-convex region itself.

Gradient-free methods are well suited to multi-objective optimisation problems as many designs are considered simultaneously, based on both dominance and diversity. This allows for effective exploration of both convex and non-convex Pareto front regions [80]. Although well suited to multi-objective problems, the high cost of gradient-free optimisation is a significant drawback. Therefore, gradient-based methods may be preferable when the Pareto front is known to be convex [80].

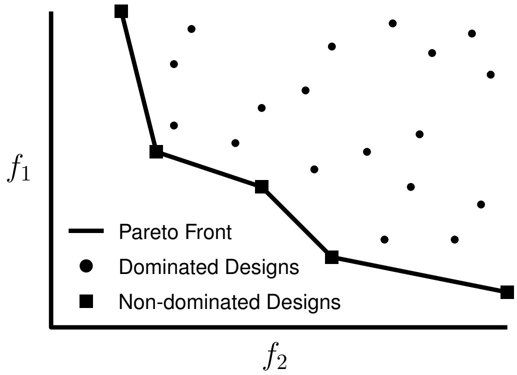

Figure 3.1: *Example of a two-objective minimisation with dominated designs, non-dominated designs and Pareto front highlighted.*

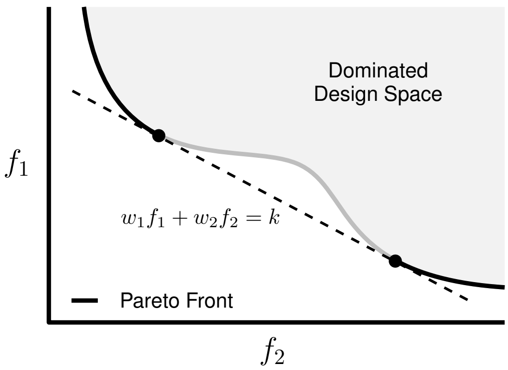

Figure 3.2: *Weighted-sum minimisation of a two objective design problem with a non-convex Pareto front.*

3.1.4 Multi-Point Optimisation

For aerodynamic components operated under constant flow conditions, optimisation at a single design point is sufficient. In reality, however, this is rarely the case. For the shape optimisation of aerodynamic surfaces on aircraft, operating and environmental conditions vary between take-off, landing and during cruise.

Single-point optimisation typically produces extensive performance improvements at the selected design conditions but almost always comes at the cost of reduced off-design performance [91]. Results of subsonic single-point optimisation approximate a Stratford profile [62] with very low drag but rapid separation above some critical angle of attack value. Transonic single-point optimisation of an aerofoil under fully turbulent conditions produces a shock-free pressure distribution but a strong shock forms at higher Mach numbers [92].

Multi-point optimisation attempts to address this issue by considering performance at several operating conditions. This is typically done optimizing a weighted sum of each objective function over the multi-point samples. The effectiveness of using multiple points is found to depend on the fidelity of the optimisation problem. As found by Drela [91], if each design variable used during an optimisation has a small area of influence on the design, an optimizer will favour obtaining local improvements to each multi-point sample, rather than a global design improvement. This is referred to as highly modal design and is seen physically as a wavy aerodynamic surface for shape optimisation problems. The conclusion drawn by Drela is that the number of multi-point samples required is equal to the number of design variables used. Further work by Li et al. [93] found that the number of multi-point samples needed was equal to the design variable number plus one.

3.2 Robust Design

When variations in operating conditions are unknown, hard or impossible to control, an alternative approach is to reduce the sensitivity of a design to variations in these conditions [94]. This approach was pioneered by Genichi Taguchi [95] and is the field of robust design. Although the mathematical definition of robust design differs depending on the approach used, robust design can be defined as the selection of design variables (x) which result in a design (f) having low variance (σ^2) to variations in some input parameter (z). This is shown in equation (3.1).

$$\sigma^2 = \int_a^b (x-\mu)^2 f(x,z)\,dz \qquad \text{where} \qquad \mu = \frac{1}{b-a}\int_a^b f(x,z)\,dz \tag{3.1}$$

Multi-point optimisation can be considered as the first step taken towards the design of robust engineering systems [96]. As performance improvements at one design point can cause a loss of performance at another, multi-point optimisation is the attempt to improve net or mean performance so as to ensure off-design performance is maintained. This approach has seen application to Mach number, lift coefficient and Reynolds number ranges under both fully turbulent conditions [97–99] and with free transition [20, 78].

The multi-point approach does not, however, take into account deviations in performance between points. This can be extremely undesirable when input conditions are probabilistic and highly predictable performance is required. This is the case for aircraft utilising extended NLF. The fuel savings obtained by NLF come primarily from the reduced fuel carried during flight. This can only be done if the amount of laminar flow obtained on the aircraft is consistent on all aircraft of this type, and for the same aircraft at different operating conditions. As such, it is often preferable to sacrifice mean performance if performance robustness can be improved.

Only considering robustness is also unwise as designs can often be found that are highly robust due to consistently poor performance. Robust design is therefore a multi-objective problem where mean performance and performance robustness are conflicting goals [96]. Obtaining a Pareto front between the two objectives is in many cases needed as the level of robustness required for a particular design problem is typically not initially known [100]. The trade-off between mean performance and performance robustness is illustrated in figure 3.3. This shows the response of three designs to variations in the parameter x where small output values are desired. Design A has the lowest output at x_0 but performs worse than the other two designs with only a small change in x. Design C sees almost no variation in output with even a large change in x but has a much higher output at x_0. Design B represents a trade-off between low output at x and insensitivity to changes in x.

For many aircraft design problems, addressing robustness by considering performance at several discrete design points is appropriate. This may be at different stages of a flight envelope or with different pre-determined payloads. This is considered deterministic robust design where specific design conditions are known and the duration at which they are experienced is used to weight their influence on performance. There are, however, design problems where conditions are not known in advance and instead take a range of values described by a probabilistic distribution. Examples of this include passenger weight, fluctuations around the cruise Mach number and altitude, or changes to aerodynamic shape due to loading. This is considered non-deterministic robust design and is strongly linked to the field of uncertainty analysis and quantification [96]. Here, the probability of a value occurring is used to weight its influence on performance.

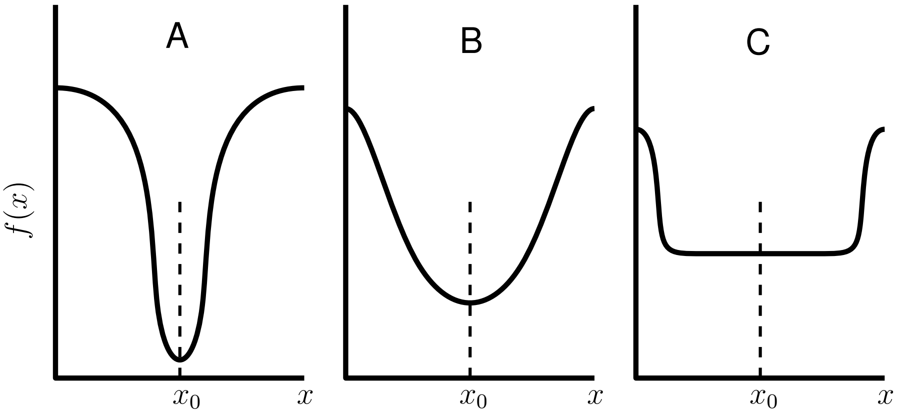

Figure 3.3: *Example designs illustrating the trade-off between mean performance and performance robustness.*

Both approaches are applicable to the design of NLF aerofoils and wings as transition is sensitive to changes in properties that could be considered deterministic such as Mach number and cruise altitude, but also stochastic conditions such as machining quality, surface roughness and contamination.

3.2.1 Uncertainty Analysis

Uncertainty analysis is the assessment of a systems performance to probabilistic variations in one or more of its input parameters. Applying a probabilistic input to an engineering system results in a probabilistic distribution of the output variables. By quantifying this output distribution, a better assessment of system performance can be made, which in turn helps with decision making and risk assessment [101].

Uncertainties can be categorized as either aleatory or epistemic [101]. Aleatory uncertainties are related to physical variables whose probabilistic uncertainty cannot be reduced. Examples of this type include uncontrollable environmental conditions or the limits of manufacturing tolerances. Epistemic uncertainties relate to controllable variables where the uncertainty comes from a lack of knowledge of the design problem. These can arise from the use of assumptions or simplifications to a model. While more detailed calibration or experimentation may reduce this error, this can be expensive or impossible to perform.

There are many different sources of uncertainty in aerodynamic design. These comes from three areas: operational conditions, geometry and the modelling method [102]. Operational conditions vary for different sections of an aircraft's flight envelope and during each flight envelope stage. Uncertainty in aircraft weight, flight speed and atmospheric conditions leads to uncertainty in Mach number, Reynolds number and lift coefficient. Uncertainty in aerodynamic geometry shape can occur due to differences between design and manufactured shape, manufacturing tolerances, undetected defects, deflection due to loading, shape change from icing or general shape degradation. Modelling method uncertainty arises from simplification of geometric shape, choice of modelling constants or predetermined decisions on flow properties such as transition prescription.

3.2.2 Uncertainty Representation

The first step to performing uncertainty analysis is to determine how the input uncertainty will be represented [101]. This is an important decision as the choice affects the output distribution shape [103] as well as the approach and computational cost of carrying out the analysis. The type of uncertainty representation needed is also strongly influenced by the type of uncertainty being modelled.

Aleatory uncertainties are usually represented using a probability distribution [101], however, selection of the probability distribution type is often difficult due to limited experimental data [101]. If this is the case, Aleatory uncertainties may be considered as epistemic until further information is obtained [96]. If a probability distribution representation is used, a distribution type needs to be selected. A common choice for aerospace applications is a Gaussian distribution [19, 104–106] although half-normal and skewed distributions may be more appropriate depending on the uncertainty variable considered.

Epistemic uncertainties are difficult to represent using a probability distribution as the inherent lack of knowledge prevents an accurate definition of the uncertainty [101]. Highly inaccurate uncertainty estimations can be made as it may not be known if the uncertainty is even probabilistic in nature [107]. As such, alternative representations such as an interval uncertainty can be used. For this, a lower and upper limit are placed on the input variable and the minimum and maximum output values are found within that limit. This information is then used to quantify robustness.

Additional difficulties occur when considering multiple uncertain variables. Treating all variables as Aleatory may result in artificially low performance variance [107]. This has led to the development of mixed uncertainty methods [107].

3.2.3 Uncertainty Propagation

The next step to uncertainty analysis is the propagation of uncertainty through the system of interest to produce an output distribution. This is the complex and computationally expensive part of uncertainty analysis [101]. When uncertainty is represented by a probability distribution, uncertainty analysis is concerned with computing mean performance (μ) and performance variance (σ^2) or standard deviation. Equations (3.2) and (3.3) give the continuous formulation and discrete approximation of μ and σ^2 where $P(x)$ is the probability density function (PDF).

$$\mu = \int P(x)\, dx \qquad \approx \frac{1}{W}\sum_{i=1}^{N} P(x_i)x_i \tag{3.2}$$

$$\sigma^2 = \int P(x)(x-\mu)^2\, dx \qquad \approx \frac{1}{W}\sum_{i=1}^{N} P(x_i)(x_i-\mu)^2 \tag{3.3}$$

$$\text{where} \quad W = \sum_{i=1}^{N} P(x_i)$$

Possible propagation methods can be placed into three categories: sampling techniques, quadrature methods and spectral methods [101]. Sampling-based methods are simple to implement while being highly effective and as such are widely used [101, 103]. Methods of this type obtain an output distribution by evaluating the modelled system at sampled input values selected using the chosen sampling strategy. The Monte Carlo method is the most popular sample-based approach [101] and often used for aerospace applications [96, 106]. With this method, sample points are randomly selected based on the input variable probability distribution. The appealing characteristic of this approach is that accuracy is guaranteed when the number of samples is large. For a small number of sample points, however, the Monte Carlo method has poor convergence due to low sample equidistribution [108].

Applied to aerodynamics, each sample point represents a flow solution, thus accuracy of the Monte Carlo method has a high computational cost. Quasi-Monte Carlo methods attempt to solve this by generating samples using low-discrepancy sequences such as of Sobol or Halton. An alternative approach is Latin Hypercube, which enforces better equidistribution by selecting samples within a sequence of sub-ranges [103]. Figure 3.4 provides a comparison of Monte-Carlo, Quasi-Monte Carlo and Latin Hypercube sampling of two variables.

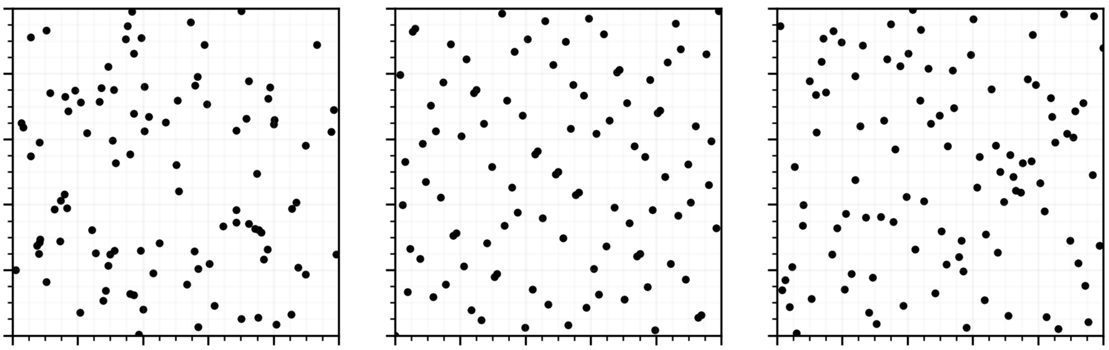

(a) *Monte Carlo* **(b)** *Quasi-Monte Carlo (Sobol)* **(c)** *Latin Hypercube*

Figure 3.4: *Example of* 100 *two-dimensional samples from various sampling strategies.*

Quadrature-based approaches use quadrature integration methods to solve the integral forms of the first and second statistical moment equations. Quadrature integration replaces a complex function which requires integration with a set of basis polynomials whose integral is easier to calculate. Mathematically, the integral of the output function $f(x)$ within the range $a - b$ is found using equation 3.4, where w_i are weights corresponding to the sample point x_i locations.

$$I = \int_a^b w(x)f(x)dx \approx \sum_{i=1}^{\nu} w_i f(x_i)dx \tag{3.4}$$

When quadrature integration is applied to uncertainty analysis, it is referred to as stochastic collocation [101]. This is typically Gaussian quadrature. For this, both the weights and sample points in equation 3.4 are allowed to move. Furthermore, if the function being integrated is a polynomial of order $2\nu - 1$, then it is possible to find the exact integral with the correct selection of both. The sample points are found to be the roots of orthogonal polynomials $p_n(x)$. This orthogonality is shown in equation 3.5 where $W(x)$ is a weighting term. The weights are found by evaluating the integral of the polynomial passing through the root. As these polynomials are chosen, this is easy to calculate.

$$\langle p_i(x), p_j(x) \rangle = \int_a^b p_i(x)p_j(x)W(x) = \delta_{ij} \tag{3.5}$$

$$\text{where} \quad \delta_{ij} = \begin{cases} 0 & \text{if} \quad i \neq j \\ 1 & \text{if} \quad i = j \end{cases}$$

Stochastic collocation is excellent at providing the first and second integral of a function that is or closely resembles a polynomial. The method is however, unsuited for functions which are not polynomial or contain discontinuities. Furthermore, at times it may be desirable to obtain a full description of the output distribution, rather than purely the statistical moments. This is something that stochastic collocation is unable to provide.

If the output function can be adequately represented as a polynomial and a full probability density function is required for the output distribution, then a surrogate modelling method is most appropriate. A popular choice in the field of uncertainty analysis is Polynomial Chaos (PC) [109]. The core concept of PC is that the output distribution of a quantity of interest $q(x)$ with random variations in the input variable x can be defined as an infinite series of orthogonal basis polynomials ϕ_i with respect to an alternative random variable ζ, scaled with deterministic coefficients x_i, as shown in equation 3.6. In practice, a finite number of polynomials Q are chosen based on the number of uncertain inputs n and the desired order of basis polynomial p.

$$q(x) = \sum_{i=0}^{\infty} x_i \phi_i(\zeta) \approx \sum_{i=0}^{Q} x_i \phi_i(\zeta) \tag{3.6}$$

$$\text{where} \quad Q = \frac{(p+n)!}{p!\, n!} - 1 \tag{3.7}$$

Hermite polynomials of order n are used for Gaussian input variables, which take the form shown in equation 3.8. This is because the input distribution is typically Gaussian which matches the weighting function of the Hermite polynomial inner product, as shown in equation 3.9.

$$H_n(\zeta) = (-1)^n e^{\frac{\zeta^2}{2}} \frac{d^n}{d\zeta^n} e^{-\frac{\zeta^2}{2}} \tag{3.8}$$

$$\langle H_i, H_j \rangle = \int_{-\infty}^{\infty} H_i(\zeta) H_j(\zeta) W(\zeta)\, d\zeta \tag{3.9}$$

$$\text{where} \quad W(\zeta) = \frac{1}{\sqrt{2\pi}} e^{-\frac{\zeta^2}{2}} \tag{3.10}$$

To calculate the deterministic coefficients x_i, the Galerkin projection is used, where the inner product of each order polynomial is calculated, as shown in equation 3.11. This can be carried out using an intrusive and non-intrusive approach. As CFD solvers are complex and treated as a black box, the non-intrusive approach (NIPC) is preferred [109]. For this, the integral of the original function $q(x)$ is found using Gaussian quadrature described previously.

$$x_i = \frac{\langle x H_i(\zeta) \rangle}{\langle H_i^2(\zeta) \rangle} = \frac{1}{\langle H_i^2 \rangle} \int_{-\infty}^{\infty} q(x) H_i(\zeta) e^{-\frac{\zeta^2}{2}} d\zeta \tag{3.11}$$

As NIPC requires a low number of samples to construct the surrogate response surface due to the use of Gaussian quadrature, it is highly efficient for functions of polynomial form. Using Polynomial Chaos methods to represent non-polynomials is difficult and an active research area [109]. Un-smooth or discontinuous functions are not modelled well and sampling based approaches may be better suited [110].

3.3 Application to Natural Laminar Flow

There are many examples of NLF aerofoil and wing optimization under deterministic flow conditions, using both gradient-based and gradient-free approaches. Gradient-based algorithms require derivatives of the solver and transition model with respect to the design variables. The simplest method of obtain these is via finite difference. An early use of this was by Dodbele [111] who optimized a NLF aerofoil to extend laminar length. In this study, a VII-based flow solver was used with an e^N transition model to calculate objective function values. For derivative calculations, the e^N model was replaced with Granville's empirical transition criteria to further reduce computational costs. Studies by Rashad and Zingg [112] and Robitaille et al. [78] are more recent examples of NLF design using gradient-based optimisation with derivatives calculated using finite difference. Both performed drag minimization of a NLF aerofoil using a RANS-based flow solver. Rashad and Zingg uses a simplified e^N method for transition prediction while Robitaille et al. used the $\gamma - Re_{\theta,t}$ transport equation model.

The more popular method for calculating the objective function gradients is via adjoint sensitivity analysis. Amoignon et al. [113] used this to find derivatives for a VII-based flow solver with PSE transition model and applied the method to NLF aerofoil optimization. Driver and Zingg [114] used a VII-based flow solver and e^N transition model to calculate transition locations which were then used to fix transition in a RANS-based flow solver. Both solvers were used to calculate terms within the adjoint equation. Lee and Jameson [115] carried out NLF aerofoil and wing optimisation with derivatives from a RANS-based flow solver and e^N transition model, found using the adjoint approach. Transition analysis of the wing was performed on two-dimensional boundary layer sections taken from a full three-dimensional flow solution. Rashad and Zingg [20] obtained derivatives for a RANS-based solver and simplified e^N model using the adjoint approach while Khayatzadeh and Nadarajah [116] formulated the adjoint for a RANS-based solver and $\gamma - Re_{\theta,t}$ transition model. Both studies applied this to NLF aerofoil design.

Many of these gradient-based studies focus on coupling of the transition model with the flow solver, and so few consider off-design performance or robustness. The study by Robitaille et al. [78] looked at designing a morphing NLF aerofoil for operation at a range of conditions. This involved performing multi-point drag minimizing over a range of Mach and lift coefficients to find a baseline static design with good off-design performance. The morphing section of the aerofoil was then optimized at each single-point independently to find different morphed shapes for minimum drag at those conditions. Part of the work carried out by Driver and Zingg [114] focused on the effect of premature transition on a NLF aerofoil. For this, several optimization cases where run with identical starting profiles and operating conditions and but with different objective functions. These were derived from a weighted sum of lift over drag found with free transition and with fully turbulent flow. Further work by Rashad and Zingg [20] also generated a Pareto front using this approach after having performed multi-point optimisation of a NLF aerofoil. To ensure that the final design found during the optimisation is insensitive to variations in cruise conditions, a range of aircraft weights, Mach numbers, Reynolds numbers and lift coefficients were considered. Optimization of a NLF aerofoil over a multi-point range of critical N-factors was also carried out.

Both genetic algorithm and particle swarm gradient-free approaches have seen application to NLF design. Gardner and Selig [83] used a genetic algorithm to carried out both inverse and direct design optimisation of aerofoils with free transition using a VII-based flow solver with simplified e^N transition model. Zhang et al. [117] performed drag minimization of NLF aerofoils using a genetic algorithm with RANS-based flow solver and $\gamma - Re_{\theta,t}$ transition model. A particle swarm algorithm was used by Khurana and Winarto [118] and Wickramasinghe et al. [119] who both looked to minimise drag on a UAV aerofoil with free transition using a VII-based flow solver and simplified e^N transition model.

Several studies use surrogate models to avoid the high computational cost of gradient-free optimisation. Cameron et al. [84] used kriging to perform cheap genetic algorithm optimisation of a high-altitude long endurance UAV using a VII-based flow solver and e^N transition model. Studies by Fan et al. [87] and Han et al. [120] both employ surrogate models to reduce the cost of optimisation using a RANS-based flow solver with coupled e^N transition model. In both cases, initial samples are taken and a response surface constructed. An optimization algorithm then locates promising areas of the surface for additional sampling until convergence is obtained. This approach is used for a combined inverse and direct design of NLF aerofoils by Fan et al. and for direct design of NLF aerofoils and wings by Han et al.

Some consideration for off-design conditions is made within the gradient-free and surrogate model assisted NLF optimisation studies mentioned. Gradient-free optimization carried out by Cameron et al. [84] explored the trade-off between drag at two primary operating conditions, cruise and loiter, of a high-altitude long endurance UAV. Khurana and Winarto [118] also optimised a high-altitude long endurance UAV but considered two lift coefficient values to obtain good performance over a desired operating envelope. Zhang et al. [117], after having optimized a number of NLF aerofoils with various constraints on favourable pressure gradient, analysed each design over a range of attack angles to compare performance robustness. Han et al. [120] also performed off-design analysis of an optimized NLF wing over a range of lift coefficients, Mach numbers and critical N-factors. Multi-point optimisation was then carried out at two Mach number and attack angle combinations.

For non-deterministic optimisation, a large amount of research has been applied to fully turbulent aerofoil design, mainly focusing on uncertainty in Mach and Reynolds number [93, 96, 121–128]. Much less research has been carried out applying robust analysis and optimisation to NLF designs with free transition. Zhao et al. [104] looked at improving $C_{l,\max}$ robustness to uncertainty in transition location which was treated as a stochastic property. Mean and standard deviation of $C_{l,\max}$ are found at each iteration via polynomial chaos uncertainty analysis and optimisation is carried out to improve both. Jing et al. [19] performed optimisation to independently improve drag robustness to Mach and C_l uncertainty with free transition. Due to the large number of flow simulations required, a surrogate model was used with a particle swarm optimisation algorithm. Zhao et al. [105] also improved robustness of drag to Mach number uncertainty for a NLF aerofoil via genetic algorithm based optimisation using surrogate models.

3.3.1 Gap Within the Existing Research

The vast majority of research on the robust design of NLF aerofoils and wings only considers net performance over a set of discrete design points. Typically this is done for variables such as Mach number, Reynolds number or lift coefficient [20, 78, 84, 117, 118, 120]. These variables are also often considered in studies using probabilist uncertainty to represent design conditions [19, 105]. As a result, research on NLF robustness to uncertainty in surface and flow quality has been very limited. Uncertainty in flow quality can be represented by varying free-stream turbulent intensity when using a RANS-based flow solver and $\gamma - Re_{\theta,t}$ transition model. This was done by Salahudeen and Baeder [106], who performed uncertainty analysis of a NLF aerofoil with a probability distribution applied to free-stream turbulent intensity.

Uncertainty in both flow and surface quality can be represented by varying the critical N-factor used in the e^N transition model. This is due to the dependence of boundary layer disturbance amplitude on turbulent intensity and surface roughness, wear and contamination. As was discussed in section 2.1.5, increasing turbulent intensity or surface roughness results in boundary layer disturbances with larger initial amplitudes. As initial amplitude is larger, less amplification is required before secondary instability develops and transition occurs. Therefore, increasing turbulent intensity or surface roughness results in a lower critical N-factor. It then follows that critical N-factor can be altered to simulate variations in turbulent intensity and surface roughness.

Only a few applications of this approach can be found within the literature. Deng and Qiao [129] used an inverse design approach to match an $N(x)$ envelope designed to limit the effects of varying critical N-factor. The target N-factor envelope featured little growth over most of the chord length before growing quickly at the desired point of transition. This ensures that as critical N-factor is reduced, transition remains at approximately the same position. Rashad and Zingg [20] optimized a NLF aerofoil at several critical N-factors and compared the performance of each at off-design N-factor values. A key finding of this study was that optimizing for a reduced N_{cr} was no guarantee of performance at higher N_{cr} given that extended laminar flow can increase the risk of flow separation. The authors then carried out multi-point optimisation over three N_{cr} values to ensure aerofoil performance is maintained at off-design N-factor values. Han et al. [120] performed optimisation of a NLF wing using N_{cr} values lower than expected to account for uncertainty in real flight conditions. The original and optimized wings were then analysed at different critical N-factor multi-points to assess the robustness of each design. Both designs saw no reduction in performance when critical N-factor was increased from that used at design.

Given the wide use of linear stability and the e^N transition model within the aerospace industry, the limited amount of flight test date available and high sensitivity of transition location to variations in surface and flow quality, the design of NLF aerofoils should include analysis with uncertainty in critical N-factor. The work carried out in this field so far has been limited and only considers deterministic analysis at discrete design points. A clear gap within the field is thus the application of uncertainty analysis and robust optimisation to the design of NLF aerofoils and wings with uncertainty in critical N-factor.

3.4 Objectives of this Work

The importance of NLF robustness to surface and flow quality, the probabilistic nature of these two variables and the current gap within the literature on this topic, have been highlighted. The overall goal of this work is therefore to study the effect of uncertainty in surface and flow quality on the performance of NLF aerofoils and wings by varying the critical N-factor used in the e^N transition model. To achieve this, the objectives of this work are to:

- Quantify the robustness of aerofoil performance to uncertainty in critical N-factor, used to model uncertainty in surface and flow quality. This is done to investigate aerofoil performance sensitivity to uncertainty in critical N-factor, to highlight factors effecting robustness and determined any links between deterministic and stochastic performance.

- Carry out optimisation of NLF aerofoils at subsonic and transonic flow conditions with uncertainty in critical N-factor. This is done to determine the effectiveness of robust optimisation of NLF aerofoils, highlighting any trade-offs between deterministic and stochastic performance and the design methods used by the optimiser to improve robustness.
- Expand the design problem to consider NLF aerofoil performance and robustness with uncertainty in critical N-factor over a range of additional flight conditions. This is done to examine how performance and robustness with uncertainty in critical N-factor is effected when considered at other off-design flight conditions, and to assess any differences in aerofoil design as a result.
- Quantify the robustness of wing performance to uncertainty in critical N-factor, so that optimisation of NLF wing sections can be carried out to improve performance and robustness with critical N-factor uncertainty. This is done to examine how the inclusion of three-dimensional instability affects performance, robustness, trade-offs between the two and the aerofoil designs generated by the optimiser.

Chapter 4

Tools and Methods

4.1 Optimisation Framework

A python-based optimisation framework has been developed for this work. This is able to perform multi-objective, multi-point and robust aerodynamic shape optimisation with geometric and flow variable constraints and supports parallel processing. An overview of the framework is shown in figure 4.1. A genetic algorithm is used to drive the optimisation process. By replicating the selection, mating and mutation process found in natural evolution, a genetic algorithm allows for a global search of the design space with successive generations combining favourable characteristics until a highly evolved aerofoil design is found. The use of a gradient-free optimisation algorithm avoids the need to obtain flow solver and transition model derivatives, and works well for highly modal design problems or multi-objective problems with non-convex Pareto fronts.

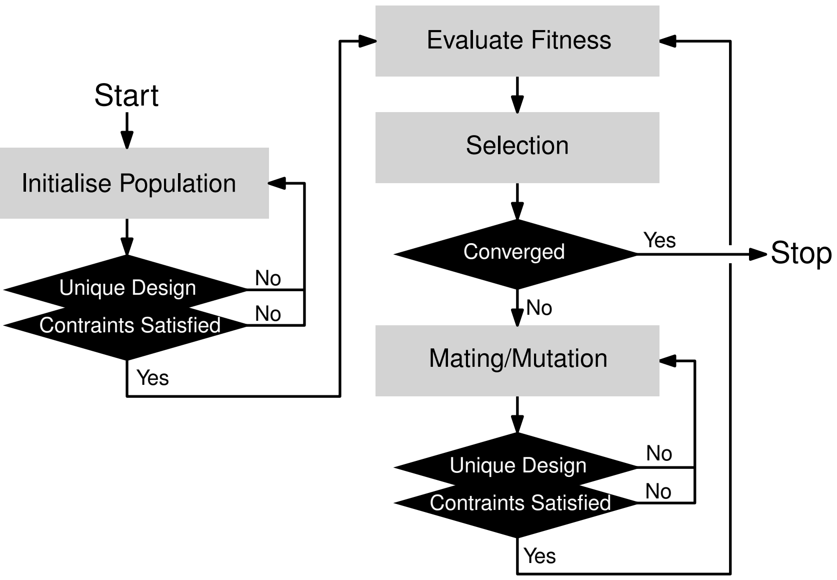

Figure 4.1: *Optimisation workflow.*

At the time of development, the author found there to be no widely used or well documented implementations of a genetic algorithm optimiser available in python, which was the programming language selected for the project. The Distributed Evolutionary Algorithms in Python (DEAP) package [130], however, provided components for the construction of evolutionary algorithms and was found to be well documented and used by other researchers publishing in peer reviewed journals.

An initial population of N_{pop} designs are first initialized by random generation of design variables within the specified bounds. During population generation, each design is checked against any geometric constraints in place and is also checked for uniqueness within the population. This ensures that designs can only exist once within the optimisation history. The fitness of each design is then evaluated via calls to the flow solver. The evaluation of every design at each design point can be carried out in parallel. Convergence of a design requires that the flow solver is able to converge at all design points. If this is not the initial generation, these new designs are then grouped with the current generation's population, resulting in $2 \times N_{pop}$ designs.

Designs from this combined pool are then selected using the non-dominated sorting method, presented as part of the NSGA-2 optimisation method [131]. This involves sorting the population into Pareto fronts, depending on their dominance, and then selecting N_{pop} designs based on their Pareto front rank and diversity within their rank. Tournament selection based on dominance is then used to choose designs to be mated or mutated. This involves randomly selecting two designs and comparing dominance. If neither design dominates the other, their diversity within the Pareto front is used.

Mating is done using bound simulated binary crossover [132] with a 50 percent chance of occuring. The mating process is applied variable-by-variable to two parent designs. For each design variable index selected, a random number u is generated between $0 \rightarrow 1$. This is used to obtain two spread factors β_1 and β_2 using equation (4.1), where $P(\beta)$ is a probability distribution.

$$u = \frac{1}{P_1} \int_0^{\beta_1} P(\beta)\, d\beta \qquad u = \frac{1}{P_2} \int_0^{\beta_2} P(\beta)\, d\beta \tag{4.1}$$

$$\text{where } P(\beta) = \begin{cases} 0.5(\eta + 1)\beta^{\eta} & \beta \leq 1 \\ 0.5(\eta + 1)\frac{1}{\beta^{\eta+2}} & \beta > 1 \end{cases} \tag{4.2}$$

The values P_1 and P_2 are obtained using equations (4.3) where the spread factors β_u and β_l are based on the upper and lower design variable bounds x_u and x_l specified. Once β_1 and β_2 have been obtained, child design variable values are obtained using equations (4.4).

$$\begin{aligned} P_1 &= \int_0^{\beta_l} P(\beta) d\beta \qquad \text{where } \beta_l = \frac{p_1 + p_2 - 2x_l}{|p_2 - p_1|} \\ P_2 &= \int_0^{\beta_u} P(\beta) d\beta \qquad \text{where } \beta_u = \frac{2x_u - p_1 + p_2}{|p_2 - p_1|} \end{aligned} \tag{4.3}$$

$$c_1 = 0.5((p_1 + p_2) - \beta_1(p_2 - p_1)) \qquad c_2 = 0.5((p_1 + p_2) + \beta_2(p_2 - p_1)) \tag{4.4}$$

Bound polynomial mutation is used [133, 134] to modify a single parent design based on a polynomial probability distribution. This is again done per design variable where each has a 50 percent chance of being selected. For a selected parent variable, a child variable value is obtained from equation (4.5) using a random value u selected between $0 \rightarrow 1$.

$$c = \begin{cases} p + \delta(p - x_l) & x \leq 0.5 \\ p + \delta(x_u - p) & x > 0.5 \end{cases} \quad \text{where} \quad \delta = \begin{cases} 2u^{\frac{1}{\eta+1}} - 1 & u \leq 0.5 \\ 1 - (2(1-1))^{\frac{1}{\eta+1}} & u > 0.5 \end{cases} \tag{4.5}$$

As with population initialisation, mating and mutation is rerun if the resulting offspring do not satisfy the geometric constraints or are not unique within the optimisation history. A limited number of mating attempts is allowed before mutation is carried out instead as it may not be possible to produce a constrained or unique offspring through the mating process. This limit is 4× the design variable number.

For both mating and mutation, the crowding number η controls how similar offspring are to their parents and can be scaled during optimisation to aid in design space exploration. During this study, η is linked to the current generation n_i and overall generation number n_t by the relationship given in equation (4.6). As the optimisation progresses, the crowding number increases from $0 \rightarrow \eta_{\max}$. Smaller values mean less similarity between parent and child, allowing the optimiser to initially spread out over the design space before converging on the final Pareto front designs.

$$\eta = \eta_{\max} \frac{n_i}{n_t} \tag{4.6}$$

Constructing an optimisation framework from individual components, rather than using an off-the-shelf tool did represent a large time investment early in this study. However, it was felt to be beneficial. Having access to the inner workings of the optimiser allowed for easy parallelisation of the code, as well as tailoring of the workflow to the problem being addressed. One such example of this was moving the assessment of geometric constraints and design uniqueness prior to the analysis of design fitness. This represented a change within the population generation, mating and mutation methods that avoided carrying out unnecessary flow solver runs, saving substantial computational time. The author also feels that the knowledge gained by developing a tool rather than using off-the-shelf or black box alternatives cannot be understated.

4.2 Aerofoil Parametrisation

The optimisation process selects new design variable values that, when used with the selected parametrisation method, define the shape of the optimised aerofoil. There are various approaches to aerofoil parametrisation that can be grouped into two distinct categories: constructive and deformative [135].

Constructive approaches directly fit parametrisation variables to a starting aerofoil shape. This aerofoil and deformed variants can then be derived from these variables alone. Deformative methods take a starting aerofoil and apply deformation using a perturbation profile. The parametrisation variables therefore control the perturbation shape rather than the final aerofoil directly. Given the use of a genetic algorithm, it is desirable to use a low design variable number as this directly affects the number of individuals required per generation. The ratio of population size to design variable number (N_{dv}) depends on the problem being addressed and vary from $0 < N_{pop} < 2 \times N_{dv}$ [136] to $N_{pop} \approx 10 \times N_{dv}$ [137].

A deformation approach is used in this study as it allows for optimisation of a complex starting aerofoil using a low number of design variables. New aerofoil shapes are found via summation of the original aerofoil and a perturbation profile, represented mathematically in Eq. (4.7) where z_o is the original z coordinate, z_p is the perturbation z coordinate and u is the chord length position x/c.

$$z(u) = z_o(u) + z_p(u) \tag{4.7}$$

The Class Shape Transformation (CST) method developed by Kulfan [138] is used here to parametrise the perturbation profile and generates the z_p term. This is shown in Eq. (4.8) where $\Delta_{z_{te}}$ is the trailing edge thickness, $C(u)$ is the class function and $S(u)$ is the shape function from the CST method.

$$z_p(u) = C(u)\ S(u) + (u\ \Delta_{z_{te}}) \tag{4.8}$$

The class function is defined in Eq. (4.9) where n_1 and n_2 are exponents that determine the basic shape of the CST fitting. The values $n_1 = 0.5$ and $n_2 = 1.0$ are used to define a round-nosed aerofoil with finite trailing edge gradient as the CST is commonly used for constructive aerofoil parametrisation. For this deformative application, the values used are $n_1 = n_2 = 1$.

$$C(u) = u^{n_1}\,(1-u)^{n_2} \tag{4.9}$$

The shape function given in Eq. (4.10) contains the CST coefficients, A_r, used as design variables during the optimisation. These control the magnitude of the polynomial curves at their peak which each scale the class function and gives the resulting perturbation profile. The number of design variables available depends on the number of polynomial curves used.

$$S(u) = \sum_{r=0}^{n} A_r\ \frac{n!}{r!(n-r)!} u^r\,(1-u)^{n-r} \tag{4.10}$$

4.3 Computational Solvers

Undertaking uncertainty analysis can be computationally expensive, due to the potentially high number of sample points required to accurately propagate certainty through a model. At its essence, uncertainly analysis is an increase in the dimensions of the problem and so suffers from the well known curse of dimensionality. This is compounded when the problem is extended so that uncertainty analysis of one variable is assessed at multiple conditions of another, such as critical N-factor uncertainty at a range of Mach numbers, lift coefficients or Reynolds number combinations

Uncertainty analysis is also multi-objective and so optimisation is best performed using gradient-free methods. These too are computationally expensive compared to gradient-based approaches more popularly used for aerodynamic optimisation. Consequently, low cost flow solvers are required for the aims and objectives outlined. This excludes the use of RANS-based flow solvers as these are highly accurate but computationally expensive. Instead, VII-based flow solvers have been selected for this study.

4.3.1 Viscous-Inviscid Interaction

The key observation enabling use of the viscous-inviscid interaction approach to modelling flow is that when Reynolds number is sufficiently large, viscous effects are only found within a thin shear layer close to aerodynamic surfaces within a flow. As such, a flow field can be split into an inviscid flow region and the viscous shear layer [139]. The benefit of this is that with the assumption of inviscid flow, fluid dynamics equations can be greatly simplified so as to allow for faster calculation. As such, each flow regime is solved using a different model and the two flows combined to produce a solution over the entire domain. While it is desirable for the two flow regions to be independent, typically some interaction between them occurs due to the presence of wall curvature leading to a stream-wise pressure gradient and boundary layer thickness changes [139]. An iterative solution process between the two regions is therefore required.

An important decision is the location where the two flow regions are split. While the outer edge of the viscous sheer layer is logical, this is rarely selected as it changes during the solution process. The preferred approach is instead to model the inviscid flow down to the aerofoil surface, with a modification of either the surface shape by some displacement thickness or the surface boundary condition via the introduction of a transpiration mass flow rate. One of these alterations is needed to account for the change in mass flow rate caused by the presence of the viscous shear flow. The latter approach is most often used as changes to the boundary conditions avoid the need to re-mesh the inviscid flow-field [139].

Once an approach is selected, the general workflow of a VII-based flow models is as follows:

1. First the external inviscid flow region is solved using zero transpiration mass flow rate or the original aerofoil geometry shape.
2. This is then used as the boundary condition for the viscous shear layer solver
3. Once a viscous solution is found, the boundary layer displacement thickness or transpiration mass flow rate is calculated
4. This is then used to re-run the inviscid solver

This process is repeated until both inviscid and viscous flows converged. When transition modelling is included, laminar and turbulent boundary layer methods are used, with the laminar boundary layer solution passed to the stability analysis code and the predicted transition location returned.

4.3.2 Subsonic Flow Solver

For analysis of subsonic flows, the flow solver XFOIL was used. This is a two-dimensional VII-based solver developed by Drela [140]. Although considered a low fidelity solver, given its use of VII over the Reynolds Averaged Navier-Stokes approach, it is a highly reliable tool when operated within its limitations and has been used extensively in industry.

Inviscid flow is modelled within XFOIL using the panel method, where a stream function for the flow-field is constructed by superposition of the free-stream flow with vortex and source sheets over the aerofoil surface and a source sheet along the aerofoil wake. The surface and wake are discretised into N_s and N_w panels respectively, with vortex strength γ varying linearly between panel nodes and source strength σ remaining constant over each panel. This is shown in figure 4.2. If a blunt trailing edge is used, an additional panel is used with uniform source and vortex strengths σ_{TE} and γ_{TE}. This is defined by equation (4.11) where $\hat{s}$ and $\hat{t}$ are unit vectors normal and tangential to the trailing edge surface. This is also shown in figure 4.2.

$$\sigma_{TE} = \frac{1}{2}(\gamma_1 - \gamma_{N_s})|\hat{s} \times \hat{t}| \qquad \gamma_{TE} = \frac{1}{2}(\gamma_1 - \gamma_{N_s})|\hat{s} \cdot \hat{t}| \tag{4.11}$$

Following discretisation, the stream function can be evaluated at any (x, y) flow field position using equation (4.12). The terms u_∞ and v_∞ are the free-stream velocity components in the x and y directions. The terms $\psi_j^{\gamma+}$, $\psi_j^{\gamma-}$ and ψ_j^{σ} are unit stream functions given by equations (4.13), (4.14) and (4.15) in terms of local x and y coordinates, $\bar{x}_{1/2}$, $\bar{y}_{1/2}$, $r_{1/2}$ and $\theta_{1/2}$. The relation between these and the (x, y) point selected can be seen in figure 4.2.

$$\begin{aligned} \psi(x,y) = u_\infty y - v_\infty x &+ \frac{1}{4\pi} \sum_{j=1}^{N_s+N_w-1} \psi_j^{\sigma}(x,y) 2\sigma_j \\ &+ \frac{1}{4\pi} \sum_{j=1}^{N_s-1} \psi_j^{\gamma+}(x,y)(\gamma_{j+1} + \gamma_j) + \psi_j^{\gamma-}(x,y)(\gamma_{j+1} - \gamma_j) \\ &+ \frac{1}{4\pi} \left(\psi_{N_s}^{\sigma}(x,y)|\hat{s} \times \hat{t}| + \psi_{N_s}^{\gamma+}(x,y)|\hat{s} \cdot \hat{t}|\right)(\gamma_1 - \gamma_{N_s})] \end{aligned} \tag{4.12}$$

$$\psi_j^{\gamma+}(x,y) = \bar{x}_1 \ln r_1 - \bar{x}_2 \ln r_2 + \bar{x}_2 - \bar{x}_1 + \bar{y}(\theta_1 - \theta_2) \tag{4.13}$$

$$\psi_j^{\gamma-}(x,y) = \left[(\bar{x}_1 + \bar{x}_2)\psi_j^{\gamma+}(x,y) + r_2^2 \ln r_2 - r_1^2 \ln r_1 + \frac{1}{2}(\bar{x}_1^2 - \bar{x}_2^2)\right] \frac{1}{\bar{x}_1 - \bar{x}_2} \tag{4.14}$$

$$\psi_j^{\sigma}(x,y) = \bar{x}_2\theta_2 - \bar{x}_1\theta_1 + \bar{y} \ln \frac{r_1}{r_2} \tag{4.15}$$

If a stream function value ψ_0 is specified at each surface node, then a system of n linear equations can be obtained. This is shown in equation (4.16), where a_{ij} and b_{ij} are coefficient matrices determined by the unit stream functions $\psi_j^{\gamma+}$, $\psi_j^{\gamma-}$ and ψ_j^{σ}.

$$\sum_{j=1}^{N_s} a_{ij}\gamma_j - \psi_0 = -u_\infty y_i + v_\infty x_i - \sum_{j=1}^{N_s+N_w-1} b_{ij}\sigma_j \qquad \text{for } j = 1 \rightarrow N_s \tag{4.16}$$

Combining these with the Kutta condition defined in equation (4.17) results in a system of $n + 1$ linear equations.

$$\gamma_1 + \gamma_{N_s} = 0 \tag{4.17}$$

For aerofoils with a sharp trailing edge, equation (4.16) for $i = N_s$ is replaced with a value extrapolated from the upper and lower panels, as given in equation (4.18).

$$(\gamma_3 - 2\gamma_2 + \gamma_1) - (\gamma_{N_s-2} - 2\gamma_{N_s-1} + \gamma_{N_s}) = 0 \tag{4.18}$$

The viscous flow is modelled using the compressible integral momentum and energy shape parameter equations (4.19) and (4.20). The later is obtained by combining the former with

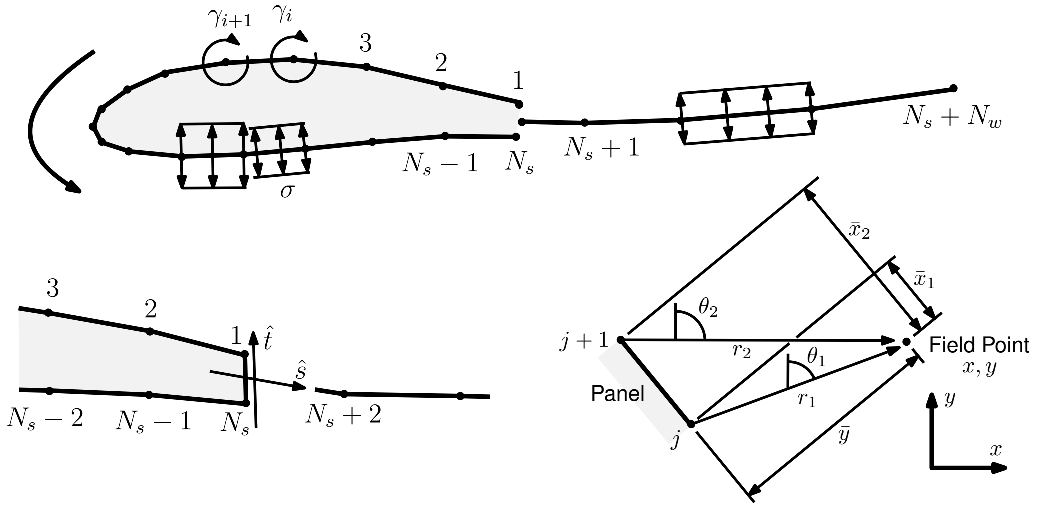

Figure 4.2: *Schematic of the panel discretisation method used by XFOIL [140].*

the kinetic energy thickness equation. In these equations, ξ is the stream-wise coordinate and u_e and M_e are the boundary layer edge velocity and Mach number. H, H^*, H_ρ and θ are the boundary layer shape factor, kinetic energy shape factor, density shape factor and momentum thickness. C_{df} is the skin friction coefficient while C_E is the outer layer dissipation, or entrainment, coefficient.

$$\frac{d\theta}{d\xi} + \left(2 + H - M_e^2\right) \frac{\theta}{u_e} \frac{du_e}{d\xi} = \frac{C_{df}}{2} \tag{4.19}$$

$$\theta \frac{dH^*}{d\xi} + \left(2H_\rho + H^*(1+H)\right) \frac{\theta}{u_e} \frac{du_e}{d\xi} = 2C_E - H^* \frac{C_{df}}{2} \tag{4.20}$$

A modified version of the compressible shear stress lag equation (4.21) from Green et al. [141] is also used. The modification is intended to improve predictions of lift and drag close to stall. In this equation, δ and H_k are boundary layer thickness and kinematic shape factor and C_τ is the sheer stress coefficient. The subscript EQ indicates equilibrium flow, defined as a flow where the kinematic shape factor does not vary in the stream-wise direction [141].

$$\frac{\delta}{C_\tau} \frac{dC_\tau}{d\xi} = 5.6 \left(C_{\tau_{EQ}}^{0.5} - C_\tau^{0.5}\right) + 2\delta \left[\frac{4}{3\delta^*} \left[\frac{C_{df}}{2} - \left(\frac{H_k - 1}{6.7H_k} \right)^2 \right] - \frac{1}{u_e} \frac{du_e}{d\xi} \right] \tag{4.21}$$

For regions of the boundary layer with laminar flow, equation (4.21) is replaced with equation (4.22). Here, N is natural log of the maximum amplification ratio obtained from the two-dimensional incompressible Orr-Sommerfeld equation. $\frac{dRe_\theta}{d\xi}$ is found for the Falkner-Skan family of aerofoils while the empirical relation $\frac{dN}{dRe_\theta}$ is found by analysing the same aerofoils at a range of shape parameters and disturbance frequencies [57]. Once $\frac{dN}{dRe_\theta}$ has been calculated along the aerofoil, transition is specified at the stream wise position where N equals some user defined limit. N is calculated using equation (4.23). This represents a simplified e^N transition model.

$$\frac{dN}{d\xi} = \frac{dN}{dRe_\theta}(H_k)\frac{dRe_\theta}{d\xi}(H_k,\theta) \tag{4.22}$$

$$N = \int_{\xi_0}^{\xi} \frac{dN}{dRe_\theta}\, d\xi \tag{4.23}$$

The key variables used to define the boundary layer are θ, δ^* and C_τ, with M and R_e specified and u_e obtained from the inviscid solution. To reduce the problem to three equations with three unknowns, all additional variables are defined as functions of the known and defined variables. A summary of the dependencies for each additional term are shown in equation (4.24). The exact formulas behind each of these expressions when applied to laminar and turbulent boundary layers are presented by Drela and Giles [57].

$$H_k = H_k(H,M) \qquad C_{\tau_{EQ}} = C_{\tau_{EQ}}(H^*,H,H_k,U_s) \tag{4.24}$$

$$H^* = H^*(H_k,M,Re_\theta) \qquad C_{df} = C_{df}(H_k,M,Re_\theta) \tag{4.25}$$

$$H_\rho = H_\rho(H_k,M) \qquad C_E = (C_{df}/2)U_s + C_\tau(1-U_s) \tag{4.26}$$

$$U_s = U_s(H^*,H,H_k) \tag{4.27}$$

Equations (4.19), (4.20), (4.21) or (4.22) are discretised along the panels, resulting in three non-linear coupled equations for each. The wake is treated as a single viscous sheet with constant θ and δ^* at each section. Interaction between the inviscid and viscous flow is done using transition mass flow. The exact method used for coupling of the inviscid and viscous models and solving of each can be found in Drela [140]. Additional corrections are included to account for weak compressibility effects and mild separation.

4.3.3 Transonic Flow Solver

For analysis and optimisation at transonic conditions, the VII-based flow solver CVGK [142] was used. This is derived from BVGK which was developed by the former Royal Aircraft Establishment. CVGK is made up of a number of models combined to produce a full VII-based solver with transition modelling capability. Figure 4.3 shows these models and the workflow used to obtain a converged solution from them.

Inviscid flow is modelled within CVGK using VGK, an implementation of the Garabedian and Korn [92] (G&K) full potential flow method with additional improvements (as outlined by Lock [143]). The full potential flow equation for steady compressible two-dimensional irrotational and isentropic compressible flow is shown in equation (4.28), where u and v are velocity components in the x and y directions, ϕ is a velocity potential and a is the speed of sound, calculated using Bernoulli's equation.

$$(a^2-u^2)\frac{\partial^2\phi}{\partial x^2} - 2uv\frac{\partial^2\phi}{\partial x\partial y} + (a^2-v^2)\frac{\partial^2\phi}{\partial y^2} = 0 \tag{4.28}$$

This is solved over a modified grid obtained by mapping the exterior of the aerofoil onto the inside of a circle using Sells transformation [144]. This results in the farfield boundary being located at the circles origin ($r = 0$) and the aerofoil surface at the circles circumference ($r = 1$). The transformation results in good clustering of cells in region of high curvature on

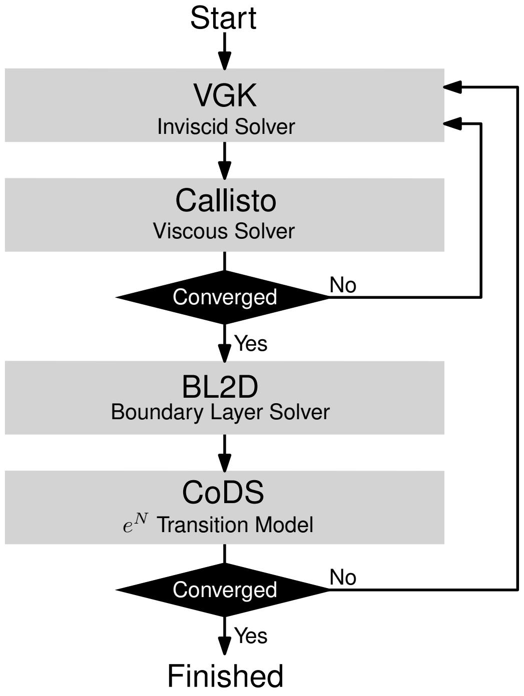

Figure 4.3: *Flow chart of the individual components used within the flow solver CVGK.*

the aerofoil, such as near the leading and trailing edges. The G&K method is post-processed within Callisto so that the inviscid flow solution can be applied to swept and tapered wings [142]. This is done using the equivalence laws derived by Lock [145]. The inviscid flow is then assumed to not vary significantly in the spanwise direction.

Viscous flow is modelled in CVGK using Callisto, an implementation of the Lag-Entrainment integral method for compressible flow as given by Green et al. [141]. Thwaites' integral boundary layer method with a compressibility correction is used for the laminar portions of the flow. Callisto solves these equations in the line of flight direction using non-orthogonal ζ and η coordinates. These are shown in figure 4.4 where the line-of-flight section is defined by points AB on an idealised swept-tapered wing with an assumed locally constant cross section and twist. The leading and trailing edges of the wing converge at an origin point O outboard. As can be seen, ζ is tangential in the line of flight direction while η is aligned in a direction towards the origin point at an angle Λ.

Within this coordinate reference frame, the compressible stream-wise momentum integral equation is given by equation (4.29), where the coefficients are defined in equations (4.30) to (4.35). As with the equations used for viscous flow within XFOIL, θ is boundary layer momentum thickness, u_e and M_e are the boundary layer edge velocity and Mach number, H is shape factor, H_ρ the density, or compressible shape factor and C_{df} is again the skin friction coefficient. In addition, κ_T represents curvature in the line-of-flight x axis related to tapering of the wing, β represents the angle between the external and limiting streamline (very close to the wall) and the different f variables represent three-dimensional shape factors. Finally, ϕ is the angle between the life-of-flight and inviscid streamline.

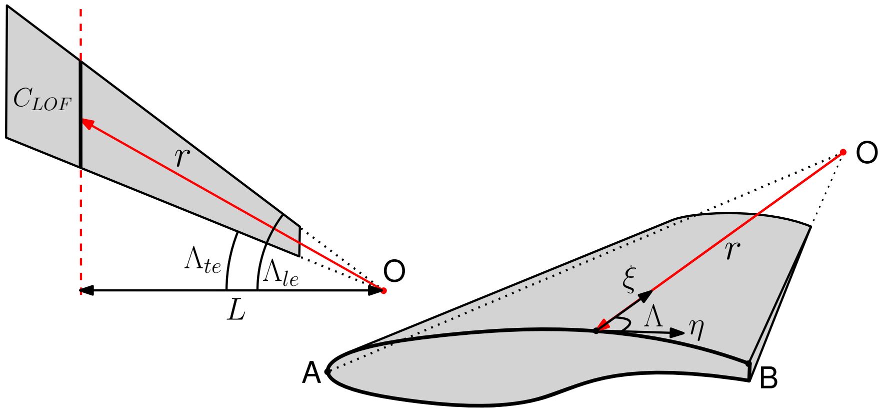

Figure 4.4: *Non-orthogonal coordinate frame used by Callisto as part of CVGK (Modified from [146]).*

$$\begin{pmatrix} A_\theta & A_{H_\rho} & A_\beta & A_u \end{pmatrix} \cdot \frac{d}{d\xi} \begin{pmatrix} \theta & H_\rho & \beta & u_e \end{pmatrix} = A_0 \tag{4.29}$$

$$A_A = \theta \left[\cos\psi \left(1 - \bar{f}\right) - \sin(\psi)\tan(\beta) f_2\right] \tag{4.30}$$

$$A_\theta = \frac{\partial A_A}{\partial \theta} = \cos(\psi)\left(1 + \bar{f} + \bar{f}_\theta \theta\right) - \sin(\psi)\tan(\beta) f_2 \tag{4.31}$$

$$A_{H_\rho} = \frac{\partial A_A}{\partial H_\rho} = \theta \left[\cos(\psi)\bar{f}_{H_\rho} - \sin(\psi)\tan(\beta)\frac{df_2}{dH_\rho}\right] \tag{4.32}$$

$$A_\beta = \frac{\partial A_A}{\partial \beta} = \theta \left[\cos(\psi)\bar{f}_\beta - \sin(\psi)\sec^2(\beta) f_2\right] \tag{4.33}$$

$$A_U = \frac{\theta}{u_e}\left[\cos(\psi)\left(H + 2 + 2\bar{f} + \bar{f}_u u_e\right) + \sin(\psi)\tan(\psi)\left(1 - \tan^2(\beta) f_4\right) - M_e^2 A_\theta\right] \tag{4.34}$$

$$A_0 = \sin(\Lambda)\left[\frac{C_{df}}{2} + \kappa_T \theta \left(\sin(\psi) + \cos(\psi)\tan(\beta) f_2\right)\right] - \kappa_T \theta \cos(\Lambda) A_\theta - \cos(\psi)\bar{f}_\xi \theta \tag{4.35}$$

The compressible normal or crossflow momentum integral equation is given in (4.36), where the coefficients are defined in equations (4.37) to (4.41).

$$\begin{pmatrix} N_\theta & N_{H_\rho} & N_\beta & N_u \end{pmatrix} \cdot \frac{d}{d\xi} \begin{pmatrix} \theta & H_\rho & \beta & u_e \end{pmatrix} = N_0 \tag{4.36}$$

$$N_\theta = \tan(\beta)\left(\cos(\psi) f_1 - \sin(\psi)\tan(\beta) f_4\right) \tag{4.37}$$

$$N_{H_\rho} = \frac{\partial N_\theta}{\partial H_\rho}\theta = \tan(\beta)\theta \left[\cos(\psi)\frac{df_1}{dH_\rho} - \sin(\psi)\tan(\beta)\frac{df_4}{dH_\rho}\right] \tag{4.38}$$

$$N_\beta = \frac{\partial N_\theta}{\partial \beta}\theta = \sec^2(\beta)\theta\left[\cos(\psi) f_1 - 2\sin(\psi)\tan(\beta) f_4\right] \tag{4.39}$$

$$N_u = \left[2\sec(\psi)\tan(\beta) f_1 - \sin(\psi)\left(1 + H + \tan^2(\beta) f_4\right) - M_e^2 N_\theta\right]\frac{\theta}{u_e} \tag{4.40}$$

$$N_0 = \sin(\Lambda)\tan(\beta)\left[\frac{C_{df}}{2} + \kappa_T \theta \left(\sin(\psi) f_1 + \cos(\psi)\tan(\beta) f_4\right)\right] - \kappa_T \theta \cos(\Lambda) N_\theta \tag{4.41}$$

The entrainment equation is given in (4.42), with coefficients defined in equations (4.43) to (4.47). In these, C_E is the entrainment coefficient and H_1 is the entrainment shape factor.

$$\begin{pmatrix} E_\theta & E_{H_\rho} & E_\beta & E_u \end{pmatrix} \cdot \frac{d}{d\xi} \begin{pmatrix} \theta & H_\rho & \beta & u_e \end{pmatrix} = E_0 \tag{4.42}$$

$$E_\theta = \cos(\psi) H_1 + \sin(\psi)\tan(\beta) f_3 \tag{4.43}$$

$$E_{H_\rho} = \frac{\partial E_\theta}{\partial H_\rho}\theta = \left[\cos(\psi)\frac{dH_1}{dH_\rho} + \sin(\psi)\tan(\beta)\frac{df_3}{dH_\rho}\right]\theta \tag{4.44}$$

$$E_\beta = \frac{\partial E_\theta}{\partial \beta}\theta = \left[\sin(\psi)\sec^2(\beta) f_3\right]\theta \tag{4.45}$$

$$E_U = \left[\sec(\psi) H_1 - M_e^2 E_\theta\right]\frac{\theta}{u_e} \tag{4.46}$$

$$E_0 = \sin(\Lambda)\left[C_E + \kappa_T\theta\left(\sin(\psi)H_1 - \cos(\psi)\tan(\beta)f_3\right)\right] - \kappa_T\theta\cos(\Lambda)E_\theta \tag{4.47}$$

The lag equation is transformed into the ξ, η non-orthogonal coordinate system, as shown in (4.48). The coefficients are defined in equations (4.49) to (4.52). In these, C_E is the entrainment coefficient, C_τ is the shear stress coefficient and H_1 is the entrainment shape factor.

$$L_E \frac{dC_E}{d\xi} = L_0 - L_u \frac{du_e}{d\xi} \tag{4.48}$$

$$L_E = \cos(\psi)\theta \tag{4.49}$$

$$L_U = \cos(\psi) F \left[1 + 0.075 M_e^2 \frac{1 + 0.2u_e^2}{1 + 0.1u_e^2}\right]\frac{\theta}{u_e} \tag{4.50}$$

$$L_0 = F\sin(\Lambda)\left[\frac{2.8}{H + H_1}\left(\sqrt{C_{\tau,EQ0}} - \lambda\sqrt{C_\tau}\right) + \left(\frac{\theta}{u_e}\frac{\partial u_e}{\partial s}\right)_{EQ}\right] \tag{4.51}$$

$$F = \frac{C_\tau}{1.2\left(0.01 + C_E\right)\left(1 + 0.1u_e^2\right)} \tag{4.52}$$

An equation for the transpiration velocity V_n is also included. This is shown in (4.53) with coefficient defined in equations (4.54) to (4.56).

$$\begin{pmatrix} W_\theta & W_{H_\rho} & W_\beta & W_U \end{pmatrix} \cdot \frac{d}{d\xi} \begin{pmatrix} \theta & H_\rho & \beta & u_e \end{pmatrix} - \sin(\Lambda)\frac{V_n}{u_e} = W_0 \tag{4.53}$$

$$W_\theta = \cos(\psi) H - \sin(\psi)\tan(\beta) f_3 \tag{4.54}$$

$$W_{H_\rho} = \frac{\partial W_\theta}{\partial H_\rho}\theta = -\sin(\psi)\sec^2(\beta) f_3\theta \tag{4.55}$$

$$W_U = \left(\cos(\psi) u_e \frac{\partial H}{\partial u_e}\right) \tag{4.56}$$

Laminar boundary layer is modelled in Callisto using Thwaites integral method with a compressibility correction. When using this, the transpiration velocity is obtained by approximating using the equation for an infinity swept wing and the shape factor found using lookup tables. These equations, and a detailed overview of the solution method for the viscous flow equations, can be found in Atkin [146].

For transition prediction, VGK is coupled with the compressible laminar boundary layer equation solver BL2D and CoDS which is an implementation of the e^N method for two-dimensional and quasi-two-dimensional flows [147]. For quasi-two-dimensional flows, the dual envelope e^N method is used where both Tollmien-schlichting and Crossflow instability critical N-factor values can be specified as well as an instability interaction region. CVGK has been extensively used for transonic wing design in the UK aerospace industry and validated at swept and un-swept transonic flow conditions [35, 142].

Chapter 5

Critical N-factor Uncertainty Analysis

To enable the robust design of NLF aerofoils, the effect of critical N-factor uncertainty on aerofoil performance first needs to be investigated. To undertake this, selection of a suitable uncertainty analysis methodology is made and its accuracy assessed. Uncertainty analysis is then carried out on two aerofoil test cases. The first aerofoil is analysed at subsonic conditions over a range of lift coefficients while the second is analysed at transonic conditions over a range of Mach numbers. The objectives of this work are to:

- Explore how critical N-factor uncertainty affects aerofoil performance uncertainty
- Determine the conditions for robust and unrobust aerofoil performance
- Determine any links betweens deterministic and non-deterministic performance
- Assess how sensitive the stochastic analysis is to the input uncertainty distribution.

5.1 Methodology

5.1.1 Uncertainty Representation

There are several uncertainty representation methods available. A probability distribution is the best choice for a precise description of uncertainty, while an interval representation is preferable if little information about the uncertainty is known. Due to the small amount of published flight test data, limited information is available for an accurate probabilist description of critical N-factor uncertainty. Under such conditions an interval representation may be more appropriate. It is, however, an unsuitable choice if the response of the system being modelled to the input uncertainty is non-linear. If an interval representation is used, only the range and midpoint of the output can be captured. Range can be very sensitive to interval size and the midpoint far from the mean value for non-linear systems.

This is illustrated in figure 5.1 showing the variation of drag coefficient with changing critical N-factor for three example designs with the same critical N-factor uncertainty interval. Within the interval, all three envelopes have identical midpoint values. However, both the red and yellow envelopes are non-linear and so their midpoint and mean values differ substantially. Changing the uncertainty interval size would also have a strong effect on both. The black envelope is linear in nature and so its midpoint and mean values are comparable.

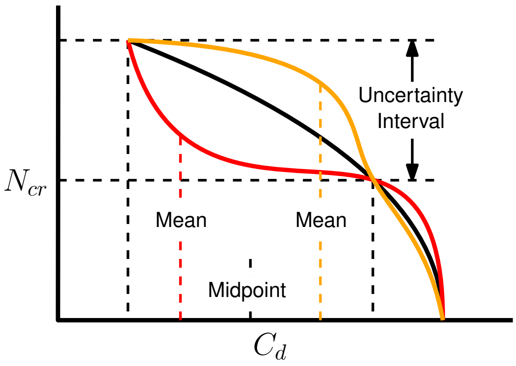

Figure 5.1: *Example critical N-factor drag envelopes with interval uncertainty analysis.*

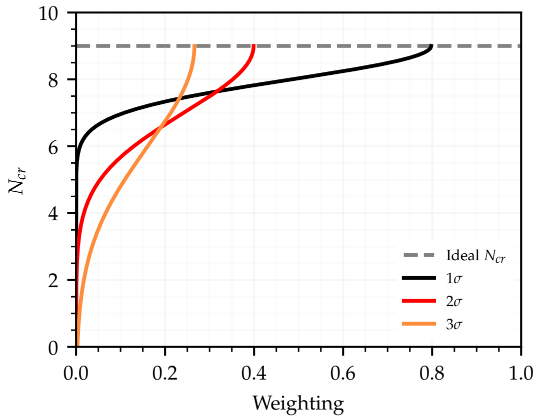

Figure 5.2: *Example negative half-normal probability distributions over critical N-factor.*

Aerofoil performance can have a highly non-linear relationship with critical N-factor, as all three of the example envelopes shown in figure 5.1 are possible. Discontinuities may also be present due to laminar separation at subsonic speeds or shock induced transition at transonic speeds. As such, a probability distribution representation of uncertainty is used in this work. Given the lack of available information on critical N-factor uncertainty, the uncertainty distribution used for this study is based on intuitive analysis of the individual uncertainty sources effecting critical N-factor. These include uncertainty in free-stream turbulence levels, machining quality, surface damage, wear and contamination.

As free-stream turbulence is an atmospheric condition, both positive and negative fluctuations are possible with equal probability. Machining accuracy on the other hand is more likely to produce surface imperfections, and thus a reduced critical N-factor, compared to a better-than-expected finish. Surface damage and wear can only cause increased instability amplification and thus reduce critical N-factor. The same is true of surface contamination from insect impacts, debris and dirt. As such, with the exception of free-stream turbulence, all sources of uncertainty have a much larger probability of increasing initial disturbance size and so reducing critical N-factor. Given that free-stream turbulent intensity is low during flight, and that surface quality, damage, wear and contamination each have a strong effect on disturbance amplitude, a negative half-normal critical N-factor uncertainty distribution has been used for this study.

Figure 5.2 shows three half-normal distributions with a mean critical N-factor value of 9 and varying critical N-factor standard deviations. Mathematically, the negative half-normal distribution is represented by the probability density function $P(N)$ shown in Eq. (5.1). In this, N_i is the ideal design critical N-factor which is the largest N_{cr} value expected and has the highest probability weighting. N_σ is the critical N-factor standard deviation and controls the shape of the distribution.

$$P(N) = \frac{\sqrt{2}}{N_\sigma \sqrt{\pi}} \exp\left(-\frac{(N - N_i)^2}{2N_\sigma^2}\right); \quad N \leq N_i \tag{5.1}$$

5.1.2 Uncertainty Propagation

There are various methods available for propagation of uncertainty through a model into the output variable, the simplest of which being sampling based. In this work, the output variable of interest is assessed at multiple critical N-factor sample points taken at regular intervals over the uncertainty range. Each output value is then weighted using the probability density function given in Eq. 5.1 with the critical N-factor value used to run that particular flow solution. These weighted output values are finally used to calculate mean output and output standard deviation.

This process is shown in figure 5.3, where samples are taken over the critical N-factor range, used to evaluate drag, and these values and weightings used to construct a probability distribution from which robustness of the output variable can be quantified. The weighted arithmetic mean $F_\mu(N)$ of the output variable $F(N_j)$ is calculated using Eq. (5.2). k_r is the number of uniformly spaced samples taken over the desired critical N-factor range, $P(N_j)$ is the probability weighting found using Eq. (5.1) and W is the sum of the probability weights found using Eq. (5.4). The standard deviation $F_\sigma(N)$ of the output variable is then calculated using Eq. (5.3).

$$F_\mu = \frac{1}{W}\sum_{j=1}^{k_r} P(N_j)F(N_j) \tag{5.2}$$

$$F_\sigma = \sqrt{\frac{1}{W}\sum_{j=1}^{k_r}\left[F(N_j) - F_\mu\right]^2} \tag{5.3}$$

$$W = \sum_{j=1}^{k_r} P(N_j) \tag{5.4}$$

This approach was selected over other sampling strategies as it requires fewer sample points while also having perfect equidistribution of points over the uncertainty variable. This is achieved by weighting each sample point with its probability, taken directly from the probability density function. This avoids repeated sampling using the probability weighting to randomly select points. Accuracy naturally increases with the number of samples used. While the exact solution is obtained as the number of samples tends to infinity, a suitable finite number of samples must be selected to give acceptable accuracy.

It is important to note that as this sampling strategy is periodic in nature, its accuracy will be low for problems where the variable of interest is also periodic over the uncertain input with frequency close to that of the sample spacing. Transition location should only move downstream as critical N-factor is increased, providing separation does not occur. In such a case, the response to critical N-factor uncertainty is not periodic and so this approach to uncertainty propagation is suitable. If a flow is seperated at the ideal critical N-factor or buffet is occuring, reducing critical N-factor could result in transition moving either forwards or backwards. In such a case, the response to critical N-factor would feature a small oscillation that may be missed by the selected sampling method if the resolution of sample points is not sufficiently high.

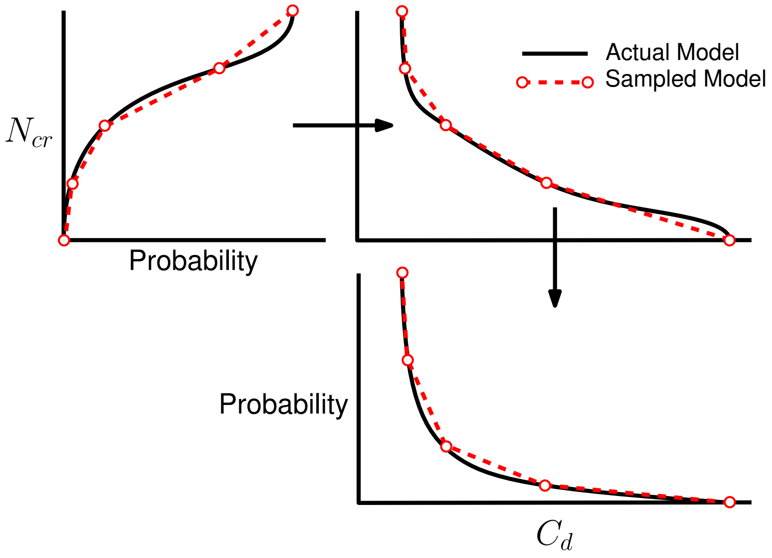

Figure 5.3: *Diagram of uniform sampling approach to uncertainty propagation.*

5.2 Uncertainty Analysis

5.2.1 Aerofoil selection

To investigate performance robustness to critical N-factor uncertainty at subsonic conditions, the NLF0215 [69] aerofoil is analysed using the proposed methodology. This is a flapped aerofoil designed for a cruise lift coefficient of $C_l = 0.2$ at $Re = 9 \times 10^6$ with 10° upwards flap deflection. The target maximum lift coefficient was $C_{l,\max} = 1.8$ at $Re = 3 \times 10^6$ with 10° downwards flap deflection. During this study, a flap deflection of 0° was used with analysis carried out at the cruise Reynolds number of $Re = 9 \times 10^6$, $M = 0.1$ and over the lift coefficients range $0 \leq C_l \leq 1.6$. The aerofoil profile is shown in figure 5.4.

To examine performance robustness to critical N-factor uncertainty at transonic conditions, the RAE2822 [148] aerofoil has been selected for analysis. This is a supercritical aerofoil designed for $C_l = 0.56$ at $M = 0.66$. Initial analysis of the aerofoil at $Re = 6.5 \times 10^6$ found that $(ML/D)_{\max}$ occurs at approximately $M = 0.715$ and $C_l = 0.76$. This was used to fix $M^2 C_l$ while varying Mach number between $0.68 \leq M \leq 0.73$. The aerofoil profile is shown in figure 5.5.

Practical implementation of NLF requires some protection of the leading edge from contamination [149]. For subsonic applications, it is assumed that a method such as liquid discharge [150] is chosen. This enables laminar flow to be obtained on both surfaces and so transition is left free on both for the subsonic case. For transonic applications such as large commercial aircraft, a popular method for protecting the leading edge is via the use of a Krueger flap [151–153]. This is a high lift device capable of shielding the leading edge from contamination when deployed while leaving the upper surface free of contamination, steps or gaps when retracted into the lower surface. This however comes at a cost of early transition on the lower surface and so, for the transonic case, transition on the lower surface is fixed at $0.03x/c$.

For both aerofoils, uncertainty in critical N-factor is represented by a negative half-normal distribution. Maximum probability in both cases is at an ideal critical N-factor of $N_{cr} = 9$. This value is often used in academic NLF studies at subsonic conditions using the simplified e^N method found within XFOIL [20, 114, 154, 155]. This value was also used for the transonic case as it lies between the N_{cr} obtained with compressible e^N stability analysis of the ATTAS and FOKKER 100 NLF flight test data when little crossflow instability growth is seen [14, 51]. Critical N-factor standard deviation is set to $N_\sigma = 2$ in both cases.

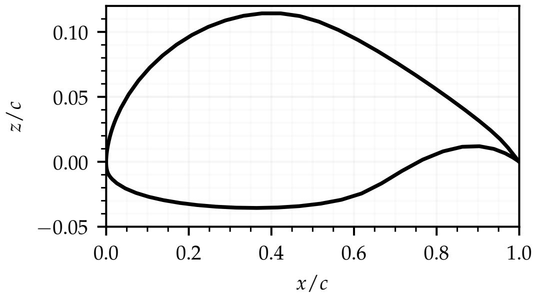

Figure 5.4: *NLF0215 aerofoil profile.*

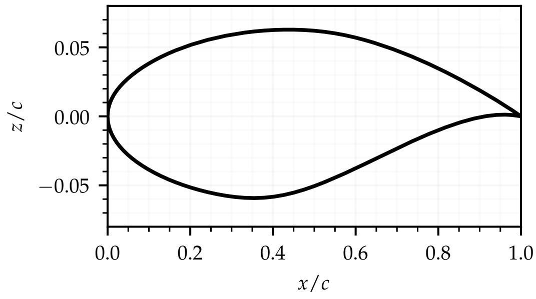

Figure 5.5: *RAE2822 aerofoil profile.*

5.2.2 Stochastic Convergence

The mean and standard deviation of the output properties are calculated using 91 critical N-factor samples taken at intervals of 0.1 from $N_i = 9$ to $N_{cr} = 0$. To ensure these are accurate, the mean and standard deviation of various aerodynamic properties are calculated with smaller sample numbers and compared against the values found when using 91 samples. This was done over the lift coefficient range $0 \leq C_l \leq 1.6$ at intervals of 0.05 for the NLF0215 and over the Mach number range $0.68 < M < 0.73$ at intervals of 0.05. In each case, the maximum mean and standard deviation error found over this range for each of the smaller number of samples is then selected.

Figure 5.6 shows the maximum C_d, Tr_u and Tr_l mean and standard deviation error against the number of samples used for the NLF0215. The maximum error for each variable decreases as the sample number rises, indicating that the mean and standard deviation for each variable is converging. The error in standard deviation is smaller than the error in mean, and reduces to a smaller value overall, in each case. This is expected as standard deviation is found to be much smaller than the mean for each variable.

Figure 5.7 shows the maximum ML/D, C_d and Tr_u mean and standard deviation error against the number of samples used for the RAE2822. Again, the general trend seen is that the maximum error of each variable decrease as the number of samples used rises. However, the maximum error in ML/D, C_d and Tr_u standard deviation sees significant oscillation. These fluctuations are due to the presence of discontinuities in the distributions of ML/D, C_d and Tr_u over critical N-factor. This makes the calculation of standard deviation sensitive to the positioning of the sample points, especially when standard deviation is very low. As increasing the number of samples causes sample positions to change, fluctuations in each variable are seen.

Overall, these results indicate that as the number of samples is increased up to the 91 selected, the maximum error of each variable reduces. For the NLF0215, this is down to a fraction of a drag count and to less than $0.003x/c$ for upper and lower surface transition locations. For the RAE2822, this is down to 0.05 ML/D, 0.1 drag count and $0.001x/c$ for transition location. This supports the use of 91 samples to provide accurate values for mean and standard deviation of aerodynamic properties.

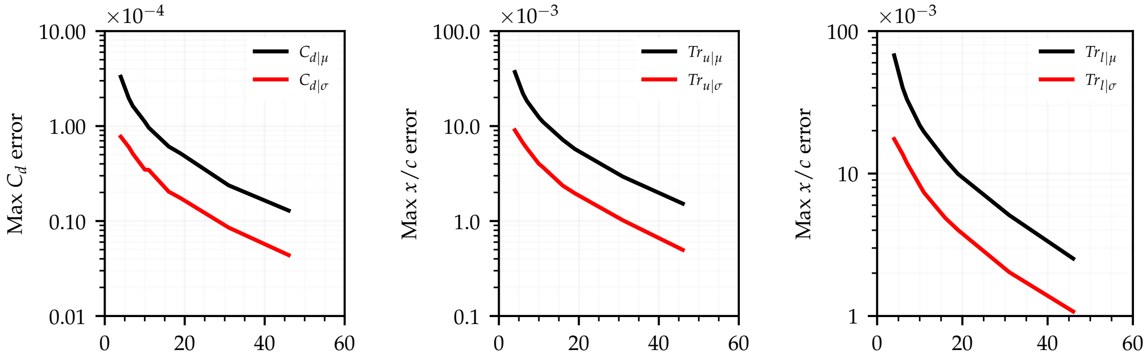

(a) *Drag* **(b)** *Upper surface transition* **(c)** *Lower surface transition*

Figure 5.6: *Maximum C_d, Tr_u and Tr_l mean and standard deviation error over $0.0 \leq C_l \leq 1.6$ when calculated with various sample numbers for the NLF0215.*

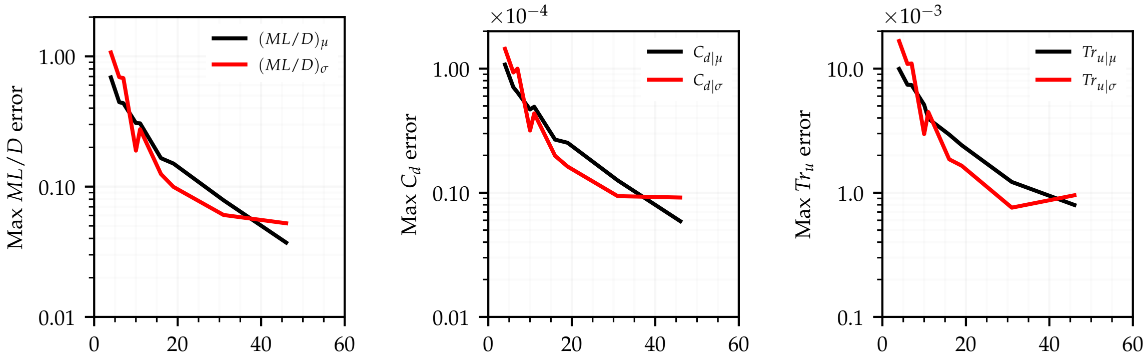

(a) *ML/D* **(b)** *Drag* **(c)** *Upper surface transition*

Figure 5.7: *Maximum ML/D, C_d and Tr_u mean and standard deviation error over $0.68 \leq M \leq 0.73$ when calculated with various sample numbers for the RAE2822.*

5.3 Subsonic Results

5.3.1 Deterministic Performance

Deterministic performance of the NLF0215 aerofoil is first assessed. Figure 5.8 shows drag and transition polars for the NLF0215 run at $N_{cr} = 9$, with the drag polar providing a breakdown of total drag (C_d) into skin friction (C_{df}) and pressure drag (C_{dp}) components. As seen in figure 5.8a, total drag is dominated by the skin friction component below $C_l = 1.1$ and exhibits a bucket shape between $0.5 < C_l < 1.0$. This is common for NLF aerofoils.

The skin friction polar shape is caused by the movement of transition location on each surface. This is shown in figure 5.8b. Lower surface transition location changes over a small lift coefficient range leading to the sharp lower drag bucket corner. Similar transition movement on the upper surface forms the upper drag bucket corner although shorter maximum laminar length and a more gradual movement results in a less strongly defined shape. To compare, decreasing lift coefficient from $C_l = 0.7$ to $C_l = 0.5$ results in a $0.54x/c$ reduction in laminar flow on the lower surface while increasing lift coefficient from $C_l = 1.0$ to $C_l = 1.2$ leads to a $0.20x/c$ reduction in upper surface laminar flow. Low drag within the bucket is due to highly extended laminar flow on both surfaces. Although drag is low within the bucket region, it quickly rises outside, leading to higher drag at off-design lift coefficients.

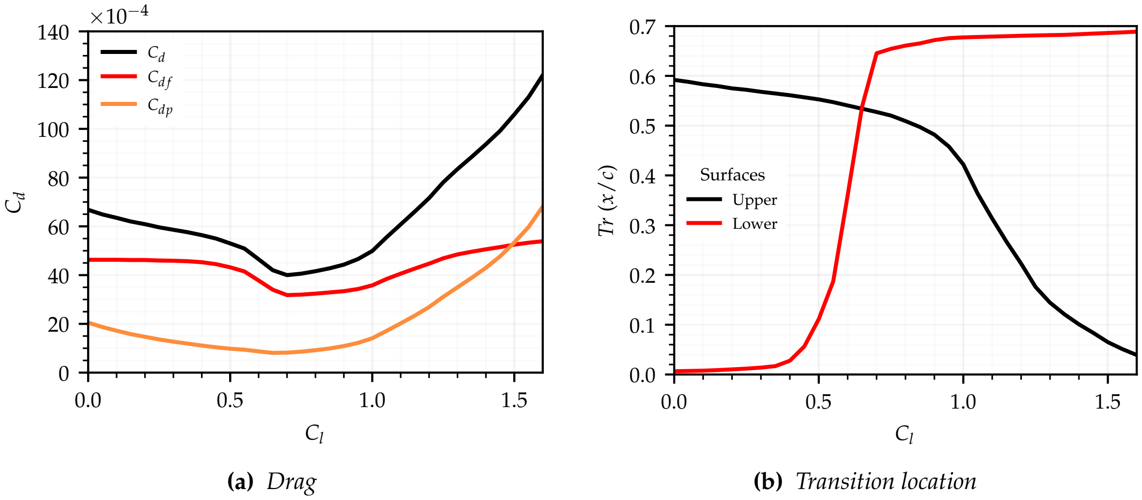

(a) *Drag* **(b)** *Transition location*

Figure 5.8: *Drag and transition location polars run at $N_{cr} = 9$ for the NLF0215.*

Figure 5.9 shows the pressure distribution and N-factor envelopes for the NLF0215 at lift coefficients of $C_l = 0.4$, $C_l = 0.7$ and $C_l = 1.0$. Markers on the pressure distribution indicate transition location for each surface at each lift coefficient. At $C_l = 0.4$, transition on the upper surface is delayed as there is a strong favourable pressure gradient over the front of the aerofoil. This suppresses upper surface instability growth, as can be seen by no growth in the N-factor envelope until $0.38x/c$. Transition occurs very close to the leading edge on the lower surface, however, as a large pressure rise followed by a strong adverse pressure gradient causes rapid TS instability amplification.

At $C_l = 0.7$, transition has remained at a similar position on the upper surface but has extended on the lower surface. Angle of attack increases with lift coefficient, which reduces the lower surface leading edge pressure peak and weakens the adverse pressure gradient. This is now favourable but weak on the lower surface at $C_l = 0.7$. As such, transition moves rapidly to the leading edge with only a small reduction in lift coefficient, as seen in figure 5.8b. At $C_l = 1.0$, upper surface transition begins to move upstream as the larger leading edge pressure rise causes an adverse pressure gradient over the front of the aerofoil. This increases instability growth, as seen on the N-factor envelope. While lower surface transition location has changed little from $C_l = 0.7$ to $C_l = 1.0$, a stronger favourable pressure gradient suppresses TS instability growth so that no growth occurs upstream of $0.6x/c$.

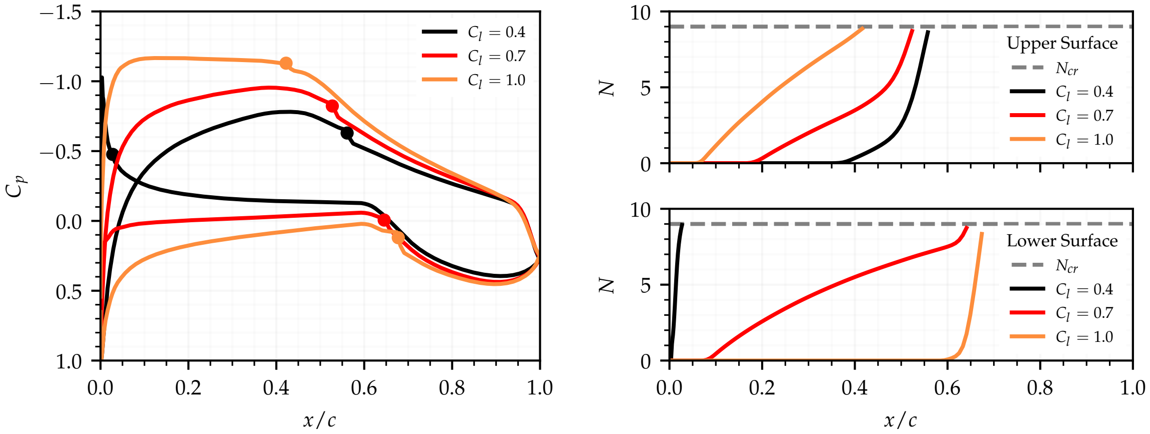

(a) *Pressure distributions* **(b)** *N-factor envelopes*

Figure 5.9: *Pressure and N-factor envelopes run at $N_{cr} = 9$ for the NLF0215 at $C_l = 0.4$, 0.7 and 1.0*

5.3.2 Stochastic Performance

Figure 5.10 shows the mean drag and transition location polars. In figure 5.10a, mean C_d, C_{df} and C_{dp} are shown, along with the range of each between the value found at the ideal critical N-factor and at a critical N-factor of zero. As can be seen in figure 5.10a, the C_d range is largest within the drag bucket lift coefficient region. This is understandable as transition is delayed on both surfaces. A total loss of laminar flow at $C_l = 0.7$ causes skin friction to rise by 32 drag counts and pressure drag to rise by 15 drag counts. Mean C_d, C_{df} and C_{dp} are each close to the value found at the ideal critical N-factor. Mean C_d has increased most at the drag bucket corners. At the lower drag bucket corner from $0.5 < C_l < 0.7$, mean C_d is larger as mean C_{df} has increased. At the upper drag bucket corner from $0.9 < C_l < 1.2$, mean C_d is larger as both mean C_{df} and C_{dp} have increased. As mean drag increases less through the drag bucket centre between $0.7 < C_l < 0.9$, the mean drag bucket has a reduced width in comparison to the drag bucket shape at ideal critical N-factor.

Figure 5.10b shows the mean Tr_u and Tr_l polars along with the Tr_u and Tr_l polars at the ideal critical N-factor for comparison. Both mean Tr_u and mean Tr_l are close to Tr_u and Tr_l at lift coefficient values below $C_l = 0.4$. As seen in figure 5.9b, instability amplification occurs far downstream on the upper surface at $C_l = 0.4$. As such, reducing critical N-factor has little effect on transition location. The same is observed on the lower surface, but instability amplification up to the critical N-factor limit happens instead at the leading edge. Mean Tr_l is also close to Tr_l above $C_l = 1.0$ as, again, instability amplification only begins downstream near the transition location.

The location of mean Tr_u and mean Tr_l differs most from Tr_u and Tr_l over the lift coefficient ranges where Tr_u and Tr_l see the most movement with changing lift coefficient. On the upper surface, mean Tr_u is close to Tr_u at high and low lift coefficients, but is reduced through $0.5 < C_l < 1.2$. As a result, the lift coefficient range where Tr_u is highly sensitive to changing lift coefficient has reduced for $Tr_{u|\mu}$. On the lower surface, the inverse is true and the lift coefficient range where $Tr_{l|\mu}$ is sensitive to changing lift coefficient is larger than for Tr_l. This has led to the smaller bucket width.

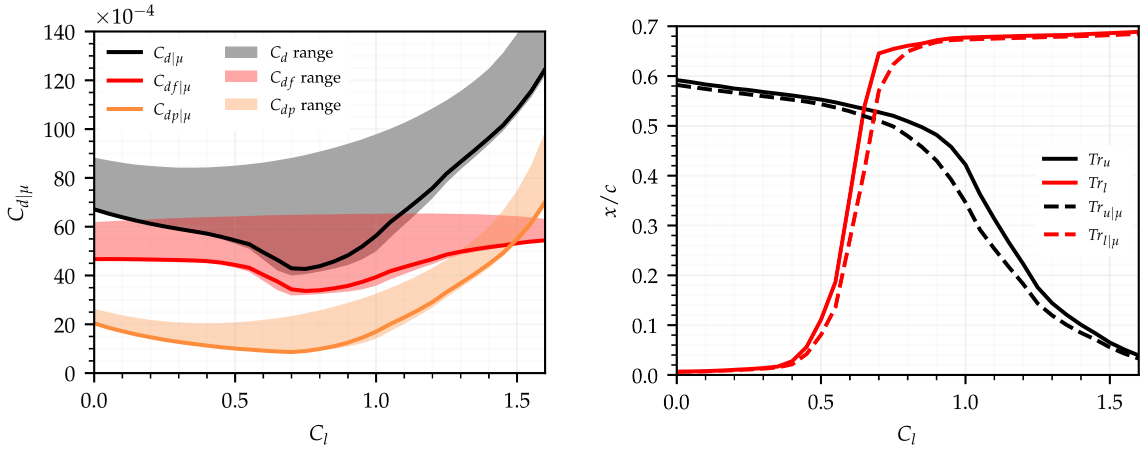

(a) *Drag* **(b)** *Transition Location*

Figure 5.10: *Mean drag and transition polars for the NLF0215 with the drag range between* $N_{cr} = 9$ *and* $N_{cr} = 0$*, and transition locations at* $N_{cr} = 9$.

Figure 5.11 shows drag and transition standard deviation polars. As with the deterministic performance, drag standard deviation is directly related to transition location standard deviation. $C_{d|\sigma}$ is largest through the drag bucket lift coefficient range, with peaks in standard deviation occurring at each drag bucket corner. Naturally, these features can be related to the transition location standard deviation polar for each surface, seen in figure 5.11b. The peak in $C_{d|\sigma}$ at $C_l = 1.0$ comes from a large rise is $Tr_{u|\sigma}$ while the peak in $C_{d|\sigma}$ at $C_l = 0.7$ is caused by a large rise in $Tr_{l|\sigma}$ around this lift coefficient. The large $C_{d|\sigma}$ peak at $C_l = 1.0$ coincides with peaks in both $C_{df|\sigma}$ and $C_{dp|\sigma}$ while the smaller $C_{d|\sigma}$ peak at $C_l = 0.7$ comes primarily from a second peak in $C_{df|\sigma}$. This indicates that the lower surface transition location standard deviation has little effect on $C_{dp|\sigma}$ and a weaker effect on $C_{df|\sigma}$ compared to upper surface location standard deviation. Thus, upper surface transition location has the stronger effect on total drag standard deviation.

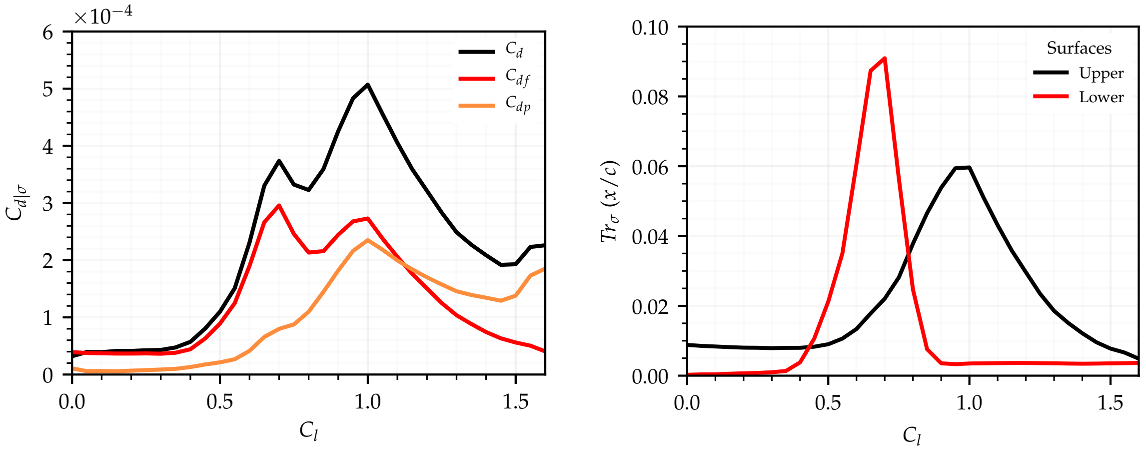

(a) *Drag* **(b)** *Transition location*

Figure 5.11: *Drag and transition location standard deviation polars for the NLF0215.*

These results show that transition location standard deviation is largest when transition is sensitive to changes in lift coefficient at the ideal critical N-factor. The cause of this can be best explained by again considering the pressure distributions and N-factor envelopes in figure 5.9. A strong adverse pressure gradient causes rapid instability growth, such as on the lower surface at $C_l = 0.4$. A strong favourable pressure gradient suppresses instability growth up to rapid amplification, as seen on the upper surface at $C_l = 0.4$. Angle of attack has little effect on instability growth and so transition location in both cases. However, if the pressure gradient strength is weak, such as on the lower surface at $C_l = 0.7$ or the upper surface at $C_l = 1.0$, instability growth is neither strongly amplified or suppressed. Angle of attack then has a stronger effect on instability growth and transition location as it may change the pressure gradient strength and direction. As the instability growth is more gradual, changes in critical N-factor also have a stronger effect on transition location. Thus, when transition location is sensitive to lift coefficient, its standard deviation is also higher.

Above $C_l = 1.4$, pressure drag standard deviation grows while upper surface transition location standard deviation reduces, showing that C_{dp} becomes more sensitive to changes in transition location as angles of attack increases. This can be seen in figures 5.12 which plots pressure drag against critical N-factor at fixed lift coefficient values $C_l = 1.4$, $C_l = 1.5$ and $C_l = 1.6$. As lift coefficient increases, the lift generated by the aerofoil becomes more sensitive to transition location. Thus, reducing critical N-factor at high lift coefficients causes a larger increase in angle of attack to compensate. This, in turn, causes a wider variation in pressure drag over the N-factor range.

This will also affect the maximum lift coefficient of the aerofoil, which is $C_{l,\max} = 1.96$, found at an angle of attack of approximately $\alpha = 20$. At this lift coefficient, transition on the upper surface is at the leading edge while the lower surface has extended laminar flow at $Tr_l = 0.713x/c$. Figure 5.13 shows how maximum lift coefficient varies with critical N-factor. The loss in maximum lift coefficient from $N_{cr} = 9 \rightarrow 0$ is $\Delta C_l = 0.095$. As over 60 percent of this loss happens below $N_{cr} = 2$, maximum lift coefficient standard deviation is very small at $C_{l,\max,\sigma} = 0.0064$ with a critical N-factor standard deviation of $N_\sigma = 2$.

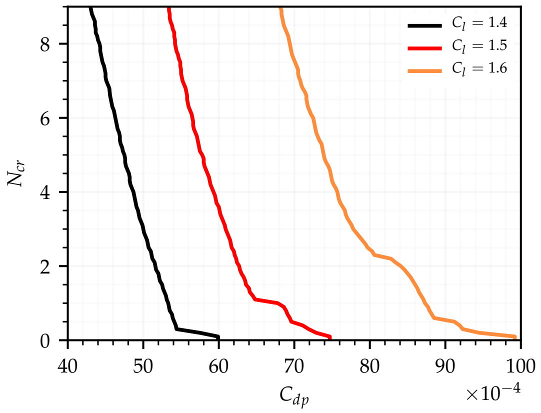

Figure 5.12: *Pressure drag against critical N-factor at various lift coefficients for the NLF0215.*

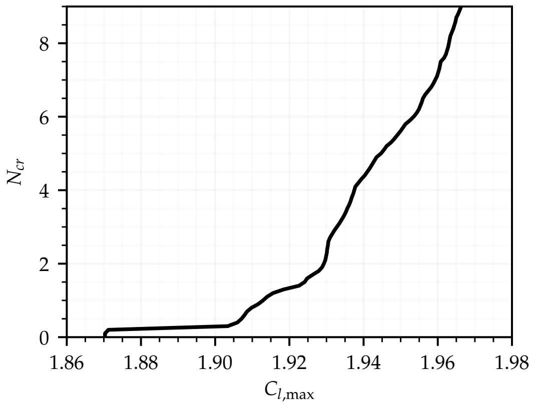

Figure 5.13: *Maximum lift coefficient against critical N-factor for the NLF0215.*

5.3.3 Effect of Uncertainty Standard Deviation

The analysis carried out is, of course, dependent on the choice of critical N-factor uncertainty distribution. The mean and standard deviation polars for C_d, Tr_u and Tr_l when calculated with various critical N-factor uncertainty standard deviation values (N_σ) are shown in figures 5.14 and 5.15. Mean C_d increases as N_σ is raised. This effect is strongest through the centre of the drag bucket where there is the largest drag range due to extended laminar flow on both surfaces. Mean C_d is least sensitive to N_σ at both high and low lift coefficients. Here, transition location on each surface sees little movement as either at the leading edge or highly extended with instability growth only occurring downstream. As N_σ is raised, the mean Tr_u polar effectively shift to a higher lift coefficient while the inverse is true of mean Tr_l. This effectively shrinks the drag bucket.

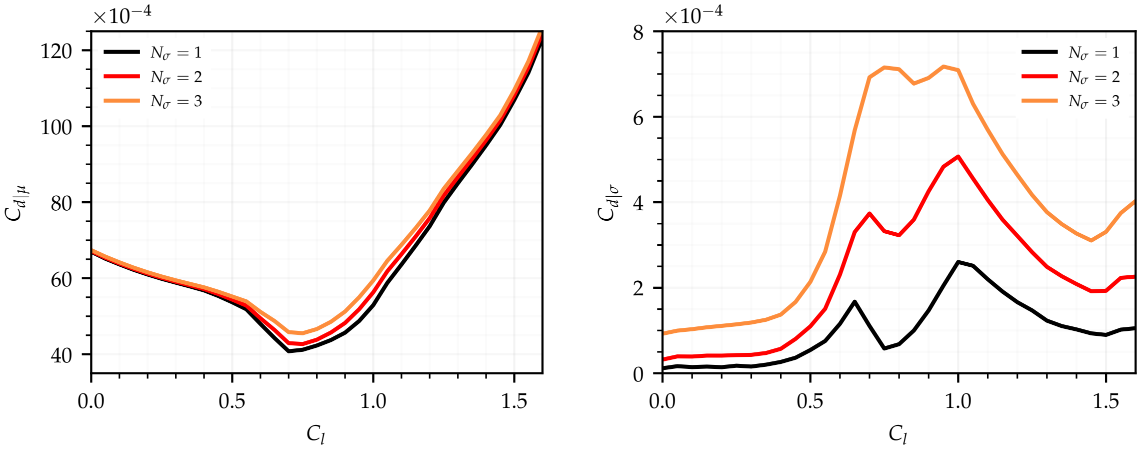

(a) *Mean* **(b)** *Standard deviation*

Figure 5.14: *C_d mean and standard deviation polars for the NLF0215 when calculated with various critical N-factor uncertainty standard deviation values.*

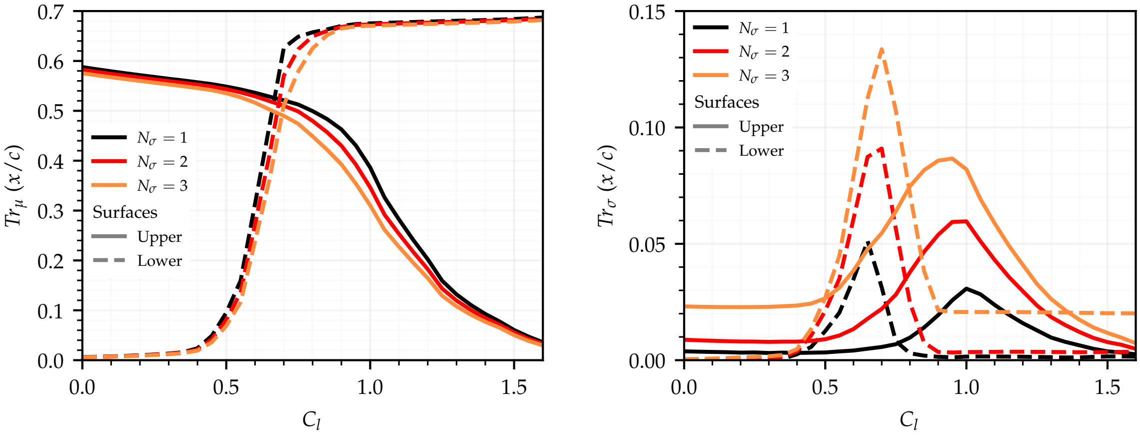

(a) *Mean* **(b)** *Standard deviation*

Figure 5.15: *Mean and standard deviation Tr polars for the NLF0215, calculated with various critical N-factor uncertainty standard deviation values.*

Both drag and transition location standard deviation grow over the entire polar range as N_σ is increased. This effect is small below $C_l = 0.4$ as transition on the lower surface is close to the leading edge at $N_{cr} = 9$. The same is true for $Tr_{u|\sigma}$ above $C_l = 1.4$. As such, the largest changes to $C_{d|\sigma}$ when N_σ is raised occurs through the drag bucket lift coefficient range. Increasing N_σ also causes the two transition location peaks, and so peaks in drag, to move together and increase in magnitude.

Thus, the selection of N_σ has the strongest effect on the mean and standard deviation where transition location is most sensitive to lift coefficient. Drag standard deviation remains dependent on transition location standard deviation at each of the N_σ values selected for lift coefficients below $C_l = 1.3$. Above this, increasing N_σ causes small changes in $Tr_{u|\sigma}$ and $Tr_{l|\sigma}$ but a large increase in $C_{d|\sigma}$. As seen in figure 5.12, pressure drag has the same sensitivity to critical N-factor at high critical N-factors, regardless of the lift coefficient value. However, at low critical N-factors, C_{dp} increases substantially with lift coefficient. Thus, $C_{d|\sigma}$ becomes more sensitive to the value of N_σ as lift coefficient increases.

5.4 Transonic Results

5.4.1 Deterministic Performance

The deterministic performance of the RAE2822 is first assessed. Figure 5.16 shows the deterministic ML/D, drag and transition location polars for the RAE2822. These have been run at the ideal critical N-factor of $N_{cr} = 9$, and the drag polar has also been split into viscous drag and wave drag components. Figure 5.17 shows the pressure distributions and N-factor envelopes for the RAE2822 at Mach numbers of $M = 0.680$, $M = 0.715$ and $M = 0.730$.

As M^2C_l has been is fixed, increasing Mach number causes the target lift coefficient to reduce. This lowers the angle of attack which, in turn, reduces the leading edge pressure peak, as can be seen in figure 5.17a. This leads to a more favourable pressure gradient over the front of the aerofoil, which helps to suppress TS instability growth. From figure 5.17b, however, it can be seen that no N-factor envelope reaches the critical N-factor. This indicates that transition is shock induced, rather than occurring from instability growth.

Upper surface transition location extends as Mach number is increased, as can be seen in figure 5.16c. This is due to a delay in shock position. Increasing Mach number from 0.68 to 0.705 also causes shock strength to reduce, as indicated in figure 5.16b by the reduction in wave drag to a minimum. As seen in figure 5.16a, minimum drag and therefore maximum ML/D is found at $M = 0.715$. This is at a slightly higher Mach number than for the location of minimum wave drag. The small increase in Mach number results in a laminar flow extension that reduces viscous drag more than wave drag increase. Increasing Mach number beyond $M = 0.715$ causes wave drag to increase at a faster rate than viscous drag decreases with additional laminar flow. Although wave drag grows in magnitude at the lower and upper limits of the Mach range investigated, total drag remains dominated by the viscous drag component over the Mach range considered. Further increases in Mach number would cause wave drag to dominate total drag as shock strength increases. This would eventually lead to shock induced separation, and buffet onset would occur.

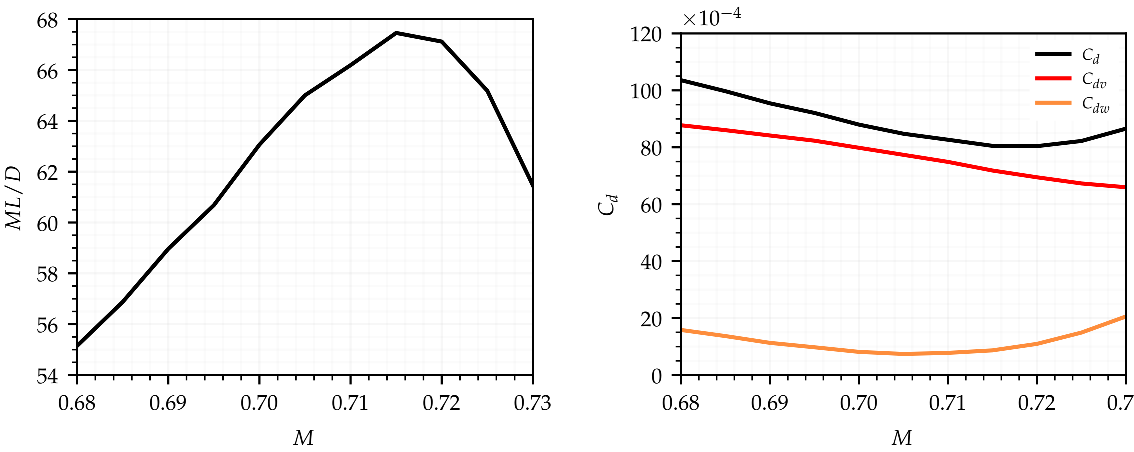

(a) *ML/D*

(b) *Drag*

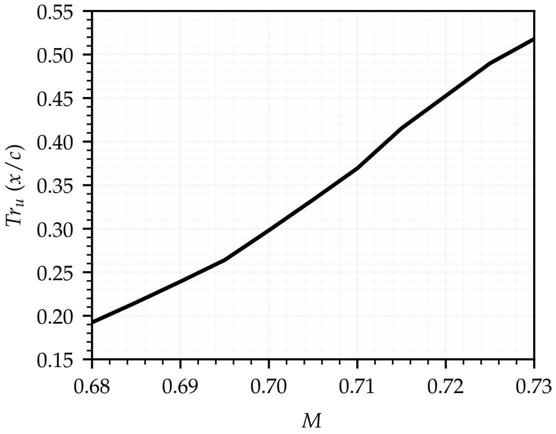

(c) *Transition location*

Figure 5.16: *ML/D, drag and upper surface transition location polars at $N_{cr} = 9$ for the RAE2822.*

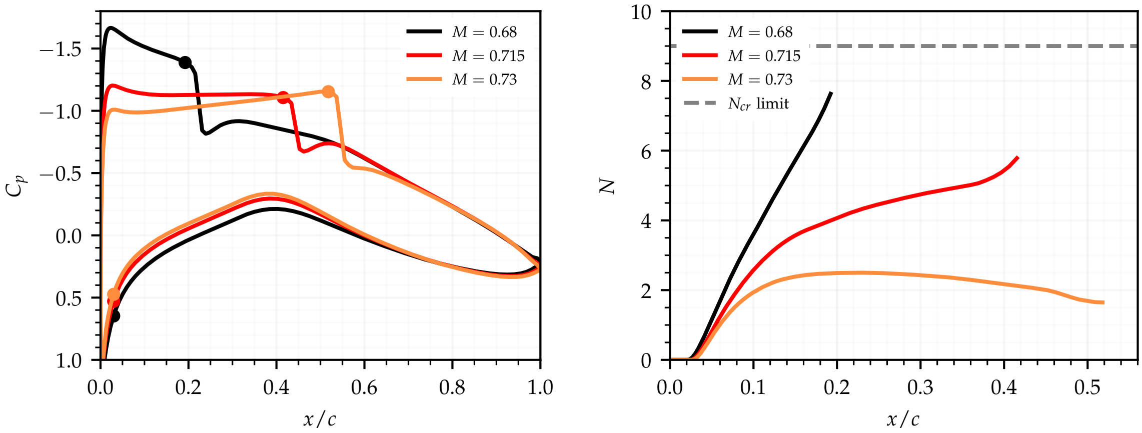

(a) *Pressure distributions*

(b) *N-factor envelopes*

Figure 5.17: *Pressure distributions and N-factor envelopes for the NLF2822 at various Mach numbers.*

5.4.2 Stochastic Performance

Figure 5.18 shows the mean ML/D, C_d and Tr_u polars for the RAE2822 over the Mach range investigated. In figure 5.18a, mean ML/D is shown with the ML/D range between values found at the ideal critical N-factor and an N-factor of zero. Mean ML/D is close to the ideal ML/D over the Mach range investigated as transition is shock induced. As such, critical N-factor must be reduced some way before it has an effect on transition location. Mean ML/D is closest to the ideal ML/D at high Mach numbers where the target lift coefficient is low. This reduced instability growth, as the pressure gradient over the front of the aerofoil is more favourable. As Mach number is reduced from $M = 0.72$, the favourable pressure gradient becomes weaker. This suppresses instability amplification less, although transition remains shock induced. Mean ML/D is furthest from the ideal ML/D at $M = 0.705$, with a reduction in ML/D of 1.8. As Mach number is further reduced, the shrinking amount of laminar flow possible at the ideal critical N-factor means that little laminar flow is lost as critical N-factor is reduced. Ideal and mean ML/D are therefore close.

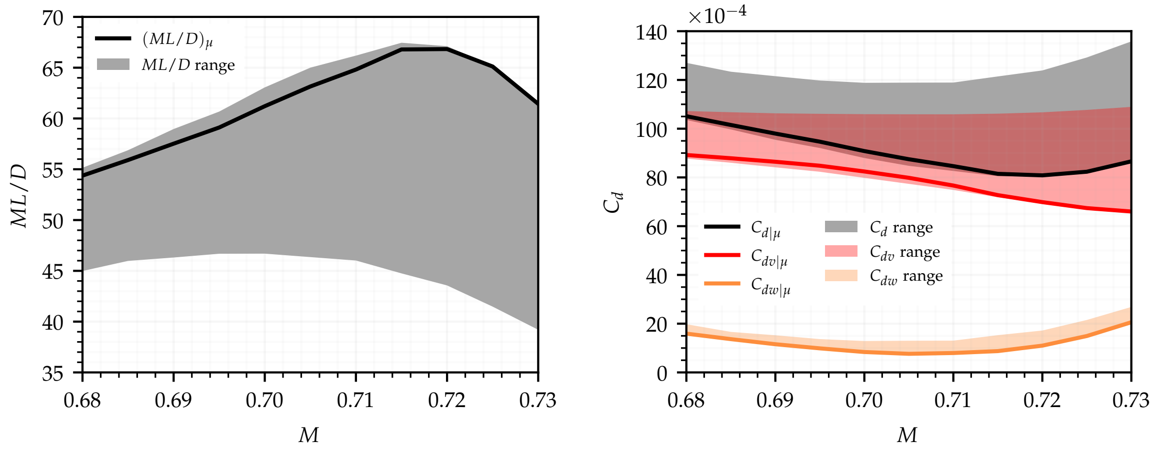

(a) ML/D **(b)** *Drag*

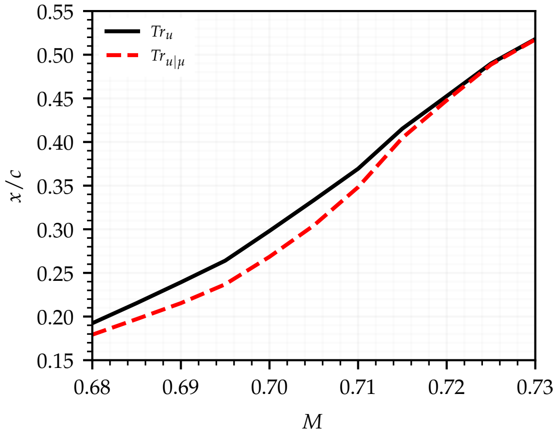

(c) *Upper surface transition Location*

Figure 5.18: *Mean ML/D, drag and upper surface transition location polars for the RAE2822 with ML/D and drag range between $N_{cr} = 9$ and $N_{cr} = 0$ and upper surface transition location at $N_{cr} = 9$.*

The range of ML/D between $N_{cr} = 9$ and $N_{cr} = 0$ is naturally largest at high Mach numbers where transition is most delayed. Figure 5.18b shows mean C_d, broken down into mean viscous and mean wave drag components with the range of each also shown. As can be seen, the increase in drag from a total loss of laminar flow comes primarily from an increase in C_{dv}. This shows that viscous drag is more sensitive to changes in transition location than wave drag at the Mach numbers considered.

Figure 5.19 shows the standard deviation polars for ML/D, C_d and Tr_u, with C_d broken down into C_{dv} and C_{dw} standard deviation components. As seen in figure 5.19a, $(ML/D)_\sigma$ peaks at $M = 0.71$ which is slightly below the Mach number for maximum ML/D at the ideal critical N-factor. This coincides with a peak in $C_{d|\sigma}$ as seen in figure 5.19b. The $C_{d|\sigma}$ polar closely resembles that of $C_{dv|\sigma}$ as $C_{dw|\sigma}$ is low over the entire Mach range investigated, and the $C_{dv|\sigma}$ polar closely matches the $Tr_{u|\sigma}$ polar. Thus, ML/D standard deviation with uncertainty in critical N-factor can be directly related to Tr_u standard deviation via the dependence of $(ML/D)_\sigma$ on $C_{d|\sigma}$ and the dependence of $C_{d|\sigma}$ on $Tr_{u|\sigma}$.

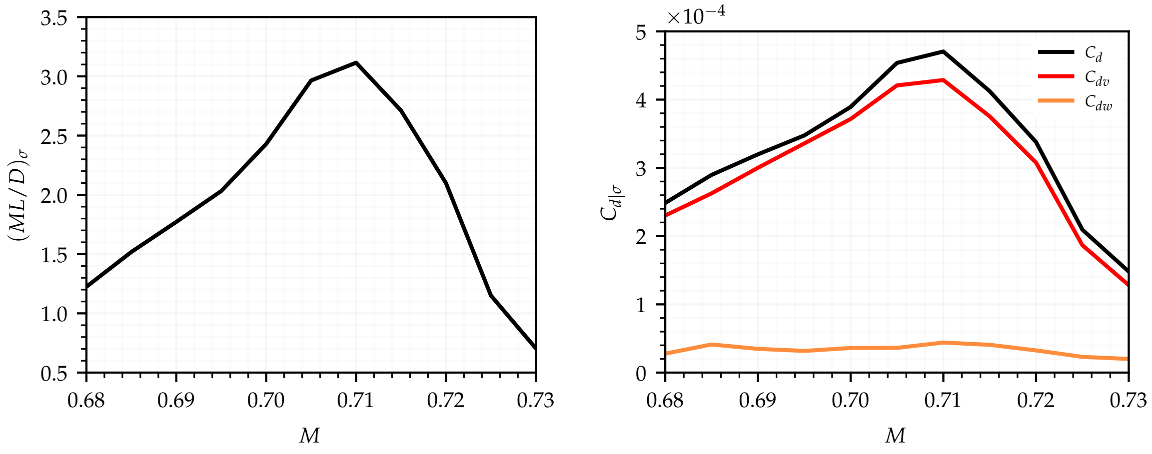

(a) *ML/D* **(b)** *Drag*

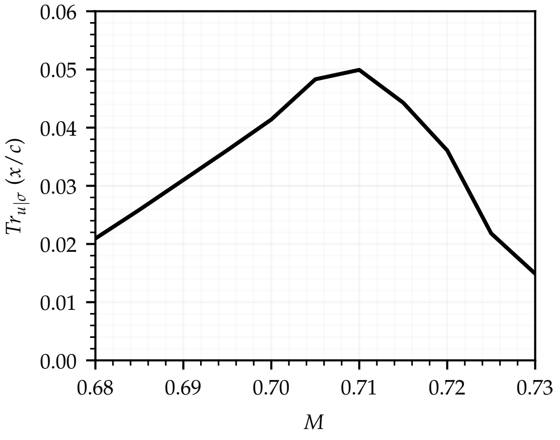

(c) *Transition Location*

Figure 5.19: *ML/D, drag and upper surface transition location standard deviation polars for the RAE2822 aerofoil.*

5.4.3 Effect of Uncertainty Standard Deviation

The sensitivity of ML/D, C_d and Tr_u mean and standard deviation to the selected uncertainty standard deviation value is assessed. Figures 5.20, 5.21 and 5.22 show the mean and standard deviation polars for ML/D, C_d and Tr_u when calculated with various critical N-factor standard deviation values.

As is expected, mean Tr_u decreases over the Mach range as N_σ is raised. This naturally causes mean C_d to rise and mean ML/D to fall. ML/D is less sensitive to changes in N_σ at high Mach numbers, so increasing N_σ causes the Mach number for maximum ML/D to increase. The low sensitivity of mean ML/D to N_σ at high Mach numbers comes from the very low instability growth. ML/D does have the largest range between values calculated at the ideal critical N-factor and a critical N-factor of zero at high Mach numbers. However, all of the ML/D reduction occurs when critical N-factor is less than 2.

The standard deviation polars for ML/D, C_d and Tr_u all increase as N_σ is raised. This happens at the same rate for each, indicating that regardless of the selected N_σ, the relationship between Tr_u, C_d and ML/D standard deviation is maintained. The Mach number at which maximum standard deviation is found also increases as N_σ is raised. Standard deviation increases more at higher lift coefficient as there is more laminar flow so a wider spread of transition locations over the critical N-factor range. As these are at lower critical N-factors, a larger increase in $(ML/D)_\sigma$ at high Mach numbers is observed when N_σ is increased from $2 \rightarrow 3$.

5.5 Summary

Analysis of performance to critical N-factor uncertainty has been carried out. This was done over a range of lift coefficients for the NLF0215 aerofoil at subsonic flow conditions and over a range of Mach numbers at transonic flow conditions for the RAE2822. Stochastic properties are obtained for each via calculation of weighted mean and standard deviation using uniformly spaced samples of N_{cr} taken every $N_{\text{step}} = 0.1$. Analysis of this approach shows that the chosen sampling rate is able to obtain accurate stochastic values.

Analysis of the NLF0215 shows that robustness of drag to uncertainty in critical N-factor is directly proportional to the robustness of transition location to uncertainty in critical N-factor. Lower surface transition location standard deviation is found to only contribute to skin friction drag standard deviation, while upper surface transition location standard deviation affects both skin friction and pressure drag standard deviations. Robustness of performance to critical N-factor uncertainty is found to be worst at locations where deterministic transition location changes rapidly with small changes in lift coefficient. Conversely, robustness is best where deterministic transition location is insensitive to changes in lift coefficient.

As transition location standard deviation is related to the rate of change of deterministic transition location with changing lift coefficient, it is possible to infer information about the robustness of an aerofoil based on its deterministic performance. A larger rate of change of transition location results in a larger peak in transition location standard deviation, but reduces the lift coefficient width over which it spans. When deterministic transition location is insensitive to changing lift coefficient, transition location standard deviation is low. The

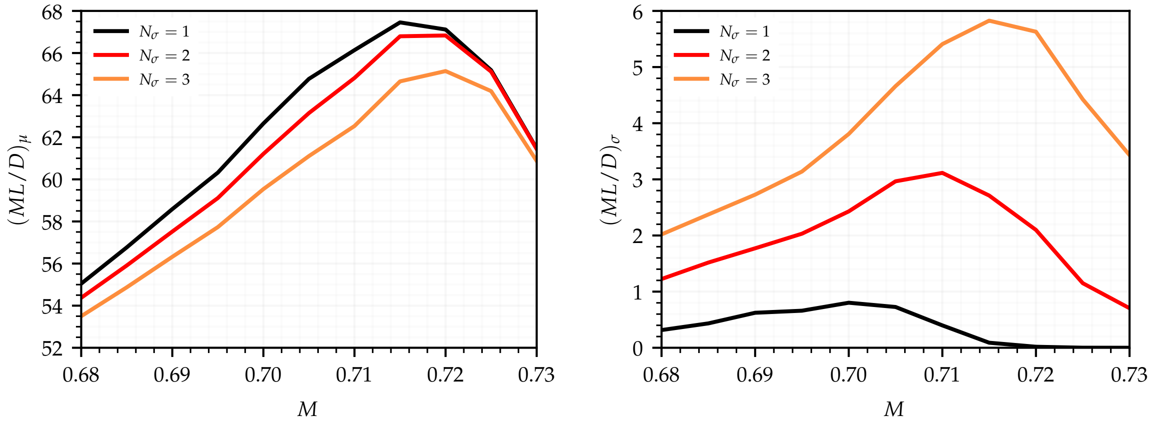

(a) *Mean* **(b)** *Standard Deviation*

Figure 5.20: *ML/D mean and standard deviation polars calculated at various critical N-factor standard deviation values for the RAE2822.*

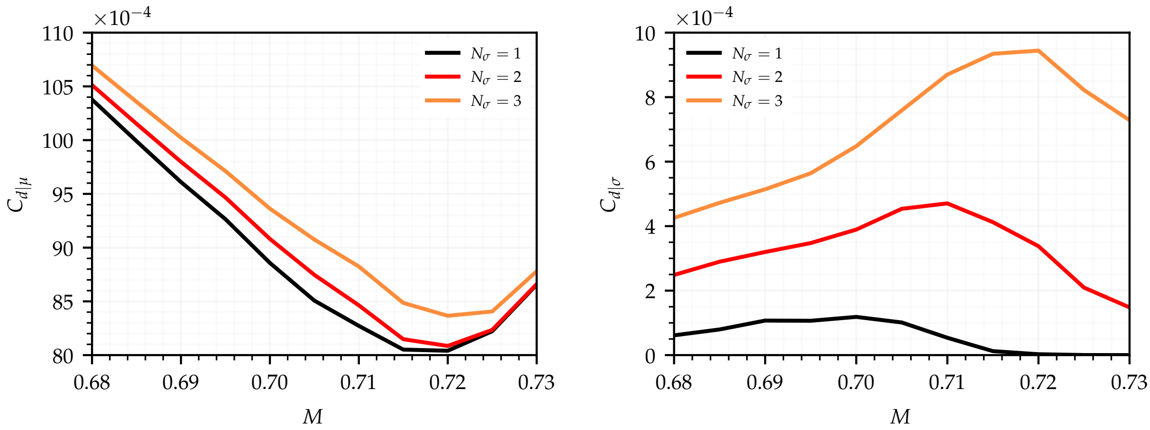

(a) *Mean* **(b)** *Standard Deviation*

Figure 5.21: *C_d mean and standard deviation polars calculated at various critical N-factor standard deviation values for the RAE2822.*

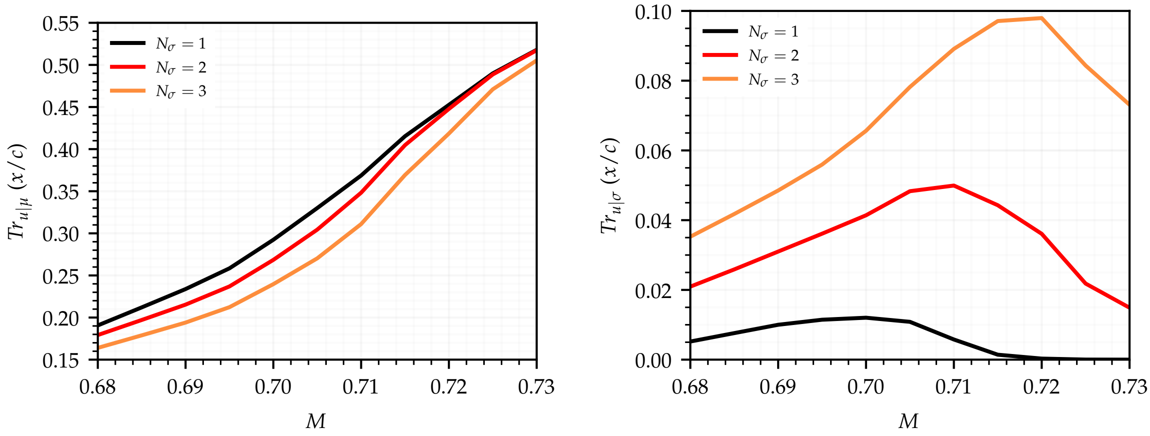

(a) *Mean* **(b)** *Standard Deviation*

Figure 5.22: *Tr_u mean and standard deviation polars calculated at various critical N-factor standard deviation values for the RAE2822.*

sensitivity of maximum lift coefficient to changing critical N-factor is significant over the full critical N-factor range, but the majority of $C_{l,\max}$ loss occurs only when critical N-factor is substantially reduced.

Analysis of the RAE2822 shows that ML/D standard deviation is directly related to upper surface transition location standard deviation. This is due to the dependence of ML/D on drag, and drag being dominated by its viscous component. Viscous drag standard deviation is found to take the same form as upper surface transition location standard deviation. Robustness to critical N-factor uncertainty is worst at Mach numbers slightly below that required for maximum deterministic ML/D, and best at the lower and upper ends of the Mach range investigated. At lower Mach numbers, a strong adverse pressure gradient forces early transition while at higher Mach numbers, a long favourable pressure gradient causes transition to remain fixed at the shock location.

For both the NLF0215 and RAE2822 aerofoils, increasing critical N-factor standard deviation causes an increase in output performance standard deviation over the entire lift coefficient or Mach range investigated. In both cases, output standard deviation increases most where transition is highly extended, and least when transition is close to the leading edge. For the NLF0215, a larger increase in maximum lower surface transition location standard deviation is seen compared to the upper surface. Increasing critical N-factor standard deviation also results in the peaks in upper and lower surface transition location moving closer together. The net effect of these changes is that the drag standard deviation polar shifts from two discrete peaks into a near single peak of increased magnitude. For the RAE2822, increasing critical N-factor standard deviation causes the peak standard deviation value for ML/D, drag and upper surface transition location to move to higher Mach numbers as output standard deviation is most increased here. Conversely, due to transition being shock induced at high Mach numbers down to low critical N-factor values, reduced critical N-factor standard deviation results in close to zero output standard deviation here.

Chapter 6

Single-Point Robust Optimisation

Following uncertainty analysis at subsonic and transonic conditions, robust shape optimisation is undertaken. This initial study is carried out at a single design point in terms of lift coefficient, Mach number and Reynolds number. The objectives of this study are to:

- Explore the effectiveness of robust optimisation with critical N-factor uncertainty
- Investigate any trade-offs between mean performance and performance robustness
- Highlight best practices for the robust design of NLF aerofoils
- Assess the effectiveness of robust optimisation at off-design flight conditions

The same methodology as used during uncertainty analysis is employed during optimisation, with a slight change in sampling fidelity so as to balance the accuracy of calculated mean and standard deviation values with the computational costs of optimisation.

6.1 Optimisation

6.1.1 Problem Formulation

Multi-objective robust shape optimisation is carried out with the goal of improving aerofoil performance with uncertainty in critical N-factor. Again, two test cases are considered, the first at subsonic and the second at transonic flow conditions. The NLF0215 is used as a starting aerofoil for the subsonic optimisation case, run at $Re = 9 \times 10^6$ and $M = 0.1$. A lift coefficient of $C_l = 0.7$ was used for the optimisation which coincides with $C_{d,\text{min}}$ for the starting geometry when analysed with XFOIL. The objectives for the optimisation are the minimisation of mean drag ($C_{d|\mu}$) and drag standard deviation ($C_{d|\sigma}$). Transition is left free on both surfaces, as was done during the uncertainty analysis carried out previously.

The RAE2822 is used as the starting aerofoil for the transonic optimisation case. This was run at $C_l = 0.76$, $Re = 6.5 \times 10^6$ and $M = 0.715$ which coincided with the maximum ML/D found when analysed with CVGK. The objectives for this optimisation case are the maximisation of mean ML/D ($(ML/D)_\mu$) and the minimisation of ML/D standard deviation ($(ML/D)_\sigma$). Transition is left free on the upper surface but is fixed on the lower surface at $0.03x/c$, as done during the uncertainty analysis carried out in the previous chapter.

For both cases, mean and standard deviation of performance quantities are calculated from a range of flow solutions run at critical N-factor sample points spaced uniformly from $N_i \rightarrow 0$. These are weighted using a negative half-normal probability distribution with peak likelyhood at the deterministic critical N-factor value of $N_i = 9$ and with a standard deviation of $N_\sigma = 2$. A constraint is placed on maximum thickness ensuring all optimised designs have a value the same as, or larger than, that of the starting aerofoil in each case. This is a thickness of $0.15z/c$ for the NLF0215 and a thickness of $0.12z/c$ for the RAE2822.

Deformation of each surface is controlled using 6 CST coefficients per surface, totalling 12 design variables controlled by the optimiser. Each design variable is bound, producing a finite search space for the optimiser. Bounds were selected based on the assumed solution shape in each case but are then expanded to ensure less predictable shapes are not missed. For the NLF0215, transition is free to move on the upper and lower surfaces and so wide bounds have been put in place on both. As transition is fixed for the lower surface of the RAE2822, it is assumed that camber will be increased to reduce the required angle of attack and so delay upper surface shock location and extend laminar flow. Appropriate bounds have thus been selected for this.

For both optimisation cases, the genetic algorithm based optimiser is run for 100 generations. There are 48 individuals per generation which is 4 times the number of design variables used. The ratio of mate to mutation change is set to 0.8 and, to aid in convergence, the crowding number is scaled linearly from $\eta = 0 \rightarrow 20$ during the optimisation.

6.1.2 Stochastic Convergence

It is desirable to minimise the number of samples used to quantify robustness while still obtaining accurate stochastic properties. This is because the number of flow solutions required directly scales with the number of robust samples used. Using 91 critical N-factor samples as was done during uncertainty analysis would, for the chosen population size of 48 and generation number of 100, require $436,800$ flow solutions. This is very computationally expensive and may be unnecessarily precise if an acceptable trade-off in computational cost and accuracy is possible. To assess this, mean and standard deviation of the chosen objective function variables are calculated with a varying number of critical N-factor samples taken at uniform intervals over the range $N_{cr} = 0 \rightarrow 9$.

Figure 6.1a shows mean and standard deviation of drag with varying sample numbers for the NLF0215 at the conditions to be used for optimisation. Figure 6.1b shows mean and standard deviation of ML/D when calculated with a varying number of samples for the RAE2822 at the optimisation flow conditions. For both cases, the values of mean and standard deviation converge as the number of samples used is increased. For the NLF0215, mean drag is within 1 drag count with as little as 6 sample points, however drag standard deviation requires 10 sample points to be within the same distance. To have less than a 5 percent error from the mean and standard deviation value calculated with 91 samples, 11 sample points or more are needed. For the RAE2822, the convergence of mean ML/D and ML/D standard deviation see some fluctuations. These fluctuations occur at sample numbers below 16, which is also the number of samples required to have an error of less than 5 percent from the ML/D mean and standard deviation calculated with 91 samples.

Based on these findings, calculation of stochastic properties for this study uses 19 critical N-factor samples spaced with step sizes of $N_{\text{step}} = 0.5$ between $N_{cr} = 0 \rightarrow 9$. This should result in mean and standard deviation values accurate to within 5 percent of the values obtained with 91 samples. By lowering the number of samples used, the computational cost of the optimisation is reduced by approximately 80 percent. This reduction in computational cost most benefits transonic analysis using the flow solver CVGK, which would be prohibitively expensive with the higher sample number.

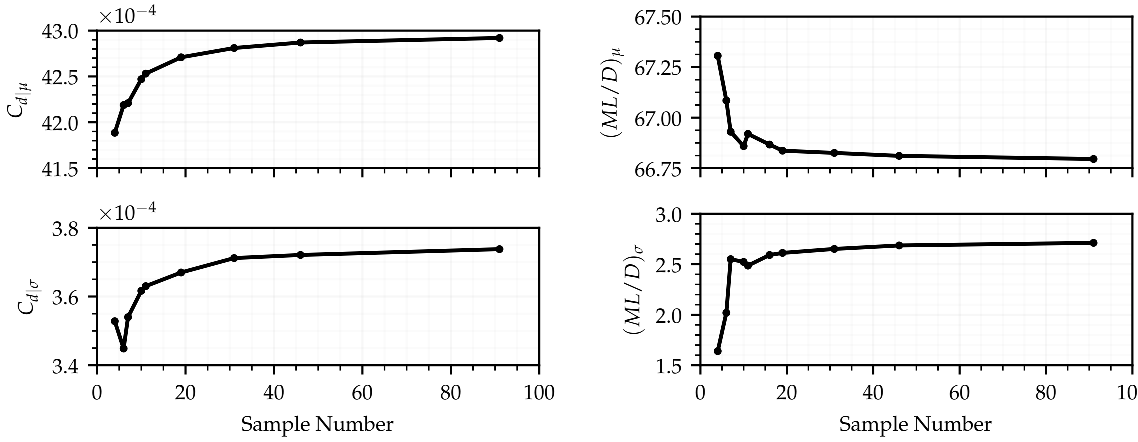

(a) *NLF0215* **(b)** *RAE2822*

Figure 6.1: *Drag mean and standard deviation for the NLF0215 and ML / D mean and standard deviation for the RAE2822 when calculated with a varying number of critical N-factor samples.*

6.2 Subsonic Results

Over the 100 generations run, the optimisation produced 3051 unique individuals that could be converged by XFOIL at all critical N-factor sample values. Figure 6.2 shows convergence history for the two objective functions by plotting the minimum value for each found over the course of the optimisation. After approximately 50 generations, the optimizer is highly converged, allowing further iterations to explore objectives trade-offs and produce a Pareto front of designs, as shown in figure 6.3.

The optimised aerofoils with minimum $C_{d|\mu}$ and $C_{d|\sigma}$ are selected for comparison against the NLF0215. These are indicated on the Pareto front in figure 6.3. Deterministic drag values when $N_{cr} = 9$ and $N_{cr} = 0$, representing laminar and turbulent flow, are shown with the stochastic drag properties in table 6.1 for each aerofoil. These are calculated using critical N-factor samples taken every $N_{\text{step}} = 0.5$ between $N_{cr} = 9 \rightarrow 0$ as used during the optimisation. The optimizer has improved both objectives as all designs found on the Pareto front are at least 2 mean drag counts lower than the NLF0215 and have a 3 drag count or more standard deviation decrease. The difference in mean drag is small between the minimum $C_{d|\mu}$ and minimum $C_{d|\sigma}$ designs, with a trade-off of 1 percent. The difference in drag standard deviation is more substantial at 9 percent, but both have been significantly reduced. Deterministic laminar performance of both selected optimised aerofoils is better than the NLF0215, but fully turbulent performance is worse.

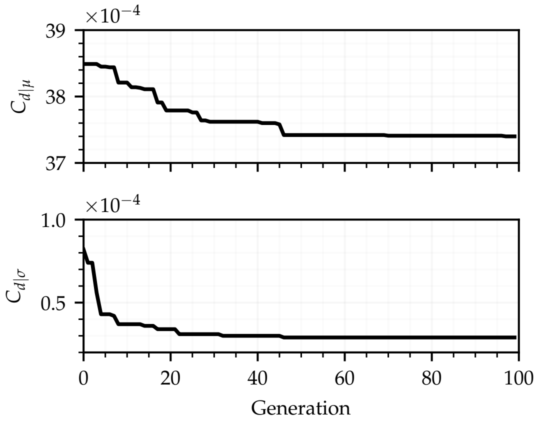

Figure 6.2: *Minimum mean drag and minimum drag standard deviation found over the course of the optimisation.*

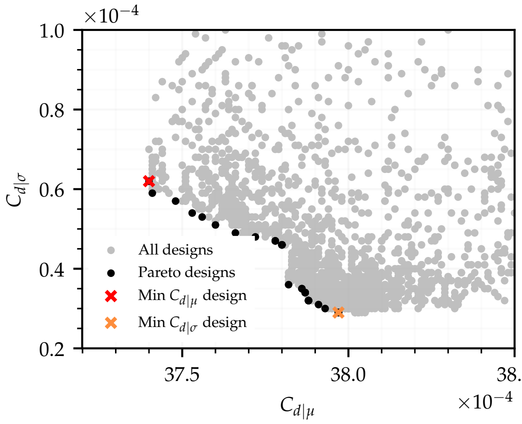

Figure 6.3: *Drag mean and standard deviation for all optimised designs with Pareto front and selected aerofoils highlighted.*

Table 6.1: *Deterministic and stochastic drag values for the NLF0215 and optimized aerofoils with minimum $C_{d|\mu}$ and $C_{d|\sigma}$. Calculated with N-factor samples taken every $N_{step} = 0.5$ from $N_{cr} = 9 \rightarrow 0$.*

Design		$C_{d,N_{cr}=9}$ ($\times 10^{-4}$)	$C_{d,N_{cr}=0}$ ($\times 10^{-4}$)	$C_{d\|\mu}$ ($\times 10^{-4}$)	$C_{d\|\sigma}$ ($\times 10^{-4}$)
NLF0215		40.0	88.2	42.71	3.67
Min $C_{d\|\mu}$	(M)	36.9 (-8%)	92.5 (+5%)	37.40 (-12%)	0.62 (-83%)
Min $C_{d\|\sigma}$	(S)	37.9 (-6%)	89.3 (+1%)	37.97 (-11%)	0.29 (-92%)

6.2.1 Design Point Changes

The design with minimum $C_{d|\mu}$ and the design with minimum $C_{d|\sigma}$ are compared against the NLF0215. These are denoted design M (mean) and design S (standard deviation) respectively. Figure 6.4 shows the design variable values for the NLF0215, design M and design S with the corresponding design variable bounds. The design variables are split into upper and lower surfaces where variables 1 and 7 are towards the front, and 6 and 12 are towards the rear of the aerofoil. Positive values indicate that material is added to the NLF0215 while negative values indicate that material is removed. Figure 6.5 shows the aerofoil profile for each of the three designs. The grey shaded area indicates the viable design region, as dictated by the design variable bounds.

Both optimised designs have similar upper surface profiles between $0 < x/c < 0.3$. Curvature at the leading edge is increased but then reduced over the front of the aerofoil. Maximum thickness is also larger and located further aft for both designs. These are common NLF design characteristics as the combined effect creates a more favourable pressure gradient which reduces instability amplification. The lower surface of both designs is also similar with both designs having increased thickness mid chord. Significant differences are seen at the rear of the upper surface. Design M has a much larger aft thickness than design S, so obtains a higher camber towards the tail.

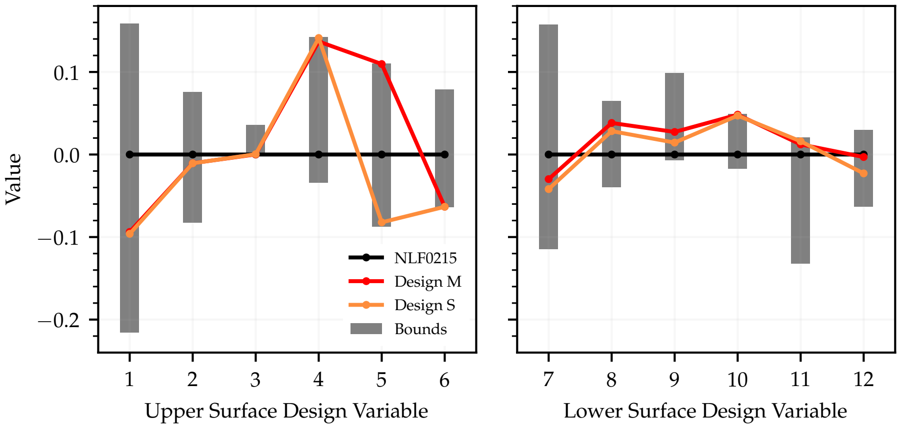

Figure 6.4: *Upper and lower surface design variable values and bounds for the NLF0215 and selected optimised designs. Values indicate addition or subtraction of material from the starting design.*

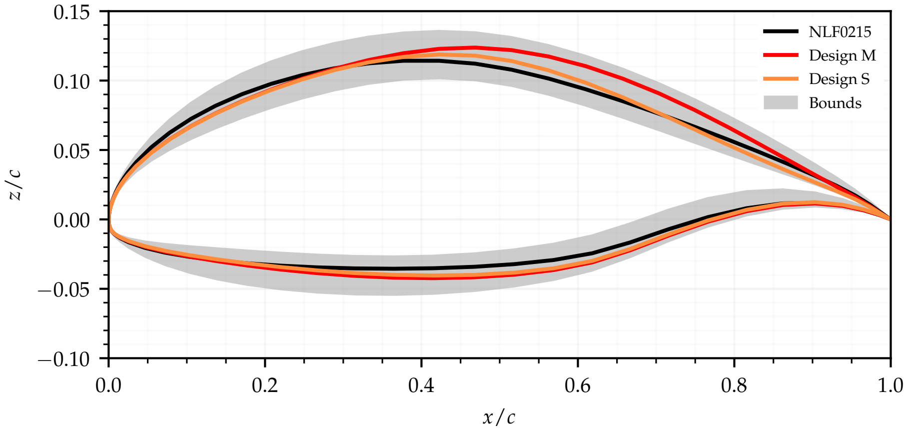

Figure 6.5: *Aerofoil profiles for the NLF0215 and selected optimised design.*

Pressure distributions and N-factor envelopes for the NLF0215 and optimised designs at $N_{cr} = 9$ are plotted in figure 6.6. The markers in figure 6.6a indicate the transition location on each surface for each design. Changes to the upper surface leading edge and the increased thickness aft on both designs has created a long favourable pressure gradient over the aerofoil. This suppresses instability growth, resulting in delayed upper surface transition for both. Additional camber towards the trailing edge of design M increases lift, allowing for a slightly reduced angle of attack compared to the NLF0215 and design S. This coupled with an increased maximum thickness located further aft extends upper surface laminar flow further. Changes to the lower surface have also led to a more favourable pressure gradient up to $0.6x/c$ for both optimised designs. This has little effect on the lower surface transition location but has reduced instability growth upstream of the transition location substantially.

Drag and transition locations are plotted against critical N-factor for the NLF0215 and optimised designs in figure 6.7. Drag is lower for both optimised aerofoils compared to the NLF0215 at critical N-factor values above $N_{cr} = 0.5$. This reduction is small at $N_{cr} = 9$ but becomes larger as N_{cr} is reduced. Below $N_{cr} = 0.5$, both optimised designs see a sudden drag rise. Drag changes little as N_{cr} is reduced from 9 → 3 for both optimised aerofoils. Design S is less sensitive to changes in N_{cr} above $N_{cr} = 5$, but has higher drag compared to design M. As critical N-factor probability is high at larger N_{cr} values, mean and standard deviation are significant affected by these small differences. Design S has a lower drag value than design M between $0.5 < N_{cr} < 5$; however, the low probability weighting here makes the effect on mean and standard designs small.

By comparing figure 6.7a with 6.7b, it can be seen that, naturally, drag is dependent on the combined extent of upper and lower laminar flow. Both optimised aerofoils have increased upper and lower surface laminar flow compared to the NLF0215. Transition is most delayed at lower N_{cr} values, leading to the large drag reductions seen on the C_d envelope when $N_{cr} < 4$. The minimum $C_{d|\mu}$ aerofoil has more, although less stable, upper surface laminar flow compared to the minimum $C_{d|\sigma}$ aerofoil. Lower surface laminar flow is largest for the the minimum $C_{d|\sigma}$ aerofoil, and remains extended over a wider N_{cr} range.

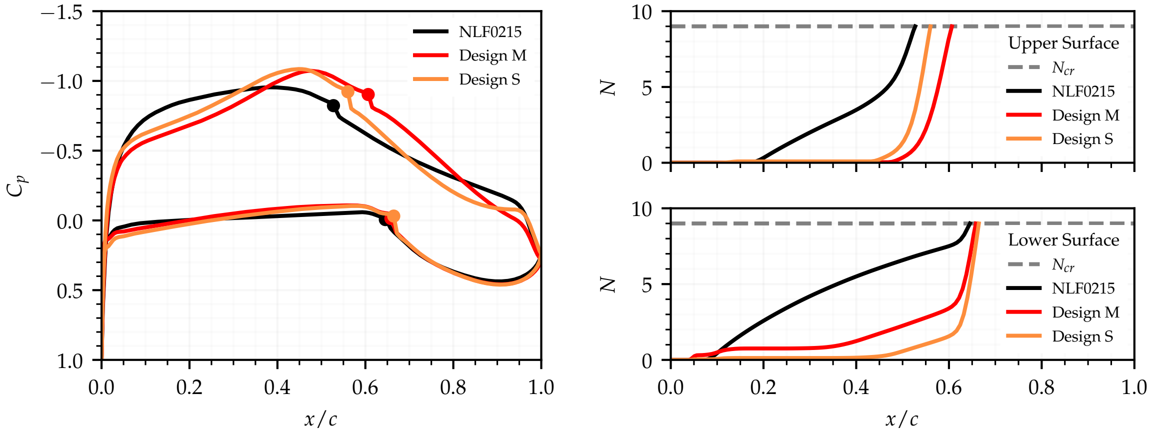

(a) *Pressure distribution*

(b) *N-factor envelope*

Figure 6.6: *Pressure distribution and N-factor envelope for the NLF0215 and selected optimised designs at* $C_l = 0.7$ *and* $N_{cr} = 9$.

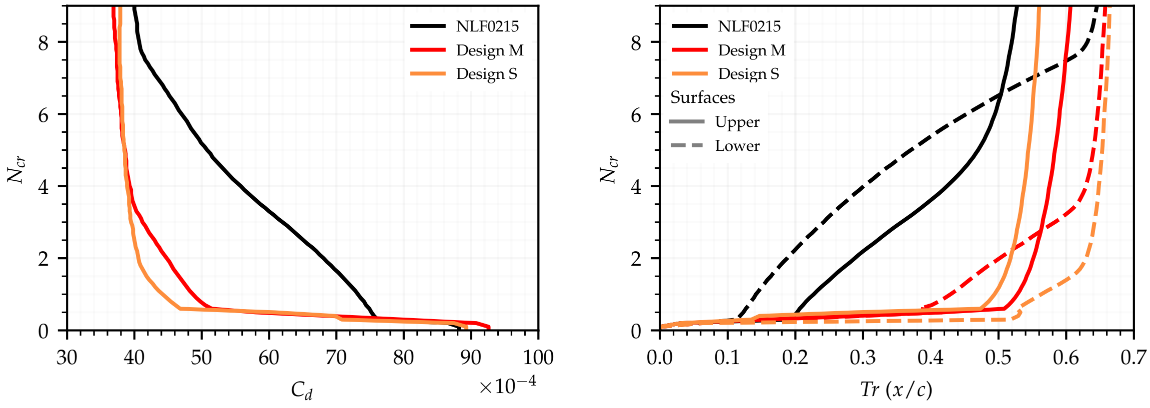

(a) *Drag*

(b) *Transition Locations*

Figure 6.7: *Drag and transition locations again critical N-factor for the NLF0215 and selected optimised designs at* $C_l = 0.7$.

6.2.2 Off-Design Analysis

Mean drag and drag standard deviation at off-design lift coefficients are shown in figure 6.8. The polars are calculated using critical N-factor samples taken at intervals of 0.1 from $N_{cr} = 9$ to $N_{cr} = 0$ as used during the uncertainty analysis carried out previously. Both optimised designs have a strong drag bucket shape with mean drag reductions over a lift coefficient range close to the design value of $C_l = 0.7$. Mean drag is comparable between the NLF0215 and optimised design below this region but has increased substantially for the optimised designs above, with design M performing worst.

Standard deviation is reduced over a small lift coefficient range centred at the design point. Below $C_l = 0.6$, standard deviation is comparable between the NLF0215 and optimised designs. Just above $C_l = 0.8$, both optimised designs perform significantly worse. Reducing standard deviation at the design lift coefficient results in a large standard deviation peak, but reduced standard deviation above and below this. As discussed in the previous chapter, pressure drag standard deviation is sensitive to small transition location changes at high attack angles. As both optimised aerofoils operates at a higher angles of attack than the NLF0215 at $C_l = 1.6$, both have a larger drag standard deviation at high lift coefficients.

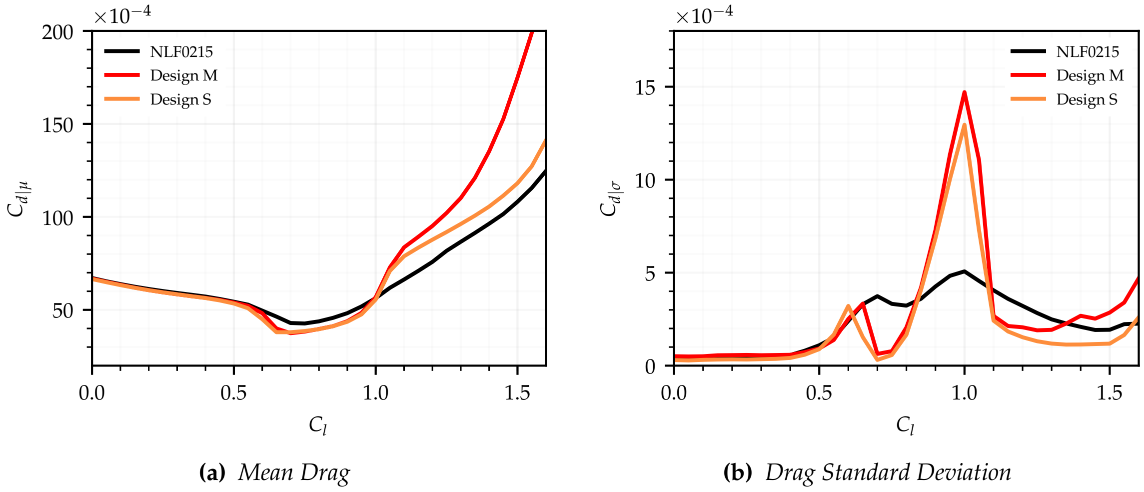

(a) *Mean Drag* **(b)** *Drag Standard Deviation*

Figure 6.8: *Performance polars for the NLF0215 and selected optimised aerofoils.*

6.2.3 Uncertainty Standard Deviation

To explore the effect of critical N-factor standard deviation, a comparison of drag standard deviation for the NLF0215 and selected optimised aerofoils with differing N_σ values is shown in figure 6.9. As previously seen with uncertainty analysis of the NLF0215, drag standard deviation grows and the lift coefficient range between its two peaks reduces as N_σ increases. At high lift coefficients, both optimised designs see drag standard deviation increase substantial, with the minimum $C_{d|\mu}$ aerofoil affected most.

Figure 6.10 shows drag against critical N-factor at $C_l = 1.6$ for the NLF0215 and optimised aerofoils. Compared to the NLF0215, both optimised aerofoils have a larger drag increase as critical N-factor is reduced from $N_{cr} = 9 \rightarrow 0$. However, the majority of this increase occurs at low critical N-factor values. This is more strongly weighted when using a high critical N-factor standard deviation, and so results in a larger drag standard deviation value.

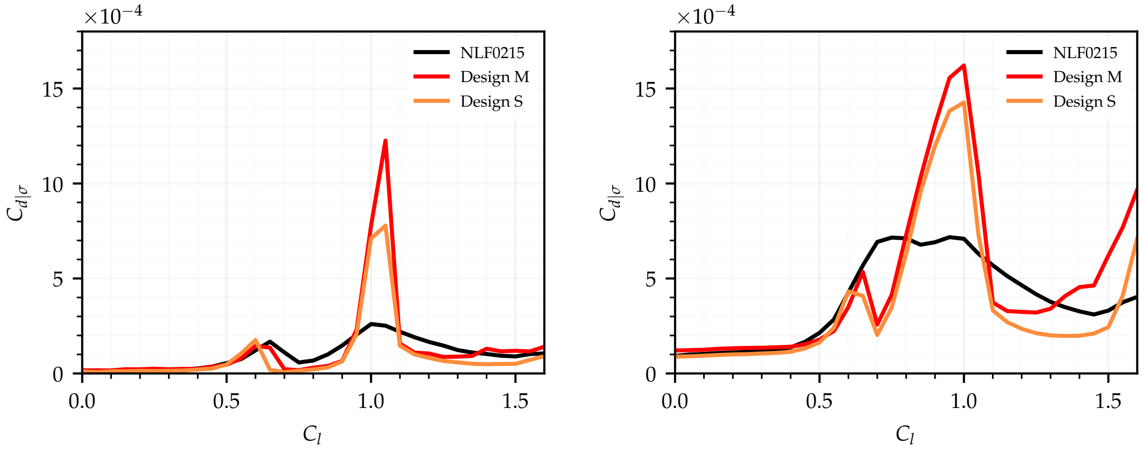

(a) $N_\sigma = 1$ **(b)** $N_\sigma = 3$

Figure 6.9: *Drag standard deviation for the NLF0215 and selected optimised designs with increased and decreased critical N-factor standard deviation.*

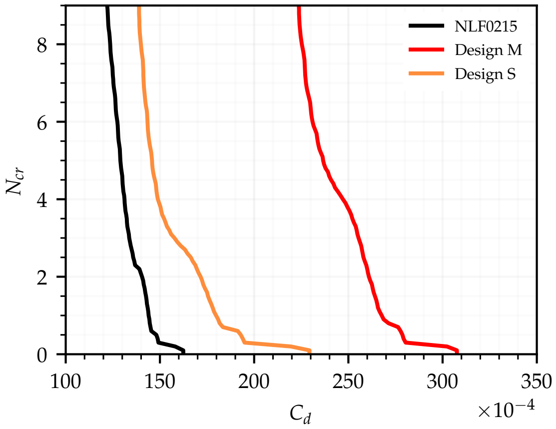

Figure 6.10: *Drag against critical N-factor at* $C_l = 1.6$ *for the NLF0215 and selected optimised designs.*

6.3 Transonic Results

CVGK was able to converge 1504 of the 4800 individuals produced during the optimisation at all of the critical N-factor sample points. Many designs at the beginning of the optimisation did not converge at all design points, resulting in the low overall percentage of converged solutions. The exact cause of this is difficult to identify, however the issue is likely due to the choice of design variable bounds. This can be inferred as early in the optimisation, mated and mutated off-spring are able to differ most from their parents. Designs at the edge of the design space may feature strong shocks or long and shallow regions of adverse pressure. CVGK can fail to converge either as both can cause separation. If this occurs at any of the 19 design points spaced over the N_{cr} range, the design is discarded.

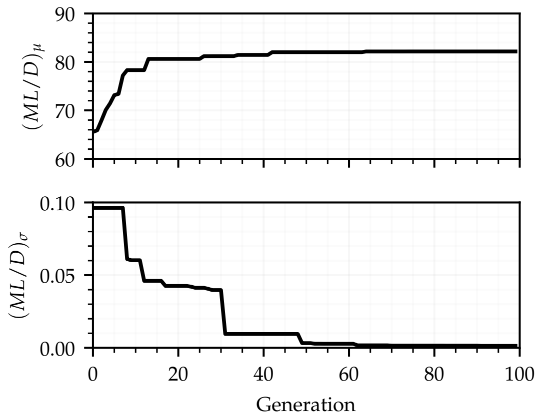

Figure 6.11: *Maximum mean ML/D and minimum ML/D standard deviation found during the optimisation.*

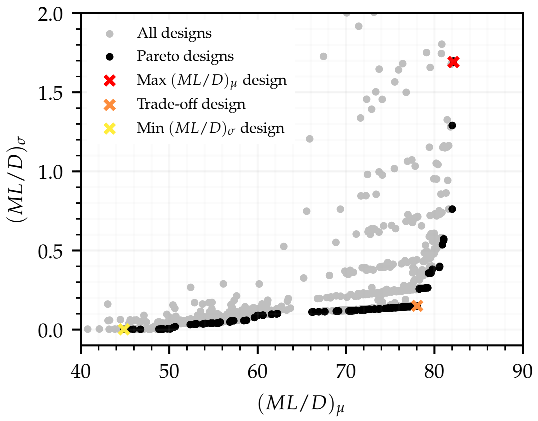

Figure 6.12: *ML/D mean and standard deviation for optimised designs with Pareto front and select designs highlighted.*

Figure 6.11 shows the convergence history for the two objectives. Although the number of converged designs was low at the start of the optimisation, large improvements are still found in both objectives. No further improvements could be found in either after approximately 65 iterations, suggesting at least a local optimum is found for each. Figure 6.12 shows $(ML/D)_\mu$ and $(ML/D)_\sigma$ for all designs generated, with Pareto front and selected designs highlighted. These are the optimised designs with maximum $(ML/D)_\mu$, maximum $(ML/D)_\sigma$ and a trade-off aerofoil between the two on the Pareto front. Table 6.2 shows ML/D mean and standard deviation, and deterministic ML/D at $N_{cr} = 9$ and $N_{cr} = 0$ for the RAE2822 and selected optimised designs. Again, these are calculated using critical N-factor samples taken every $N_{\text{step}} = 0.5$ between $N_{cr} = 9 \rightarrow 0$ as used during optimisation.

All Pareto front designs have lower $(ML/D)_\sigma$ than the RAE2822, but the values of $(ML/D)_\mu$ vary. The design with maximum $(ML/D)_\mu$ has an improved $(ML/D)_\mu$ and $(ML/D)_\sigma$ compared to the RAE2822. With a small decrease in $(ML/D)_\mu$, however, a substantial reduction in $(ML/D)_\sigma$ can be obtained. The minimum $(ML/D)_\sigma$ aerofoil has approximately zero $(ML/D)_\sigma$ but has exceptionally poor $(ML/D)_\mu$ compared to the RAE2822. The design at the lower corner of the Pareto front is therefore the logical aerofoils to select as a trade-off design with good performance for both objective variables.

Table 6.2: *Deterministic and stochastic values of ML/D for the RAE2822 and optimized aerofoil with maximum $(ML/D)_\mu$, minimum $(ML/D)_\sigma$ and an aerofoil with a trade-off between the two.*

Design		$ML/D_{N_{cr}=9}$	$ML/D_{N_{cr}=0}$	$(ML/D)_\mu$	$(ML/D)_\sigma$
RAE2822		67.46	44.75	66.84	2.61
Max $(ML/D)_\mu$	(M)	82.30 (+22%)	50.18 (+12%)	82.16 (+23%)	1.69 (-35%)
Trade-off	(T)	78.05 (+16%)	49.86 (+11%)	78.05 (+17%)	0.15 (-94%)
Min $(ML/D)_\sigma$	(S)	44.88 (-33%)	44.46 ($\approx$ 0%)	44.88 (-33%)	$\approx$ 0 (-100%)

6.3.1 Design Point Changes

To compared the selected optimised designs against the NLF0215, the design with maximum $(ML/D)_\mu$ is denoted design M (mean), the design with minimum $(ML/D)_\sigma$ is denoted design S (standard deviation) and the trade-off design is denoted design T (trade). Figure 6.13 shows the design variable values for each of the selected optimised designs and the design variable bounds used during the optimisation. These are split into upper and lower surfaces, where positive values on each surface indicate material is added to that surface and negative values indicate material is removed. Aerofoil profiles for the RAE2822 and selected optimised designs are shown in figure 6.14, with the grey shaded area indicating the viable design region as dictated by the design variable bounds.

All three optimised aerofoils have a similar maximum thickness and increased camber compared to the RAE2822. Camber is increased most towards the trailing edge, resulting in increased rear loading. Design S differs substantially from designs M and T towards the front of the upper surface, where thickness has been reduced rather than increased from that of the RAE2822. There are notable differences between design M and T towards the rear of the upper surface. Design M has a slightly less curvature mid-chord from $0.2x/c \rightarrow 0.6x/c$ on the upper surface compared to the RAE2822 and trade-off designs. This is followed by increased loading and a stronger pressure recovery at the trailing edge.

The effect of these changes on the pressure distributions and N-factor envelopes of each design is shown in figure 6.15. Design S stands out for its initial pressure peak and strong shock at the front of the aerofoil that triggers flow transition at $0.03x/c$. This designs then sees a second shock at a similar chord-wise position to the other optimised designs. While this naturally results in a lower $(ML/D)_\mu$ than even the RAE2822, transition location is near insensitive to the value of critical N-factor as indicated by its N-factor envelope. This also explains the identical performance at $N_{cr} = 9$ and $N_{cr} = 0$ shown in table 6.2.

The other two optimised designs have transition located far downstream at the shock location on the upper surface. It is worth noting that fully turbulent optimisation to increase ML/D at a single design point typically produces a shock-less aerofoil as this has minimum wave drag. As can be seen, this is not the case when upper surface transition is left free. A shock-less design has a long adverse pressure gradient to reduce shock strength. This would result in very early transition and so a large viscous drag.

The increased rear loading and reduced angle of attack has lowered the leading edge pressure rise for designs M and T. They both obtain a weaker and delayed shock in comparison to the RAE2822. Although transition does not occur from flow instability, the long favourable pressure gradient on the upper surface has suppressed instability growth more than that found for the RAE2822. Shock strength is weakest, and furthest aft, for design M as it has a relativity flat pressure rooftop upstream of the shock due to the reduced curvature here. The lift this looses compared to design T is made up by the delayed shock location and increased rear loading. Design T has a slightly earlier shock and stronger shock than design M, as the pressure gradient up to the shock is more favourable.

Stochastic performance of the RAE2822 and optimised designs is assessed by comparing ML/D and upper surface transition locations with varying critical N-factor. This is shown in figure 6.16. As indicated by the pressure distributions, all designs are shock limited at

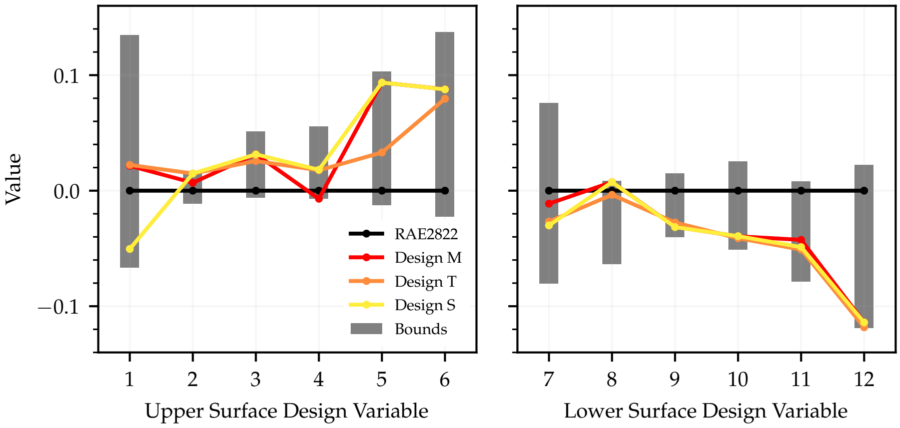

Figure 6.13: *Upper and lower surface design variable values and bounds for the RAE2822 and selected optimised designs. Values indicate addition or subtraction of material from the starting design.*

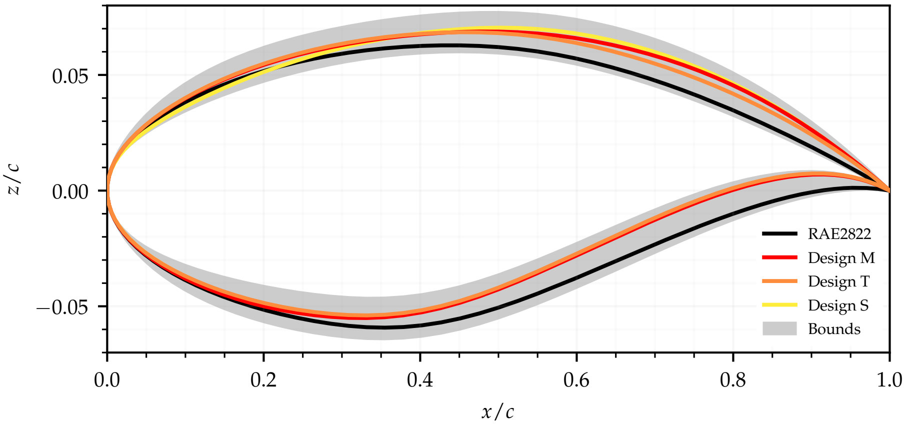

Figure 6.14: *Aerofoil profiles for the RAE2822 and selected optimised designs.*

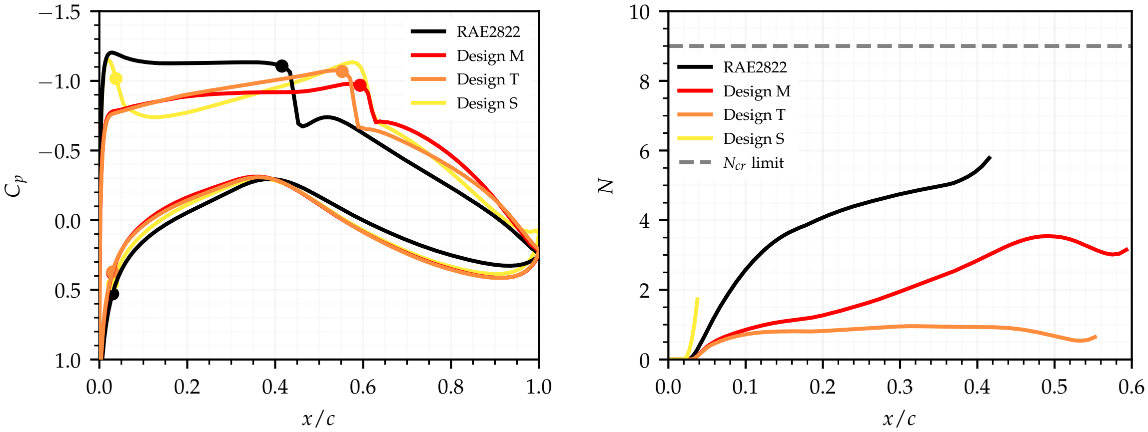

(a) *Pressure Distributions*

(b) *N-factor Envelopes*

Figure 6.15: *Pressure distributions and N-factor envelopes for the RAE2822 and selected optimised aerofoils.*

the deterministic laminar condition of $N_{cr} = 9$ and remain so as critical N-factor is reduced, although by varying amounts. This is shown by the invariance of upper surface transition location, and so ML/D, to changing critical N-factor. This also indicates that all designs have low instability amplification at the selected flow conditions.

Both design M and design T have a larger ML/D over the entire N_{cr} range compared to the RAE2822. This is due to extended laminar flow obtained by delaying shock position. This large ML/D is also maintained to a lower N_{cr} value for both designs due to instability suppression from a favourable pressure gradient. The critical N-factor value where premature transition occurs is lower for design T compared to design M. This is a result of the stronger favourable pressure gradient up to the shock location, however; design T has a reduced maximum ML/D compared to design M as a result. Of course, design S sees almost no change in ML/D as N_{cr} is reduced from $N_{cr} = 9 \rightarrow 0$ due to shock induced transition close to the leading edge. While this aerofoil has the lowest $(ML/D)_\sigma$, it is of no practical use to a designer given the extremely low $(ML/D)_\mu$.

It can be seen by comparing figures 6.17a and 6.16b that the ML/D and upper surface transition envelopes have a similar form. This was also seen during uncertainty analysis of the RAE2822. The envelopes differ most as critical N-factor reduces. This is expected given that shape changes will also affect fully turbulent performance. The ML/D and Tr_u envelopes are naturally identical for design S as its performance is essentially fully turbulent at all critical N-factors.

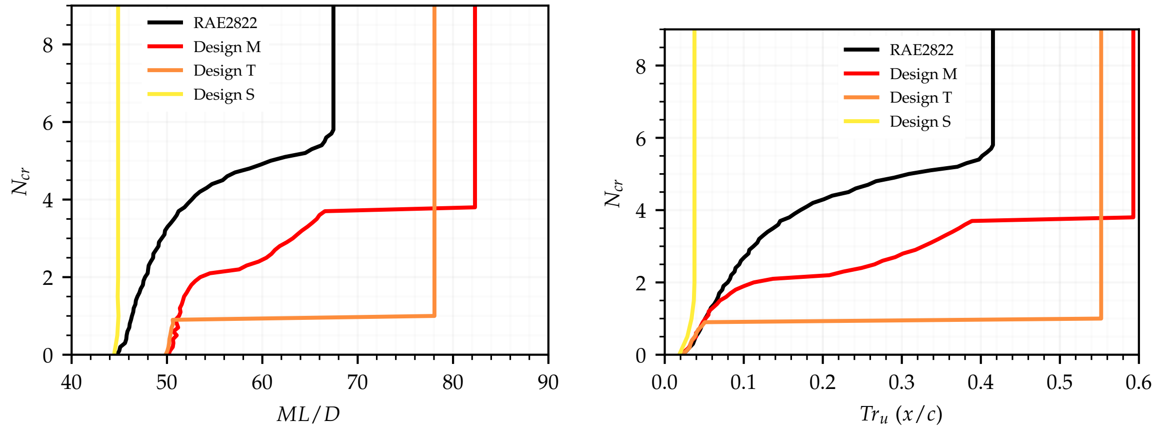

(a) *ML/D*

(b) *Upper Surface Transition Location*

Figure 6.16: *ML/D and upper surface transition location against critical N-factor for the RAE2822 and selected optimised designs.*

6.3.2 Off-Design Analysis

Off-design analysis of designs M and design T have been performed for comparison against the RAE2822. Figure 6.17 shows ML/D mean and standard deviation polars over a range of Mach numbers for each of the designs. Over the Mach range where all three polars are present, both optimised designs have increased $(ML/D)_\mu$ and decreased $(ML/D)_\sigma$. These improvements extend above the design $M = 0.715$. As Mach number is reduced, the optimised aerofoils could no longer converge at high critical N-factor values and so have not been included. At these conditions, CVGK struggles to converge transition location in a region of strong adverse pressure gradient. This suggests laminar separation is occurring.

Design T could be converged at all N_{cr} values down to a lower Mach number than design M. This is due to the more favourable pressure gradient used to reduce ML/D variation to N_{cr} degradation at the design point. Design M uses a weaker favourable pressure gradient to reduce shock strength and delay shock position at design conditions but as a result has a stronger adverse pressure gradient as Mach number reduces. Converged solutions are obtained at lower Mach numbers when N_{cr} is reduced sufficiently to cause transition as a result of instability growth.

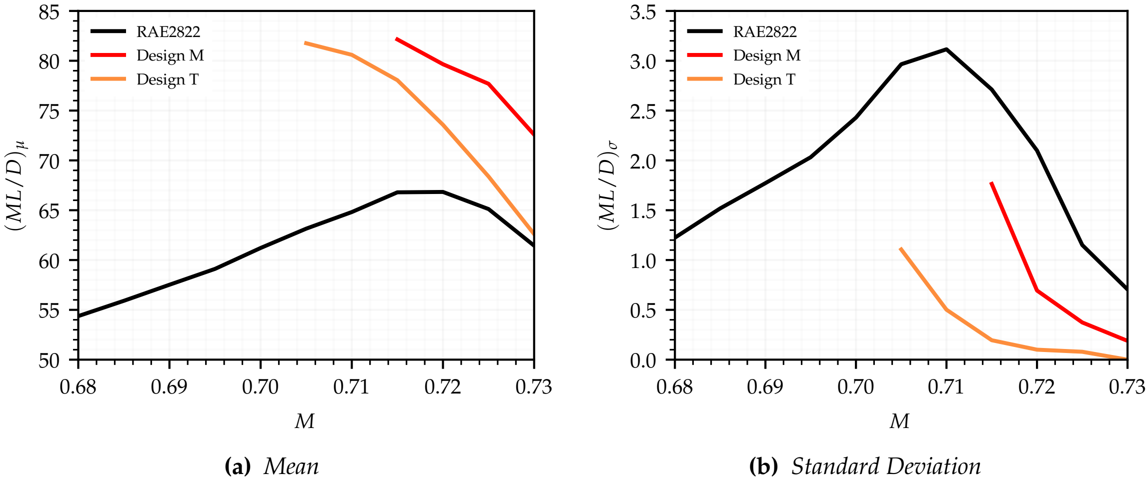

(a) *Mean* **(b)** *Standard Deviation*

Figure 6.17: *Mean ML/D and ML/D standard deviation polars for the RAE2822 and selected optimised designs.*

6.3.3 Uncertainty Standard Deviation

The sensitivity of ML/D standard deviation to the chosen critical N-factor standard deviation has been assessed for design M and design T and compared with the RAE2822. Figure 6.18a shows ML/D standard deviation with a uncertainty standard deviation of $N_\sigma = 1$. As both optimised designs have transition fixed at the shock location down to a low critical N-factor, standard deviation is essentially zero. Transition for the RAE2822 also occurs at the shock location at high critical N-factor values so its standard deviation is also very low.

Figure 6.18b shows ML/D standard deviation with an uncertainty standard deviation of $N_\sigma = 3$. ML/D standard deviation has increased for all three designs. While the maximum $(ML/D)_\mu$ design had a lower standard deviation than the RAE2822 at the design Mach number and N_σ, it has a comparable standard deviation when N_σ is increased. This is due to the maximum $(ML/D)_\mu$ design having ML/D invariant to critical N-factor changes at high N_{cr} values, but having a larger change in ML/D when critical N-factor is reduced to zero. The same is true for the optimised trade-off aerofoil; however, the critical N-factor value where this change in ML/D occurs is much lower. As low critical N-factors have a lower weighting, this has a smaller effect on standard deviation.

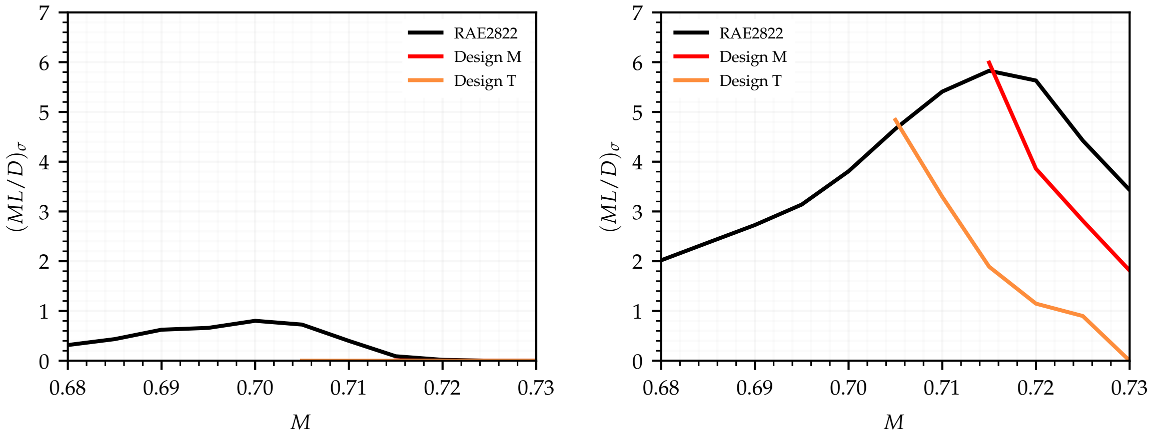

(a) $N_\sigma = 1$ **(b)** $N_\sigma = 3$

Figure 6.18: *ML/D standard deviation polars for the RAE2822 and selected optimised designs with increased and decreased critical N-factor standard deviation.*

6.4 Summary

Single-point multi-objective robust optimisation of two aerofoils has been carried out. Mean drag and drag standard deviation is reduced for the NLF0215 at subsonic flow conditions while mean ML/D and ML/D standard deviation are maximized and minimised respectively for the RAE2822 at transonic flow conditions. For both optimisation cases, a trade-off exists and a Pareto front found between mean and standard deviation of the selected objective function variable. Improving mean performance for both cases results in larger performance standard deviation.

Mean performance for both cases is improved in part by the extension of NLF. Transition is delayed on both surfaces of the subsonic aerofoil by creating a more favourable pressure gradient to suppress instability growth. As transition is shock limited on the transonic aerofoil, laminar flow is extended here by delaying shock location. For the subsonic case, minimum C_d standard deviation is found while maintaining extended laminar flow; whereas for the transonic case, minimum ML/D standard deviation is produced by shock induced transition at the leading edge. Leading edge transition is inherently robust as no laminar flow is lost when critical N-factor is reduced, but is of little practical use.

Off-design analysis of the optimised aerofoils from each optimisation case was also carried out. While mean and standard deviation are improved at the design point, off-design performance varies. For the optimised subsonic aerofoils, mean drag is comparable below the lift coefficient used but worse as lift coefficient is increased. Drag standard deviation is substantially worse just above the design point. For the optimised transonic aerofoils, mean ML/D and ML/D standard deviation are improved at Mach numbers larger than the one used but fail to converge as Mach number is reduced due to laminar separation.

The sensitivity of standard deviation to the chosen uncertainty standard deviation was also assessed for each design in both optimisation cases. For the NLF0215, increasing critical N-factor standard deviation caused the lift coefficient distance between the two spikes in drag standard deviation to reduce. Standard deviation at high lift coefficient also increased substantially. For the RAE2822, reducing critical N-factor standard deviation below a certain threshold reduced ML/D standard deviation to approximately zero when transition is shock limited. For all designs from both optimisation cases, increasing critical N-factor standard deviation causes output standard deviation to increase. Specifically, output standard deviation rises most for designs with a larger extent of laminar flow, as, inherently, these see a larger reduction as critical N-factor is reduced.

Based on these findings, it is clear that reducing performance standard deviation to critical N-factor uncertainty can help to improve the ability of NLF aerofoils to maintain laminarity. It is found that, as with deterministic single-point optimisation, off-design performance suffers if not considered during the optimisation process. Clearly there is a need to extend this methodology to allow for robust optimisation with critical N-factor uncertainty over a multi-point range of operating conditions.

Chapter 7

Multi-point Robust Optimisation

The single point optimisation carried out previously showed aerofoil robustness to critical N-factor uncertainty varied with both Mach number and lift coefficient. Robust optimisation of the selected aerofoils found improvements in both mean performance and performance standard deviation at the design lift coefficient and Mach number, respectively. It was seen, however, that these benefits are only obtained at or close to the design conditions used. Furthermore, improving critical N-factor robustness via optimisation at the design point resulted in worse robustness off-design.

As such, development of a method for multi-point optimisation of aerofoil performance and robustness to N_{cr} uncertainty is needed. A major challenge that appears when implementing such a method, however, is the well documented curse of dimensionality [156]. Varying both critical N-factor and another flight variable such as Mach number or lift coefficient increases the complexity of the design problem and drastically raises the number of flow solutions required to calculate the objective functions used during optimisation. Thus, objectives for this chapter are to:

- Develop a multi-point optimisation method with uncertainty in critical N-factor
- Avoid high computational costs due to increased problem dimensionality
- Assess the effectiveness of multi-point robust optimisation
- Highlight best practices for the robust design of NLF aerofoils

7.1 Methodology

Quantification of performance robustness to critical N-factor uncertainty at a single operating condition is done using Eqs. (5.2), (5.3) and (5.4) presented in chapter 5. To extend this to a number of operating conditions over the variable M, the robust quantification method is combined with multi-point optimisation. For a set of k_m multi-point samples, multi-point optimisation seeks to find an optimum of the weighted mean of the single-point functions, $F_\mu(M_i)$ and $F_\sigma(M_i)$. The optimisation problem is defined as:

$$\text{Minimize } F_m(x),\ F_s(x) \tag{7.1}$$

where the weighted mean of single-point mean values $F_m(x)$ is found using:

$$F_m(x) = \frac{1}{W_m} \sum_{i=1}^{k_m} w_i F_\mu(M_i) \tag{7.2}$$

$$F_\mu(M_i) = \frac{1}{W_r} \sum_{j=1}^{k_r} P(N_j) G(M_i, N_j) \tag{7.3}$$

where the weighted mean of single-point standard deviation values $F_s(x)$ is found using:

$$F_s(x) = \frac{1}{W_m} \sum_{i=1}^{k_m} w_i F_\sigma(M_i) \tag{7.4}$$

$$F_\sigma(M_i) = \sqrt{\frac{1}{W_r} \sum_{j=1}^{k_r} \left[G(M_i, N_j) - F_\mu(M_i) \right]^2} \tag{7.5}$$

and where the multi-point and robust weighting terms W_m and W_r are found using:

$$W_m = \sum_{i=1}^{k_m} w_i \qquad W_r = \sum_{j=1}^{k_r} P(N_j) \tag{7.6}$$

As can be seen from Eq. (7.3) and (7.5), there are $k_m \times k_r$ output variable $G(x)$ samples required. Even with as little as two multi-point sample points, this doubles the already high number of flow solver evaluations needed. Using 3 multi-points and as few as 5 robust samples as part of a genetic optimisation run for 100 generations with 48 individuals per generation would require 72, 000 flow solutions. This can be carried out using viscous inviscid coupling methods such as XFOIL and CVGK, but is prohibitally expensive for RANS-based solvers. While alternative optimisation methods and robust sampling strategies exist, it is preferable to avoid the increase in problem dimensionality entirely, if possible.

7.1.1 Envelope Sampling Approach

By exploiting a unique feature of the e^N transition model, an increase in problem dimensionality, when combining robust and multi-point optimisation methods, can in fact be avoided. As outlined previously, the e^N model is based on linear stability theory where flow disturbances enter the boundary layer and are either dampened, remain neutral or amplify as they propagate downstream. Excessive amplification of instabilities leads to flow transition.

Computationally, the output of a flow solver is passed to a boundary layer solver to produce velocity profiles and pressure distributions which are required by the e^N model for calculating the stability equations. As the transition location affects the shape of the boundary layer, the solution process is iterative. The flow solver is initialized with laminar flow, and then successively fed new calculated transition locations and re-computed until a converged transition location and flow solution is found. At each iteration, the e^N method calculates the amplification factor of instabilities with various frequencies along the aerofoil profile, and predicts transition at the point where an amplification factor first exceeds a specified critical N-factor threshold.

Thus from a converged solution, the maximum amplification factor at any chord-wise position along the aerofoil up to the location of transition is obtained. This is commonly referred to as an 'N-factor envelope'. While this envelope is usually only used to find the transition location at the critical N-factor specified, it can also be used to estimate transition locations for any N-factor at or below the one used when the flow solution was solved.

It is therefore possible to compute transition location mean and standard deviation with varying critical N-factor from a single flow solution using the N-factor envelope. As a result, the number of k_r samples used in Eq. (7.3) and (7.5) become independent of computational cost. To get an idea of this cost saving, the transonic optimisation case from the previous chapter run at 3 Mach numbers with 19 robust samples for $\times 48$ designs over 100 generations would require $273,600$ flow solutions. Using the proposed envelope sampling method would require almost 95 percent less at $14,400$ flow solutions.

A limitation of this approach is that only mean and standard deviation of transition location to critical N-factor uncertainty can be calculated. Typically in most optimisation cases, drag is selected over transition location as the variable of interest. This is because extending laminar flow does not always result in reduced drag and can produce poor off-design performance as laminar flow is more prone to separation. As such, mean and standard deviation of drag should be the main objective of a robust optimisation.

Results of uncertainty analysis and from single-point optimisation of the NLF0215 and RAE2822 showed that drag robustness is directly related to transition location robustness with uncertainty in critical N-factor. Thus, transition robustness can be used to indirectly improve drag robustness. Optimisation of mean transition location may, however, not be suitable for the reasons mentioned. As drag is obtained at the deterministic flow solution critical N-factor, this could be used instead of, or as an additional objective to, mean transition location. This would allows drag to be considered directly during optimisation.

7.1.2 Envelope Processing

Some processing of the N-factor envelope is required before it can be used to estimate transition location. Figure 7.1 shows the process of obtaining a critical N-factor envelope from the N-factor envelope, followed by sampling for use with the quantification equations (5.2), (5.3) and (5.4). The general steps required are as follows:

1. Remove all N-factor envelope data points beyond the transition location calculated with the critical N-factor used to generate the flow solution
2. If transition occurs due to shock induced or laminar separation, extend the N-factor envelope up to the critical N-factor limit used during the flow solution
3. Remove any dips in the N-factor envelope as transition will always occur at the earliest chord-wise location where the amplification factor exceeds a given threshold.

The resulting critical N-factor envelope can essentially be used as a surrogate model for any sampling-based uncertainty quantification method. For the sampling strategy used in this study, critical N-factor samples are uniformly spaced from $N_{cr} = 9 \rightarrow 0$ as indicated by the lower right plot in figure 7.1.

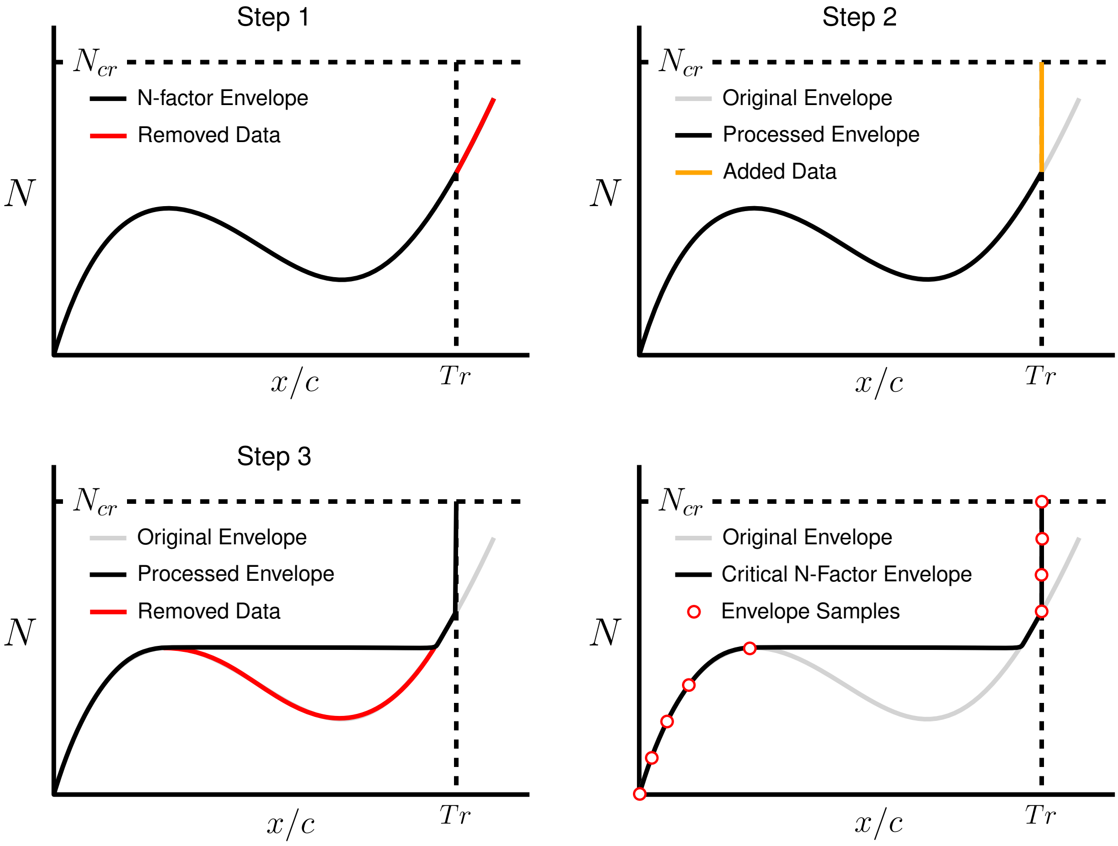

Figure 7.1: *Envelope sampling workflow.*

7.1.3 Key Assumption of Methodology

A key assumption made when using the envelope sampling method is that transition locations estimated using the N-factor envelope accurately represent the transition locations found, had a flow solution been obtained with the sampled critical N-factor value. This assumption implies that movement of transition location has negligible effect on the boundary layer and so instability growth upstream of the transition point.

In reality, varying transition location will alter the boundary layer thickness and the amount of lift generated at the current angle of attack. A different angle of attack will be required to meet any lift constraints which will in turn further alter the pressure gradients and instability growth upstream of the transition location. Due to these effects, the estimated transition locations for the envelope sampling method and the true transition locations obtained from a flow solution at the reduced critical N-factor value will differ. The magnitude of these differences will dictate the accuracy of the stochastic terms calculated using the envelope sampling method. Thus, assessment of the error between stochastic properties calculated with individual critical N-factor samples and calculated using the envelope sampling approach needs to be made.

7.2 Optimisation

7.2.1 Problem Formulation

Multi-point, multi-objective robust optimisation has been carried out to investigate the effectiveness of the proposed methodology for NLF aerofoil design with robustness to N_{cr} uncertainty over a range of operating conditions. As with the single-point optimisation, two cases are considered. Each is optimised under different flow conditions and each has differing objective functions and multi-point variables.

Optimisation at subsonic conditions is carried out using the NLF0215 as the starting aerofoil. This is run at a Reynolds number of $Re = 9 \times 10^6$ and Mach number of $M = 0.1$ with transition is left free on both surfaces. Optimisation is carried out over a multi-point range of lift coefficients. These are shown in table 7.1 with corresponding weights. Minimum drag for the NLF0215 is found at $C_l = 0.7$. To ensure good performance around the cruise lift coefficient, a highly weighted multi-point has been placed just below this at $C_l = 0.65$. A second highly weighed point is placed at $C_l = 1.0$ to create a low drag range that will widen when Reynolds number is reduced for climb. Two additional points are placed at $C_l = 0.00$ and $C_l = 1.90$ with very low weighting. This limits their influence on the optimiser but designs are required to converge here, thus avoiding any designs with large separation. The point at $C_l = 0.00$ is used to avoid laminar separation occurring at low lift coefficients while the point at $C_l = 1.90$ ensures $C_{l,\max}$ is no less than 1.90.

Optimisation at transonic flow conditions is carried out using the RAE2822 aerofoil as the starting geometry. An increased Reynolds number of $Re = 15 \times 10^6$ was selected so that the methodology proposed could be tested on a design problem with stronger instability growth. At this Reynolds number, $(ML/D)_{\max}$ is found at $C_l = 0.74$ and $M = 0.72$. These are used to represent cruise conditions. Two additional points at $+/-0.02$ Mach number from the cruise condition are used, with a lower multi-point weighting. As Mach number varies, $M^2 C_l$ remains fixed. The complete list of multi-points used are shown in table 7.2. Transition is free on the upper surface and fixed at $0.03x/c$ on the lower surface for reasons outlined during the uncertainty analysis carried out in chapter 5.

Table 7.1: *Multi-points properties and weights for optimization of the NLF0215.*

Point	Weight	C_l
1	0.01	0.00
2	1.00	0.65
3	0.80	1.00
4	1.00	1.90

Table 7.2: *Multi-points properties and weights for optimization of the RAE2822.*

Point	Weight	Ma	C_l
1	0.5	0.70	0.7829
2	1.0	0.72	0.7400
3	0.5	0.74	0.7005

Both optimisation cases have differing objective functions. For the NLF0215 case, the objectives are minimisation of the mean value of deterministic C_d at $N_{cr} = 9$, upper surface transition location standard deviation and lower surface transition location standard deviation with varying critical N-factor, over the multi-points used. Similarly, for the RAE2822 case, the objectives are the maximisation of mean deterministic ML/D at $N_{cr} = 9$ and minimisation of mean transition location standard deviation with varying critical N-factor, over the multi-points. The minimization of transition location standard deviation for both cases ensures robustness to critical N-factor is improved. As deterministic drag and ML/D are the overall performance variables, they were selected over mean transition location as the second optimisation objective. Improving these at deterministic conditions should result in the ideal amount of laminar flow being obtained. Reducing transition standard deviation ensures this is robust to changes in critical N-factor.

For both optimisation cases, the deterministic critical N-factor was set at $N_i = 9$ with a critical N-factor standard deviation of $N_\sigma = 2$. The critical N-factor envelope from each flow solution is sampled 1001 times to calculate the transition location mean and standard deviation. A geometric constraint is used for both optimisation cases enforcing maximum thickness of all designs generated to not decrease below that of the starting aerofoil in each case. Results of the single-point optimisation carried out previously found that in the pursuit of minimizing performance standard deviation to variations in critical N-factor, a trivial solution has transition fixed at the leading edge. This is of no practical use as a solution, as it has excessively large drag that negates any benefits in improved robustness. To avoid the generation of such designs, a limit is placed on the maximum deterministic C_d for the NLF0215 case and on the minimum deterministic ML/D value for the RAE2822. In both cases this limit ensures each property is no worse than that of the starting aerofoil.

The same parametrisation method and optimisation settings were used for this study as used during single-point optimisation. Due to the convergence issues seen in the single-point transonic optimisation, design variable bounds for the transonic multi-point optimisation have been altered. A total of 12 design variables, resulting from 6 design variables per surface, are controlled by the optimiser. Flow conditions are fixed with angle of attack left free to satisfy the specified lift coefficient. The genetic optimisation has a population size of 48 individuals and runs until it reaches a 100 generations limit. The chance of mating is set to 80%, resulting in a mutation chance of 20%. Crowding number was again scaled from $0 \rightarrow 20$ during the 100 generations to aid in design space exploration early in the optimisation and convergence towards the end.

7.2.2 Validation of the Methodology

The envelope sampling method's accuracy in calculating transition location mean and stochastic deviation needs to be assessed. To carry this out, mean and standard deviation are calculated using the envelope sampling approach and compared against values calculated with transition locations found from individual flow solutions at each critical N-factor sample used. In both cases, 1001 transition location samples are taken from the critical N-factor envelope for the envelope sampling method. For the actual transition location method, flow solutions are run with critical N-factor values taken every $N_{\text{step}} = 0.1$ from $N_{cr} = 9 \rightarrow 0$ resulting in 91 sample points.

Figure 7.2 shows upper and lower surface transition location mean and standard deviation for the NLF0215 over the lift coefficients range when calculated with each approach. Figure 7.3 shows upper surface transition location mean and standard deviation for the RAE2822 over a range of Mach, calculated using the two approaches.

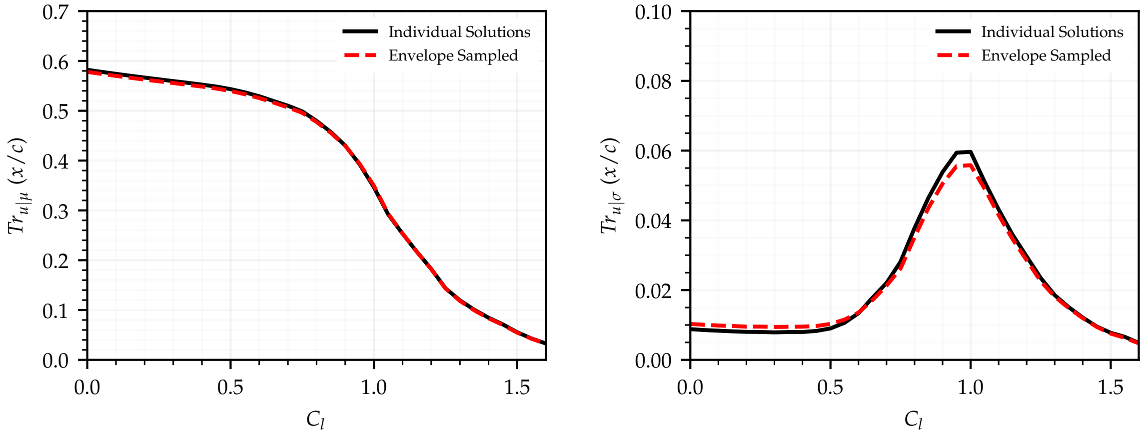

(a) *Mean upper surface transition location* **(b)** *Upper surface transition location standard deviation*

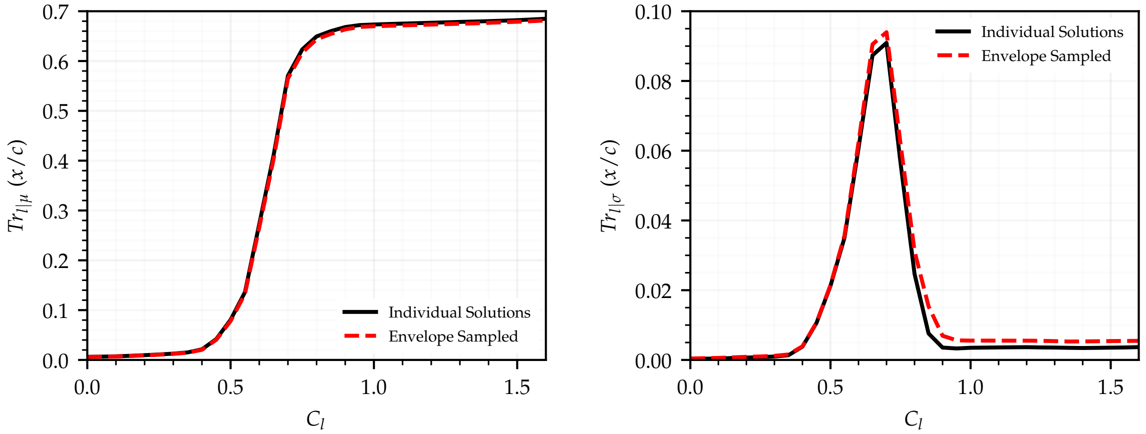

(c) *Mean lower surface transition location* **(d)** *Lower surface transition standard deviation*

Figure 7.2: *Upper and lower surface transition mean and standard deviation calculated over the span using the envelope sampling method and from individual flow solutions for the NLF0215.*

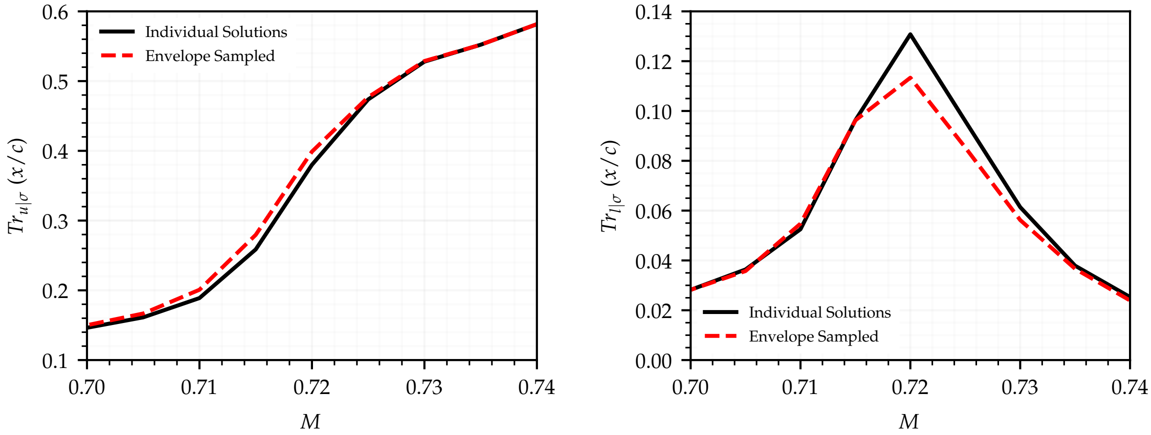

(a) *Mean upper surface transition Location* **(b)** *Upper surface transition Location standard deviation*

Figure 7.3: *Upper and lower surface transition mean and standard deviation calculated over the span using the envelope sampling method and from individual flow solutions for the RAE2822.*

As seen in figures 7.2a and 7.2c, the envelope sampling method is accurate in calculating mean transition locations over the entire lift coefficients range. As expected, accuracy is only slightly worse at lift coefficients with highly extended laminar flow. Mean upper surface transition location calculated with each approach for the RAE2822 also agrees well over the Mach number range considered, as shown in figure 7.3a. The envelope sampling method is now least accurate where transition location moves quickly over a small Mach number range, rather than where transition is highly extended. The envelope sampling method is also accurate in calculating transition location standard deviation for the NLF0215, as shown in figures 7.2b and 7.2d. Again, accuracy is worst where transition is most delayed, but also where standard deviation is largest. For the RAE2822, the method also differs most at the Mach number with largest standard deviation value.

In both cases, standard deviation calculated using envelope sampled transition locations follows the same form obtained when calculating standard deviation with transition locations from individual flow solutions. As such, peaks and minima in standard deviation are found at the correct lift coefficient or Mach number. Thus, the envelope sampling approach is able to accurately highlighting where robustness is best and worst, and so should function well when used to calculated stochastic terms for use with an optimiser.

7.3 Subsonic Results

The optimisation produced 4800 unique individuals, 4352 of which XFOIL was able to converge at each of the multi-point lift coefficient values. Objective function convergence can be seen in figure 7.4. This shows the minimum value found for mean C_d, Tr_u and Tr_l over the course of the optimisation. As can be seen, improvements in objective function become smaller as the optimisation progresses. This indicates that the optimiser is converging towards an optimum value for each. As trade-offs exist between objectives, a Pareto front is generated containing 330 designs. Figure 7.5 shows a contour plot of the Pareto front with Pareto designs highlighted. The colour map has a range of 2 drag counts up from the minimum mean C_d value found. The grey shaded region indicates designs beyond this threshold. The design with minimum mean C_d and a trade-off design balancing mean C_d, $Tr_{u|\sigma}$ and $Tr_{l|\sigma}$ are also indicated.

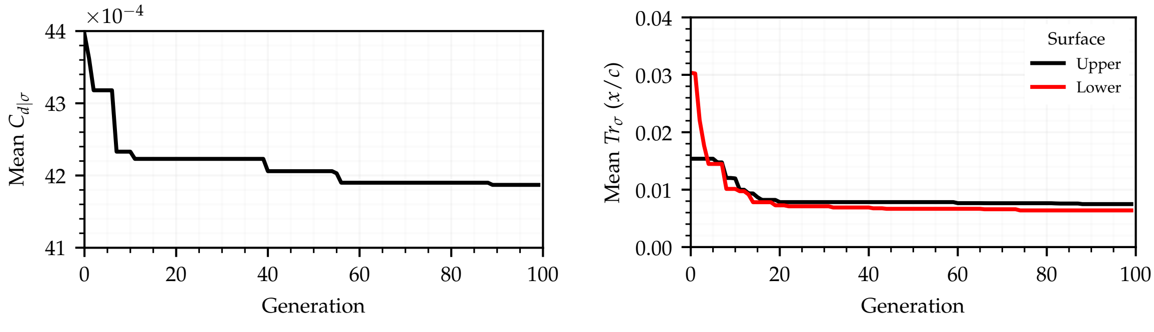

(a) *Drag* **(b)** *Transition locations*

Figure 7.4: *The optimum objective function values found during the NLF0215 optimisation history.*

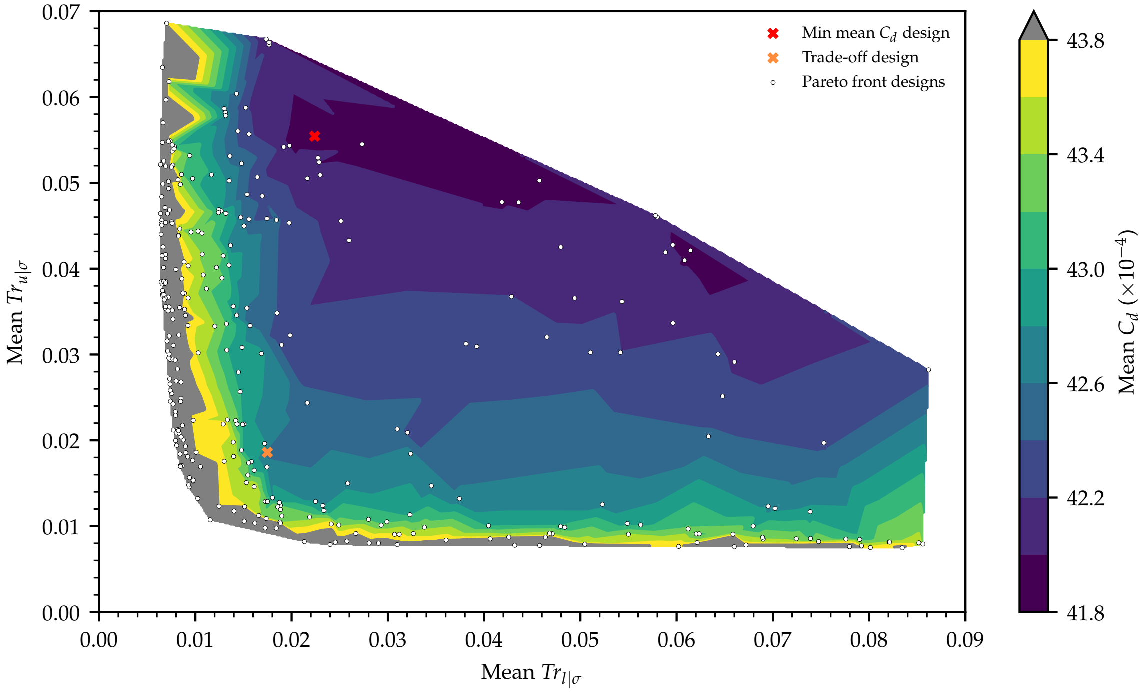

Figure 7.5: *Contour plot of the Pareto front found between objective functions during optimisation of the NLF0215.*

From the minimum mean drag design, reducing mean transition location surface standard deviation on either surface causes mean drag to grow. Above $Tr_{l|\sigma} = 0.02$, the Pareto front appears dependent only on mean upper surface transition standard deviation. Two areas within this region can be highlighted. Mean drag has a very weak trade-off with upper surface transition location standard deviation above $Tr_{u|\sigma} = 0.015$, while below sees rapid drag growth with only a small mean upper surface transition standard deviation reduction. Below $Tr_{l|\sigma} = 0.02$ and above $Tr_{u|\sigma} = 0.015$, the Pareto front is only a function of lower surface transition location standard deviation. Reducing $Tr_{l|\sigma}$ further rapidly increases mean drag. Below $Tr_{l|\sigma} = 0.02$ and $Tr_{u|\sigma} = 0.015$, mean drag shows dependence on mean transition location standard deviations from both surfaces.

Based on the placement of the design with minimum mean C_d, it is possible to obtain a similar mean C_d but substantially reduced upper surface transition location standard deviation. The trade-off design highlighted on the Pareto front makes this trade-off. Objective function values for the NLF0215, optimised aerofoil with minimum mean C_d and optimised trade-off aerofoil are shown in table 7.3. Additionally, the aerofoils with minimum mean upper and lower surface transition location standard deviations are also included.

Each of the selected designs has a lower mean C_d than the NLF0215 as this was constrained to prevent designs with leading edge transition. As transition location is unable to move, designs of this type are inherently robust. This has been effective as the design with minimum mean $Tr_{u|\sigma}$ has $0.524x/c$ mean $Tr_{u|\mu}$, while the design with minimum mean $Tr_{l|\sigma}$ has $0.646x/c$ mean $Tr_{l|\mu}$. While the Pareto front shows that both mean $Tr_{u|\sigma}$ and $Tr_{l|\sigma}$ can be reduced together, to obtain the minimum values for each requires the other to rise.

Table 7.3: *Objective function values for the NLF0215 and optimised aerofoils with minimum mean C_d, mean $Tr_{u|\sigma}$, mean $Tr_{l|\sigma}$, and a trade-off design.*

Design		Mean C_d ($\times 10^{-4}$)	Mean $Tr_{u|\sigma}$	Mean $Tr_{l|\sigma}$
NLF0215		47.57	0.034	0.052
Min mean C_d	(D)	41.87 (-12%)	0.055 (+62%)	0.022 (-58%)
Trade-off	(T)	42.48 (-10%)	0.019 (-44%)	0.017 (-67%)
Min mean $Tr_{u|\sigma}$		43.92 (-8%)	0.007 (-79%)	0.083 (+60%)
Min mean $Tr_{l|\sigma}$		46.12 (-3%)	0.046 (+35%)	0.006 (-88%)

7.3.1 Design Point Changes

The maximum mean C_d and trade-off designs are compared against the NLF0215 at the optimisation design points. The design with minimum mean C_d is denoted design D (deterministic) while the trade-off design is denoted design T (trade). Figure 7.6 shows the design variable bounds and values for each design. These are split into upper and lower surfaces where variables 1 and 7 are at the front and 6 and 12 at the rear of the aerofoil. Positive values indicate material is added to the NLF0215 while negative values indicate material has been removed. Wide bounds were given to the design variables near the front and rear of the aerofoil to allow good control over the leading edge pressure gradient and at the rear of the aerofoil to allow for different amounts of loading and camber.

Figure 7.7 shows the aerofoil profiles for each design. The grey shaded area indicates the viable design space as dictated by the bounds. Both optimised aerofoils have increased maximum thickness compared to the NLF0215. The chord-wise position of maximum thickness is similar for the NLF0215 and design T but further down-stream for design D. As such, design D has less curvature from $0.1 < x/c < 0.4$ compared to design T. Both optimised designs have a similar lower surface. Thickness is increased between $0.1 < x/c < 0.55$ and reduced towards the trailing edge. This lowers camber and increases curvature through the middle of the lower surface. Reduction of material from both surface has reduced thickness at the trailing edge and decreased camber slightly. Design variables 5, 6, 11 and 12 are close to the lower bounds so additional reductions may improve performance.

Figures 7.8 and 7.9 show the pressure distributions and N-factor envelopes for the NLF0215 and selected optimised aerofoils at the two highly weighted design points 2 and 3, run at $N_{cr} = 9$ with markers indicating transition location on each surface for each design. The lower surface of both optimised designs at both lift coefficients now features a stronger favourable pressure gradient from $0.0 < x/c < 0.4$ followed by an adverse pressure gradient from $0.4 < x/c < 0.6$. The favourable pressure gradient region has delayed instability amplification until further downstream for both optimised designs at $C_l = 0.65$. The adverse pressure gradient region then causes rapid growth up to the critical N-factor. This results in little movement of transition location at high critical N-factors, so reduces $Tr_{l|\sigma}$. These improvements have resulting in a slight reduction in laminar flow and earlier instability growth on the lower surface at $C_l = 1.00$. This design points has a lower weighting and so large improvements at $C_l = 0.65$ are favoured by the optimiser.

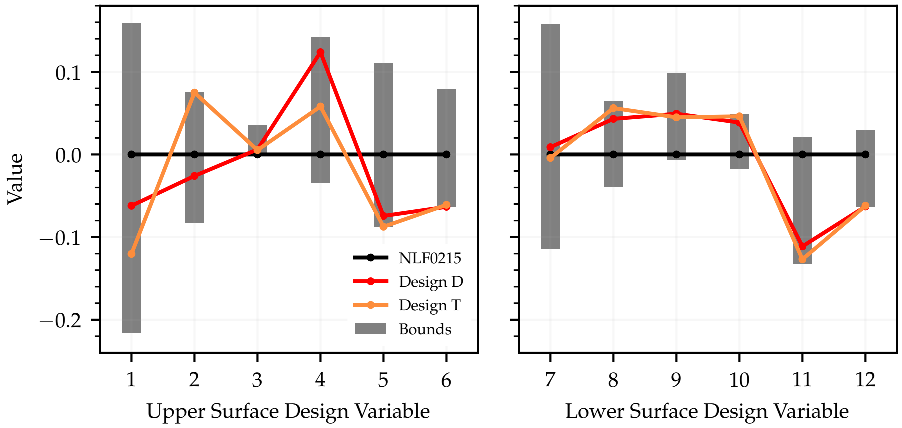

Figure 7.6: *Upper and lower surface design variable values and bounds for the NLF0215 and selected optimised designs.*

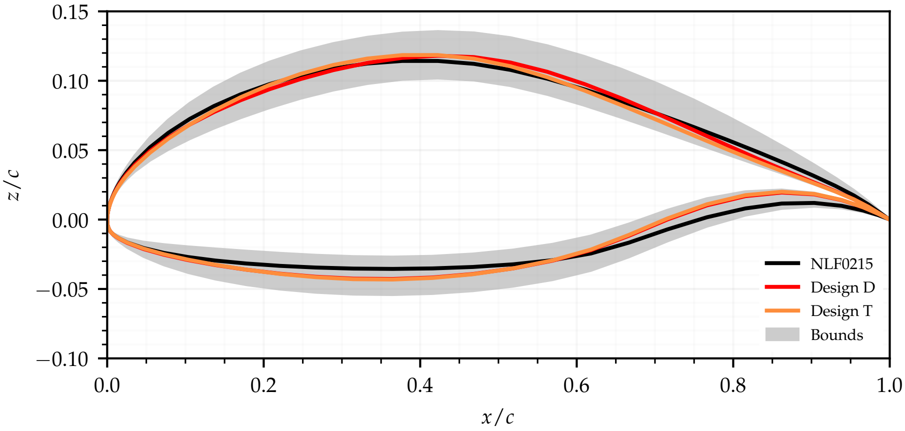

Figure 7.7: *Aerofoil profiles for the NLF0215 and selected optimised aerofoils, with the grey shaded region indicating the viable design space as dictated by the design variable bounds.*

Design changes on the upper surface have resulted in different pressure distributions over the front of each optimised aerofoil. At $C_l = 0.65$, design D has a slightly larger initial pressure rise, followed by a longer favourable pressure gradient as maximum thickness is further aft. As such, instability amplification does not occur until further downstream. Thus, design D obtains increased upper surface laminar flow. However, at $C_l = 1.00$, the initial pressure rise leads to a region of adverse pressure gradient, which increased instability amplification earlier upstream. Although designs D and T have a similar amount of upper surface laminar flow, this is maintained down to a much lower critical N-factor for design T. If critical N-factor is reduced below $N_{cr} = 6$, transition location at $C_l = 1.0$ is in fact worse for design D then the NLF0215.

Thus, both designs represent an improvement on the starting design, however a small reduction in performance at the ideal critical N-factor can allow for a more robust performance to critical N-factor uncertainty.

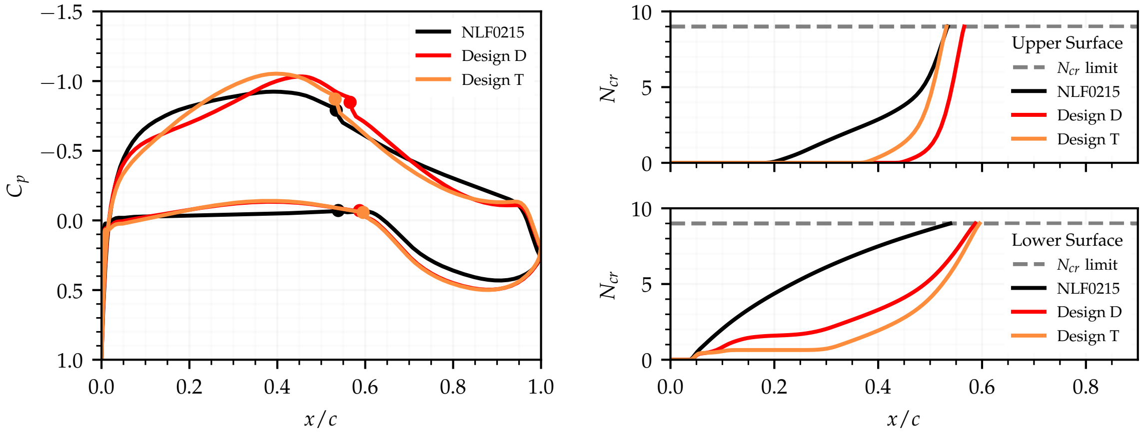

(a) *Pressure distributions* **(b)** *Transition envelopes*

Figure 7.8: *Pressure distributions and transition envelopes for the NLF0215 and selected optimised aerofoil at design point* 2 *with* $C_l = 0.65$

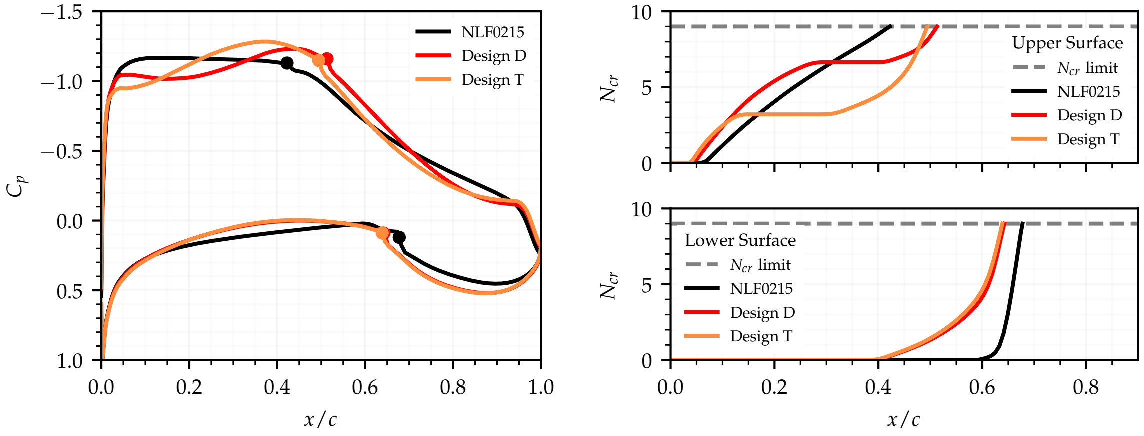

(a) *Pressure distributions* **(b)** *Transition envelopes*

Figure 7.9: *Pressure distributions and transition envelopes for the NLF0215 and selected optimised aerofoil at design point* 3 *with* $C_l = 1.0$.

7.3.2 Performance Polars

Figure 7.10 shows the deterministic drag and transition location polars for the NLF0215 and selected optimised aerofoils when run at the ideal critical N-factor of $N_{cr} = 9$. As seen in figure 7.10a, C_d is reduced for both optimised designs through the lift coefficient range $0.65 \leq C_l \leq 1.0$. This has strengthened the drag bucket shape already found for the NLF0215. Design D has a lower C_d through the bucket lift coefficient range but this range is smaller than for design T. Drag reduction within the bucket comes in part from extended upper surface laminar flow, as seen in figure 7.10b. The strong drag bucket shape comes from a larger shift in upper surface transition location over a smaller lift coefficient range. Design T has this shift in transition location occur at a higher lift coefficient than design D, enabling it to obtain a wider drag bucket but less laminar flow through the bucket itself.

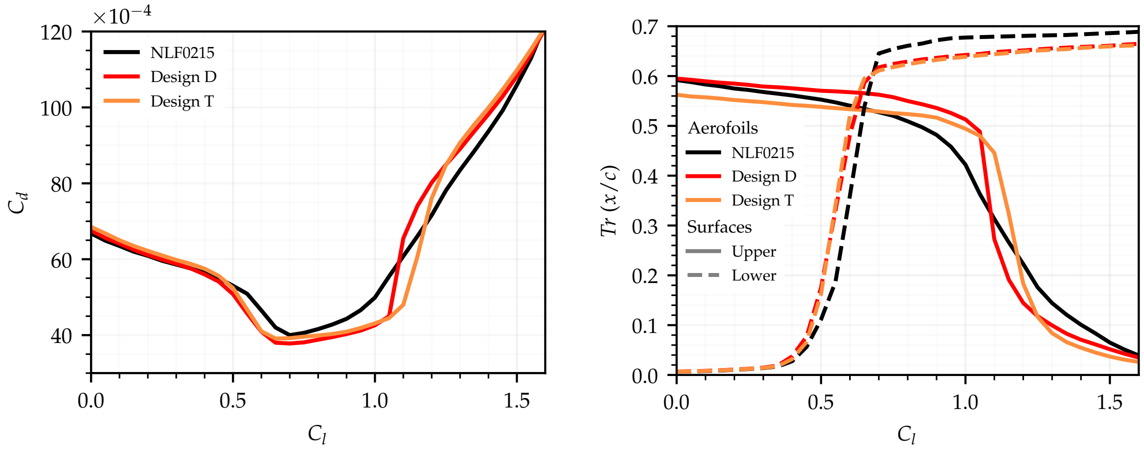

(a) *Drag* **(b)** *Transition locations*

Figure 7.10: *Drag and transition location polars run at the ideal critical N-factor of $N_{cr} = 9$ for the NLF0215 and optimised aerofoils.*

Strengthening of the drag bucket upper corner has also caused an increase in C_d above the drag bucket for both optimised designs. This is also caused by transition movement being confined to a small lift coefficient range. This helps keep extended upper surface laminar flow up to a higher lift coefficient, but then reduces laminar flow at lift coefficients above the position where transition moves.

To assess stochastic performance of the NLF0215 and selected optimised aerofoils, mean and standard deviation of drag and transition location have been calculated over a range of lift coefficients. This was done using flow solutions obtained at critical N-factor samples taken every $N_{\text{step}} = 0.1$ from $N_{cr} = 9 \rightarrow 0$. Mean drag and transition location polars are shown in figure 7.11. The ideal drag polars are also shown for comparison.

The most noticeable differences between the mean and deterministic performance of the NLF0215 and optimised designs occurs through the drag bucket lift coefficient range. Mean drag is naturally higher than deterministic drag, and has increased most between $0.5 < C_l < 1.2$. $C_{d|\mu}$ is furthest from C_d for the NLF0215 at the cruise lift coefficient of $C_l = 0.7$. The analysis at subsonic conditions carried out previously found that the difference between mean and deterministic performance was largest where deterministic transition location is sensitive to changing lift coefficient. This is again seen as Tr_u is less sensitive to lift coefficient through the drag bucket and so both have similar $C_{d|\mu}$ and C_d values.

As mean drag and deterministic drag are comparable through the drag bucket range for designs D and T, the effect of including critical N-factor uncertainty is instead a reduction of the drag bucket width. In both cases this comes primarily from the upper edge of the drag bucket moving to a lower lift coefficient value. This is far more pronounced for design D. Importantly, the drag bucket no longer extends over the climb range chosen. Mean drag for design D is 9 drag counts higher than deterministic drag at $C_l = 1.0$. As the drag bucket for design T was over-extended at the ideal critical N-factor, the mean drag polar bucket width still exceeds the upper highly weighted design point.

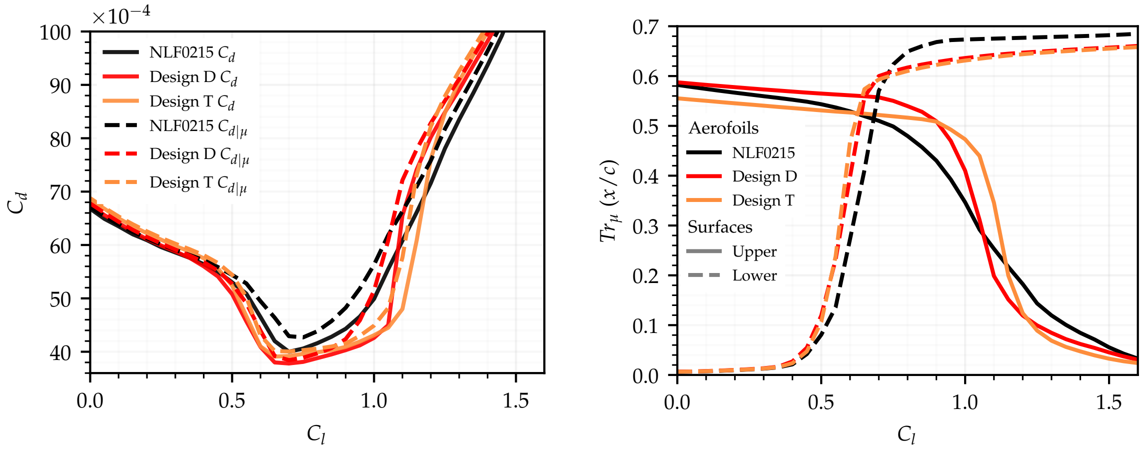

(a) *Mean ideal drag* **(b)** *Mean transition location*

Figure 7.11: *Mean drag, ideal drag and mean transition location polars for the NLF0215 and optimised aerofoils.*

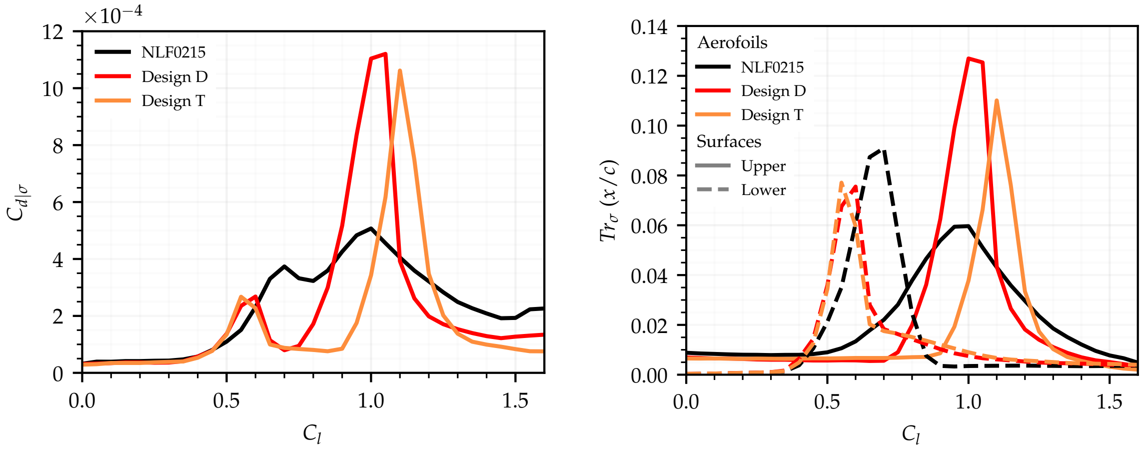

(a) *Drag* **(b)** *Transition location*

Figure 7.12: *Drag and transition location standard deviation polars for the NLF0215 and optimised aerofoils.*

Figure 7.12 shows the drag and transition location standard deviation polars for the NLF0215 and selected optimised aerofoils. Below $C_l = 0.6$, $C_{d|\sigma}$ is comparable between all three designs while at the cruise lift coefficient, it has substantially reduced after optimisation. Design D has a large spike in $C_{d|\sigma}$ at $C_l = 1.0$, thus leading to large differences between deterministic and mean drag. Design T has a $C_{d|\sigma}$ peak of similar magnitude but reduced width and centred at a slightly higher lift coefficient. Both these spikes in $C_{d|\sigma}$ match a corresponding spikes in $Tr_{u|\sigma}$ and $Tr_{l|\sigma}$. $Tr_{u|\sigma}$ is much larger for the optimised designs due to the increased rate of change of deterministic transition location with changing lift coefficient. Although the peaks in $Tr_{u|\sigma}$ have increased, their width has been reduced as transition location is less sensitive to changing lift coefficient above and before the large transition location shift. Transition location standard deviation is then reduced by moving the two peaks away from the selected lift coefficient design range. This leaves the centre of the drag bucket with exceptionally low drag and transition location standard deviation.

7.3.3 Sensitivity to Uncertainty Standard Deviation

Figures 7.13 and 7.14 show the C_d mean and standard deviation polars when calculated with different critical N-factor standard deviation (N_σ) values. This is done to assess their sensitivity to the chosen value of N_σ. The results of this mirror those seen during single-point optimisation. Increasing N_σ causes $C_{d|\mu}$ and $C_{d|\sigma}$ to rise for both optimised aerofoils. In both cases, $C_{d|\mu}$ increases most at the upper end of the drag bucket, reducing its effective width. For both designs, increasing N_σ causes the peaks seen in $C_{d|\sigma}$ to grow in magnitude and move towards the same lift coefficient. The effect of increasing N_σ is stronger for the spike in drag corresponding to the upper surface transition location movement. As such, increasing the value of N_σ quickly reduces the robustness of drag to critical N-factor uncertainty at the upper end of the chose design range.

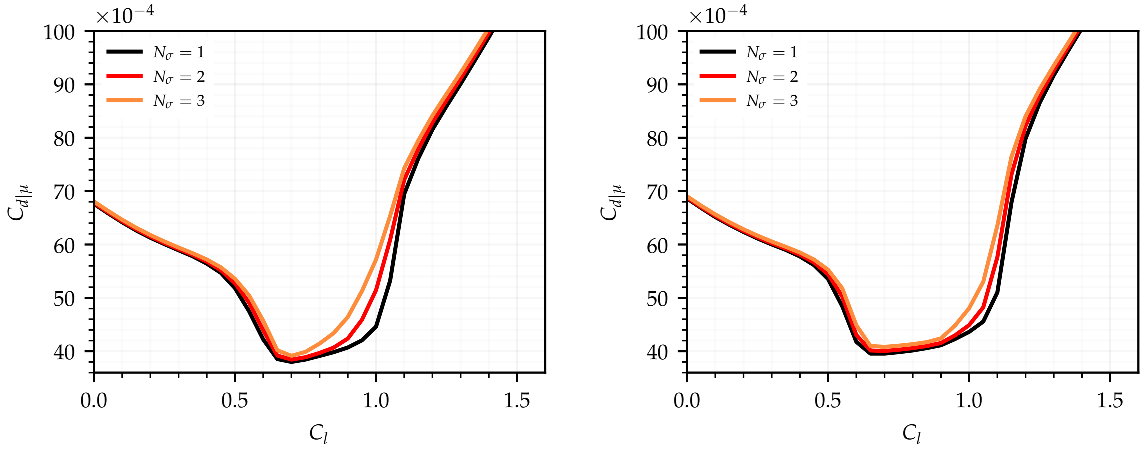

(a) *Design D* **(b)** *Design T*

Figure 7.13: *Mean drag polars for design D and T when calculated with critical N-factor standard deviation values of* $N_\sigma = 1, 2$ *and* 3.

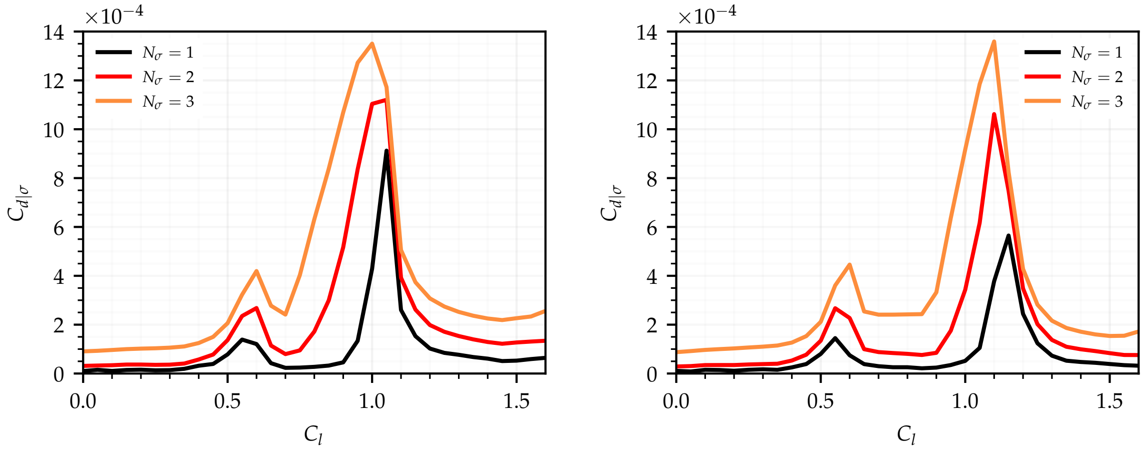

(a) *Design D* **(b)** *Design T*

Figure 7.14: *Drag standard deviation polars for design D and T when calculated with critical N-factor standard deviation values of* $N_\sigma = 1, 2$ *and* 3.

7.4 Transonic Results

A total of 4800 designs were produced during the optimisation, of which 3925 could be converged by CVGK at all three design points. Figure 7.15 shows convergence history of the two objective functions by plotting the optimum value of each over the course of the optimisation. Although a small improvement of 0.25 mean ML/D is found late in the optimisation at generation 89, good convergence is seen for both objectives. A trade-off between maximum mean ML/D and minimum mean $Tr_{u|\sigma}$ is found. Figure 7.16 shows mean ML/D and mean $Tr_{u|\sigma}$ for the entire population generated, with Pareto front designs highlighted.

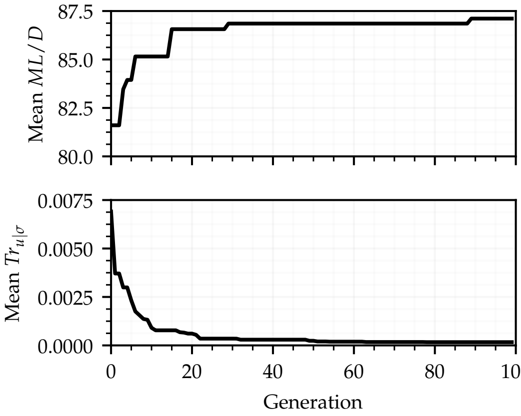

Figure 7.15: *The optimum objective function values found during the RAE2822 optimisation history.*

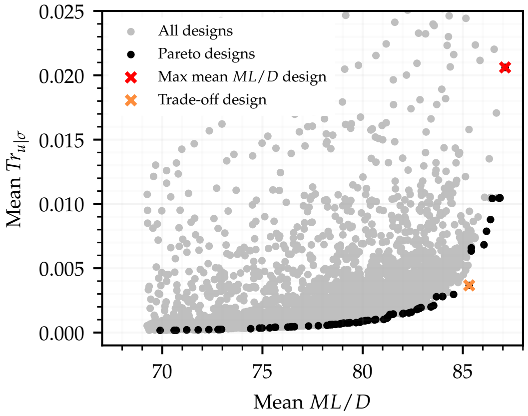

Figure 7.16: *Mean ML/D and mean $Tr_{u|\sigma}$ for all optimised designs with Pareto front and selected aerofoils highlighted.*

The Pareto front is similar in shape to that found during transonic single-point robust optimisation. Mean $Tr_{u|\sigma}$ has been reduced to near zero; however, these designs have the lowest mean ML/D. Mean ML/D can be increased by approximately 15 with only a $0.003x/c$ rise in $Tr_{u|\sigma}$, but increasing mean ML/D further causes $Tr_{u|\sigma}$ grow rapidly. A design at the corner of the Pareto front therefore represents a good trade-off between objectives. This design is highlighted on the Pareto front, along with the design with maximum mean ML/D. As was seen during the single-point robust optimisation, there are some gaps in the Pareto front. There are few designs found at high mean ML/D values, suggesting improvements around the maximum mean ML/D design may be possible as this design region is not well explored. This also suggests that $Tr_{u|\sigma}$ can be more easily improved than ML/D.

The objective function values for the RAE2822 and optimised design with maximum mean ML/D, minimum mean $Tr_{u|\sigma}$ and the trade-off design are shown in table 7.4. The constraint on mean ML/D has been effective as each optimised design has a higher ML/D value, while $Tr_{u|\sigma}$ has not been prevented from reducing. The minimum mean $Tr_{u|\sigma}$ design is at the constrained limit for mean ML/D; however, the minimum mean $Tr_{u|\sigma}$ found is so low that any additional improvements found by removing the constraint on mean ML/D would only produce aerofoils of little use to a designer. $Tr_{u|\sigma}$ has been reduced for the design with maximum mean ML/D, thus any Pareto front design is an improvement on the RAE2822 at the conditions selected.

Table 7.4: *Objective function values for the RAE2822 and optimised aerofoils with maximum mean ML/D, minimum mean $Tr_{u|\sigma}$ and a trade-off design.*

Design		Mean ML/D	Mean $Tr_{u\|\sigma}$
RAE2822		69.24	0.0531
Max mean ML/D	(D)	87.11 (+26%)	0.0206 (-61%)
Trade-off	(T)	85.32 (+23%)	0.0037 (-93%)
Min mean $Tr_{u\|\sigma}$		69.89 (+1%)	0.0002 (-99%)

7.4.1 Design Point Changes

The maximum mean ML/D and trade-off designs are selected for comparison against the RAE2822. There are denoted as designs D (deterministic) and T (trade) respectively. Figure 7.17 shows the design variable values and bounds on each surface for both optimised aerofoils. Variables 1 and 7 are towards the front of the aerofoil while variables 6 and 12 are at the rear. The design variable sign indicates if material is added or removed from the RAE2822. Based on the single-point transonic optimisation results, large upper limits were set for the upper surface design variables, and reduced lower bounds were given to the lower surface design variables. Designs D and T see similar deformation on the upper and lower surfaces. As expected, material is added on the upper surface and removed from the lower. As such, most design variables for both designs are away from the bounds. The exception to this is at the rear of the lower surface where both designs may benefit from wider lower bounds.

Figure 7.18 shows the aerofoil profiles for the RAE2822 and selected optimised designs with the grey shaded region indicating the viable design space as dictated by the design variable bounds. Both optimised designs are very similar in shape. The deformation seen on each surface has resulted in a camber increase. This is most pronounced towards the rear of the aerofoil. As the maximum thickness was constrained, it is the same for the RAE2822 and both optimised designs. Its chord-wise position has also not changed. The differences between optimised designs are found over the upper surface. Design D has larger thickness and increased upper surface curvature from $0 \rightarrow 0.2x/c$.

Figures 7.19, 7.20 and 7.21 show the pressure and N-factor envelopes for the RAE2822 and selected optimised aerofoils at each of the design points used during the optimisation. The increase in camber has reduced the angle of attack required to meet the target lift coefficient for both optimised designs. This is a reduction of approximately 1.7° at each of the design points. This reduces the initial pressure rise and allows for a long favourable pressure gradient over the front of the aerofoil, as seen in each of the previous optimisations cases. This has suppressed instability growth at each design point, extending laminar flow up to the shock position. The smaller pressure rise also reduces shock strength and delays the shock position. This reduces wave drag and viscous drag. As transition is shock induced, it is completely insensitive to critical N-factor near the ideal critical N-factor. This is seen on the transition envelopes as a vertical line extending up to the critical N-factor limit. It is important to note that these changes also cause a large increase in rear loading. As such, the mean moment coefficient has increased from $C_m = -0.097$ to $C_m = -0.178$ for design D and to $C_m = -0.177$ for design T.

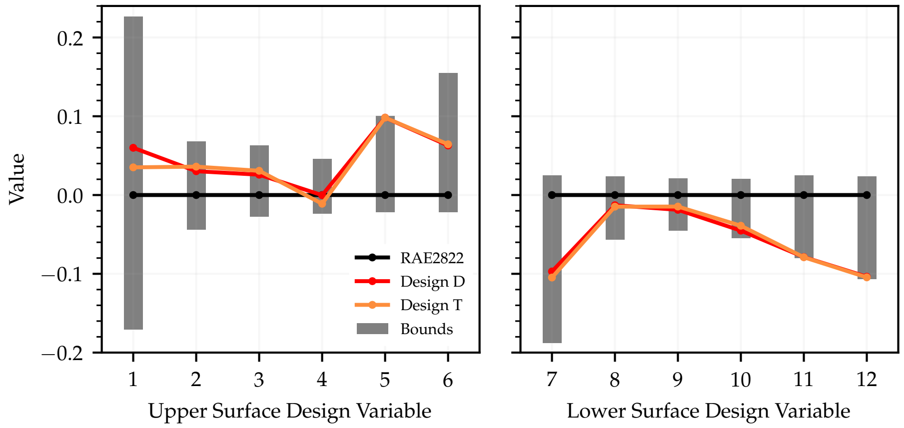

Figure 7.17: *Upper and lower surface design variable values and bounds for the RAE2822 and selected optimised designs.*

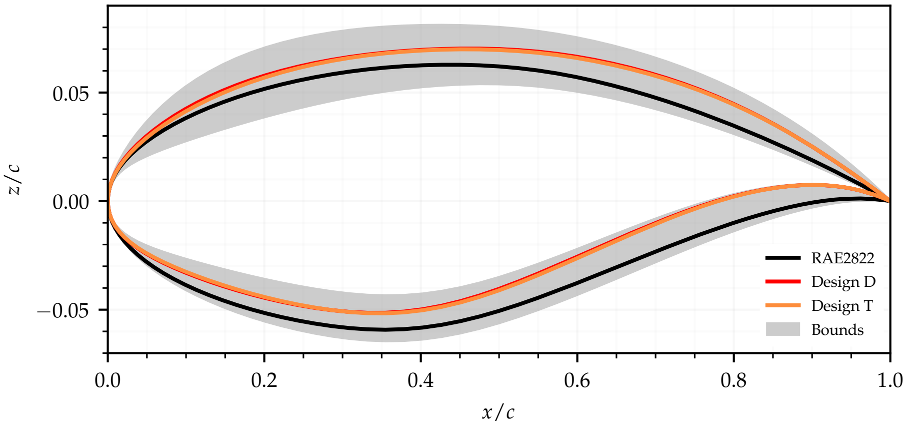

Figure 7.18: *Aerofoil profiles for the RAE2822 and selected optimised aerofoils, with the grey shaded region indicating the viable design space as dictated by the design variable bounds.*

The pressure distributions between designs differ most at the front of the upper surface. At design point 2, design D has a small region of adverse pressure before the shock. This helps to reduce shock strength and further delay the shock, therefore extending laminar flow. The region of adverse pressure, however, causes increased instability growth. While this is not enough to trigger early transition, transition location moves upstream with a smaller reduction in critical N-factor. Design T has a stronger pressure gradient up to the shock. This causes a stronger shock further upstream so the combined increase in wave drag and reduction in laminar length causes drag to increase by 3 counts. The benefit of this is the increased instability suppression obtained. Design T remains insensitive to critical N-factor changes down to $N_{cr} = 4$, and so has better transition location robustness.

At both the upper and lower design points, transition location is very robust to critical N-factor changes for designs D and T. Shock strength has been significantly reduced at the ideal critical N-factor for both designs at both points with drag for design D and design T being more than 10 counts lower than the RAE2822 at both design points.

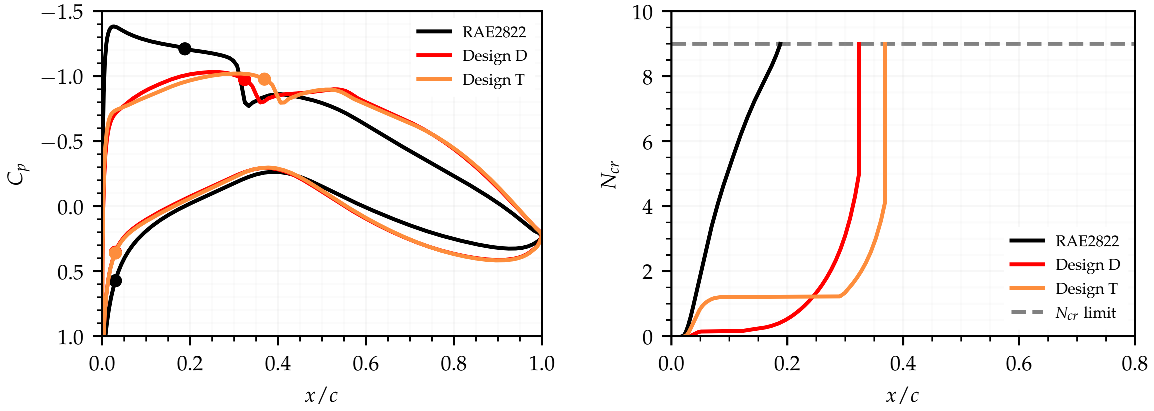

(a) *Pressure distributions* **(b)** *Transition envelopes*

Figure 7.19: *Pressure distributions and transition envelopes for the RAE2822 and selected optimised designs at design point 1 with* $M = 0.70$ *and* $C_l = 0.7829$.

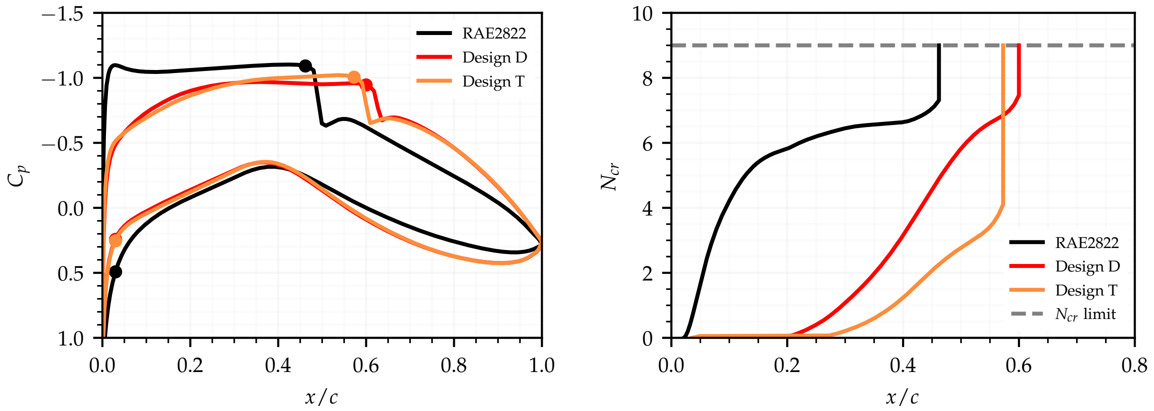

(a) *Pressure distributions* **(b)** *Transition envelopes*

Figure 7.20: *Pressure distributions and transition envelopes for the RAE2822 and selected optimised designs at design point 2 with* $M = 0.72$ *and* $C_l = 0.7400$.

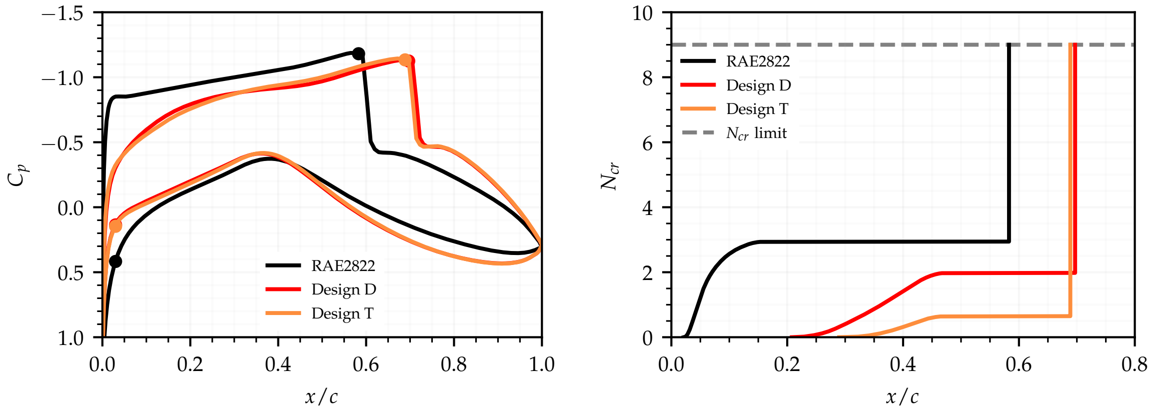

(a) *Pressure distributions* **(b)** *Transition envelopes*

Figure 7.21: *Pressure distributions and transition envelopes for the RAE2822 and selected optimised designs at design point 3 with* $M = 0.74$ *and* $C_l = 0.7005$.

7.4.2 Performance Polars

Figures 7.22 and 7.23 show the ideal, mean and standard deviation ML/D and Tr_u polars over the Mach range investigated for the RAE2822 and selected optimised designs. In each case, the mean and standard deviation of ML/D and Tr_u are found by running individual flow solutions at critical N-factor sample points taken every $N_{\text{step}} = 0.1$ from $N_{cr} = 9 \rightarrow 0$. This results in 91 samples per Mach number sample point over the Mach number range.

ML/D at the ideal critical N-factor is improved over the entire Mach range for both optimised designs. Design D has a higher ideal ML/D at and above $M = 0.72$, but design T has a higher ideal ML/D below. This is in part due to increased laminar flow on the upper surface of both optimised designs over the full Mach number range considered. The largest increase in laminar flow from the RAE2822 is found at $M = 0.70$. Transition on the RAE2822 occurs early here due to instability growth, as shown in figure 7.19a.

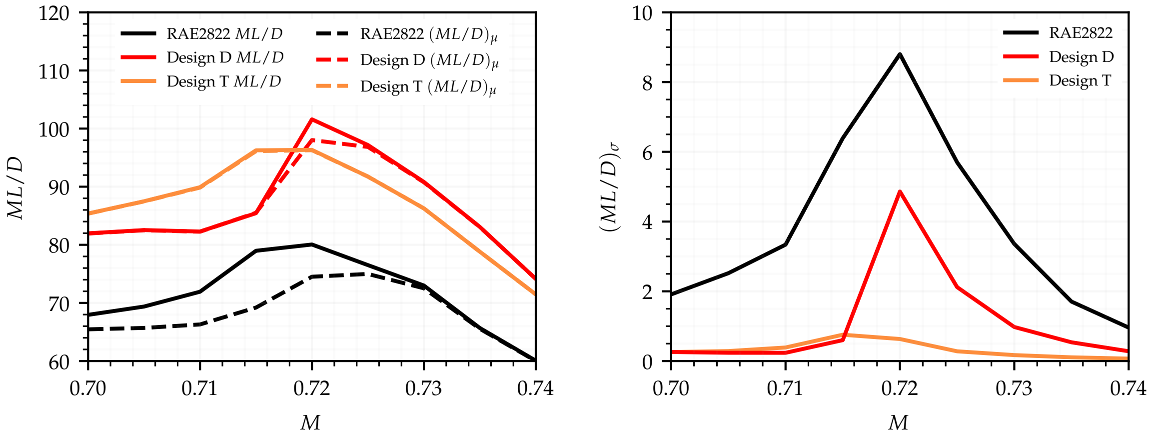

(a) *Ideal and mean performance* **(b)** *Performance standard deviation*

Figure 7.22: *ML/D polars for the RAE2822 and selected optimised designs.*

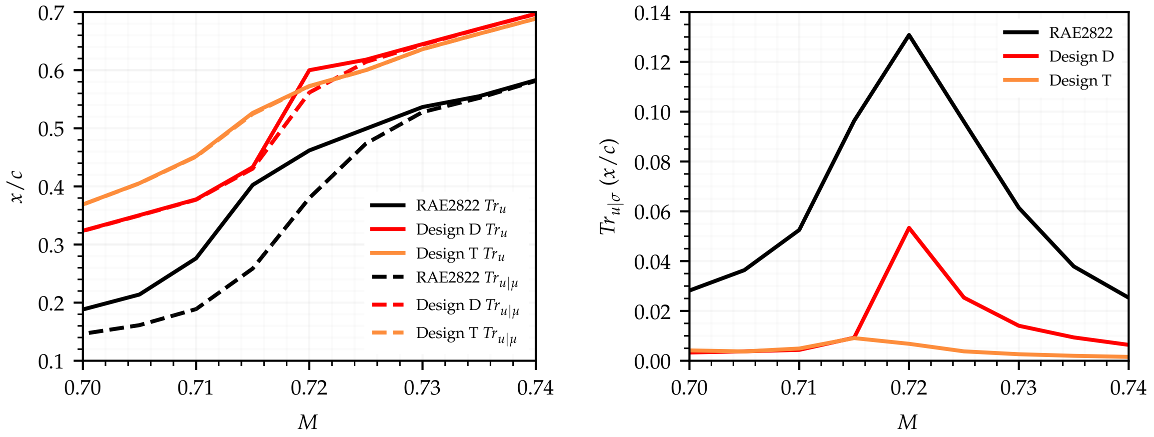

(a) *Ideal and mean performance* **(b)** *Performance standard deviation*

Figure 7.23: *Upper surface transition location polars for the RAE2822 and selected optimised designs.*

The RAE2822 has a large difference between ML/D at the ideal critical N-factor and mean ML/D. At $M = 0.72$ where $(ML/D)_{\text{max}}$ is found, mean ML/D is lower than the ideal ML/D by 5. This is due to low transition location robustness to critical N-factor. At $M = 0.72$, mean Tr_u is $0.08x/c$ further upstream than the value at the ideal critical N-factor. Mean ML/D is much closer to the ideal value for design D over the Mach range, with the exception of design point 2 at $M = 0.72$. Design D has extended Tr_u at the ideal critical N-factor here, but mean Tr_u is now worse than design T. As Design T has a near identical ideal and mean ML/D and Tr_u, both design T and design D have a similar maximum mean ML/D.

The ML/D and Tr_u standard deviation polars for each design clearly show this difference in design robustness to critical N-factor uncertainty. For each design, the ML/D and Tr_u standard deviation polars have a similar form. Standard deviation is lower for both optimised design; however, design D still has a spike in standard deviation at $M = 0.72$. Design T in comparison sees little to no standard deviation at all.

It is clear from these results that the trade-off design T is the better optimised design. While its performance at the ideal critical N-factor is marginally worse than Design D, its mean performance is comparable and its performance robustness is excellent over the entire Mach range.

7.4.3 Sensitivity to Uncertainty Standard Deviation

The sensitivity of stochastic performance to critical N-factor uncertainty standard deviation has again been assessed. ML/D mean and standard deviation polars for designs D and T are calculated at various values of N_σ and are shown in figures 7.24 and 7.25.

As N_σ is increased, mean ML/D changes little for design T but reduces substantially between $0.715 < M < 0.73$ for design D. At $M = 7.2$, increasing N_σ from 1 to 3 reduces mean ML/D by 6. This is understandable as design D has highly extended laminar flow at $M = 0.72$, but with instability amplification beginning $0.4x/c$ upstream. Thus, mean ML/D is reduced when N_σ is raised as the probability weighting at low critical N-factors is increased. This also causes ML/D standard deviation to grow as transition locations far upstream from the mean transition location have a higher probability weighting. Design D sees standard deviation rise the most at $M = 0.72$ and above as N_σ is increased. Again, upper surface transition location is highly extended at higher Mach numbers, but initial amplification occurs far upstream. In comparison, design T has delayed transition but early initial instability growth at low Mach numbers. As such, ML/D standard deviation rises the most at $M = 0.72$ and below when N_σ is increased. As the initial instability amplification is to a low N-factor at $M = 0.70$, the largest increase in ML/D standard deviation occurs when N_σ is increased from $2 \rightarrow 3$.

These results again show that the selection of N_σ does have a strong effect on the calculated stochastic values. However, the design selected for its robustness to critical N-factor uncertainty when calculated with $N_\sigma = 2$ was still found to be more robust than alternative designs at $N_\sigma = 3$.

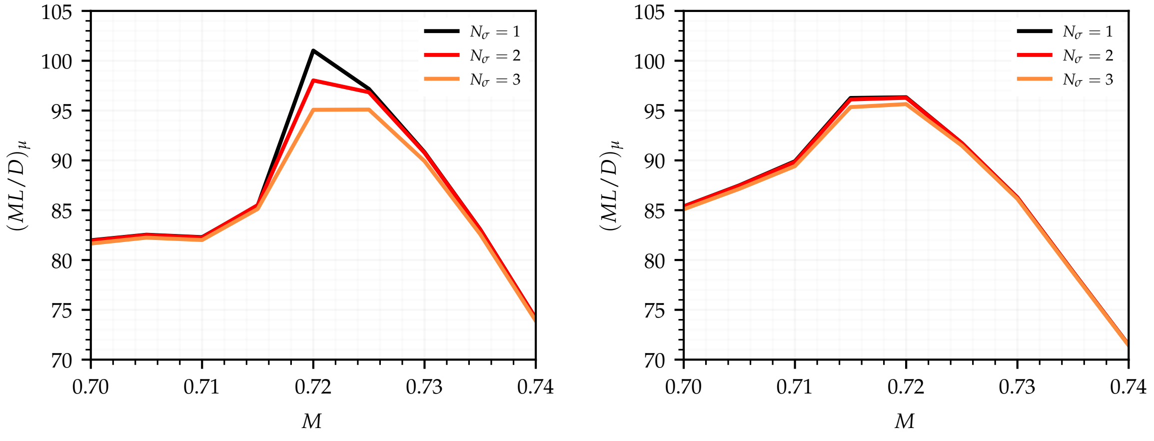

(a) *Design D* **(b)** *Design T*

Figure 7.24: *ML/D standard deviation polars for the RAE2822 and selected optimised designs at critical N-factor standard deviation values of* $N_\sigma = 1, 2$ *and* 3.

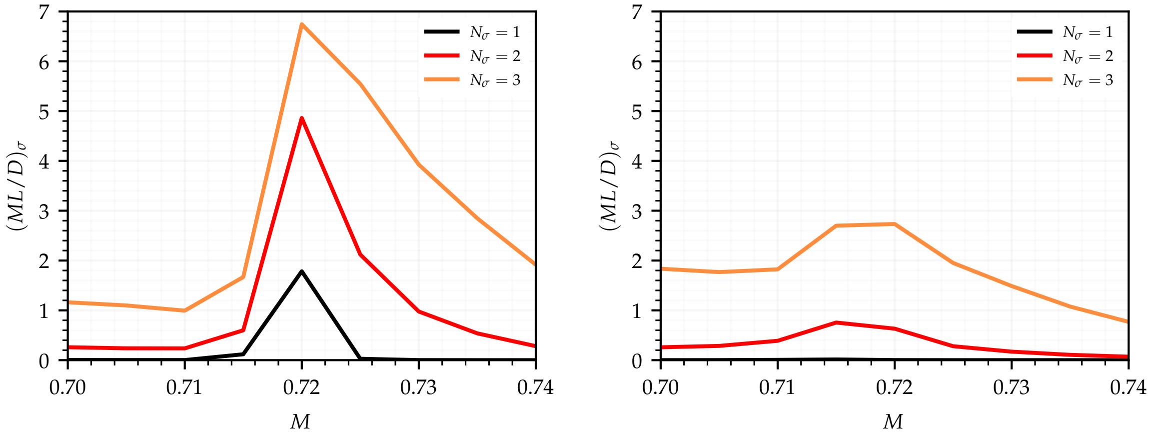

(a) *Design D* **(b)** *Design T*

Figure 7.25: *ML/D standard deviation polars for the RAE2822 and selected optimised designs at critical N-factor standard deviation values of* $N_\sigma = 1, 2$ *and* 3.

7.5 Summary

In this chapter, a computationally cheap method has been developed for the robust aerodynamic shape optimisation of NLF aerofoils with uncertainty in critical N-factor over a range of multi-point conditions. This has been accomplished by utilising the N-factor envelope, obtained from stability analysis of a single flow solution. Following this approach, the increased dimensionality of robust optimisation is avoided.

The accuracy of the envelope sampling method in providing transition location estimations from the N-factor envelope was assessed. The envelope sampling method is found to be accurate for subsonic speeds at a range of lift coefficients and for transonic speeds at a range of Mach numbers. Accuracy is found to be worst for designs that see transition location move rapidly over a small critical N-factor range located at a high critical N-factor. The envelope sampling method is, however, still able to obtain the correct trend in transition location mean and standard deviation and locate the Mach number value for maximum mean and standard deviation.

As such, this method was used to perform robust aerodynamic shape optimisation with critical N-factor uncertainty. This was done at subsonic conditions over a range of lift coefficients and at transonic conditions over a range of Mach numbers. In both cases, use of the envelope sampling method allowed for a range of designs to be obtained, trading deterministic performance for performance robustness. Using this Pareto front of designs, a trade-off aerofoil could be selected in each case that had a slightly reduced deterministic performance but comparable mean performance, and much improved performance robustness to critical N-factor uncertainty. Importantly, performance and performance robustness of the selected designs were maintained over the multi-point range selected for each optimisation case.

The sensitivity of performance mean and standard deviation to the chosen critical N-factor uncertainty standard deviation was also evaluated. The results of this showed that designs selected for better robustness at a certain uncertainty standard deviation also have better robustness when assessed with a different uncertainty standard deviation.

Chapter 8

Extension to Swept Flows

The assumption of two-dimensional flow over a wing can be made at locations away from three-dimensional flow sources such as the fuselage, propulsion system and wing-tip, on un-swept wings only. At high transonic speeds, however, wing sweep is required as it reduces the flow velocity normal to the wings leading edge, thus reducing shock strength and so wave drag. Many commercial transport aircraft have over 25° of leading edge wing sweep [157] as a result. Three-dimensional flows can have both crossflow (CF) and Tollmien-Schlichting (TS) instabilities. Transition is dominated by the former at sweep angles above 25° and becomes difficult to control passively via pressure gradient design. Further complications arise due to mixing of both instability types, effectively lowering the critical N-factor limit of each. This results in a complex design problem that is well suited to optimisation. Thus, the objectives of this chapter are to:

- Extend the multipoint robust optimisation method for swept wing aerofoil design.
- Apply this to optimisation of a typical narrow-body transonic swept wing.
- Investigate changes to the optimisation output by reducing wing sweep angle.

8.1 Methodology

The dual envelope strategy [12] is one of the preferred approaches used by the European aerospace industry for e^N stability analysis of three-dimensional flows [41, 51], and is the method implemented within CVGK. This involves the separation of TS and CF waves based on wave angle and a critical N-factor limit specified for each. An example of this is given in figure 8.1a, which shows individual TS and CF N-factor envelopes plotted against chordwise position with separate limits defined. These are commonly combined to produce an N_{ts} vs N_{cf} envelope plot, as shown in figure 8.1b. To account for interactions between the two instability types, a mixing region is defined. In practice this takes the form of a continuous curve on the N_{ts} vs N_{cf} plot, however to simplify implementation, it is described in CVGK using a linear relationship defined by points ($N_{cf,mix}$, N_{ts}) and (N_{cf}, $N_{ts,mix}$), as indicated in figure 8.1b.

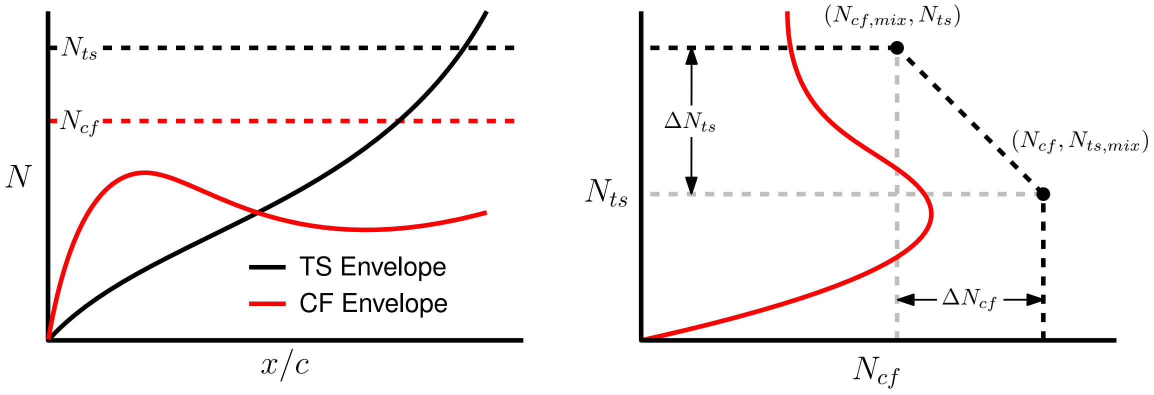

(a) *N against x/c envelope plot*

(b) *N_{ts} against N_{cf} envelope plot*

Figure 8.1: *Example of swept wing N-factor envelope plots.*

8.1.1 Calculation of Transition Envelope

Estimating transition locations at reduced critical N-factors using the information obtained from stability analysis requires some processing of the N-factor envelopes. The goal is to produce a single transition (Tr) envelope that gives the transition location at all N-factors below the critical N-factors used to obtain the original flow solution. Due to the additional CF instability N-factor envelope and instability mixing region, this requires more steps than for the two-dimensional method used in the previous chapter. Starting with the dual TS and CF N-factor envelopes, the steps required to calculate the transition envelope are shown schematically in figure 8.2 and described as follows:

1. Increase the N-factor values of the instability envelope with the smaller critical N-factor limit by the difference between the two critical N-factor limits. This results in both the TS and CF envelopes having the same N_{cr} limit.

2. Generate a mixing (Mx) envelope, defined as the distance N_{mx} of each (N_{cf}, N_{ts}) point from the line defined by the points $(N_{cf} - N_{cf,mix}, 0)$ and $(0, N_{ts} - N_{ts,mix})$. This is done using equation 8.1 and then normalised by the, now mutual, critical N-factor limit N_{cr}.

$$N_{mx} = \frac{|kN_{cf} + N_{ts} + \Delta N_{ts}|}{\sqrt{k^2+1}} \quad \text{where:} \quad k = \frac{\Delta N_{ts}}{\Delta N_{cf}} \tag{8.1}$$
$$\Delta N_{ts} = N_{ts} - N_{ts,mix} \qquad \Delta N_{cf} = N_{cf} - N_{cf,mix}$$

3. This results in three critical N-factor envelopes, one for TS instability waves, one for CF instability waves and a mixing envelope. These are of the same scale and have the same critical N-factor limit. The transition envelop is found from these by taking the furthest upstream chord-wise location of all envelopes for each critical N-factor value.

The transition location mean and standard deviation can then be calculated using equations 5.2 and 5.3 as outlined in chapter 7, with transition location estimations taken from the transition envelope.

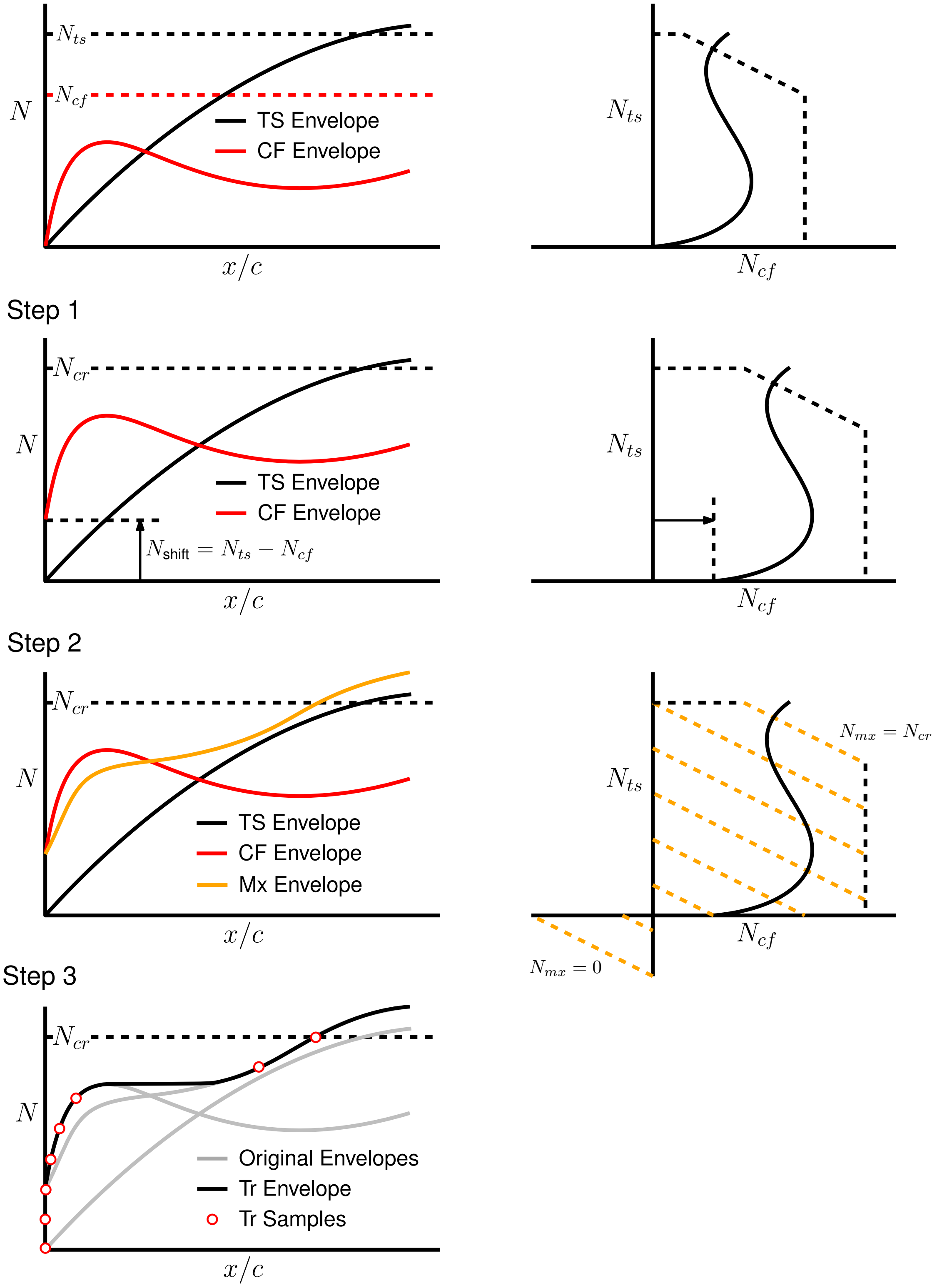

Figure 8.2: *Steps required to calculate the transition envelope from dual TS and CF instability N-factor envelopes obtained from stability analysis of a three-dimensional flow.*

8.1.2 Key Methodology Assumption

A key assumption of the envelope sampling method is again that transition locations estimated from the critical N-factor envelope are accurate. For the estimated transition locations to be accurate, the N-factor envelopes should not change as critical N-factor is reduced and transition location moves upstream. In reality, varying transition location will alter the aerofoil pressure distribution and lift coefficient to some degree. To obtain the same lift coefficient, a change in the angle of attack will be required, further affecting the pressure distribution and amplification of instabilities over the aerofoil. The greater this change in instability amplification, the less accurate the envelope sampling method will be for predicting transition locations at reduced critical N-factors.

To use the envelope sampling method, its accuracy in predicting mean and standard deviation of transition location must be assessed. Given that accuracy of the method may depend on critical N-factor envelope shape, the conditions under which the envelope sampling method is most and least accurate should also be highlighted. Although this has been done for two-dimensional flows, the inclusion of CF instability and interaction of instability types will affect the envelope sampling methods accuracy and so this must be checked.

8.2 NLF Wing Optimisation

This methodology has been used to perform robust shape optimisation of two swept wing test cases. The goal in each case is to reduce drag over a wing section via the extension of NLF while reducing variations in drag due to uncertainty in critical N-factor. The first optimisation case is of a high-sweep wing typical of a narrow-body commercial aircraft. As a high sweep angle is used, it is expected that the optimisation of this wing will struggle to obtain extended NLF due to strong CF amplification, especially inboard where Reynolds number will be highest due to the larger chord length. As such, the second optimisation case is of a low-sweep wing of comparable span, aspect ratio, area and two-dimensional Mach number. Due to the reduced sweep angle, it is expected that optimisation of this wing should obtain a larger extent of NLF over a wider span range.

8.2.1 Swept Wing Design

Both test cases are based on cruise flight conditions shown in table 8.1, which are similar to those of the Airbus A320-200 aircraft [157]. An aircraft weight of 64500kg and cruise altitude of $33,000$ft (10058m) are used, with atmospheric conditions taken from the International Standard Atmosphere. A cruise Mach number of $M = 0.78$ is selected. With a quarter chord wing sweep of 25°, the two-dimensional Mach number over the wing is $M_{2D} = 0.707$.

The high-sweep wing is also based on that of the Airbus A320-200 [157]. A wingspan of 34m is selected with an aspect ratio of 9.4, resulting in a wing area of 122.98m^2. Leading and trailing edge sweep angles of 28° and 16° are chosen, resulting in a quarter-chord wing sweep of 25°. From this, root and tip chord lengths are calculated as 5.699m and 1.535m respectively, resulting in a taper ratio of 0.27 and mean aerodynamic chord length of 4.017m. These values are summarised in table 8.2 and the wing planform is shown in figure 8.3a. The aircraft line-of-flight Mach number with this wing sweep is $M = 0.78$, and so aircraft lift

Table 8.1: *Typical narrow-body aircraft cruise properties and atmospheric conditions [157].*

Property	Value
Weight	64500 kg
Altitude	10058 m (37500 ft)
Mach Number (2D)	0.707
Temperature	222.77 °k
Density	0.40972 kg.m^{-3}
Dynamic Viscosity	1.466×10^{-5} Pa.s
Speed of Sound	299.21 m.s^{-1}

Table 8.2: *High-sweep wing properties.*

Property	Value
Wing Span	34.0 m
Aspect Ratio	9.4
Wing Area	122.98 m^2
Lead Edge Sweep	28°
Trailing Edge Sweep	16°
Quarter-chord Sweep	25°
Taper Ratio	0.27
Mean Chord	4.01 m

Table 8.3: *Low-sweep wing properties.*

Property	Value
Wing Span	34.0 m
Aspect Ratio	9.4
Wing Area	122.98 m^2
Lead Edge Sweep	20°
Trailing Edge Sweep	10°
Quarter-chord Sweep	17.5°
Taper Ratio	0.39
Mean Chord	3.851 m

coefficient at this speed, weight and wing area is calculated as $C_{l,ac} = 0.5254$. An elliptical loading distribution is used, as shown in figure 8.3b, resulting in lift coefficient and Reynolds number distributions over the wing as shown in figures 8.3c and 8.3d.

The low-sweep wing has reduced leading and trailing edge sweep angles of 20° and 10°, resulting in a quarter chord sweep of 17.5°. Root and tip chord lengths of 5.212m and 2.022m are selected to match the high-sweep wing area of $S_{ref} = 122.98\text{m}^2$. This results in a reduced mean aerodynamic chord length of 3.851m and increased taper ratio of 0.39. All wing properties are given in table 8.3. and the wing planform is shown in figure 8.3a. To obtain the same two-dimensional Mach number over the low-sweep wing, a reduced line-of-flight Mach number of $M = 0.741$ is used. At this speed, aircraft lift coefficient is calculated as $C_{l,ac} = 0.5818$. With an elliptical loading distribution, shown in figure 8.3b, lift coefficient and Reynolds number distributions are as shown in figures 8.3c and 8.3d.

Obtaining NLF over the entire wing span is not possible as turbulence from the fuselage, engine and pylon and strong span-wise flow at the wing-tip will all trigger early transition. The Airbus A320-200 has engine and pylon positioned approximately 5.75m outboard and a maximum nacelle width of approximately 2.4m [157]. Therefore, the span-wise range on each wing considered for optimisation is from 8 $\rightarrow$ 15m, as shown in figure 8.3a. This is 2.25m outboard of the pylon (1m outboard of the nacelle) and 2m inboard of the wing-tip.

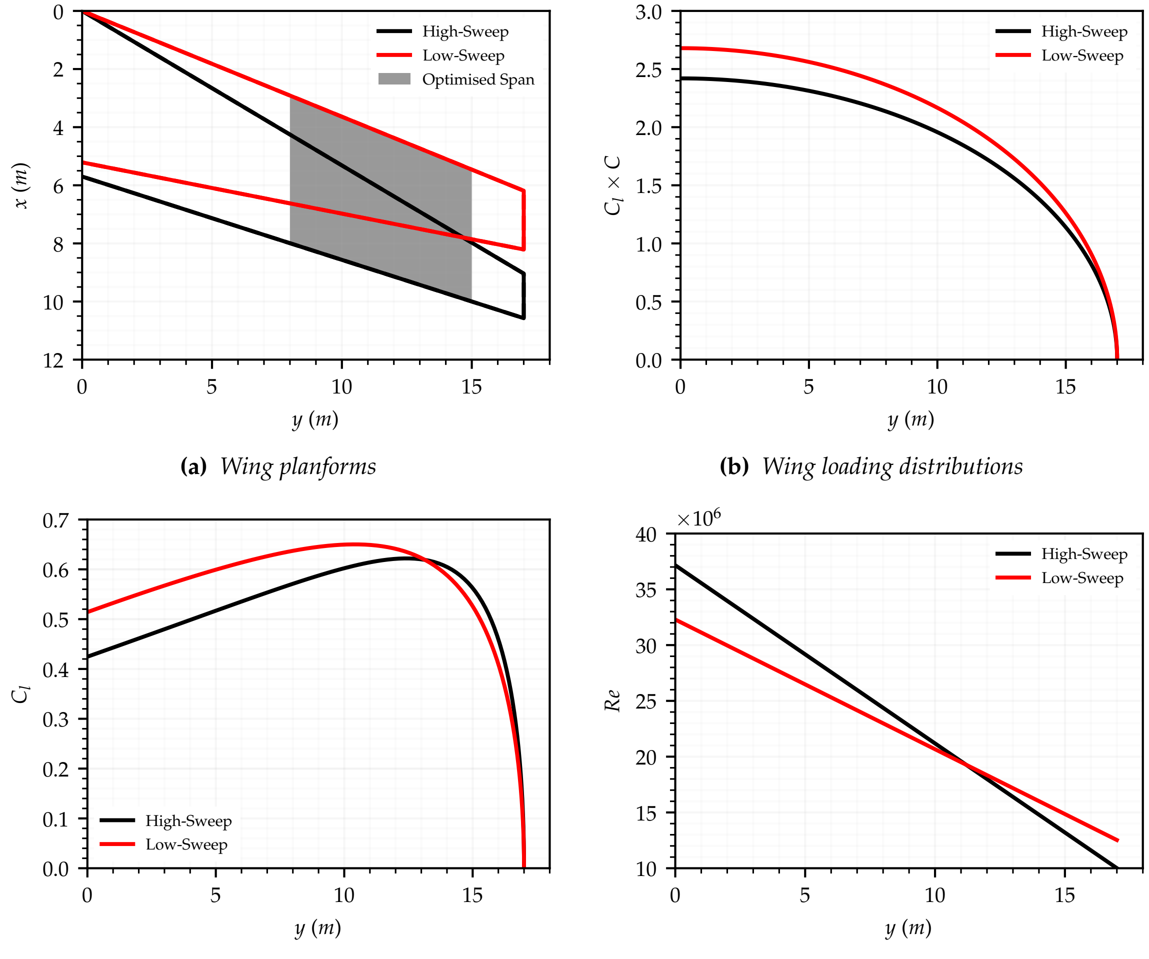

(a) *Wing planforms* **(b)** *Wing loading distributions*

(c) *Lift coefficient distributions* **(d)** *Reynolds number distributions*

Figure 8.3: *Planform and span-wise distribution of aerodynamic properties for the high and low-sweep wings.*

8.2.2 Problem Formulation

For each test case, multi-objective shape optimisation is carried out over three span-wise stations along the wing. Reynolds number and lift coefficient are fixed at each, with angle of attack left free. As such, the goal is to design a wing section of constant aerofoil shape but with variable twist along the span. The objective functions used in each case are maximisation of mean ML/D, maximisation of mean $Tr_{u|\mu}$ and minimisation of mean $Tr_{u|\sigma}$.

The three span-wise stations chosen for optimisation are, in each case, the inner and outer edges of the range where NLF can be obtained, and between this at the point of maximum target lift coefficient over the span. For the high-sweep case, the stations used during the optimisation are at outboard distances of 8m, 12.5m and 15m. For the low-sweep case, the three stations chosen are at 8m, 10.5m and 15m along the wing. The lift coefficient, Reynolds number and design point weighting at each span-wise station are shown for the high and low-sweep test cases in tables 8.4 and 8.5. In both cases, transition is left free on the upper surface but fixed at $0.03x/c$ on the lower surface for the reasons outlined in chapter 5.

Table 8.4: *Multi-point conditions and weights used for optimisation of the high-sweep wing.*

Point	Span	Weight	C_l	Re
1	8.0m	1.0	0.5710	24.38×10^6
2	12.5m	1.0	0.6219	17.19×10^6
3	15.m	1.0	0.5624	13.20×10^6

Table 8.5: *Multi-point conditions and weights used for optimisation of the low-sweep wing.*

Point	Span	Weight	C_l	Re
1	8.0m	1.0	0.6371	22.99×10^6
2	10.5m	1.0	0.6501	20.08×10^6
3	15.m	1.0	0.5260	14.85×10^6

Mean $Tr_{u|\mu}$ was included as an objective function as, with the extension to three-dimensional flow, designs may be found with large CF amplification towards the leading edge but with a highly extended Tr_u, and therefore large ML/D, at the ideal critical N-factor. Designs of this type will have both a large ML/D and small $Tr_{u|\sigma}$, but are naturally very undesirable as $Tr_{u|\mu}$ is extremely low. This issue was not seen during two-dimensional optimisation as TS instabilities have less leading edge amplification, although depending on the design conditions could also produce such designs. Including $Tr_{u|\mu}$ as an objective will push the optimiser to obtain designs with extended Tr_u at the ideal critical N-factor, but also over a wider N-factor range so as to increase $Tr_{u|\mu}$ and lower $Tr_{u|\sigma}$.

In each test case, the RAE2822 is used to derive an equivalent swept and tapered line of flight aerofoil which is used as the starting design. This is done using lock's equivalence laws [145] as implemented in ESDU 78009 [158] . Optimised designs are generated via deformation of the starting aerofoil using a perturbation profile. This is parametrised using the CST method, resulting in 6 design variables per surface, totalling 12 that are controlled by the optimiser.

Bounds are placed on each design variable so that a finite search space is defined. In both cases, a geometric constraint is used to ensure maximum aerofoil thickness of all optimised designs cannot reduce below $0.11z/c$. A constraint is also placed on mean ML/D, requiring that optimised designs have a value larger than that of the starting design in each optimisation case. The genetic algorithm optimisation method produces 48 designs per generation, and was set to run for a total of 150 generations. A mutation chance of 20 percent was used and crowding number was linearly increased from $\eta = 0 \rightarrow 20$ during the optimisation to initially aid in design space exploration and later in design convergence.

8.2.3 Critical N-factor Calibration

As the optimisation cases being considered represent a more realistic transonic design problem that includes both TS and CF instability types, accurate ideal TS and CF critical N-factor limits are needed. As the compressible e^N method is used, and both optimisation cases use a different line-of-flight Mach number, each must be calibrated separately.

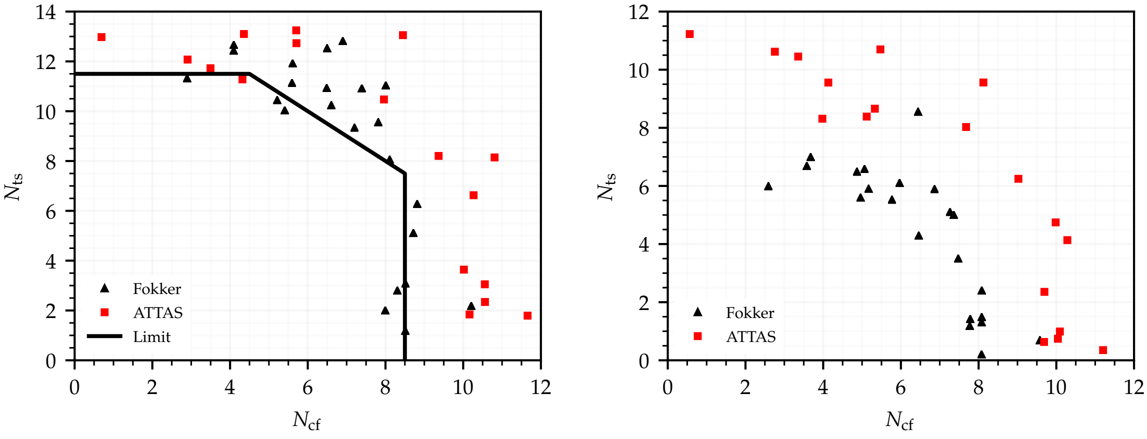

(a) *Incompressible*

(b) *Compressible*

Figure 8.4: *(N_{cf}, N_{ts}) data points calculated using incompressible and compressible linear stability theory with pressure distributions obtained from the Fokker 100 and ATTAS NLF glove flight tests [51].*

To obtain calibrated TS and CF critical N-factor limits, flow solutions for the starting aerofoil in each optimisation case first need to be obtained at each of the three span-wise stations using the incompressible e^N method. The incompressible critical N-factor limits used for this are obtained from the ATTAS and Fokker 100 flight test data [12], originally shown in figure 2.10a and repeated here in figure 8.4a. The limits chosen are $N_{ts} = 11.5$ and $N_{cf} = 8.5$, each with a mixing region spanning $\Delta N_{ts} = \Delta N_{cf} = 4$, as indicated in figure 8.4a.

Flow solutions should then be obtained using the compressible e^N method with TS and CF critical N-factor limits varied so as to match the transition locations found with the incompressible e^N analysis. These critical N-factor limits can then be used during the optimisation. During calibration, the size of the mixing region was left fixed as this does not vary significantly between the compressible and incompressible experimental results shown in figures 8.4a and 8.4b. Table 8.6 shows the calibrated critical N-factor limits for both the high-sweep and low-sweep optimisation test cases. Tables 8.7 and 8.8 show results of the calibration process for each test case. Shown on these two tables are the dominant instability type, incompressible and compressible upper surface transition locations and the minimum error between them at each span-wise position.

The calibrated critical N-factors that gave the smallest error for the high-sweep test case were found to be $N_{ts} = 5.9$ and $N_{cf} = 7.9$. The calibration process for the high-sweep wing case was helped as each span-wise station is dominated by a different instability type. As such, the CF instability limit was calibrated at 8m span, the TS instability limit calibrated at 15m span and the point between used as confirmation of a good match. The calibrated critical N-factors that gave the smallest error for the low-sweep test case are $N_{ts} = 6.0$ and $N_{cf} = 7.9$. In this case, TS instability amplification causes transition at all three span-wise points, which makes it difficult to estimate the CF critical N-factor limit. As CF instability amplification is far less sensitive to changes in Mach number than TS amplification when using the compressible e^N method, this was left at $N_{cf} = 7.9$.

Table 8.6: *Calibrated compressible e^N critical N-factor limits.*

Test Case	N_{ts}	N_{cf}	ΔN_{ts}	ΔN_{cf}
High-sweep	5.9	7.9	4.0	4.0
Low-sweep	6.0	7.9	4.0	4.0

Table 8.7: *Limiting instability type and transition locations found with incompressible and calibrated compressible e^N method at each spanwise station for the high-sweep optimisation case.*

Span	Limiting Instability	Incompressible Tr_u (x/c)	Compressible Tr_u (x/c)	Error
8.0m	CF	0.0296	0.0300	0.0004 (1.4%)
12.5m	Mixed	0.1245	0.1285	0.0040 (3.2%)
15.0m	TS	0.2414	0.2439	0.0025 (1.0%)

Table 8.8: *Limiting instability type and transition locations found with incompressible and calibrated compressible e^N method at each spanwise station for the low-sweep optimisation case.*

Span	Limiting Instability	Incompressible Tr_u (x/c)	Compressible Tr_u (x/c)	Error
8.0m	TS	0.0953	0.0939	0.0014 (1.5%)
10.5m	TS	0.1062	0.1027	0.0035 (3.3%)
15.0m	TS	0.2149	0.2150	0.0001 ($\approx$ 0%)

8.2.4 Validation of the Methodology

The envelope sampling methods accuracy in estimating transition locations for quantification of robustness to critical N-factor uncertainty has been assessed. This is done by comparing the upper surface transition location mean and standard deviation when calculated using transition locations from the envelope sampling method and from individual flow solutions run at a range of critical N-factor sample points. This has been carried out over the span being considered for optimisation for both high-sweep and low-sweep test cases using their respective starting aerofoil designs.

In both test cases, N_{cf} is the higher critical N-factor limit. The TS instability envelope is therefore shifted upwards so that N_{ts} and N_{cf} match, resulting in a common critical N-factor limit of $N_{cr} = 7.9$ for both test cases. Individual flow solutions are run every $N_{\text{step}} = 0.1$ from $N_{cr} = 7.9$ ($N_{ts} = 5.9/N_{cf} = 7.9$) down to $N_{cr} = 3.0$ ($N_{ts} = 1.0/N_{cf} = 3.0$) where instability mixing causes transition at its earliest possible position. The flow solution at $N_{cr} = 3.0$ with early transition is then replicated for sample points down to $N_{cr} = 0$. This is needed to match the critical N-factor range of the envelope sampling method.

The upper surface transition location mean and standard deviation values calculated with each approach are shown in figure 8.5 for the starting aerofoil used in the high-sweep test case. Figure 8.6 shows the same for the starting aerofoil used in the low-sweep test case.

As can be seen from the results of both test cases, the envelope sampling method is generally able to match the mean and standard deviation values found using individual flow solutions.

The agreement between methods is worst for mean transition location compared to transition location standard deviation, and is worse for both further outboard along the wing. As mean transition location is most extended here, this suggests that accuracy of the envelope sampling method is influenced by the amount of laminar flow present. The envelope method's accuracy in predicting transition location standard deviation appears insensitive to standard deviation value found. As mean upper surface transition location is not greatly extended over the span for both test cases, further validation is needed to determine if the envelope sampling method remains accurate when transition is highly extended over a wide critical N-factor range.

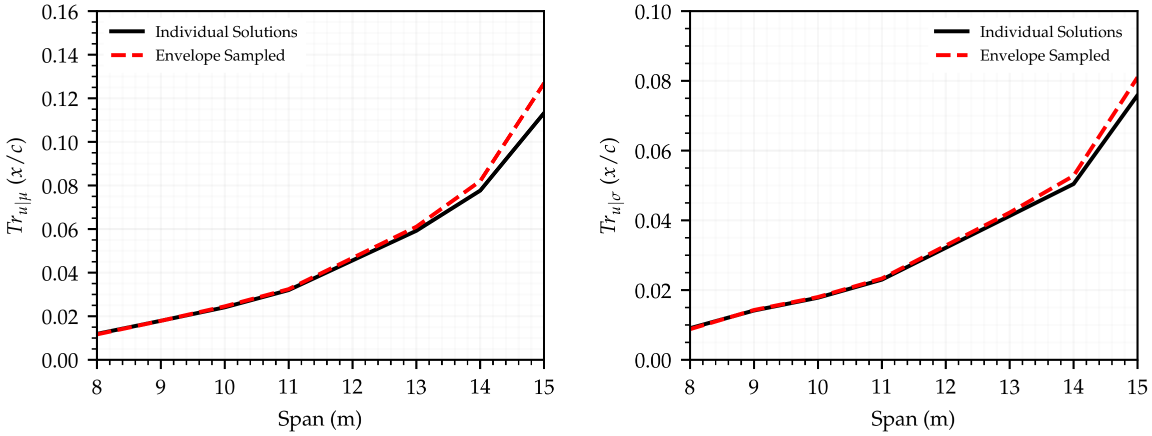

(a) *Mean* **(b)** *Standard Deviation*

Figure 8.5: *Upper surface transition mean and standard deviation calculated over the span using the envelope sampling method and from individual flow solutions for the high-sweep wing starting aerofoil*

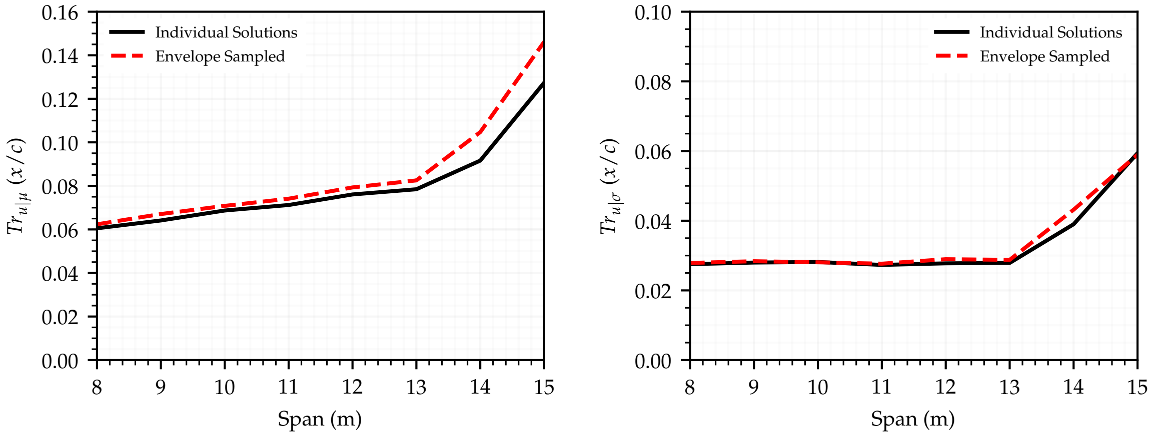

(a) *Mean* **(b)** *Standard Deviation*

Figure 8.6: *Upper surface transition mean and standard deviation calculated over the span using the envelope sampling method and from individual flow solutions for the low-sweep wing starting aerofoil.*

8.3 High-Sweep Optimisation Results

The high-sweep wing optimisation produced 7200 individuals, 5562 of which CVGK was able to converge at all three design points. Figure 8.7 shows the optimum mean value of ML/D, $Tr_{u|\mu}$ and $Tr_{u|\sigma}$ found over the optimisation history, compared against that of the starting design. Large improvements are found for each objective function within the first 25 generations. There is no increase in the maximum mean $Tr_{u|\mu}$ after generation 100, suggesting an optimum value is obtained. Small increases in mean ML/D and reductions in mean $Tr_{u|\sigma}$ continue to occur towards the end of the optimisation, suggesting further improvements in both may be possible. A trade-off is again found between objective functions. Figure 8.8 shows the resulting Pareto front, plotting mean $Tr_{u|\mu}$ against mean $Tr_{u|\sigma}$ with contours representing mean ML/D. Pareto front individuals are also highlighted.

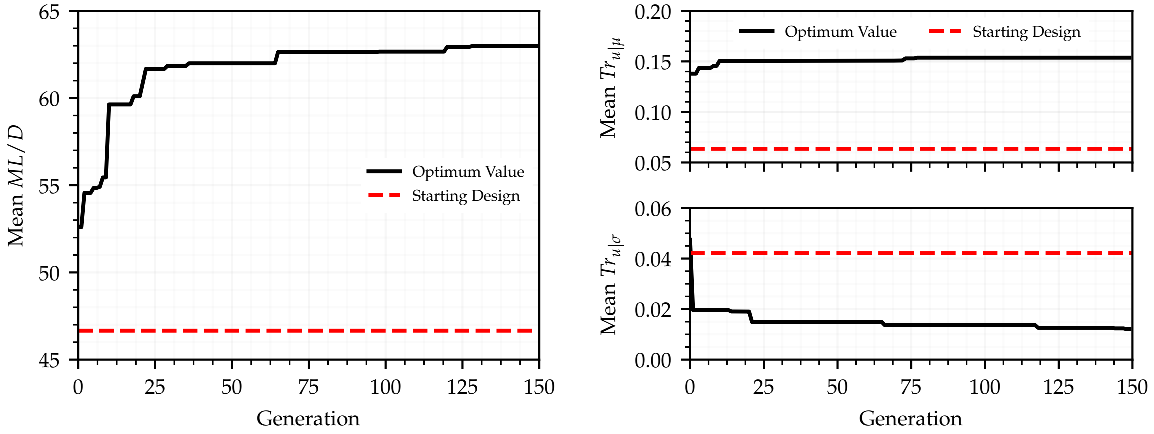

(a) ML/D **(b)** *Upper surface transition location*

Figure 8.7: *The optimum objective function values found during high-sweep wing optimisation history.*

There is a clear interdependence between mean $Tr_{u|\mu}$ and $Tr_{u|\sigma}$ seen on the Pareto front, where increasing one causes the other to rise. An increase in both would occur if the rise in $Tr_{u|\mu}$ comes from an increase in Tr_u over the critical N-factor range that moves Tr_u values away from the mean. This is expected as the high wing sweep should result in large CF amplification that would make it difficult to extended Tr_u anywhere but at critical N-factors close to the ideal value. Thus the increase in $Tr_{u|\mu}$ would come about from a large extension of Tr_u over a small critical N-factor range, increasing $Tr_{u|\sigma}$ in the process.

The lower edge of the contour region therefore represents the best possible trade-off between mean $Tr_{u|\mu}$ and $Tr_{u|\sigma}$. This ideal trade-off is worse at higher $Tr_{u|\mu}$ values, suggesting high $Tr_{u|\mu}$ values can only be obtained by a large increase in Tr_u over a small N-factor range. Mean ML/D is found to be higher for designs away from the lower edge. Therefore, at a fixed $Tr_{u|\sigma}$ value, ML/D can be increased at the cost of $Tr_{u|\mu}$. This represents a trade-off between deterministic and probabilistic performance and is often seen. The design with maximum mean ML/D is both away from the lower edge and does not have the maximum mean $Tr_{u|\mu}$ for this reason. Obtaining the largest $Tr_{u|\mu}$ does not result in the largest Tr_u, although its value is still high.

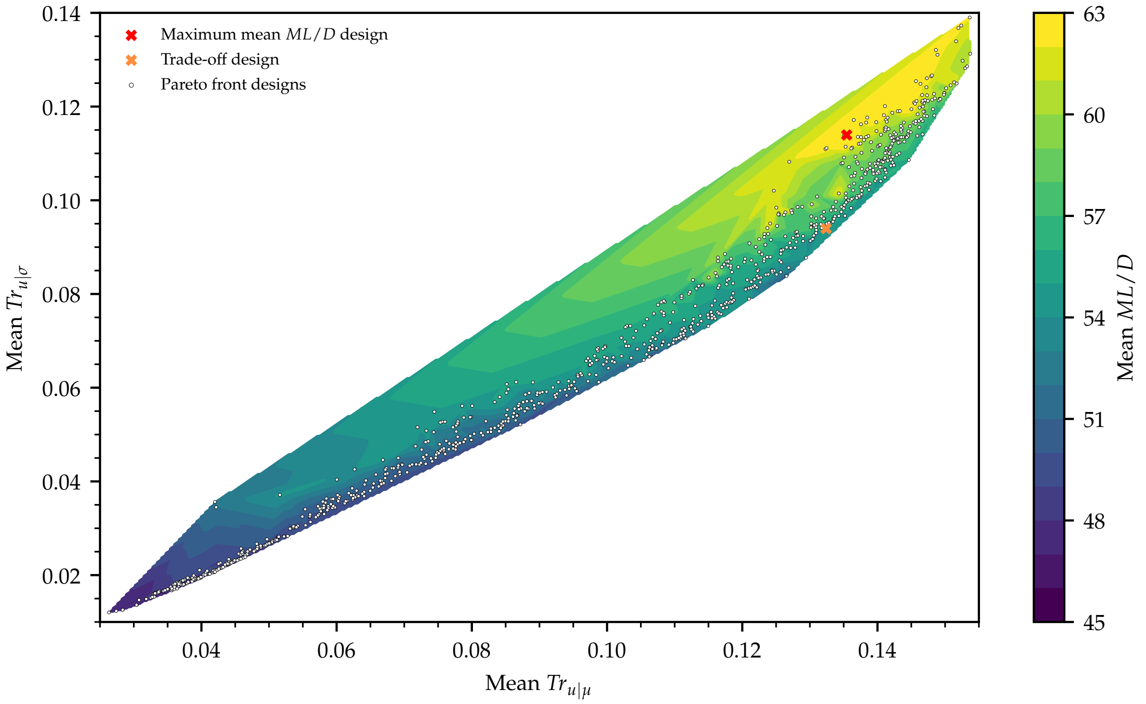

Figure 8.8: *Contour plot of the Pareto front found between objective functions during optimisation of the high-sweep wing.*

To get a better understanding of the contributions to the Pareto front from each span-wise design point, figure 8.9 shows the value of $Tr_{u|\mu}$ and $Tr_{u|\sigma}$ for each of the Pareto front designs at each of the three span-wise positions. No design on the Pareto front has extend laminar flow at 8m span as the high Reynolds number here produce strong instability amplification.

Extended laminar flow can be found at 12.5m and 15m span as Reynolds number reduces outboard. The largest extent of laminar flow is possible at 15m span and the trade-off between $Tr_{u|\mu}$ and $Tr_{u|\sigma}$ is also best here. The relationship between $Tr_{u|\mu}$ and $Tr_{u|\sigma}$ is close to linear, where an increase in $Tr_{u|\mu}$ causes a 0.77× increase in $Tr_{u|\sigma}$. At 12.5m span, an increase in $Tr_{u|\mu}$ when below $0.14x/c$ leads to an 0.81× increase in $Tr_{u|\sigma}$. Above $Tr_{u|\mu} = 0.14x/c$, $Tr_{u|\sigma}$ increases more rapidly. This causes the worsening trade-off between mean $Tr_{u|\sigma}$ and mean $Tr_{u|\mu}$ seen on the Pareto front above $Tr_{u|\mu} = 0.13x/c$.

Figure 8.10 provides a breakdown of the $Tr_{u|\mu}$ contribution from each span-wise station to the mean $Tr_{u|\mu}$ over the three positions. As little laminar flow is found at 8m span, the value of mean $Tr_{u|\mu}$ comes almost exclusively from $Tr_{u|\mu}$ at 12.5m and 15m span. Designs with mean $Tr_{u|\mu} > 0.13$ have extended $Tr_{u|\mu}$ at both span-wise positions, although $Tr_{u|\mu}$ is extended most at 15m span. Designs with a mean $Tr_{u|\mu}$ below this can be placed into two groups. One group of designs extends $Tr_{u|\mu}$ at 15m span as much as possible, which results in little $Tr_{u|\mu}$ at 12.5m. This is beneficial as a better trade-off between $Tr_{u|\mu}$ and $Tr_{u|\sigma}$ is found at 15m span. The other set of designs have a more balanced amount of $Tr_{u|\mu}$ at 12.5m and 15m span. The majority of designs in this group have a high mean $Tr_{u|\mu}$ as this approach is required to obtain the maximum mean $Tr_{u|\mu}$.

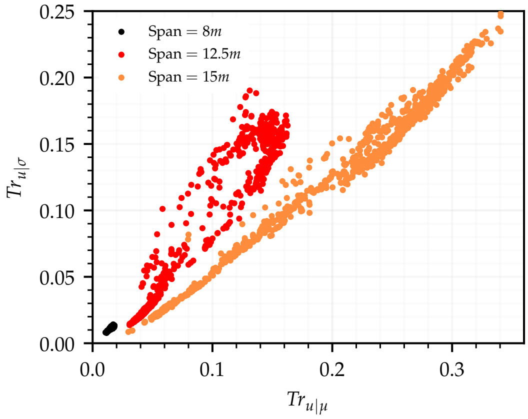

Figure 8.9: *$Tr_{u|\mu}$ and $Tr_{u|\sigma}$ at each span-wise design point for all Pareto front designs.*

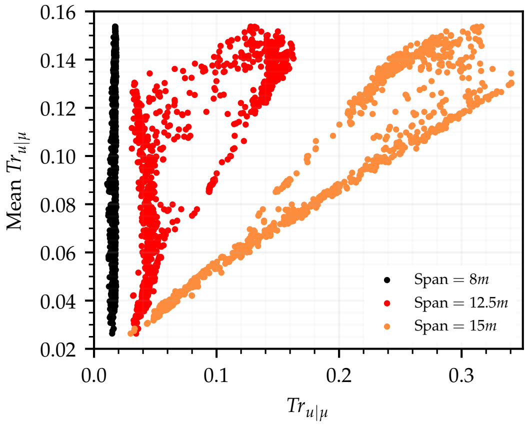

Figure 8.10: *The value of $Tr_{u|\mu}$ at each span-wise design point for the corresponding mean $Tr_{u|\mu}$ for each Pareto front design.*

Table 8.9 shows objective function values for the starting design, the designs with maximum mean ML/D, maximum mean $Tr_{u|\mu}$, minimum mean $Tr_{u|\sigma}$ and a trade-off between objectives. The trade-off design is selected from the lower edge of the contour region on the Pareto front. This represents the best trade between $Tr_{u|\mu}$ and $Tr_{u|\sigma}$, having a similar $Tr_{u|\mu}$ as obtained by the design with maximum mean ML/D but with a reduced mean $Tr_{u|\sigma}$.

As minimum mean ML/D was constrained during the optimisation, it has increased for each of the selected optimised designs. Each of the optimised designs shown on table 8.9 also has an increased mean $Tr_{u|\mu}$ compared to the starting aerofoil, except for the design with minimum mean $Tr_{u|\sigma}$. Mean $Tr_{u|\mu}$ was unconstrained and so many designs on the Pareto front have a value far below that of the starting aerofoil. Although these all obtain a larger ML/D than the starting design, their mean performance is likely too poor to be of use.

While a constraint on mean ML/D was effective during two-dimensional optimisation with low instability amplification, it appears a further constraint on mean $Tr_{u|\mu}$ is needed to avoid poor designs and wasted computational resources for three-dimensional problems. For two-dimensional flows, TS instability amplification is more gradual and so the optimiser is able to reduce $Tr_{u|\sigma}$ by either suppressing TS growth, and so having highly extended laminar flow, or by inducing transition at the leading edge due to formation of a shock. The latter case was prevented by the constraint on ML/D. For three-dimensional flows, the optimiser is able to produce very early transition over most of the critical N-factor range with strong CF instability growth, but can then obtain extended laminar flow at the ideal critical N-factor. This results in a low mean $Tr_{u|\sigma}$ and $Tr_{u|\mu}$, but high mean ML/D.

Each of the optimised designs on table 8.9 except the design with minimum mean $Tr_{u|\sigma}$ has a larger $Tr_{u|\sigma}$ than the starting aerofoil. As $Tr_{u|\mu}$ and $Tr_{u|\sigma}$ are linked, these designs must see a $Tr_{u|\sigma}$ rise for any increase in $Tr_{u|\mu}$. The starting design has a small mean $Tr_{u|\mu}$ and so the $Tr_{u|\sigma}$ is also low. This indicates that its performance was poor but its robustness to critical N-factor good. Thus, an improvement in deterministic and mean performance requires that $Tr_{u|\sigma}$ increase. This again highlights the issue with only reducing standard deviation.

Table 8.9: *Objective function values for the starting design, optimised aerofoil with maximum mean ML/D, trade-off design and optimised designs with maximum mean $Tr_{u|\mu}$ and minimum mean $Tr_{u|\sigma}$.*

Design		Mean ML/D	Mean $Tr_{u\|\mu}$	Mean $Tr_{u\|\sigma}$
Starting		46.66	0.0636	0.0421
Max mean ML/D	(D)	62.97 (+34%)	0.1354 (+113%)	0.1139 (+171%)
Trade-off	(T)	55.14 (+18%)	0.1324 (+108%)	0.0940 (+123%)
Max mean $Tr_{u\|\mu}$		59.98 (+29%)	0.1537 (+142%)	0.1313 (+212%)
Min mean $Tr_{u\|\sigma}$		46.96 (+1%)	0.0263 (-59%)	0.0120 (-71%)

8.3.1 Design Point Changes

The optimised trade-off design and the optimised design with maximum mean ML/D are selected for a more detailed comparison against the unoptimised starting design. The design with maximum mean ML/D is denoted as design D (deterministic), while the trade-off design is labelled design T (trade).

Figure 8.11 shows the design variable bounds and values for the starting and selected optimised designs. These are split into upper and lower surface, where design variables 1 and 7 are towards the front of the aerofoil, and 6 and 12 are towards the tail. Positive values indicate material is added to the starting design while negative values indicate material is removed. Bounds were chosen that allowed for an increase in camber and rear loading as both were features observed in the transonic robust multi-point optimisation results of the previous chapter. Additionally, large bounds were given to design variables 1 and 7. This was done to give the optimiser good control over the leading edge shape which strongly effects CF amplification. On the upper surface, design variables for both optimised designs are far from the bound with the exception of variables 3 and 4 which were kept tight. Design variables on the lower surface, however are much closer. In particularly, towards the trailing edge where both optimised designs are close to or at the lower limits.

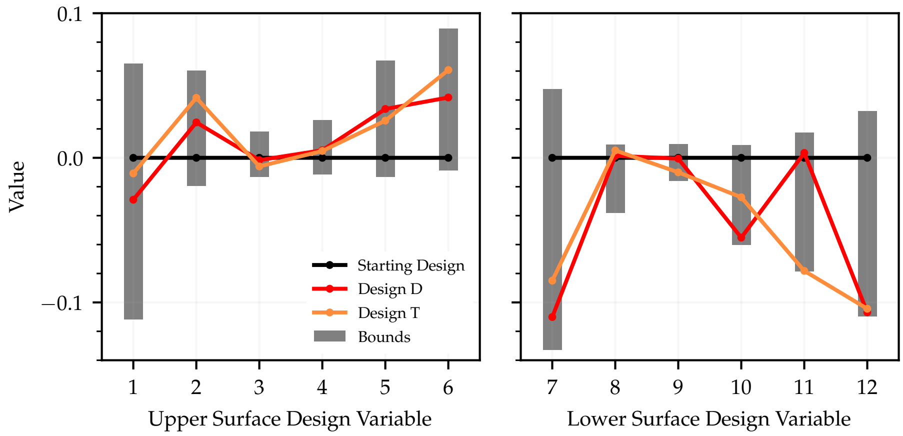

Figure 8.11: *Upper and lower surface design variable values and bounds for the starting and selected optimised designs.*

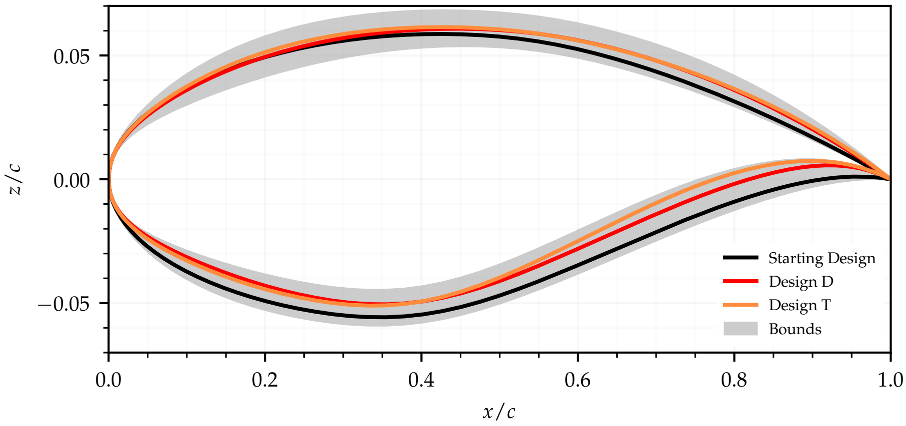

Figure 8.12: *Aerofoil profiles for the starting and selected optimised designs with grey shaded region indicating the viable design space as dictated by the design variable bounds.*

Figure 8.12 shows the aerofoils and viable design region as dictated by the design variable bounds for the starting and selected optimised designs. Maximum thickness for the starting design was $0.1137z/c$. This has been reduced to the constrained limit of $0.1100z/c$ for both optimised designs. This reduction in thickness occurs on the lower surface, increasing camber, lift generation and lowering the angle of attack both optimised designs use at all three design points. This reduces the leading edge pressure rise and so allows for a favourable pressure gradient over the front of the aerofoil. This, in turn, reduces shock strength, wave drag and helps to suppress TS instability amplification, as seen in figures figures 8.13, 8.14 and 8.15 showing pressure distributions and N_{ts} versus N_{cf} envelopes for the starting and selected optimised designs at each of the design points.

Material is removed from the leading edge of both optimised designs, leading to a small reduction in leading edge radius and causing a slightly faster leading edge pressure rise. CF amplification is reduced at each design point as a result. This has little effect on transition location at 8m span where leading edge transition occurs due to CF amplification, but does have an effect at the other two design points. At 8m span, the optimiser is either unable to reduce CF amplification, or doing so would cause a larger reduction of laminar flow elsewhere. Regardless, extended laminar flow is not viable inboard at the current sweep angle and flight conditions.

Design D has a smaller increase in trailing edge camber so operates at a slightly larger angle of attack. This allows for a more gradual and further extended favourable pressure gradient, resulting in the most delayed transition of all three designs at the ideal critical N-factor. However, instabilities have been suppressed only enough to extend laminar flow at this critical N-factor, and so transition moves upstream rapidly as critical N-factor is reduced. This is most apparent at 12.5m span where the N-factor envelope of design D skirts close to the critical N-factor limit but fails to trigger transition until further downstream.

Envelopes of this type see transition jump far upstream with only a small reduction in critical N-factor. This can be seen in figure 8.16 showing, at each design point, transition envelopes for the starting and optimised designs. Only values down to $N_{cr} = 3$ are shown as

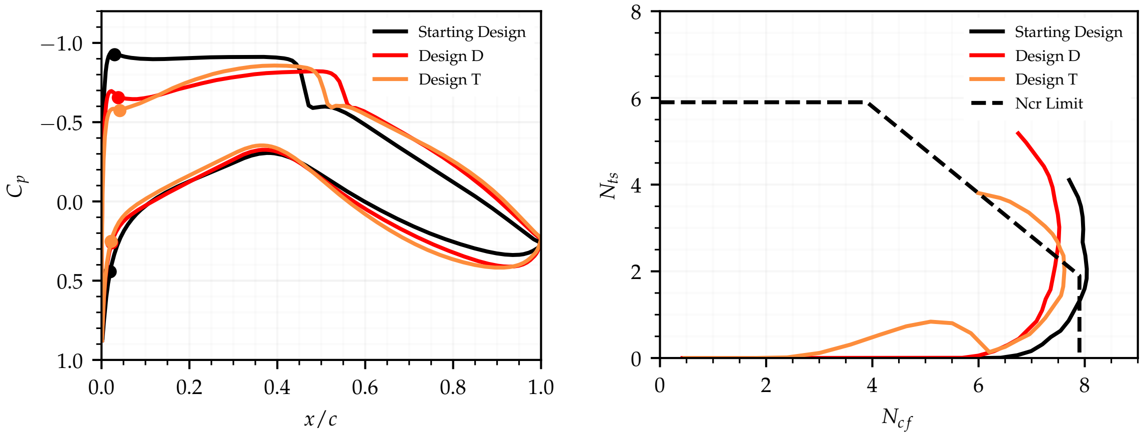

(a) *Pressure Distribution* **(b)** *N_{ts} vs N_{cf} envelope*

Figure 8.13: *Ideal critical N-factor performance of the starting and selected optimised designs span* $= 8m$.

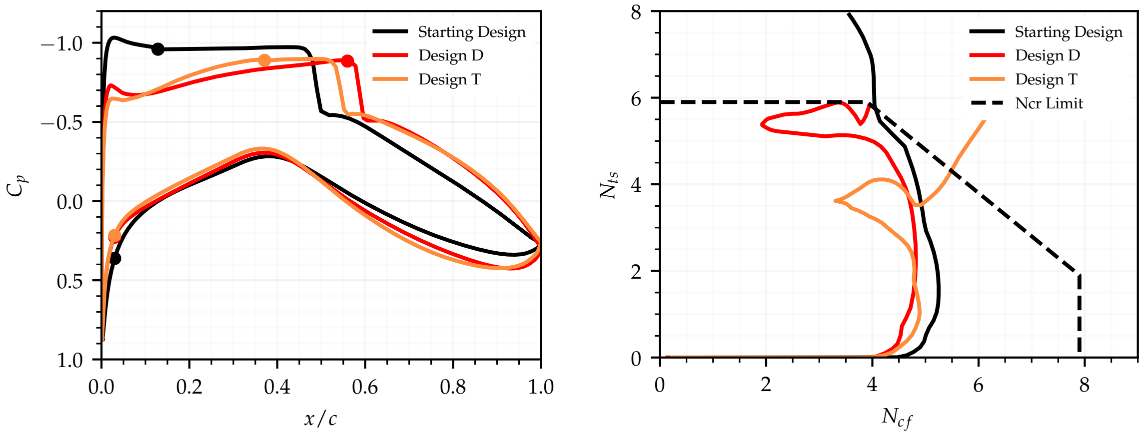

(a) *Pressure Distribution* **(b)** *N_{ts} vs N_{cf} envelope*

Figure 8.14: *Ideal critical N-factor performance of the starting and selected optimised designs span* $= 12.5m$.

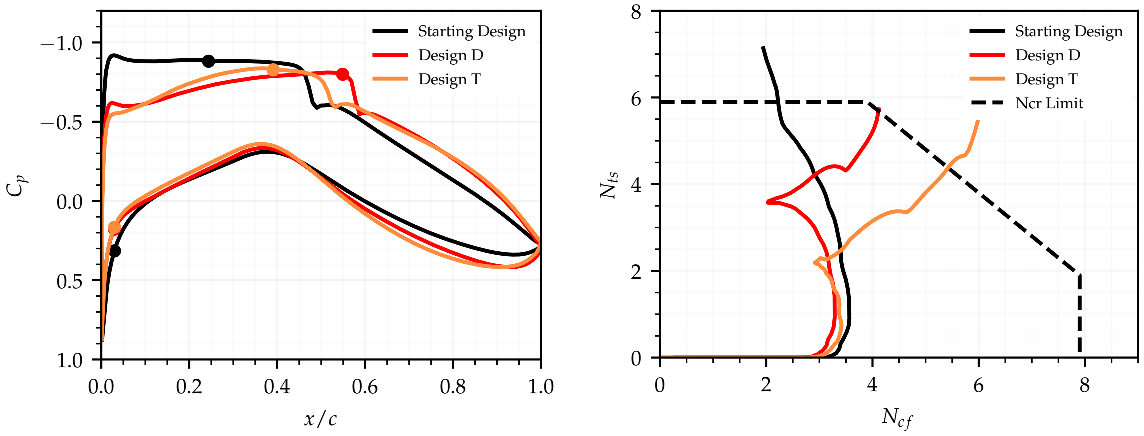

(a) *Pressure Distribution* **(b)** *N_{ts} vs N_{cf} envelope*

Figure 8.15: *Ideal critical N-factor performance of the starting and selected optimised designs span* $= 15m$.

below this, transition occurs at the leading edge due to instability mixing. This is clearly undesirable behaviour; however, designs of this type obtain a high ML/D and low $Tr_{u|\sigma}$. This is because, with the exception of Tr_u at the ideal critical N-factor, Tr_u is close to the leading edge with mean $Tr_{u|\mu}$. As $Tr_{u|\mu}$ is very low, these designs are undesirable and so a constraint on $Tr_{u|\mu}$ would help avoid their creation. As the N-factor envelope of design D is close to the limit, the small CF amplification reduction does help to increase both Tr_u and $Tr_{u|\mu}$.

Design T has increased trailing edge camber almost as far as allowed by the design variable bounds, and so operates at the lowest angle of attack. It thus has the smallest leading edge pressure rise and most favourable pressure gradient. TS amplification at transition is lowest for this design. Transition now occurs due to TS and CF instability mixing as both amplify at a similar rate. The N-factor envelope now moves towards the mixing limit in a direction normal to the mixing limit. As such, transition moves upstream more gradually as critical N-factor is reduced at both 12.5 and 15m span, as seen in figures 8.16b and 8.16c. This is a desirable feature and is indicative of a robust design. The same is seen for design D at 15m span but to a lesser extent.

Overall, the optimiser has attempted to reduce CF amplification as much as possible on both designs to help increase both ML/D and $Tr_{u|\mu}$, but struggles due to the high sweep angle. The same two-dimensional NLF design methods are then used by the optimiser to reduce TS amplification. To improve robustness to critical N-factor uncertainty, camber is increased further to lower angle of attack and strengthen the favourable pressure gradient. As expected, improving stochastic performance requires some deterministic performance loss. Robust designs also see neither instability type dominating transition as transition instead occurs due to instability mixing. This prevents transition from jumping upstream as critical N-factor reduces. Thus, a trade-off between CF and TS instability suppression is needed.

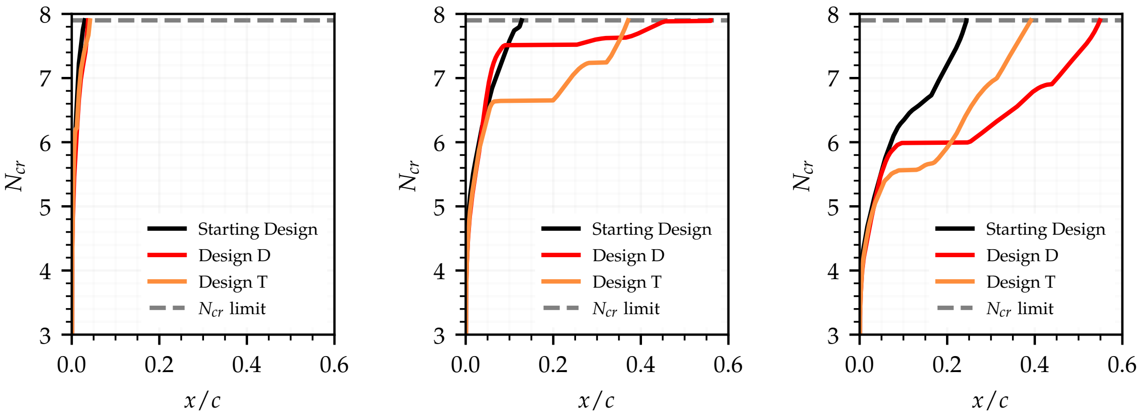

(a) *Span* = 8*m* **(b)** *Span* = 12.5*m* **(c)** *Span* = 15*m*

Figure 8.16: *Transition envelopes for the starting and selected optimised designs at each span-wise station.*

8.3.2 Additional Validation of the Methodology

Accuracy of the $Tr_{u|\mu}$ and $Tr_{u|\sigma}$ values calculated using transition locations obtained from the envelope sampling method is assessed using design D and design T. $Tr_{u|\mu}$ and $Tr_{u|\sigma}$ for both optimised designs are compared when calculated using the envelope sampling method and from individual flow solutions run at multiple critical N-factor sample points. As with previous validation of the envelope sampling methodology, individual flow solutions are run every $N_{\text{step}} = 0.1$ from $N_{cr} = 7.9$ down to $N_{cr} = 3.0$ where transition occurs at the leading edge. The flow solution at $N_{cr} = 3.0$ with leading edge transition is then replicated for sample points down to $N_{cr} = 0$. This has been carried out at 1m intervals over the span, and at the 12.5m span design point. Figures 8.17 and 8.18 shows $Tr_{u|\mu}$ and $Tr_{u|\sigma}$ for design D and design T when calculated using each approach.

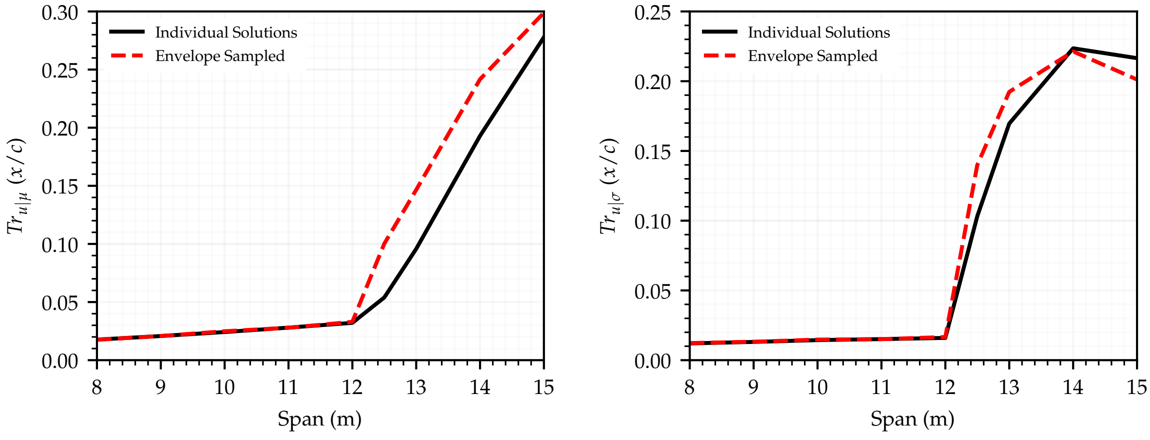

(a) *Mean* **(b)** *Standard deviation*

Figure 8.17: *Upper surface transition mean and standard deviation calculated over the span using the envelope sampling method and from individual flow solutions for optimised design D.*

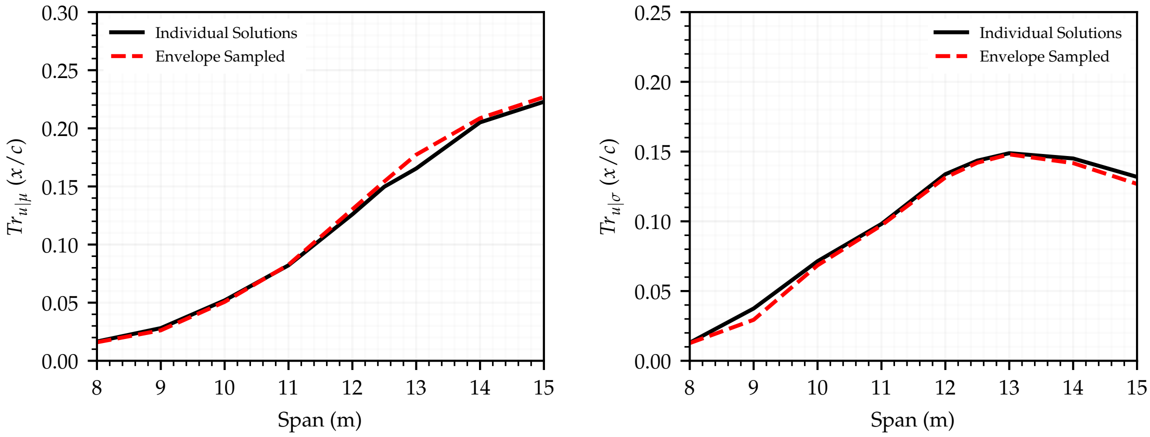

(a) *Mean* **(b)** *Standard deviation*

Figure 8.18: *Upper surface transition mean and standard deviation calculated over the span using the envelope sampling method and from individual flow solutions for optimised design T.*

At 8m span, $Tr_{u|\mu}$ and $Tr_{u|\sigma}$ calculated with the envelope sampling method exactly match the values found from individual flow solutions for both optimised designs. This is expected given that both designs have less than $0.05x/c$ laminar flow at the ideal critical N-factor, and therefore see little change as critical N-factor is reduced. For this reason, the envelope sampling method remains accurate for design D from 8 → 12 span.

At 12.5m span, design D has $Tr_u = 0.56x/c$ at the ideal critical N-factor but sees transition move $0.46x/c$ upstream when critical N-factor is reduced by only 0.6. This large transition location movement causes pressure and so instability amplification over the aerofoil to change, reducing the accuracy of the envelope sampling method. As this happens close to the ideal critical N-factor used to obtain the critical N-factor envelopes, accuracy of the envelope sampling method is reduced over most of the N-factor range. High critical N-factors also have the largest probability weighting, making their effect on $Tr_{u|\mu}$ and $Tr_{u|\sigma}$ most significant.

At 15m span, transition location for design D is less sensitive to N-factor changes at high critical N-factors. As such, the accuracy of the envelope sampling method is slightly improved. Whereas $Tr_{u|\sigma}$ was over-predicted by the envelope sampling method from 12 → 14m span, it is now under-predicted here. This indicates that over-prediction of Tr_u brings values closer to the mean at 15m span, and away from the mean between 12 → 14m span.

The envelope sampling method is accurate over the entire span for design T, even when $Tr_{u|\mu}$ is highly extended and $Tr_{u|\sigma}$ is large. As transition location is less sensitive to critical N-factor at high critical N-factor values for this design, agreement between the methods is much better. Where the error between methods is largest, $Tr_{u|\mu}$ is over-predicted and $Tr_{u|\sigma}$ is under-predicted. Thus, the envelope method in general appears to over predict $Tr_{u|\mu}$ but depending on the envelope shape, can either over or under-predict $Tr_{u|\sigma}$.

8.3.3 Span-wise Performance Distribution

Using the results calculated from individual flow solutions run at multiple critical N-factor sample points, performance of the selected optimised aerofoils is investigated along the span. Table 8.10 shows the mean value over the span of ML/D at the ideal critical N-factor, ML/D at a critical N-factor of zero, $(ML/D)_\mu$ and $(ML/D)_\sigma$.

Design D has the highest mean ML/D at the ideal critical N-factor over the span. This is expected given it has the largest value when is is calculated over the three span-wise design points used during the optimisation. Now calculated over more span-wise positions, the value of mean ML/D at the ideal critical N-factor has reduced for design D by 4.85 but increased for design T by 1.90. While design D has a higher mean $Tr_{u|\sigma}$ when calculated over the three span-wise span-wise design points, it is now found to have less $(ML/D)_\sigma$ than design T. This is not linked to the envelope sampling method's accuracy as $Tr_{u|\sigma}$ was well predicted for design T while being both over and under-predicted for design D. This is instead due to the distribution of $Tr_{u|\sigma}$ over the span and placement of the initial three design points. Figure 8.19 shows, for both optimised designs, the span-wise distribution of ML/D and Tr_u mean and range between values found at the ideal critical N-factor and a critical N-factor of $N_{cr} = 0$. Figure 8.20 shows the span-wise distribution of ML/D and Tr_u standard deviation for both.

Table 8.10: *The mean value over the span of ML/D at the ideal critical N-factor, ML/D at a critical N-factor of 0, $(ML/D)_\mu$ and $(ML/D)_\sigma$ for the starting and optimised designs.*

Design	Mean ML/D ($N_{cr} = 7.9$)	Mean ML/D ($N_{cr} = 0$)	Mean $(ML/D)_\mu$	Mean $(ML/D)_\sigma$
Starting	45.86	41.82	43.44	1.23
Design D	58.12 (+27%)	46.98 (+12%)	50.03 (+15%)	3.67 (+298%)
Design T	57.04 (+24%)	45.96 (+10%)	49.94 (+15%)	3.84 (+312%)

Design D has a highly non-uniform ML/D range over the span. As no laminar flow could be obtained at 8m span, the optimiser focused on improving performance further outboard. At 12.5m span, TS and CF instability amplification has been reduced enough for highly extended upper surface transition at the ideal critical N-factor, but $Tr_{u|\mu}$ remains low. Span-wise positions outboard of 12.5m have a lower Reynolds number and so are still able to obtain extended laminar flow. Inboard of 12.5m, however, Reynolds number increases so TS and CF instabilities amplify. As only a slight rise in TS amplification is enough trigger transition far upstream at the ideal critical N-factor, transition is found close to the leading edge from 8 $\rightarrow$ 12.5m. This results in the mean Tr_u, and therefore mean ML/D at the ideal critical N-factor, being much lower than the values calculated using only the three span-wise design points. This also causes mean $Tr_{u|\sigma}$, and therefore mean $(ML/D)_\sigma$, to be much lower as early transition is inherently robust to critical N-factor changes.

Design T has a more uniform range over the span. Stronger upstream TS instability suppression leads to a more conservative ideal Tr_u at 12.5m span but increases Tr_u over a wider critical N-factor range. As transition is less sensitive to critical N-factor changes, Tr_u at the ideal critical N-factor remains extended and moves forward more gradually as Reynolds number increases the further inboard. Calculations of mean $(ML/D)_\mu$ and mean Tr_u at the ideal critical N-factor over the three design points are therefore more representative of the true mean value over the span.

Thus, pursuing a deterministic design can hurt both mean performance at a specific span-wise position, and also deterministic performance off-design. As span-wise position is linked to Reynolds number and lift coefficient that both affect instability amplification, improving robustness at one span-wise position improves performance inboard. This is expected as a robust design is less sensitive to factors effecting instability growth, such as Reynolds number which is linked to span-wise position.

The design with the best mean ML/D varies depending on the span-wise position. Far outboard, design D is best, however, its ML/D standard deviation is larger than for design T when $(ML/D)_\sigma$ is not low on design D due to early transition. In general, design T has a more conservative performance but is a more robust design that would likely be preferable due to its more consistent performance over the span with critical N-factor uncertainty. Performance of this design is still very much limited by CF instability growth, with only half the chosen span width obtaining a meaningful $Tr_{u|\mu}$. A reduction in wing sweep should enable a larger maximum length of laminar flow and a more robust transition location to critical N-factor reduction over a wider span.

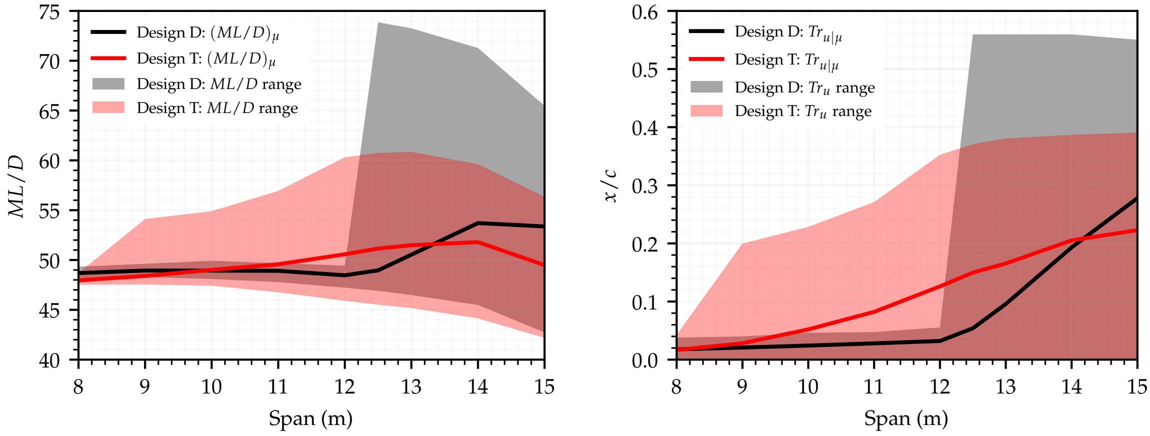

(a) ML/D **(b)** *Upper surface transition location*

Figure 8.19: *Span-wise distribution of* ML/D *and* Tr_u *mean and range between values at* $N_{cr} = 7.9$ *and* $N_{cr} = 0$ *for design D and design T.*

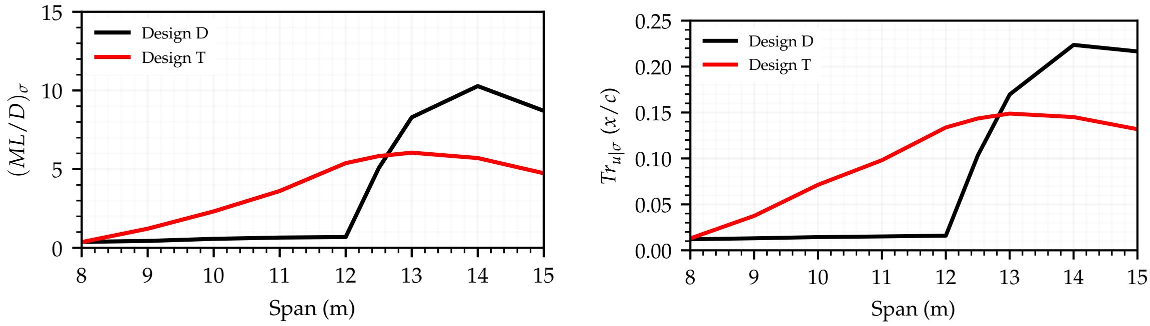

(a) ML/D **(b)** *Upper surface transition location*

Figure 8.20: *Span-wise distribution of* ML/D *and* Tr_u *standard deviation for design D and design T.*

8.3.4 Sensitivity to Uncertainty Standard Deviation

The effect of varying critical N-factor standard deviation on the span-wise distribution of performance has been assessed for each design. Figure 8.21 shows the span-wise distribution of $(ML/D)_\mu$ while figure 8.22 shows the span-wise distribution of $(ML/D)_\sigma$ for designs D and T when calculated with a critical N-factor standard deviation value of 1, 2 and 3. The ML/D range is also shown in figure 8.21.

Increasing N_σ causes $(ML/D)_\mu$ to reduce over the span, as is expected given this lowers the probability weighting at high N-factor values where both design D and design T obtain the most laminar flow. This can be seen in figure 8.23 showing probability distributions with different uncertainty standard deviation values, and the distribution of ML/D over the critical N-factor range for designs D and T at 13m and 15m span. For both designs, $(ML/D)_\mu$ is reduced most when N_σ is increased from $1 \rightarrow 2$, as the probability weightings above $N_{cr} = 6.5$ decrease substantially. The reduction in $(ML/D)_\mu$ is larger outboard where more laminar flow is obtained. The loss in $(ML/D)_\mu$ outboard on the wing is smaller for design T than design D as ML/D is large over a wider critical N-factor range.

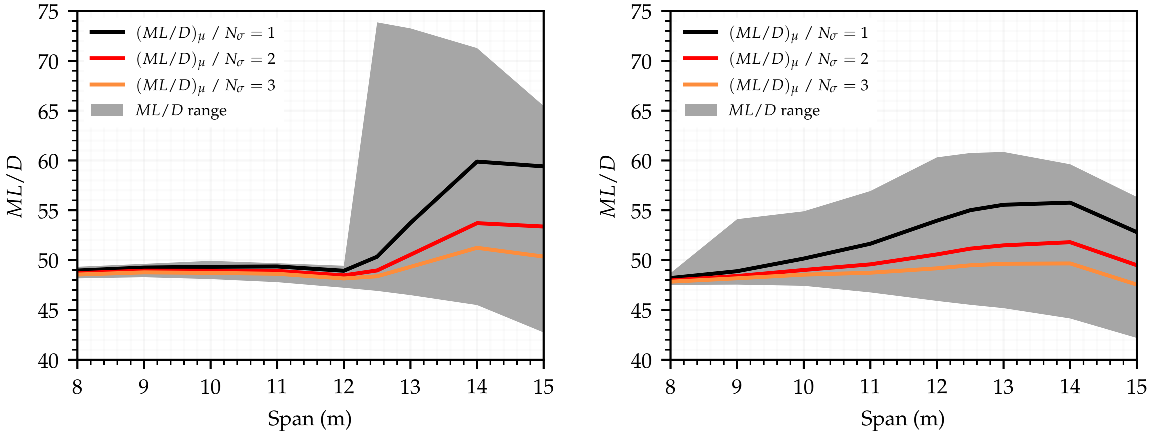

(a) *Design D* **(b)** *Design T*

Figure 8.21: *Span-wise distribution of ML/D range between values at $N_{cr} = 7.9$ and $N_{cr} = 0$ and mean ML/D when calculated with various N_σ values for design D and design T.*

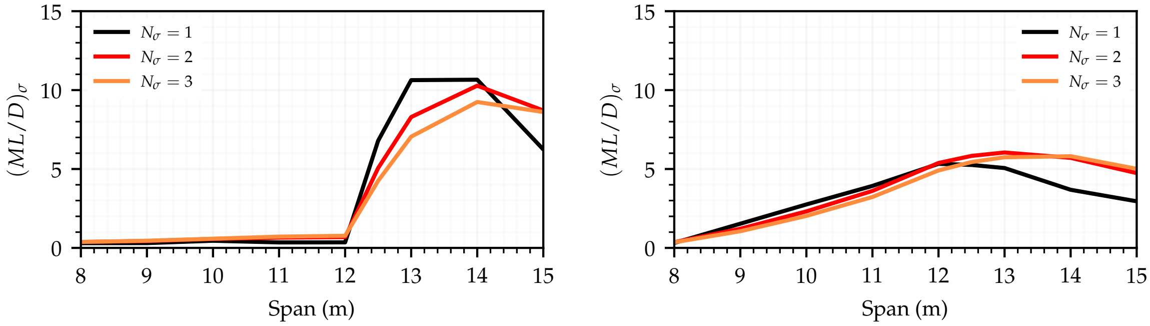

(a) *Design D* **(b)** *Design T*

Figure 8.22: *Span-wise distribution of ML/D standard deviation when calculated with various N_σ values for design D and design T.*

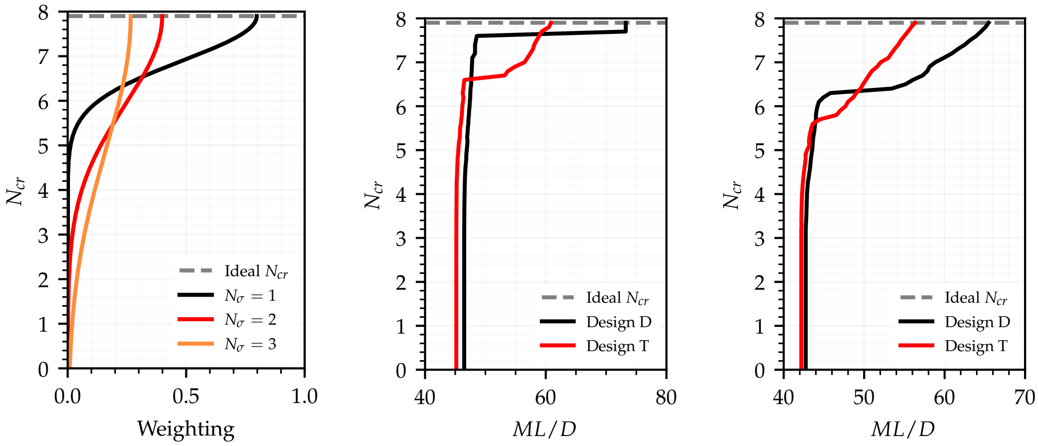

(a) *Critical N-factor weighting* **(b)** *Span= 13m* **(c)** *Span= 15m*

Figure 8.23: *Critical N-factor weighting with different uncertainty standard deviation values and transition envelopes for designs D and T at 13m and 15m span.*

Changes to $(ML/D)_\sigma$ are also dependent on the N-factor envelope shape. $(ML/D)_\sigma$ increases as N_σ is raised from 1 to 2, outboard of 14m span for design D and outboard of 12m span for design T. This happens when probability weighting is increased at N-factor values where ML/D is far from $(ML/D)_\mu$. This is the case for both designs at 15m span as ML/D is large over most of the critical N-factor range above $N_{cr} = 6$. When $N_\sigma = 1$, the probability of N_{cr} being below this value is only 2.7 percent. The probability of N_{cr} being below 6 increases to 13.3 percent when $N_\sigma = 2$, giving lower ML/D values a higher weighting. This reduces $(ML/D)_\mu$ and increases $(ML/D)_\sigma$. At 13m span, $(ML/D)_\mu$ is low except at a small N-factor range near the ideal critical N-factor. As $Tr_{u|\mu}$ is low, reducing the probability weighting at the ideal critical N-factor causes $Tr_{u|\sigma}$ to drop.

8.4 Low-Sweep Optimisation Results

The low-sweep wing optimisation produced 7200 optimised designs of which 3750 could be converged at all three span-wise design points by CVGK. Designs that cannot be converged will feature separated flow at one or more of the design points, due to either shock induced or laminar separation. As the percentage of converged solutions is lower than seen for the high-sweep optimisation, and similar starting aerofoils and design variable bounds were used, new flow conditions are the likely cause.

Figure 8.24 shows the optimum value found for each objective function over the course of the optimisation. The value of the starting design is also shown for comparison. Designs with much improved mean ML/D, $Tr_{u|\mu}$ and $Tr_{u|\sigma}$ are found within the first few generations, but this is followed by a period of stagnation where CVGK is unable to converge many of the designs at all three design points. As convergence is slowed, improved mean ML/D and $Tr_{u|\mu}$ values are found up to the last generation. This suggests that both mean ML/D and $Tr_{u|\mu}$ could be improved with additional generations. In comparison, no improvement in $Tr_{u|\sigma}$ was found after generation 125, indicating an optimum value has been obtained.

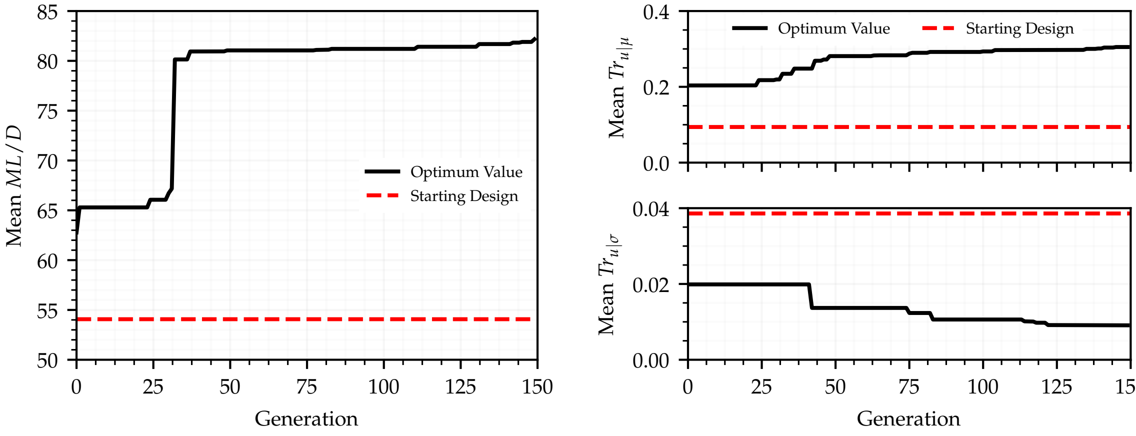

(a) *ML/D* **(b)** *Upper surface transition location*

Figure 8.24: *The optimum objective function values found during the low-sweep optimisation history.*

Figure 8.25 shows the Pareto front found between objectives. Mean $Tr_{u|\sigma}$ is plotted against mean $Tr_{u|\mu}$ with contours of mean ML/D. The 856 designs on the Pareto front are also highlighted. The Pareto front is similar to that found during the high-sweep case. There is again an interdependence between mean $Tr_{u|\mu}$ and $Tr_{u|\sigma}$, where the lower edge of the contour region represents the minimum mean $Tr_{u|\sigma}$ possible for a given mean $Tr_{u|\mu}$. Designs here have a lower mean ML/D than those with a larger $Tr_{u|\sigma}$. This again indicates that Tr_u at the ideal critical N-factor is reduced to extend Tr_u over a wider N-factor range to reduce $Tr_{u|\sigma}$ for a given $Tr_{u|\mu}$. As such, the maximum mean $Tr_{u|\mu}$ design does not have the maximum mean ML/D. For the high-sweep wing optimisation, the optimum trade-off between mean $Tr_{u|\mu}$ and $Tr_{u|\sigma}$ became worse as $Tr_{u|\mu}$ increased. The optimum trade-off on the low-sweep wing Pareto front can be split into two distinct regions. Below $Tr_{u|\mu} = 0.21x/c$, the trade-off is weaker where a change in $Tr_{u|\mu}$ causes a 0.46× change in $Tr_{u|\sigma}$. Above $Tr_{u|\mu} = 0.21x/c$, the trade-off becomes stronger where changing $Tr_{u|\mu}$ causes a 1.15× change in $Tr_{u|\sigma}$.

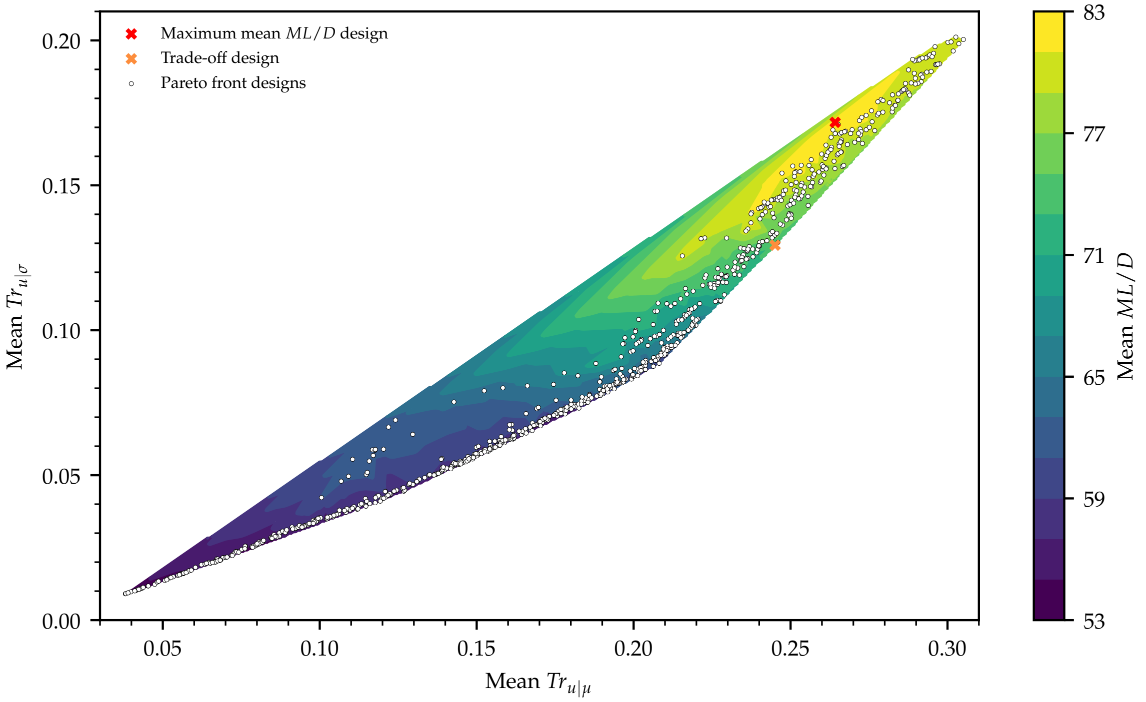

Figure 8.25: *Contour plot of the Pareto front found between objective functions during optimisation of the low-sweep wing.*

To get a better understand of this, $Tr_{u|\mu}$ and $Tr_{u|\sigma}$ for each Pareto front design at each of the three designs points are plotted in figure 8.26. The best trade-off between $Tr_{u|\mu}$ and $Tr_{u|\sigma}$ differs depending on the span-wise position. Designs obtain a larger $Tr_{u|\mu}$ outboard where Reynolds number is lowest, and also obtain a better trade-off between $Tr_{u|\mu}$ and $Tr_{u|\sigma}$. Less instability amplification outboard allows Tr_u to be extended over a wide critical N-factor range by a small amount, rather than extended over a small critical N-factor range by a large amount. The trade-off between $Tr_{u|\mu}$ and $Tr_{u|\sigma}$ at 15m span remain relatively constant as $Tr_{u|\mu}$ is increased. In comparison the trade-off between $Tr_{u|\mu}$ and $Tr_{u|\sigma}$ at 8m span is much worse when $Tr_{u|\mu} > 0.18$. The trade-off is also worse at 10.5m span when $Tr_{u|\mu} > 0.22$.

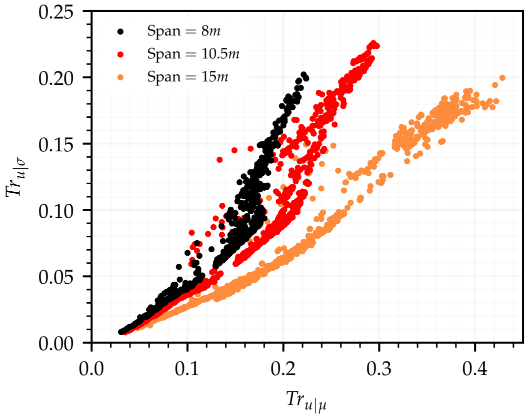

Figure 8.26: *$Tr_{u|\mu}$ and $Tr_{u|\sigma}$ at each span-wise design point for all Pareto front designs.*

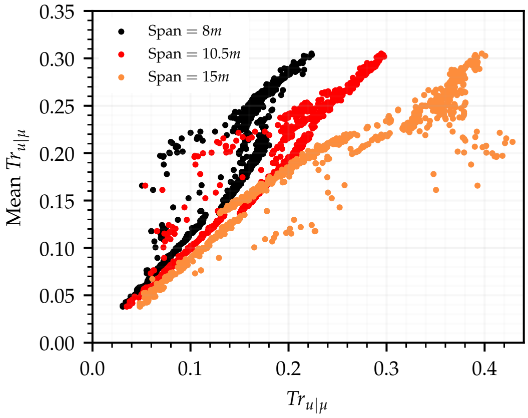

Figure 8.27: *The value of $Tr_{u|\mu}$ at each span-wise design point for the corresponding mean $Tr_{u|\mu}$ for each Pareto front design.*

Figure 8.27 shows, for each Pareto front design, the value of $Tr_{u|\mu}$ at each of the span-wise design points and the resulting mean $Tr_{u|\mu}$. Most Pareto front designs with mean $Tr_{u|\mu} < 0.2x/c$ have a similar $Tr_{u|\mu}$ at all span-wise positions. Some designs do have more $Tr_{u|\mu}$ at 15m span but these don't obtain a larger mean $Tr_{u|\mu}$ as $Tr_{u|\mu}$ has reduced at 8 and 10.5m span. Designs with mean $Tr_{u|\mu} > 0.2x/c$ have a larger proportion of $Tr_{u|\mu}$ at 15m span compared to 8m span. Given the trends seen in figure 8.26, this is understandable as the trade-off between $Tr_{u|\mu}$ and $Tr_{u|\sigma}$ is poor at 8m span and therefore the optimiser favours increasing $Tr_{u|\mu}$ at 10.5 and 15m span to keep mean $Tr_{u|\sigma}$ low.

As was done with the high-sweep wing optimisation case, the design with maximum mean ML/D and a trade-off design are selected for comparison against the starting design. The trade-off design was selected to have a similar mean $Tr_{u|\mu}$ to the design with maximum mean ML/D, but with a substantially reduced $Tr_{u|\sigma}$. As indicated in figure 8.25, it sits at the lower edge of the contour region to obtain the best trade-off possible between mean $Tr_{u|\mu}$ and mean $Tr_{u|\sigma}$, at a cost of mean ML/D. The objective function values obtained by the starting design, design with maximum mean ML/D, maximum mean $Tr_{u|\mu}$, minimum mean $Tr_{u|\sigma}$ and trade-off design are shown in in table 8.11.

Each design in table 8.11 has a larger mean ML/D value than the starting design as this was constrained during the optimisation to avoid designs with very early transition at the ideal critical N-factor. These designs are highly robust but have extremely low ML/D and $Tr_{u|\mu}$. Indeed, the design with minimum $Tr_{u|\sigma}$ is at this limit as it has no improvement in ML/D compared to the starting design. Mean ML/D and $Tr_{u|\mu}$ have been increased for each optimised design shown in table 8.11 except the design with minimum mean $Tr_{u|\sigma}$. The improvements in mean $Tr_{u|\mu}$ are substantial as this is low for the starting design. As a result, however, the starting design has a very low $Tr_{u|\sigma}$ and so each designs except the design with minimum mean $Tr_{u|\sigma}$ see this increase substantially. The trade-off design obtains 20 percent less mean $Tr_{u|\mu}$ than the design with maximum $Tr_{u|\mu}$, but 40 percent less mean $Tr_{u|\sigma}$ as a result. The increase in mean ML/D compared to the starting design is smaller than obtained by the design with maximum mean ML/D, but is still substantial.

Table 8.11: *Objective function values for the starting design, optimised aerofoil with maximum mean ML/D, trade-off design and optimised designs with maximum mean $Tr_{u|\mu}$ and minimum mean $Tr_{u|\sigma}$.*

Design		Mean ML/D	Mean $Tr_{u\|\mu}$	Mean $Tr_{u\|\sigma}$
Starting		54.07	0.0940	0.0386
Max mean ML/D	(D)	82.17 (+52%)	0.2642 (+181%)	0.1717 (+345%)
Trade-off	(T)	73.73 (+36%)	0.2451 (+161%)	0.1293 (+235%)
Max mean $Tr_{u\|\mu}$		80.14 (+48%)	0.3051 (+225%)	0.2003 (+419%)
Min mean $Tr_{u\|\sigma}$		54.24 ($\approx$ 0%)	0.0381 (-59%)	0.0091 (-76%)

8.4.1 Design Point Changes

The design with maximum mean ML/D, denoted design D (deterministic), and the trade off design, denoted design T (trade), are selected for more detailed analysis and comparison against the starting design. Figure 8.28 shows the upper and lower surface design variable values and bounds for the starting and selected optimised designs. Positive values indicate material is added to the surface while negative values indicate material is removed. Design variables 1 and 7 are towards the leading edge while design variables 6 and 12 are close to the trailing edge.

The design variable bounds selected for the low-sweep wing case are similar to those used in the high-sweep wing case. Wide bounds are placed on design variables 1 and 7 at the front of the aerofoil to give good control over leading edge curvature. Large positive bounds were used aft on the upper surface and large negative bounds were used on the lower surface to allow for designs with increased camber. A notable difference from the high-sweep design variable bounds is the reduced lower limit for design variable 2. This was done to allow designs with reduced curvature over the front of the aerofoil. As material was added towards the front of the aerofoil and removed from the rear for design T, design variables 2, 3, 4 and 5 are found close to the design variable bounds. Design D has also had material added to the upper surface except at the trailing edge, and so has variables 2 and 6 close to the bounds. Both designs have had material removed from the lower surface. Design D has larger deformation towards the rear of the aerofoil and so design variables 10, 11 and 12 are close to the lower bounds while only variable 12 sits near the lower bounds for design T.

Figure 8.29 shows aerofoil profiles for the starting and optimised designs, with the grey shaded region indicating the viable design space as dictated by the design variable bounds. The maximum thickness of both optimised aerofoils has reduced from $0.118x/c$ to the constrained limit of $0.110z/c$. The reduction of thickness in both cases comes from lower surface deformation, increasing camber and lift generation. As a result, both optimised designs operate at a reduced angle of attack at all three span-wise stations.

The effect of these changes can be seen in figures 8.30, 8.31 and 8.32 showing pressure distributions at the ideal critical N-factor and N-factor envelopes for each design at each of the span-wise design points. both optimised aerofoils have a smaller leading edge pressure rise and favourable pressure gradient over the front of the aerofoil. The pressure gradient is stronger for design T but over a shorter length compared to design D. Both see an extension

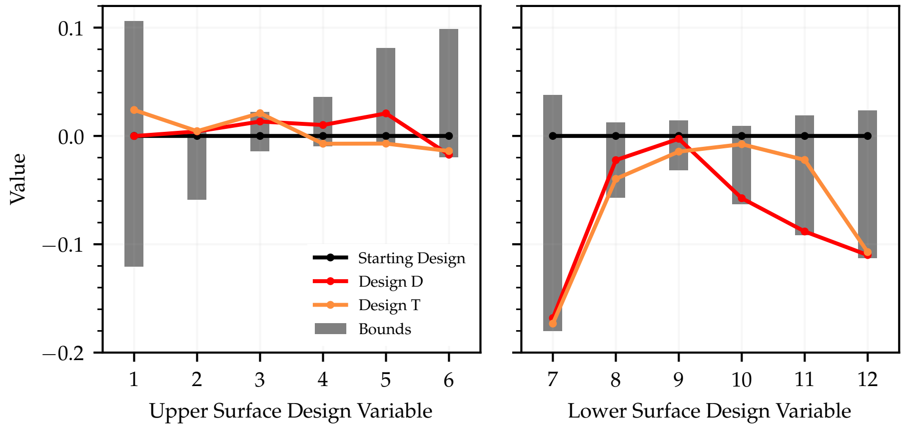

Figure 8.28: *Upper and lower surface design variable values and bounds for the starting and selected optimised designs.*

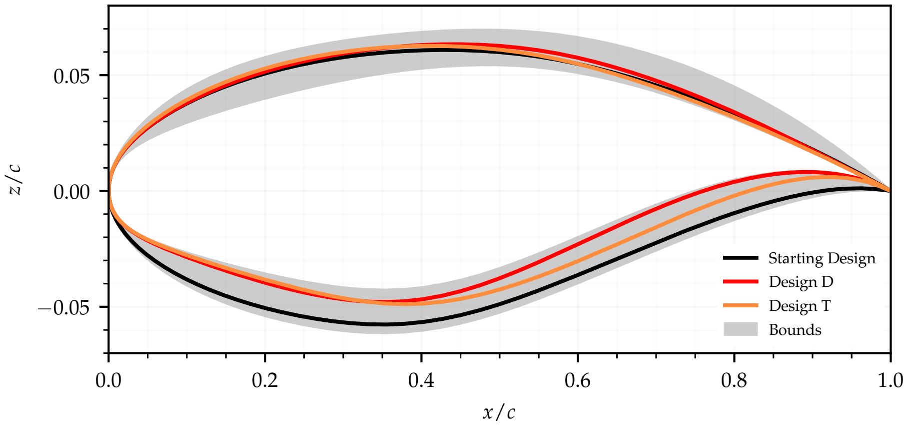

Figure 8.29: *Aerofoil profiles for the starting and selected optimised designs with grey shaded region indicating the viable design space as dictated by the design variable bounds.*

in laminar flow at all three design points compared to the starting design. The maximum amount of laminar flow found on the starting design is $0.215x/c$ at 15m span. In comparison, design D has over $0.5x/c$ of laminar flow, and design T has over $0.4x/c$ of laminar flow, at all three span-wise positions.

Neither of the optimised designs feature a leading edge peak in pressure, as was seen on the selected high-sweep optimised designs. This is due to the reduced wing sweep lowering CF instability amplification at all three design points, as seen in figures 8.30b, 8.31b and 8.32b. Transition on each design now occurs as a result of TS instability amplification or instability mixing due to high TS growth. The leading edge pressure peak was used to reduce CF amplification, but the small region of adverse pressure gradient following this causes TS instability amplification and so is not present on the low-sweep optimised designs.

As was seen in figure 8.27, laminar flow can be found inboard at 8m span now that wing-sweep is lower. As a result, performance over the span varies less for both optimised designs in comparison to the high-sweep results. Design D has the most delayed Tr_u at all

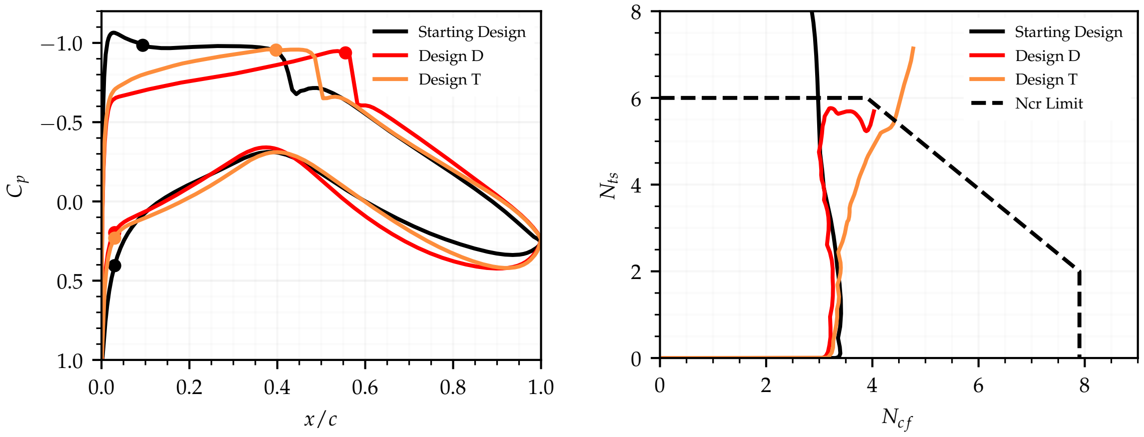

(a) *Pressure Distribution* **(b)** *N_{ts} vs N_{cf} envelope*

Figure 8.30: *Ideal critical N-factor performance of the starting and selected optimised designs span* $= 8m$.

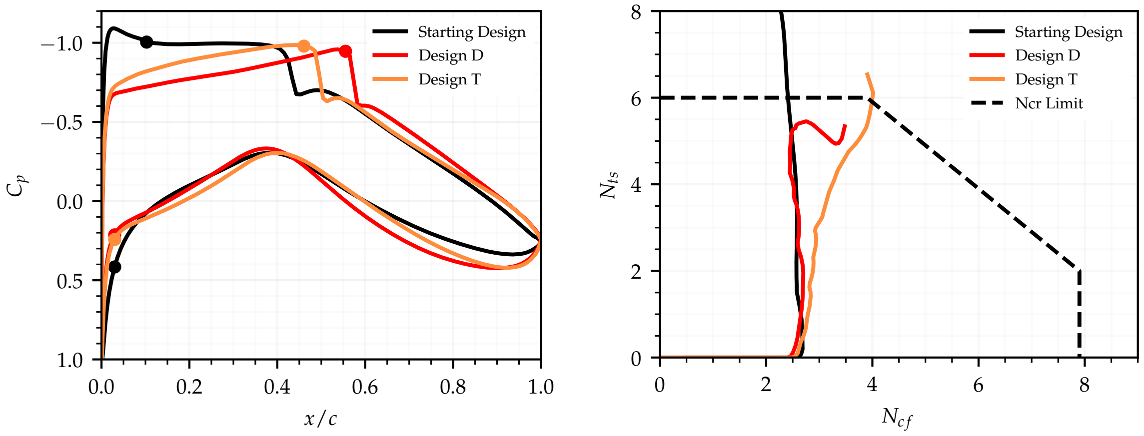

(a) *Pressure Distribution* **(b)** *N_{ts} vs N_{cf} envelope*

Figure 8.31: *Ideal critical N-factor performance of the starting and selected optimised designs span* $= 10.5m$.

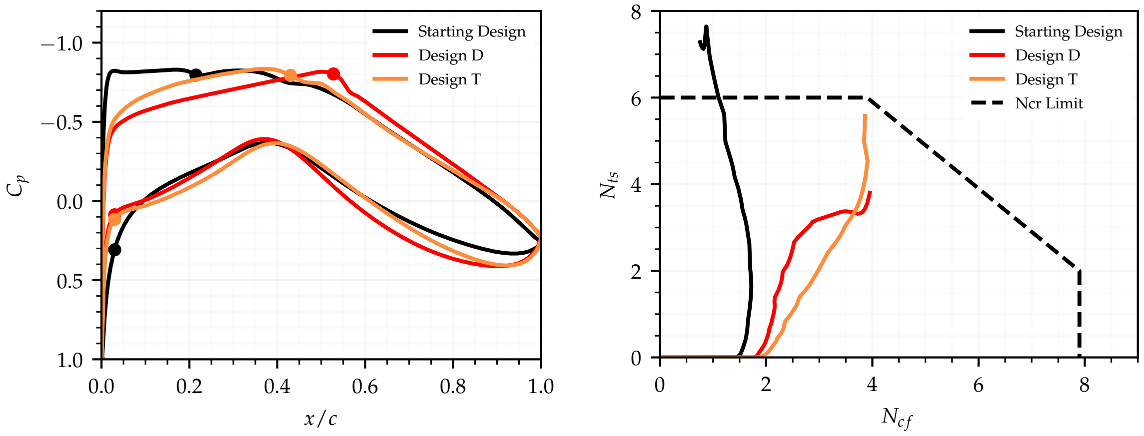

(a) *Pressure Distribution* **(b)** *N_{ts} vs N_{cf} envelope*

Figure 8.32: *Ideal critical N-factor performance of the starting and selected optimised designs span* $= 15m$.

three span-wise positions, as is expected given that this design has the maximum mean ML/D. However, delaying Tr_u at the ideal critical N-factor as far as possible results in poor transition location robustness to critical N-factor uncertainty. The N-factor envelopes for design D at 8m and 10.5m span are shown in figures 8.30b and 8.31b. At both span-wise positions, the N-factor envelope approaches but remains below the TS instability limit until shock induced transition occurs further downstream. This causes transition location to move upstream rapidly as critical N-factor is reduced. This is seen in figure 8.33, showing the transition envelope above $N_{cr} = 3$ for the starting and optimised designs at each span-wise design point. The starting design has the least laminar flow, but sees little loss of laminar flow as critical N-factor is reduced. At 8 and 10.5m span, design D has a highly extended Tr_u at the ideal critical N-factor but this reduces by $0.357x/c$ and $0.328x/c$ when critical N-factor is reduced by 1.

Upper surface transition at the ideal critical N-factor occurs earlier for design T. However, this makes transition location less sensitive to critical N-factor changes as, at 8m and 10.5m span, only $0.171x/c$ and $0.163x/c$ laminar length is lost when critical N-factor is reduced by 1. This can be seen on the critical N-factor envelop plots as the smoother and more direct path that design T takes to the limit at each of the span-wise stations. This prevents rapid movement of transition location upstream as critical N-factor is reduced.

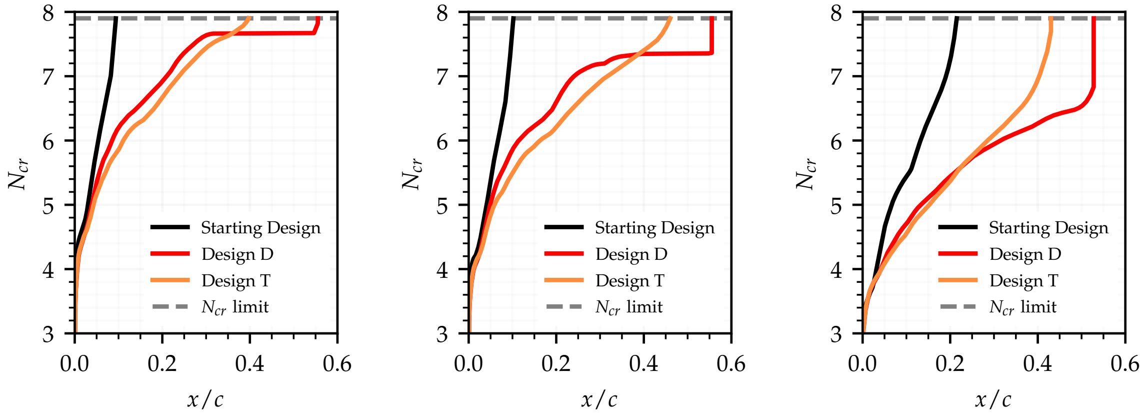

(a) *Span* $= 8m$ **(b)** *Span* $= 10.5m$ **(c)** *Span* $= 15m$

Figure 8.33: *Transition envelopes for the starting and selected optimised designs at each span-wise station.*

8.4.2 Additional Validation of the Methodology

Additional validation of the envelope sampling method has been carried out using optimised designs D and T. For this, $Tr_{u|\mu}$ and $Tr_{u|\sigma}$ are calculated using the envelope sampling method and compared against values found using transition locations from individual flow solutions run at multiple critical N-factor sample points. These were again taken at $N_{\text{step}} = 0.1$ intervals from the ideal critical N-factor of $N_{cr} = 7.9$ down to $N_{cr} = 3.0$ and the flow solution at $N_{cr} = 3.0$ with leading edge transition replicated for sample points down to $N_{cr} = 0$. This was carried out at 1m intervals over $8 \rightarrow 15$m span, and at the 10.5m span-wise station. The results of this are shown in figure 8.34 for design D and in figure 8.35 for design T.

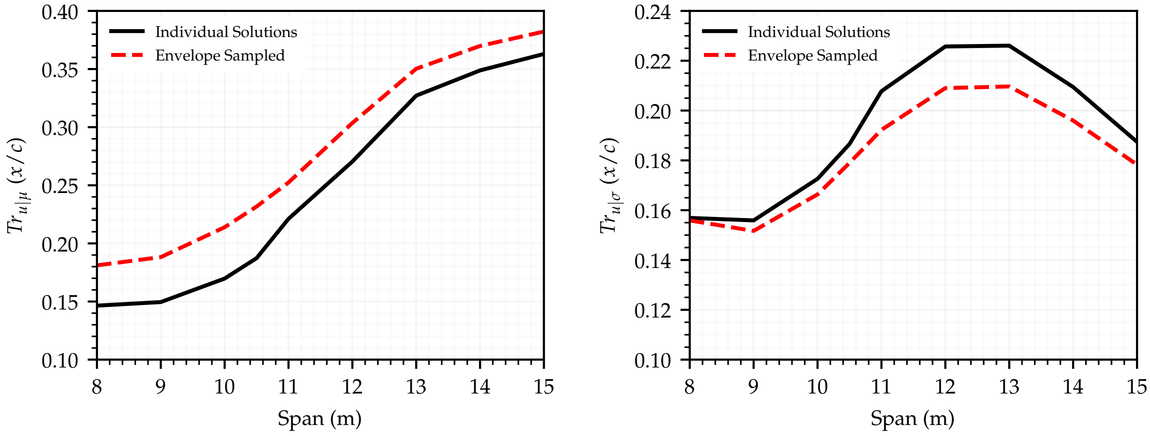

(a) *Mean* **(b)** *Standard Deviation*

Figure 8.34: *Upper surface transition mean and standard deviation calculated over the span using the envelope sampling method and from individual flow solutions for optimised design D.*

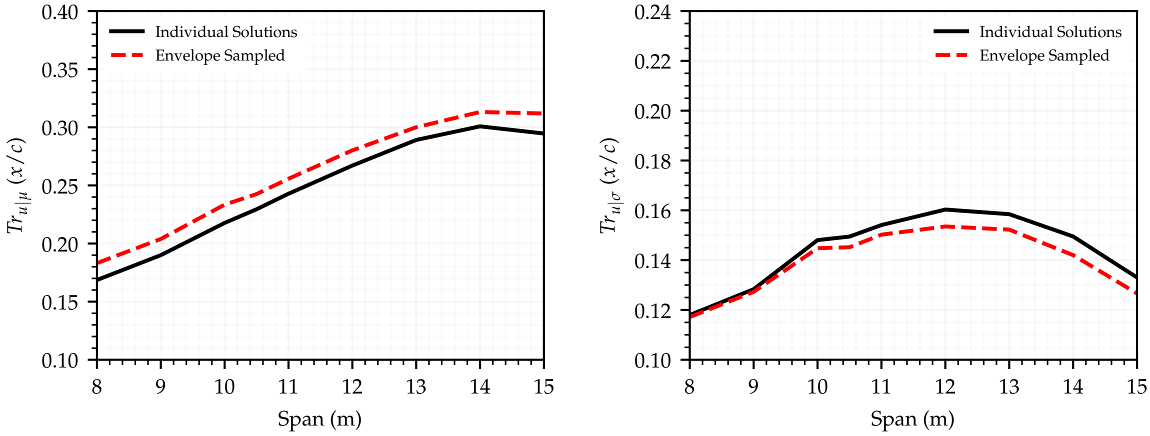

(a) *Mean* **(b)** *Standard Deviation*

Figure 8.35: *Upper surface transition mean and standard deviation calculated over the span using the envelope sampling method and from individual flow solutions for optimised design T.*

The accuracy of the envelope sampling method is low for design D, with $Tr_{u|\mu}$ consistently over-predicted and $Tr_{u|\sigma}$ consistently under-predicted along the span. The is worst for $Tr_{u|\mu}$ inboard, where design D has highly extended laminar flow at the ideal critical N-factor but sees a large reduction in Tr_u when this is reduced by a small amount. This large shift in transition location alters the pressure distribution and so instability amplification upstream. As this occurs at a high critical N-factor, accuracy of the N-factor envelope is low over most of the critical N-factor range. Poor accuracy for this type of critical N-factor envelope was also observe during validation of the high-sweep wing optimised designs. The envelope sampling method has better accuracy in calculating $Tr_{u|\mu}$ and $Tr_{u|\sigma}$ over the span for design T. This design is less sensitive to critical N-factor changes at high N-factor values. Thus, the N-factor envelope provides good Tr_u predictions at high N-factor values, which have the highest probability weighting.

The accuracy of $Tr_{u|\sigma}$ calculated using the envelope sampling method is best inboard for both designs. The value of $Tr_{u|\sigma}$ is consistently under-predicted on both optimised designs. As $Tr_{u|\mu}$ is over-predicted, it is closer to the values of Tr_u at high N-factors, which have a high probability weighting. The amount of under-prediction is dictated by the movement of transition location and the critical N-factor range where this movement occurs. At high critical N-factors, Tr_u is downstream of $Tr_{u|\mu}$ so an over-prediction of Tr_u causes $Tr_{u|\sigma}$ to increase. As a large change in Tr_u occurs very close to the ideal critical N-factor for design D at 8 and 10.5m span, $Tr_{u|\sigma}$ is least under-predicted here. The inverse is true at low critical N-factors values where Tr_u is upstream of $Tr_{u|\mu}$ so over-prediction of Tr_u reduces $Tr_{u|\sigma}$. While this is the case further outboard, movement of transition at lower critical N-factors increases the accuracy of the envelope sampling method so the under-prediction again reduces.

8.4.3 Span-wise Performance Distribution

The span-wise distribution of deterministic and stochastic performance has been investigated for the starting and selected optimised designs. Performance over the span was calculated using multiple flow solutions run over the critical N-factor range, as done during assessment of the envelope sampling method's accuracy. This is used to construct table 8.12, showing the mean value of ML/D at the ideal critical N-factor, ML/D at a critical N-factor of 0, $(ML/D)_\mu$ and $(ML/D)_\sigma$ over the span for the starting and optimised designs.

Table 8.12: *The mean value over the span of ML/D at the ideal critical N-factor, ML/D at a critical N-factor of 0, $(ML/D)_\mu$ and $(ML/D)_\sigma$ for the starting and optimised designs.*

Design	Mean ML/D ($N_{cr} = 7.9$)	Mean ML/D ($N_{cr} = 0$)	Mean $(ML/D)_\mu$	Mean $(ML/D)_\sigma$
Starting	54.83	49.60	52.85	1.39
Design D	84.33 (+54%)	53.66 (+8%)	65.52 (+24%)	11.67 (+840%)
Design T	77.11 (+40%)	52.81 (+6%)	64.66 (+22%)	8.28 (+596%)

Mean ML/D at the ideal critical N-factor has increased from the value calculated using only three design points for both optimised designs. This is an increase of 2.16 for design D and 3.38 for design T. Design D had a slightly higher mean $Tr_{u|\mu}$ and slightly lower mean $Tr_{u|\sigma}$ than design T when calculated over the three design points. The same is seen for mean $(ML/D)_\mu$ and mean $(ML/D)_\sigma$ now calculated using more span-wise positions and multiple flow solutions over the N-factor range. Mean performance over the span when calculated at the three design points is therefore representative of the true performance over the span for each aerofoil. Design T obtains a very similar mean $(ML/D)_\mu$ to design D, but has a reduced mean $(ML/D)_\sigma$ which comes in part from a reduction of mean ML/D at the ideal critical N-factor. A by-product of this is a small reduction in fully turbulent mean ML/D compared to design D although this is still larger than for the starting design.

Figure 8.36 shows, for both designs, the span-wise distributions of ML/D and Tr_u mean and range when calculated at the ideal critical N-factor and a critical N-factor of zero. Design D has a wider ML/D range than design T over the entire span as it has on average $0.1x/c$ more laminar flow at the ideal critical N-factor. Outboard, this has helped design D obtain a higher $Tr_{u|\mu}$, but $Tr_{u|\mu}$ is low inboard where Tr_u is most extended at the ideal critical N-factor. In contrast, $(ML/D)_\mu$ for design T is closer to ML/D at the ideal critical N-factor over the entire span. This is helped inboard as Tr_u at the ideal critical N-factor reduces by $0.07x/c$ between 10m and 8m span. While design T has a reduced ML/D at the ideal critical N-factor, $(ML/D)_\mu$ exceeds the value obtained by design D and $(ML/D)_\sigma$ is lower.

Figure 8.37 shows the span-wise distribution of $(ML/D)_\sigma$ and $Tr_{u|\sigma}$ for designs D and T. $(ML/D)_\sigma$ and $Tr_{u|\sigma}$ distributions are similar to each other for each designs as drag and transition location inversely scale so long as extended laminar flow does not cause separation. Some differences are seen as ML/D is dependent on lift coefficient which varies over the span. $(ML/D)_\sigma$ and $Tr_{u|\sigma}$ are lower for design T over the entire span as this design sees less transition movement at high critical N-factors. $Tr_{u|\sigma}$ is smallest at 8m span for both designs as the least amount of laminar flow is possible here. As Reynolds number decrease outboard, instability amplification reduces and Tr_u is extended at high critical N-factors. This causes $(ML/D)_\sigma$ and $Tr_{u|\sigma}$ to increase as transition locations are more spread out over the critical N-factor range. Further outboard, $(ML/D)_\sigma$ and $Tr_{u|\sigma}$ begin to decrease as Tr_u is extended over a wider critical N-factor range, bringing $Tr_{u|\mu}$ downstream.

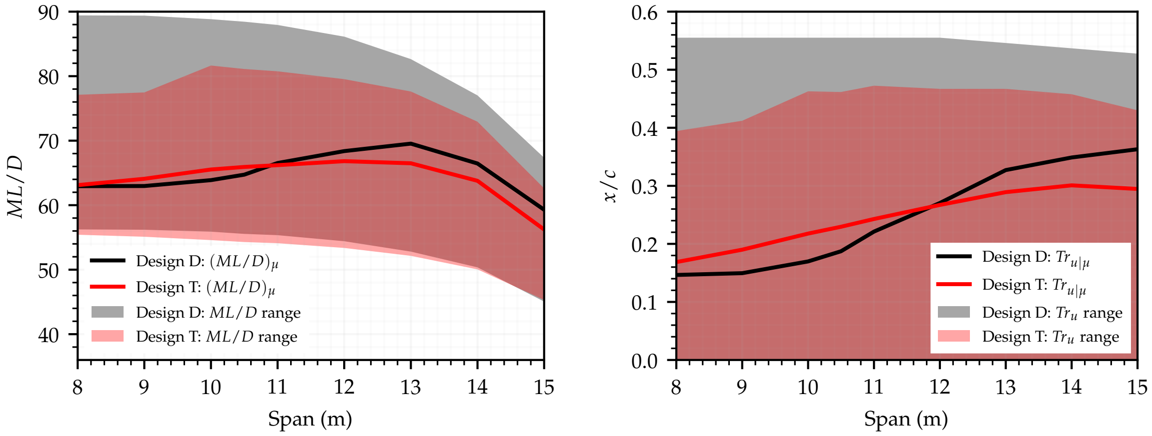

(a) ML/D **(b)** *Upper surface transition location*

Figure 8.36: *Span-wise distribution of ML/D and Tr_u mean and range between values at $N_{cr} = 7.9$ and $N_{cr} = 0$ for design D and design T.*

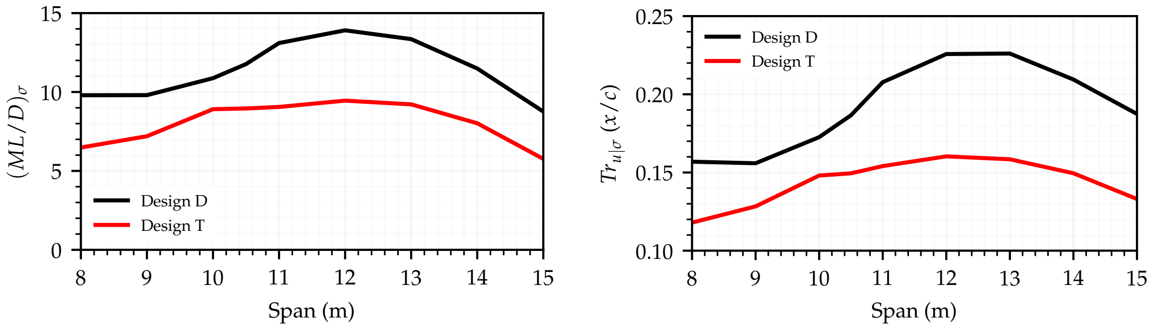

(a) ML/D **(b)** *Upper surface transition location*

Figure 8.37: *Span-wise distribution of ML/D and Tr_u standard deviation for design D and design T.*

8.4.4 Sensitivity to Uncertainty Standard Deviation

The sensitivity of performance to critical N-factor standard deviation has been assessed for designs D and T. Figure 8.38 shows the span-wise distribution of $(ML/D)_\mu$ when calculated with different values of N_σ as well as the range between ML/D values when calculated at the ideal critical N-factor and at a critical N-factor of zero. The span-wise distribution of $(ML/D)_\sigma$ when calculated with different values of N_σ is shown in figure 8.39.

$(ML/D)_\mu$ again reduces most mid-chord as N_σ increases for both designs. $(ML/D)_\mu$ is close to the fully turbulent ML/D value inboard so increasing N_σ causes a small reduction in $(ML/D)_\mu$. ML/D is more uniformly distributed over a wider N_{cr} range outboard so raising N_σ has a weaker effect. $(ML/D)_\sigma$ changes most when N_σ is raised from $1 \rightarrow 2$. This causes $(ML/D)_\sigma$ to increase over the entire span for design T. Design D has a large ML/D range inboard, with $(ML/D)_\mu$ sitting close to the fully turbulent value. ML/D at high N_{cr} values contribute most to $(ML/D)_\sigma$ so increasing N_σ from $1 \rightarrow 2$ lowers $(ML/D)_\sigma$ there. $(ML/D)_\mu$ is close to ML/D at the ideal N_{cr} further outboard. ML/D at lower N_{cr} values contribute more to $(ML/D)_\sigma$ so increasing N_σ from $1 \rightarrow 2$ causes $(ML/D)_\sigma$ to rise here.

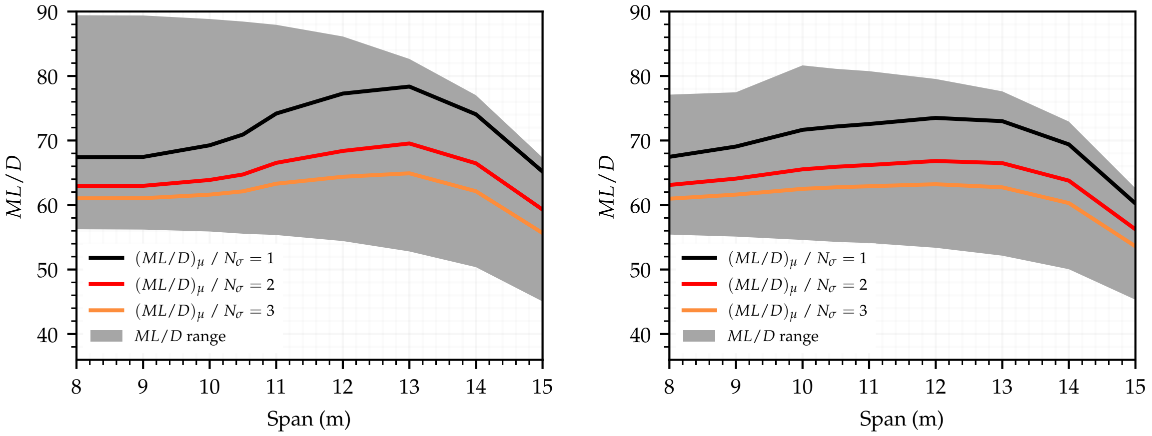

(a) *Design D* **(b)** *Design T*

Figure 8.38: *Span-wise distribution of ML/D range between values at $N_{cr} = 7.9$ and $N_{cr} = 0$ and mean ML/D when calculated with various N_σ values for design D and design T.*

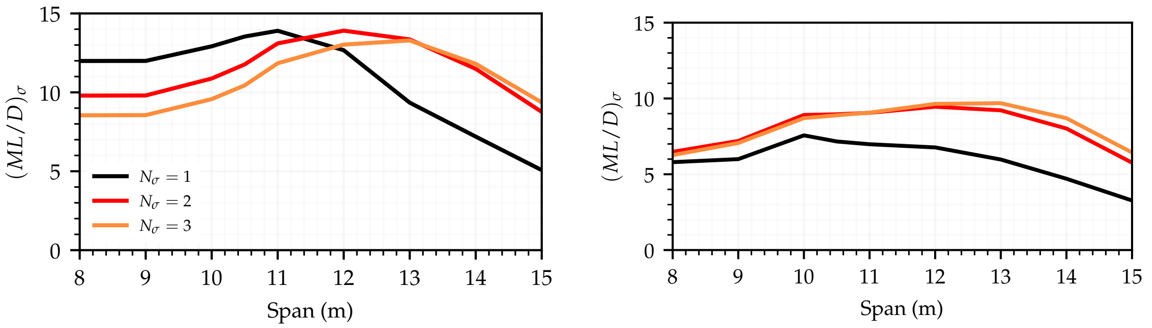

(a) *Design D* **(b)** *Design T*

Figure 8.39: *Span-wise distribution of ML/D standard deviation when calculated with various N_σ values for design D and design T.*

8.5 Summary

In this chapter, the envelope sampling method has been extended to allow for the robust quantification of transition location mean and standard deviation for three-dimensional flows. The motivation behind extending the method was the need for wing-sweep on transonic aircraft, which results in both two and three-dimensional instabilities. Using the three-dimensional envelope sampling method, robust shape optimisation of two swept-wing sections was carried out. The design problem in each case was based on flight conditions for a typical narrow-body commercial aircraft. The first optimisation case was a high-sweep wing typical of a current commercial aircraft while the second was a low-sweep alternative.

In both test cases, a range of designs were produced with varying mean ML/D, $Tr_{u|\mu}$ and $Tr_{u|\sigma}$. The Pareto front between these objectives showed that the mean value of $Tr_{u|\mu}$ and $Tr_{u|\sigma}$ are strongly linked, where one scales with the other. The rate at which $Tr_{u|\sigma}$ increases with $Tr_{u|\mu}$ becomes worse as $Tr_{u|\mu}$ is extended. The trade-off between $Tr_{u|\mu}$ and $Tr_{u|\sigma}$ differs over the span, where $Tr_{u|\mu}$ can be extended with a smaller increase in $Tr_{u|\sigma}$ further outboard on the wing. Thus, robust designs favour increased $Tr_{u|\mu}$ outboard over $Tr_{u|\mu}$ inboard as this maximises $Tr_{u|\mu}$ while minimising mean $Tr_{u|\sigma}$. To obtain large mean $Tr_{u|\mu}$ values, however, a more even extension of $Tr_{u|\mu}$ over the span is required.

No high-sweep Pareto front designs were found with laminar flow at even the ideal critical N-factor inboard along the wing-span selected as strong CF instability amplification occurs. In comparison, many of the low-sweep Pareto front designs have over $0.5x/c$ laminar flow at the ideal critical N-factor or $0.2x/c$ mean laminar flow with critical N-factor uncertainty. Clearly a reduction in sweep angle is required for laminar flow to be obtained over the full span range where three-dimensional flow effects are not present. This does, however, require a reduction in cruise speed to avoid the increased wave from a higher two-dimensional Mach number.

For the same mean laminar flow, transition location standard deviation is lower for designs with reduced laminar flow at the ideal critical N-factor. Thus, designs which pursue the best deterministic performance typically loss some performance robustness to critical N-factor uncertainty as a result. Designs with highly extended laminar flow at the ideal critical N-factor also commonly feature early instability amplification to the critical N-factor limit but remain below it until further downstream. This results in poor mean performance and means the distribution of performance of a swept wing optimised at a single critical N-factor can reduce substantially with a small critical N-factor reduction.

Envelopes of this type do, however, have a low performance standard deviation. This is a trivial case as obtaining no laminar flow inherently makes an aerofoil insensitive to critical N-factor changes. As standard deviation is low, designs of this type sit on the Pareto front but are of little use to a designer. As such, an additional constraint could be placed on mean performance or a different definition of standard deviation used to avoid their retention.

The overall accuracy of the envelope sampling method for three three-dimensional flows is good and the approach is able to match the trends seen. The accuracy of the method is however, worst for N-factor envelopes that see a large movement of transition location at high critical N-factors. This is both due to the change in instability amplification affecting a wider critical N-factor range but also due to the high probability weighting near the ideal critical N-factor. As such, avoiding the creation of these types of designs will increase the overall accuracy of the optimisation.

The design changes made to increasing NLF and improve its robustness over the span are similar in both cases. For the high sweep case, CF instability growth was difficult to reduce but could be enough to bring it under the N_{cf} instability limit. As instability mixing then triggered transition, methods for the suppression of TS instability growth were used. For the low-sweep case, CF growth was small and therefore only methods for TS suppression were seen. This involved reducing thickness on the lower surface to increase camber. This lowers the leading edge pressure rise and allows a favourable pressure gradient over the front of the aerofoil. To reduce performance standard deviation, a stronger favourable pressure gradient is required.

An increase in camber is the primary mechanism by which laminar flow is extended over the critical N-factor range. Pitching moment will increase as a result of this, requiring additional trim to compensate. This leads to a trim drag penalty that can outweigh the benefits of NLF. Pitching moment is a well known trade-off variable with NLF. Although this was not considered during this study, it should be investigated in future work on this topic.

Finally, it is worth mentioning that selection of suitable design bounds proved difficult during the optimisation cases carried out. Large bounds reduce the optimisation convergence rate as many designs are generated with shock induced or laminar separation. However, tight design variable bounds can over-constrained the design space. The results presented in this work can be used to better inform any future design problems. Dynamic bounds may also be an appropriate choice.

Chapter 9

Conclusion

The key aim of this study was to investigate how optimisation and robust design methods could be used to develop NLF aerofoils and wings that are robust off-design and to uncertainty in operating conditions.

A survey of the current state-of-the-art on this topic found that many studies have considered performance of NLF aerofoils and wings at different deterministic operating conditions. However, much less research has been carried out on NLF design with uncertainty in operating conditions. A current gap within the research is on the design of NLF aerofoils and wings with uncertainty in surface and flow quality. Variation in surface and flow quality can be introduced into a flow solution by varying transition amplification factor, or critical N-factor, from the e^N transition model.

The main objectives of this work were to first quantify robustness of NLF aerofoil performance to uncertainty in critical N-factor, so that the sensitivity of performance to this uncertainty could be assessed. The next objective was to perform robust optimisation of NLF aerofoils to improve performance and performance robustness to uncertainty in critical N-factor. To further improve NLF aerofoil robustness, the next objective was to perform optimisation with uncertainty in critical N-factor at a range of operating conditions. The final objective was to extend this to the design of NLF swept and tapered wing sections.

9.1 Summary

In chapter 5: *Critical N-factor Uncertainty Analysis*, an uncertainty representation method for critical N-factor was chosen, and an approach to propagating critical N-factor uncertainty into the output variables of interest was selected. This was then used to assess the variation in performance of aerofoils with free transition, at subsonic and transonic conditions. For the subsonic case, this was done over a range of lift coefficients while for the transonic case, over a range of Mach numbers.

In chapter 6: *Single-Point Robust Optimisation*, the uncertainty quantification method outlined in chapter 5 is used to perform robust shape optimisation of NLF aerofoils at subsonic and transonic flow conditions with uncertainty in critical N-factor. This was done at a single lift coefficient and Mach number.

In chapter 7: *Multi-Point Robust Optimisation*, a novel method for quantifying transition locations mean and standard deviation with critical N-factor uncertainty was proposed. This uses an N-factor envelope obtained from e^N stability analysis of a single flow solution to estimate transition locations at all lower critical N-factor values. This envelope sampling approach removes the dimensionality of robust design, so allows for computationally cheap multi-point robust optimisation. Using this approach, robust shape optimisation of NLF aerofoils with uncertainty in critical N-factor was carried out at a range of Mach numbers and lift coefficients. This was done at subsonic and transonic conditions. The accuracy of envelope sampling method was also assessed.

In chapter 8: *Extension to Swept Flow*, the envelope sampling method proposed in chapter 7 was extended for three-dimensional flows where two and three-dimensional instabilities occur. This enables the robust optimisation of swept and tapered wings. Robust optimisation of an NLF wing section for a typical narrow-body commercial aircraft is carried out. Two wing sections are considered with different sweep angles and, again, accuracy of the three-dimensional envelope sampling method is assessed.

9.2 Key Findings

From the critical N-factor uncertainty analysis carried out, it was found that robustness of drag is directly related to robustness of transition location to critical N-factor uncertainty. Thus it is naturally found that robustness of ML/D is also linked to robustness of transition location via the dependence of ML/D on C_d.

For subsonic flows, variation in transition location due to critical N-factor uncertainty has a stronger effect on skin friction than pressure drag at low lift coefficients. As such, the drag standard deviation polar is similar in form to the combined upper and lower surface transition location standard deviation polars. However, as lift coefficient is increased, pressure drag becomes more sensitive to changes in transition location and so the drag and combined transition location polars no longer match. Transition location standard deviation is found to be strongly linked to the rate of change of transition location with changing lift coefficient. A faster rate of change leads to increased transition location standard deviation with uncertainty in critical N-factor. Robustness of transition location to critical N-factor uncertainty can be improved by reducing the sensitivity of transition location to lift coefficient changes.

For transonic flows, robustness to critical N-factor uncertainty is best at high and low Mach numbers when M^2C_l is fixed, as Mach number is linked to lift coefficient. At high Mach numbers, lift coefficient is low, which allows for better instability suppression and therefore less sensitivity of transition location to changing critical N-factor. At low Mach numbers, lift coefficient is high, so rapid instability growth occurs, which causes very early transition. Early transition is inherently robust as little laminar flow is lost as critical N-factor is reduced.

Single-point robust optimisation was able to improve both mean performance and performance standard deviation with a trade-off between the two found. At subsonic conditions, performance standard deviation is reduced by making extended NLF more robust to changes in critical N-factor. However, at transonic conditions, performance standard deviation was reduced by trigger transition close to the leading edge via the formation of a small shock. While this design is robust to changes in critical N-factor, it is of no practical use to a designer. As such, robust design with critical N-factor uncertainty requires the careful selection of suitable bounds, constraints or tailoring of the design problem to avoid designs of this type.

As the optimisation produces a Pareto front, designs with robust and extended laminar flow can still be obtained. While performance and robustness at the design lift coefficient and Mach number are improved, off-design performance and robustness varies. For subsonic flows, performance and robustness have become worse at higher lift coefficients as a result of single-point optimisation. For transonic flows, as Mach number is reduced, and thus lift coefficient raised, extended laminar flow leads to laminar separation. From this, it is clear that robust optimisation with critical N-factor uncertainty needs to be performed over a range of operating conditions for robustness to be ensured.

The envelope sampling method, developed to avoid the high computational requirements of multi-point robust optimisation, is found to calculate transition location mean and standard deviation with good accuracy. This is checked over a range of lift coefficients and Mach numbers. The method is found to be least accurate for designs with a large movement of transition with changing critical N-factor close to the critical N-factor used to obtain the N-factor envelope. However, the overall trends in transition location mean and standard deviation are still observed.

Multi-point robust shape optimisation using the envelope sampling method is found to be effective at subsonic and transonic flow conditions. Optimised designs are found with better performance and performance robustness to critical N-factor over the multi-point range selected. A constraint placed on performance at the ideal critical N-factor is able to prevent designs with leading edge transition as seen during the single-point robust optimisation. Optimised designs pursuing the maximum performance at the ideal critical N-factor are found to have worse performance robustness to critical N-factor uncertainty. From the Pareto front of designs, it is possible to select a design with a similar although reduced ideal performance but with comparable mean performance and improved performance robustness.

It is found that the envelope sampling method can be extended to three-dimensional flows with both two and three-dimensional instabilities. The accuracy of the extended envelope sampling method is again found to be good at a range of lift coefficients, Reynolds numbers and at different wing sweep angles. Accuracy is again lowest for designs with a large movement of transition location with only a small reduction in critical N-factor from the ideal value.

For swept wings, this becomes more of an issue as designs can have strong crossflow instability growth near the leading edge but highly delayed transition at the ideal critical N-factor. These designs are sought after by the optimiser as they obtain low transition location standard deviations and high deterministic performance. As such, they are not prevented by the constraint on deterministic transition location used previously.

Optimisation of a high-sweep tapered wing section found that strong crossflow instability growth prevents laminar flow inboard along the wing-span. Reduced sweep angle is required to obtain laminar flow over the full span. This does, however, come with a trade-off in reduced cruise Mach number. For both high and low sweep angles, mean laminar flow can be extended furthest outboard due to the reduced Reynolds number. Extending mean laminar flow outboard is also found to have the best trade-off with transition location standard deviation.

The effect of varying the critical N-factor uncertainty standard deviation was also assessed at each stage of this work. The overall trend seen is that the difference in performance robustness of two designs at a specific critical N-factor uncertainty standard deviation is found to be similar when critical N-factor uncertainty standard deviation is changed. As such, the choice of critical N-factor uncertainty standard deviation does not significantly change the quality of one design over the other, but does change mean performance and performance standard deviation and their distribution over lift coefficient, Mach number or wing-span.

9.3 In Conclusion

The aim set out at the beginning of this research project to develop NLF aerofoils and wings with increased robustness to off-design and uncertain conditions has been addressed. This was achieved by first applying the current state-of-the-art in robust design and optimisation to NLF aerofoil and wing design with a previously un-addressed source of uncertainty. This approach was then improved and extended to account for variation in additional parameters. This study therefore make an original contribution to the field of NLF design and optimisation.

Further work that could be undertaken on this topic includes consideration of pitching moment, extended laminar flow on both upper and lower surface at transonic speeds, alternative approaches to quantifying robustness and a focus on leading edge optimisation for crossflow instability reduction.

References

[1] High Level Group on Aviation Research. *Flightpath 2050: Europe's Vision for Aviation*. Tech. rep. EUR 098 EN. Luxembourg: European Commission, Mar. 2011. DOI: `10.2777/50266`.

[2] A. S. W. Thomas. "Aircraft Drag Reduction Technology - A Summary". In: *Aircraft Drag Prediction And Reduction*. Vol. 723. Advisory Group for Aerospace Research and Development (AGARD), July 1985. Chap. 1.

[3] G. Schrauf. "Status and Perspectives of Laminar Flow". In: *The Aeronautical Journal* 109.1102 (Dec. 2005), pp. 639–644. DOI: `10.1017/S000192400000097X`.

[4] S. F. Hoerner. *Fluid-Dynamic Drag*. The Author, 1965.

[5] C. D. Harris. *NASA Supercritical Airfoils: A Matrix of Family-Related Airfoils*. Tech. rep. 2969. Hampton, Virginia: NASA, Mar. 1990.

[6] N. Qin, Y. Zhu and S. Shaw. "Numerical Study of Active Shock Control for Transonic Aerodynamics". In: *International Journal of Numerical Methods for Heat & Fluid Flow* 14.4 (2004), pp. 444–466. DOI: `10.1108/09615530410532240`.

[7] H. L. Reed, W. S. Saric and D. Arnal. "Linear Stability Theory Applied to Boundary Layers". In: *Annual review of fluid mechanics* 28.1 (1996), pp. 389–428.

[8] E. Coustols and A. M. Savill. "Turbulent Skin-friction Drag Reduction By Active And Passive Means: Part 1". In: *Special Course on Skin Friction Drag Reduction*. Vol. 786. Advisory Group for Aerospace Research and Development (AGARD), 1992.

[9] R. D. Joslin. "Aircraft Laminar Flow Control". In: *Annual Review of Fluid Mechanics* 30.1 (1998), pp. 1–29. DOI: `10.1146/annurev.fluid.30.1.1`.

[10] W. S. Saric. "Boundary-Layer Transition: T-S Waves and Crossflow Mechanisms". In: *Aircraft Drag Prediction And Reduction*. Vol. 723. 2. Advisory Group for Aerospace Research and Development, July 1985, pp. 2.1–2. 18.

[11] A. L. Braslow. *A History of Suction-Type Laminar-Flow Control with Emphasis on Flight Research*. NASA Headquarters, Washington DC, USA: NASA History Office, Office of Policy and Plans, July 1999.

[12] G. Redeker, K. H. Horstmann, H. Koster, P. Thiede and J. Szodruch. "Design Of A Natural Laminar Flow Glove For A Transport Aircraft". In: *Flight Simulation Technologies Conference*. AIAA 90-3043-CP. Dayton, OH, USA, Sept. 1990, pp. 375–384. DOI: `10.2514/6.1990-3043`.

[13] R. D. Joslin. *Overview of Laminar Flow Control*. Tech. rep. TP-1998-208705. Langley Research Center, Hampton, Virginia, USA: NASA, Oct. 1998.

[14] V. Schmitt, J. P. Archambaud, K. H. Horstmann and A. Quast. "Hybrid Laminar Fin Investigations". In: *Active Control Technology for Enhanced Performance Operational Capabilities of Military Aircraft, Land Vehicles and Sea Vehicles*. RTO-MP-051. Braunschweig, Germany, June 2001. DOI: `10.14339/RTO-MP-051`.

[15] N. Beck, T. Landa, A. Seitz, L. Boermans, Y. Liu and R. Radespiel. "Drag Reduction by Laminar Flow Control". In: *Energies* 11.1 (Jan. 2018). DOI: `10.3390/en11010252`.

[16] P. Pigeyre. *BLADE Focus*. 2017. URL: `https://airbus-h.assetsadobe2.com/is/image/content/dam/products-and-solutions/commercial-aircraft/a340-family/a340-300/Blade-039.jpg` (visited on 25/05/2018).

[17] O. Gur, J. A. Schetz and W. H. Mason. "Aerodynamic Considerations in the Design of Truss-Braced-Wing Aircraft". In: *Journal of Aircraft* 48.3 (June 2011), pp. 919–939. DOI: `10.2514/1.C031171`.

[18] A. L. Braslow and M. C. Fischer. "Design Considerations for Application of Laminar Flow Control Systems". In: *Aircraft Drag Prediction And Reduction*. 723. Advisory Group for Aerospace Research and Development (AGARD), July 1985. Chap. 4.

[19] L. Jing, G. Zhenghong, H. Jiangtao and Z. Ke. “Robust Design of NLF Airfoils”. In: *Chinese Journal of Aeronautics* 26.2 (2013), pp. 309–318. DOI: `10.1016/j.cja.2013.02.007`.

[20] R. Rashad and D. W. Zingg. “Aerodynamic Shape Optimization for Natural Laminar Flow Using a Discrete-Adjoint Approach”. In: *AIAA Journal* 54.11 (Nov. 2016), pp. 3321–3337. DOI: `10.2514/1.J054940`.

[21] Z. Huan, G. Zhenghong, G. Yuan and W. Chao. “Effective robust design of high lift NLF airfoil under multi-parameter uncertainty”. In: *Aerospace Science and Technology* 68 (June 2017), pp. 530–542.

[22] H. Schlichting and K. Gersten. *Boundary Layer Theory*. Ed. by F. J. Cerra. 6th ed. McGraw-Hill, 1968. DOI: `10.1007/978-3-662-52919-5`.

[23] M. V. Morkovin. “On the Many Faces of Transition”. In: *Viscous Drag Reduction*. Boston, MA, USA: Springer, 1969. DOI: `10.1007/978-1-4899-5579-1_1`.

[24] M. V. Morkovin, E. Reshotko and T. Herbert. “Transition in Open Flow Systems - A Reassessment”. In: *47th Annual Meeting of the Division of Fluid Dynamics*. Atlanta, Georgia, USA, Nov. 1994.

[25] D. Arnal. “Description and Prediction of Transition in Two-Dimensional, Incompressible Flow”. In: *Special Course on Stability and Transition of Laminar Flow*. Vol. 709. 1. Advisory Group for Aerospace Research and Development, June 1984, pp. 2.1–2.71.

[26] J. D. Crouch, L. L. Ng, Y. S. Kachanov, Borodulin and A. V. Ivanov. “Influence Of Surface Roughness And Free-stream Turbulence On Crossflow-instability Transition”. In: *Procedia IUTAM* 14 (2015), pp. 295–302. DOI: `10.1016/j.piutam.2015.03.052`.

[27] J. Elder. “An Experimental Investigation of Turbulent Spots and Breakdown to Turbulence”. In: *Journal of Fluid Mechanics* 9.02 (1960), pp. 235–246.

[28] M. Gad-El-Hak. *Flow Control: Passive, Active and Reactive Flow Management*. Cambridge University Press, 2000.

[29] W. Saric and H. Reed. “Crossflow Instabilities - Theory & Technology”. In: *41st Aerospace Sciences Meeting and Exhibit*. American Institute of Aeronautics and Astronautics, Oct. 2003.

[30] L. M. Mack. “Boundary-layer Linear Stability Theory”. In: *Special Course on Stability and Transition of Laminar Flow*. Vol. 709. 3. Advisory Group for Aerospace Research and Development, June 1984, pp. 3.1–3.88.

[31] W. S. Saric and H. L. Reed. “Toward Practical Laminar Flow Control- Remaining Challenges”. In: *2nd AIAA Flow Control Conference*. Portland, Oregon: AIAA, June 2004. DOI: `10.2514/6.2004-2311`.

[32] H. L. Reed and W. S. Saric. “Stability of Three-Dimensional Boundary Layers”. In: *Annual Review of Fluid Mechanics* 21 (Jan. 1989), pp. 235–284. DOI: `10.1146/annurev.fl.21.010189.001315`.

[33] W. S. Saric, H. L. Reed and E. B. White. “Stability and Transition of Three-Dimensional Boundary Layers”. In: *Annual Review of Fluid Mechanics* 35.1 (2003), pp. 413–440.

[34] J. R. Dagenhart and W. S. Saric. *Crossflow Stability and Transition Experiments in Swept-Wing Flow*. Tech. rep. TP-1999-209344. Langley Research Center, Hampton, Virginia, USA: NASA, July 1999.

[35] E. R. Gowree. “Influence of Attachment Line Flow on Form Drag”. PhD thesis. London, UK: City Univeristy, May 2014.

[36] T. Herbert. “Parabolized Stability Equations”. In: *Annual Review of Fluid Mechanics* 29.1 (1997), pp. 245–283.

[37] Z. Sui-han, Y. Yong and L. Dong. “Experiments of Cross-Flow Instability in a Swept-Wing Boundary Layer”. In: *27th International Congress of the Aeronautical Sciences*. Nice, France: ICAS, Sept. 2010.

[38] G. Schrauf. “Transition Prediction Using Different Linear Stability Analysis Strategies”. In: *12th Applied Aerodynamics Conference*. AIAA 94-1848-CP. Colorado Springs, CO, USA, June 1994. DOI: `10.2514/6.1994-1848`.

[39] L. M. Mack. “On the Stability of the Boundary Layer on a Transonic Swept Wing”. In: *17th Aerospace Sciences Meeting*. AIAA 79-0264. New Orleans, LA, USA, 1979. DOI: `10.2514/6.1979-264`.

[40] L. M. Mack. “Review of Linear Compressible Stability Theory”. In: *Stability of Time Dependent and Spatially Varying Flows*. Ed. by D. L. Dwoyer and M. Y. Hussaini. ICASE NASA LaRC. New York, NY, USA: Springer, 1987. DOI: `https://doi.org/10.1007/978-1-4612-4724-1_9`.

[41] D. Arnal, G. Casalis and R. Houdeville. “Practical Transition Prediction Methods: Subsonic and Transonic Flows”. In: *VKI Lecture Series: Advances in Laminar-Turbulent Transition Modeling*. RTO-EN-AVT-151. The Research and Technology Organisation (RTO) of NATO, 2008. Chap. 7. DOI: `10.14339/RTO-EN-AVT-151`.

[42] H. Raposo, S. Mughal and R. Ashworth. "Acoustic receptivity and transition modeling of Tollmien-Schlichting disturbances induced by distributed surface roughness". In: *Physics of Fluids* 30.4 (Apr. 2018). DOI: `10.1063/1.5024909`.

[43] R. H. Radeztsky, M. S. Reibert, W. S. Saric and S. Takagi. "Effect of Micron-Sized Roughness on Transition in Swept-Wing Flows". In: *31st Aerospace Sciences Meeting*. AIAA 93-0076. Reno, Navada, USA, Jan. 1993. DOI: `10.2514/6.1993-76`.

[44] S. Zuccher and P. Luchini. "Boundary-layer Receptivity To External Disturbances Using Multiple Scales". In: *Meccanica* 49.2 (Feb. 2014), pp. 441–467. DOI: `10.1007/s11012-013-9804-x`.

[45] R. B. Langtry and F. R. Menter. "Correlation-Based Transition Modeling for Unstructured Parallelized Computational Fluid Dynamics Codes". In: *AIAA Journal* 47.12 (Dec. 2009), pp. 2894–2906. DOI: `10.2514/1.42362`.

[46] D. Arnal. "Boundary Layer Transition: Prediction, Application To Drag Reduction". In: *Special Course on Skin Friction Drag Reduction*. 786. Advisory Group for Aerospace Research and Development (AGARD), 1992.

[47] F. R. Menter, R. Langtry, S. Likki, Y. Suzen, P. Huang and S. Völker. "A Correlation-Based Transition Model Using Local Variables—part I: Model Formulation". In: *Journal of turbomachinery* 128.3 (2006), pp. 413–422.

[48] A. M. O. Smith and N. Gamberoni. *Transition, Pressure Gradient and Stability Theory*. Tech. rep. 26388. El Seguno, CA, USA: Douglas Aircraft Company Inc., Aug. 1956.

[49] J. Van Ingen. *A Suggested Semi-Empirical Method for the Calculation of the Boundary Layer Transition Region*. Tech. rep. 74. Delft University of Technology, Sept. 1956.

[50] C. J. Atkin and G. H. Scrauf. "Progress In Linear Stability Methods For Design Applications". In: *European Congress on Computational Methods in Applied Sciences and Engineering*. Barcelona, Spain, Sept. 2000.

[51] G. Schrauf. "Large-Scale Laminar Flow Tests Evaluated with Linear Stability Theory". In: *19th Applied Aerodynamics Conference*. AIAA, June 2001.

[52] G. Schrauf, J. Perraud, D. Vitiello and F. Lam. "Comparison of Boundary-Layer Transition Predictions Using Flight Test Data". In: *Journal of Aircraft* 35.6 (1998), pp. 891–897.

[53] G. Schrauf and K.-H. Horstmann. "Linear Stability Theory Applied to Natural and Hybrid Laminar Flow Experiments". In: *Aerodynamic Drag Reduction Technologies*. Springer, June 2001, pp. 157–163. DOI: `10.1007/978-3-540-45359-8_17`.

[54] F. Menter, R. Langtry and S. Völker. "Transition Modelling for General Purpose CFD Codes". In: *Flow, Turbulence and Combustion* 77.1-4 (Aug. 2006), pp. 277–303. DOI: `10.1007/s10494-006-9047-1`.

[55] R. B. Langtry. "A Correlation-Based Transition Model using Local Variables for Unstructured Parallelized CFD codes". PhD thesis. Stuttgart, Germany: Univeristy of Stuttgart, May 2006.

[56] J. G. Coder and M. D. Maughmer. "A CFD-Compatible Transition Model Using an Amplification Factor Transport Equation". In: *51st AIAA Aerospace Sciences Meeting*. 2013-0253. 2013.

[57] M. Drela and M. B. Giles. "Viscous-Inviscid Analysis of Transonic and Low Reynolds Number Airfoils". In: *AIAA Journal* 25.10 (1987), pp. 1347–1355.

[58] D. Arnal, M. Habiballah and E. Coustols. "Laminar Instability Theory And Transition Criteria In Two-And Three-dimensional Flows". In: *La Recherche Aérospatiale* 2 (1984), pp. 45–63.

[59] R. Narasimha, M. Narayanan and C. Subramanian. "Turbulent Spot Growth in Favorable Pressure Gradients". In: *AIAA Journal* 22.6 (1984), pp. 837–839.

[60] Boeing Co. *Selected Advanced Aerodynamic and Active Control Concepts Development - Summary Report*. Tech. rep. NASA-CR-3220. Langley Research Center, Hampton, Virginia, USA: NASA, Jan. 1980.

[61] M. S. Selig, M. D. Maughmer and D. M. Somers. "Natural-Laminar-Flow Airfoil for General-Aviation Applications". In: *Journal of Aircraft* 32.4 (1995), pp. 710–715.

[62] B. S. Stratford. "An experimental flow with zero skin friction throughout its region of pressure rise". In: *Journal of Fluid Mechanics* 5.1 (Jan. 1959), pp. 17–35.

[63] M. Drela. "Low-Reynolds-Number Airfoil Design for the M.I.T. Daedalus Prototype: A Case Study". In: *Journal of Aircraft* 25.8 (Aug. 1988), pp. 724–732.

[64] R. Wagner and M. Fischer. "Developments in the NASA Transport Aircraft Laminar Flow Program". In: *21st Aerospace Sciences Meeting*. AIAA 83-0090. Reno, Navada, USA, Jan. 1983. DOI: `10.2514/6.1983-90`.

[65] C. P. van Dam and B. J. Holmes. "Boundary-Layer Transition Effects on Airplane Stability and Control". In: *Journal of Aircraft* 25.8 (Aug. 1988), pp. 702–709. DOI: `10.2514/3.45647`.

[66] I. H. Abbott, A. E. von Doenhoff and J. Louis S. Stivers. *Summary of Airfoil Data*. Report 824. Langley Field, VA, USA: National Advisory Committee for Aeronautics, 1945.

[67] M. Fujino, Y. Yoshizaki and Y. Kawamura. “Natural-Laminar-Flow Airfoil Development for a Lightweight Business Jet”. In: *Journal of Aircraft* 40.4 (2003), pp. 609–615.

[68] J. Driver and D. W. Zingg. “Optimized Natural-Laminar-Flow Airfoils”. In: *AIAA Aerospace Sciences Meeting and Exhibit*. Vol. 44. University of Toronto. Reno, Navada, USA, Jan. 2006, pp. 1–16.

[69] D. M. Somers. *Design and Experimental Results for a Flapped Natural-Laminar-Flow Airfoil for General Aviation Applications*. TP 1865. Langley Research Center, Hampton, Virginia, USA: NASA, June 1981.

[70] J. K. Viken, S. A. Watson-Viken, W. Pfenninger, H. L. Morgan Jr and R. L. Campbell. “Design of the Low-Speed NLF(1)-0414f and the High-Speed HSNLF(1)-0213 Airfoils with High-Lift Systems”. In: *Research in Natural Laminar Flow and Laminar-Flow Control* 3 (Dec. 1987), pp. 637–671.

[71] I. Kroo and P. Sturdza. “Design-Oriented Aerodynamic Analysis for Supersonic Laminar Flow Wings”. In: *41st Aerospace Sciences Meeting*. AIAA 2003-0774. Reno, Navada, USA, Jan. 2003.

[72] M. D. Gunzburger. *Perspectives in Flow Control and Optimization*. Ed. by J. A. Burns. 1st. Advances in Design and Control. Lowa State University: Society for Industrial and Applied Mathematics, 2003.

[73] S. Nadarajah and A. Jameson. “A Comparison of the Continuous and Discrete Adjoint Approach to Automatic Aerodynamic Optimization”. In: *AIAA paper* 667 (2000).

[74] A. Jameson. “Control Theory for Optimum Design of Aerodynamic Shapes”. In: *Proceedings of the 29th IEEE Conference on Decision and Control*. IEEE. Honolulu, Hawaii, Dec. 1990, pp. 176–179.

[75] S. N. Skinner and H. Zare-Behtash. “State-of-the-art in Aerodynamic Shape Optimisation Methods”. In: *Applied Soft Computing* 62 (Jan. 2018), pp. 933–962. DOI: `10.1016/j.asoc.2017.09.030`.

[76] K. V. Price, R. M. Storn and J. A. Lampinen. *Differential Evolution: A Practical Approach to Global Optimization*. Springer, 2005.

[77] Y. Yu, Z. Lyu, Z. Xu and J. R. R. A. Martins. “On The Influence Of Optimization Algorithm And Initial Design On Wing Aerodynamic Shape Optimization”. In: *Aerospace Science and Technology* 75 (Apr. 2018), pp. 183–199. DOI: `10.1016/j.ast.2018.01.016`.

[78] M. Robitaille, A. Mosahebi and É. Laurendeau. “Design of Adaptive Transonic Laminar Airfoils Using the $\gamma - Re_{\theta t}$ Transition Model”. In: *Aerospace Science and Technology* 46 (Oct. 2015), pp. 60–71. DOI: `10.1016/j.ast.2015.06.027`.

[79] H. Youngren. “Multi-Point Design and Optimization of a Natural Laminar Flow Airfoil for a Mission Adaptive Compliant Wing”. In: *46th Aerospace Sciences Meeting and Exhibit*. Reno, Navada, USA: AIAA, Jan. 2008.

[80] D. W. Zingg, M. Nemec and T. H. Pulliam. “A Comparative Evaluation Of Genetic And Gradient-Based Algorithms Applied To Aerodynamic Optimization”. In: *European Journal of Computational Mechanics* 17.1-2 (2008), pp. 103–126. DOI: `10.3166/remn.17.103-126`.

[81] J. H. Holland. *Adaptation in Natural and Artificial Systems*. The Univeristy of Michigan, 1975.

[82] R. Eberhart and J. Kennedy. “A New Optimizer Using Particle Swarm Theory”. In: *Micro Machine and Human Sciences (MHS 95)*. Nagoya, Japan, Oct. 1995. DOI: `10.1109/MHS.1995.494215`.

[83] B. A. Gardner and M. S. Selig. “Airfoil Design Using A Genetic Algorithm And An Inverse Method”. In: *41st Aerospace Sciences Meeting*. AIAA 2003-43. Reno, Navada, USA, Jan. 2003.

[84] L. Cameron, J. M. Early and R. McRoberts. “Metamodel Assisted Multi-Objective Global Optimisation of Natural Laminar Flow Aerofoils”. In: *29th AIAA Applied Aerodynamics Conference*. AIAA 2011-3001. Honolulu, Hawaii, USA, June 2011. DOI: `10.2514/6.2011-3001`.

[85] J. Zoltak. “Multi-objective and multi-disciplinary design using evolutionary methods applied to aerospace design problems”. In: *Journal of Aerospace Engineering* 232.4 (Jan. 2018), pp. 613–625. DOI: `10.1177/0954410016684362`.

[86] Z.-H. Han, J. Chen, Z. Zhu and W.-P. Song. “Aerodynamic Design of Transonic Natural-Laminar-Flow (NLF) Wing via Surrogate-based Global Optimization”. In: *54th AIAA Aerospace Sciences Meeting*. AIAA 2016-2041. San Diago, CA, USA, Jan. 2016. DOI: `10.2514/6.2016-2041`.

[87] T.-L. Fan, W.-P. Song, J. Chen and Z.-H. Han4. “Hybrid Optimization Design of Natural-Laminar-Flow (NLF) Supercritical Airfoil and Infinite Swept Wing”. In: *35th AIAA Applied Aerodynamics Conference*. AIAA 2017-3061. Denver, Colorado, USA, June 2017. DOI: `10.2514/6.2017-3061`.

[88] L. M. Rios and N. V. Sahinidis. “Derivative-free Optimization: A Review Of Algorithms And Comparison Of Software Implementations”. In: *Journal of Global Optimization* 56.3 (July 2013), pp. 1247–1293. DOI: `10.1007/s10898-012-9951-y`.

[89] G. Chiandussi, M. Codegone, S. Ferrero and F. Varesio. “Comparison Of Multi-objective Optimization Methodologies For Engineering Applications”. In: *Computers and Mathematics with Applications* 63.5 (Mar. 2012), pp. 912–942. DOI: `10.1016/j.camwa.2011.11.057`.

[90] X. Liu and A. C. Reynolds. “Gradient-based Multi-objective Optimization With Applications To Waterflooding Optimization”. In: *Computational Geosciences* 20.3 (June 2016), pp. 677–693. DOI: `https://doi.org/10.1007/s10596-015-9523-6`.

[91] M. Drela. “Pros and Cons of Airfoil Optimization”. In: *Frontiers of Computational Fluid Dynamics*. Ed. by D. A. Caughey and M. M. Hafez. Vol. 1. World Science, 1998. Chap. 19, pp. 363–382.

[92] P. R. Garabedian and D. G. Korn. “Analysis of Transonic Airfoils”. In: *Communications on Pure and Applied Mathematics* 24.6 (1971), pp. 841–851.

[93] W. Li, L. Huyse and S. Padula. *Robust Airfoil Optimization to Achieve Consistent Drag Reduction Over a Mach Range*. Contractor Report 211042. Langley Research Center, Hampton, Virginia, USA: NASA, Aug. 2001.

[94] G.-J. Park, T.-H. Lee, K. H. Lee and K.-H. Hwang. “Robust Design: An Overview”. In: *AIAA Journal* 44.1 (2006), pp. 181–191. DOI: `10.2514/1.13639`.

[95] G. Taguchi and Y. Wu. *Introduction to off-line quality control*. Central Japan Quality Control Assoc., 1979.

[96] L. W. Cook and J. P. Jarrett. “Robust Airfoil Optimization and the Importance of Appropriately Representing Uncertainty”. In: *AIAA Journal* 55.11 (Nov. 2017), pp. 3925–3939. DOI: `10.2514/1.J055459`.

[97] Y. Zhang, H. Chen, M. Zhang, M. Zhang and T. Lie. “Supercritical Wing Design and Optimization for Transonic Civil Airplane”. In: *49th AIAA Aerospace Science Meeting*. AIAA 2011-27. Orlando, Florida, USA, Jan. 2011. DOI: `10.2514/6.2011-27`.

[98] H. P. Buckley, K. Y. Zhou and D. W. Zingg. “Airfoil Optimization Using Practical Aerodynamic Design Requirements”. In: *Journal of Aircraft* 47.5 (Oct. 2010), pp. 1707–1719. DOI: `10.2514/1.C000256`.

[99] H. P. Buckley and D. W. Zingg. “An Approach to Aerodynamic Design Through Numerical Optimization”. In: *AIAA Journal* 51.8 (Aug. 2013), pp. 1972–1981. DOI: `10.2514/1.J052268`.

[100] V. Gabrel, C. Murat and A. Thiele. “Recent advances in robust optimization: An overview”. In: *European Journal of Operational Research* 235.3 (June 2014), pp. 471–483. DOI: `10.1016/j.ejor.2013.09.036`.

[101] G. Iaccarino. *Quantification of Uncertainty in Flow Simulations Using Probabilistic Methods*. Tech. rep. RTO-EN-AVT-162. The Research and Technology Organisation (RTO) of NATO, Sept. 2008. DOI: `10.14339/RTO-EN-AVT-162`.

[102] T. P. Evans, P. Tattersall, M. Nash and J. J. Doherty. “Robust Design using the Constrained Optimisation Design Method CODAS”. In: *49th AIAA/ASME/ASCE/AHS/ASC Structures, Structural Dynamics, and Materials Conference*. AIAA 2008-2149. Schaumburd, Illinois, USA, Apr. 2008. DOI: `10.2514/6.2008-2149`.

[103] J. Helton, J. Johnson, C. Sallaberry and C. Storlie. “Survey of sampling-based methods for uncertainty and sensitivity analysis”. In: *Reliability Engineering and System Safety 91* 91.10-11 (Oct. 2006), pp. 1175–1209. DOI: `10.1016/j.ress.2005.11.017`.

[104] L. Zhao, W. N. Dawes, G. parks, J. P. Jarrett and S. Yang. “Robust Airfoil Design with Respect to Boundary Layer Transition”. In: *50th AIAA/ASME/ASCE/AHS/ASC Structures, Structural Dynamics, and Materials Conference*. AIAA 2009-2273. Palm Springs, California, USA, May 2009. DOI: `10.2514/6.2009-2273`.

[105] K. Zhao, Z.-h. Gao and J.-t. Huang. “Robust Design of Natural Laminar Flow Supercritical Airfoil by Multi-Objective Evolution Method”. In: *Applied Mathematics and Mechanics* 35 (2014), pp. 191–202. DOI: `10.1007/s10483-014-1783-6`.

[106] A. Salahudeen and J. D. Baeder. “Uncertainty Quantification for Free Stream Turbulence Intensity Effects on Airfoil Characteristics”. In: *AIAA Aerospace Sciences Meeting*. AIAA 2018-0033. Kissimmee, FL, USA, Jan. 2018. DOI: `10.2514/6.2018-0033`.

[107] S. Hosder and B. R. Bettis. “Uncertainty and Sensitivity Analysis for Reentry Flows with Inherent and Model-Form Uncertainties”. In: *Journal of Spacecraft and Rockets* 49.2 (Mar. 2012), pp. 193–206. DOI: `10.2514/1.A32102`.

[108] Z. Sándor and P. András. “Alternative Sampling Methods for Estimating Multivariate Normal Probabilities”. In: *Journal of Econometrics* 120 (June 2004), pp. 207–234.

[109] M. Dodson and G. T. Parks. “Robust Aerodynamic Design Optimization Using Polynomial Chaos”. In: *Journal of Aircraft* 46.2 (Mar. 2009), pp. 635–646.

[110] L. W. Cook. “Effective Formulations of Optimization Under Uncertainty for Aerospace Design”. PhD thesis. Cambridge, UK: University of Cambridge, Mar. 2018. DOI: `10.17863/CAM.23427`.

[111] S. S. Dodbele. “Design Optimization of Natural Laminar Flow Bodies in Compressible Flow”. In: *Journal of Aircraft* 29.3 (May 1992), pp. 343–347.

[112] R. Rashad and D. W. Zingg. “Toward High-Fidelity Aerodynamic Shape Optimization for Natural Laminar Flow”. In: *21st AIAA Computational Fluid Dynamics Conference*. AIAA 2013-2583. San Diago, CA, USA, June 2013. DOI: `10.2514/6.2013-2583`.

[113] O. Amoignon, J. Pralits, A. Hanifi, M. Berggren and D. Henningson. “Shape Optimization for Delay of Laminar-Turbulent Transition”. In: *AIAA Journal* 44.5 (May 2006), pp. 1009–1024.

[114] J. Driver and D. W. Zingg. “Numerical Aerodynamic Optimization Incorporating Laminar-Turbulent Transition Prediction”. In: *AIAA Journal* 45.8 (Aug. 2007), pp. 1810–1818. DOI: `10.2514/1.23569`.

[115] J.-D. Lee and A. Jameson. “Natural-Laminar-Flow Airfoil and Wing Design by Adjoint Method and Automatic Transition Prediction”. In: *47th Aerospace Sciences Meeting*. AIAA 2009-897. Orlando, Florida, USA, Jan. 2009. DOI: `10.2514/6.2009-897`.

[116] P. Khayatzadeh and S. K. Nadarajah. “Aerodynamic Shape Optimization of Natural Laminar Flow (NLF) Airfoils”. In: *50th AIAA Aerospace Sciences Meeting*. AIAA 2012-0061. Nashville, Tennessee, USa, Jan. 2012. DOI: `10.2514/6.2012-61`.

[117] Y. Zhang, X. Fang, H. Chen, S. Fu, Z. Duan and Y. Zhang. “Supercritical Natural Laminar Flow Airfoil Optimization for Regional Aircraft Wing Design”. In: *Aerospace Science and Technology* 43 (Mar. 2015), pp. 152–164.

[118] M. Khurana and H. Winarto. “Development And Validation Of An Efficient Direct Numerical Optimisation Approach For Aerofoil Shape Design”. In: *The Aeronautical Journal* 114.1160 (Oct. 2010), pp. 611–628. DOI: `10.1017/S0001924000004097`.

[119] U. K. Wickramasinghe, R. Carrese and X. Li. “Designing Airfoils using a Reference Point based Evolutionary Many-objective Particle Swarm Optimization Algorithm”. In: *IEEE Congress on Evolutionary Computation*. Barcelona, Spain, July 2010, pp. 1857–1864. DOI: `10.1109/CEC.2010.5586221`.

[120] Z.-H. Han, J. Chen, K.-S. Zhang, Z.-M. Xu, Z. Zhu and W.-P. Song. “Aerodynamic Shape Optimization of Natural-Laminar-Flow Wing Using Surrogate-Based Approach”. In: *AIAA Journal* 56.7 (June 2018), pp. 2579–2593. DOI: `10.2514/1.J056661`.

[121] L. Huyse and R. M. Lewis. *Aerodynamic Shape Optimization of Two-dimensional Airfoils Under Uncertain Conditions*. ICASE Report 2001-1. Langley Research Center, Hampton, Virginia, USA: NASA, Jan. 2001.

[122] W. Li and S. Padula. *Using High Resolution Design Spaces for Aerodynamic Shape Optimization Under Uncertainty*. TP 2004-213003. Langley Research Center, Hampton, Virginia, USA: NASA, Mar. 2004.

[123] D. Lee, L. Gonzalez, J. Periaux and K. Srinivas. “Robust Design Optimisation Using Multi-Objective Evolutionary Algorithms”. In: *Computers and Fluids* 37 (2008), pp. 565–583. DOI: `10.1016/j.compfluid.2007.07.011`.

[124] K. Shimoyama, A. Oyama and K. Fujii. “Development of Multi-Objective Six-Sigma Approach for Robust Design Optimization”. In: *Journal Of Aerospace Computing, Information, And Communication* 5.8 (Aug. 2008), pp. 215–233. DOI: `10.2514/1.30310`.

[125] Z. Xiaopinga, D. Jifengb, L. Weijia and Z. Yong. “Robust Airfoil Optimization with Multi-objective Estimation of Distribution Algorithm”. In: *Chinese Journal of Aeronautics* 21 (Oct. 2008), pp. 289–295. DOI: `10.1016/S1000-9361(08)60038-2`.

[126] A.-M. Croicu, M. Y. Hussaini, A. Jameson and G. Klopfer. “Robust Airfoil Optimization Using Maximum Expected Value and Expected Maximum Value Approaches”. In: *AIAA Journal* 50.9 (Sept. 2012), pp. 1905–1919. DOI: `10.2514/1.J051467`.

[127] H. Shah, S. Hosder, S. Koziel, Y. A. Tesfahunegn and L. Leifsson. “Multi-fidelity robust aerodynamic design optimization under mixed uncertainty”. In: *Aerospace Science and Technology* 45 (Sept. 2015), pp. 17–29. DOI: `10.1016/j.ast.2015.04.011`.

[128] L. W. Cook, J. P. Jarrett and K. E. Willcox. “Extending Horsetail Matching for Optimization Under Probabilistic, Interval, and Mixed Uncertainties”. In: *AIAA Journal* 56.2 (Feb. 2018), pp. 849–861. DOI: `10.2514/1.J056371`.

[129] L. Deng and Z. D. Qiao. “A Multi-point Inverse Design Approach of Natural Laminar Flow Airfoils”. In: *27th International Congress of the Aeronautical Sciences*. Nice, France, Sept. 2010.

[130] F.-A. Fortin, F.-M. D. Rainville, M.-A. Gardner, M. Parizeau and C. Gagné. “DEAP: Evolutionary Algorithms Made Easy”. In: *Journal of Machine Learning Research* 13 (2012).

[131] K. Deb, A. Pratap, S. Agarwal and T. Meyarivan. “A Fast and Elitist Multiobjective Genetic Algorithm: NSGA-II”. In: *IEEE Transactions on Evolutionary Computation* 6.2 (Apr. 2002), pp. 182–197. DOI: `10.1109/4235.996017`.

[132] K. Deb and R. B. Agrawal. “Simulated Binary Crossover for Continuous Search Space”. In: *Complex Systems* 9 (1995), pp. 115–148.

[133] K. Deb and S. Agrawal. “A Niched-Penalty Approach for Constraint Handling in Genetic Algorithms”. In: *Artificial Neural Nets and Genetic Algorithms*. Indian Institute of Technology Kanpur. Slovenia: Springer, 1999, pp. 235–243.

[134] K. Deb and D. Deb. *Analyzing Mutation Schemes for Real-Parameter Genetic Algorithms*. KanGAL Report 2012016. Kanpur, India: Kanpur Genetic Algorithms Laboratory, Oct. 2012.

[135] D. A. Masters, N. J. Taylor, T. C. S. Rendall, C. B. Allen and D. J. Poole. "Review of Aerofoil Parameterisation Methods for Aerodynamic Shape Optimisation". In: *53rd AIAA Aerospace Sciences Meeting and Exhibit*. AIAA 10.2514/6.2015-0761. Kissimmee, FL, USA, Jan. 2015. DOI: `10.2514/6.2015-0761`.

[136] J. T. Alander. "On Optimal Population Size of Genetic Algorithms". In: *Computer Systems and Software Engineering 1992*. The Hague, Netherlands: IEEE, May 1992, pp. 65–70. DOI: `10.1109/CMPEUR.1992.218485`.

[137] R. Storn. "On the Usage of Differential Evolution for Function Optimization". In: *North American Fuzzy Information Processing*. Berkeley, California, USA: IEEE, June 1996, pp. 519–523.

[138] B. M. Kulfan. "Universal Parametric Geometry Representation Method". In: *Journal of Aircraft* 45.1 (Jan. 2008), pp. 142–158. DOI: `10.2514/1.29958`.

[139] R. C. Lock and B. R. Williams. "Viscous-inviscid Interactions In External Aerodynamics". In: *Progress in Aerospace Sciences* 24 (Aug. 1987), pp. 51–171.

[140] M. Drela. "XFOIL: An Analysis and Design System for Low Reynolds Number Airfoils". In: *Low Reynolds Number Aerodynamics*. Ed. by T. J. Mueller. Notre Dame, Indiana, USA: Springer Berlin Heidelberg, June 1989, pp. 1–12. DOI: `10.1007/978-3-642-84010-4_1`.

[141] J. E. Green, D. J. Weeks and J. W. F. Brooman. *Prediction of Turbulent Boundary Layers and Wakes in Compressible Flow by a Lag-Entrainment Method*. Tech. rep. 3791. Aerodynamics Deptartment, RAE Farnborough, UK: Aeronautical Research Council, 1977.

[142] C. J. Atkin and E. R. Gowree. "Recent Developments to the Viscous Garabedian and Korn Method". In: *28th International Congress of the Aeronautical Sciences*. Brisbane, Australia, Sept. 2012.

[143] R. C. Lock. "A Review Of Methods For Predicting Viscous Effects On Aerofoils And Wings At Transonic Speeds". In: *Computation of Viscous-Inviscid Interactions*. 291. Advisory Group for Aerospace Research and Development (AGARD), May 1981. Chap. 2.

[144] C. C. L. Sells. "Plane Subcritical Flow Past a Lifting Aerofoil". In: *Proceedings of the Royal Society of London. Series A, Mathematical and Physical Sciences* 308.1494 (Jan. 1969), pp. 377–401. DOI: `10.1098/rspa.1969.0016`.

[145] R. C. Lock. *An Equivalence Law Relating Three- and Two- Dimensional Pressure Distributions*. Tech. rep. 3346. Royal Aircraft Establishment, Bedford, UK: Aeronautical Research Council, May 1964.

[146] C. J. Atkin. *Summary of the swept-tapered lag-entrainment boundary layer method in Callisto version 3.4*. Tech. rep. QinetiQ/08/00064. QinetiQ, Jan. 2008.

[147] C. J. Atkin. "Convergence of Calculated Transition Loci During Compuational Analysis of Transonic Aerofoils and Infinite Swept Wings". In: *29th Congress of the International Council of the Aeronautical Sciences*. St. Petersburg, Russia, Sept. 2014.

[148] P. H. Cook, M. A. McDonald and M. C. P. Firmin. "Aerofoil RAE 2822 - Pressure Distributions, and Boundary Layer and Wake Measurments". In: *Experimental Data Base For Computer Program Assessment*. 138. Advisory Group for Aerospace Research and Development (AGARD), May 1979. Chap. A6.

[149] K. Wicke, F. Linke, V. Gollnick and M. Kruse. "Insect Contamination Impact on Operational and Economic Effectiveness of Natural-Laminar-Flow Aircraft". In: *Journal of Aircraft* 53.1 (Jan. 2016), pp. 158–167. DOI: `10.2514/1.C033237`.

[150] T. M. Young and B. Humphreys. "Liquid anti-contamination systems for hybrid laminar flow control aircraft - a review of the critical issues and important experimental results". In: *Journal of Aerospace Engineering* 218.4 (Apr. 2004), pp. 267–277. DOI: `10.1243/0954410041872825`.

[151] T. L. B. Tamigniaux, S. E. Stark and G. W. Brune. "An Experimental Investigation of the Insect Shielding Effectiveness of a Krueger Flap/Wing Airfoil Configuration". In: *5th Applied Aerodynamics Conference*. 87-2615. Monterey, CA, USA: AIAA, Aug. 1987. DOI: `10.2514/6.1987-2615`.

[152] Boeing Co. *High Reynolds Number Hybrid Laminar Flow Control (HLFC) Flight Experiment II. Aerodynamic Design*. Technical Report CR-1999-209324. Langley Research Center, Hampton, Virginia, USA: NASA, Apr. 1999.

[153] C. P. van Dam. "The Aerodynamic Design of Multi-Element High-Lift Systems for Transport Airplanes". In: *Progress in Aerospace Sciences* 38.2 (Feb. 2002), pp. 101–144. DOI: `10.1016/S0376-0421(02)00002-7`.

[154] M. Drela. "Design and Optimization Method for Multi-Element Airfoils". In: *Aerospace Design Conference*. AIAA 93-0969. Irvine, CA, USA, Feb. 1993. DOI: `10.2514/6.1993-969`.

[155] J.-D. Lee. "NLF Wing Design by Adjoint Method and Automatic Transition Prediction". PhD thesis. Stanford, CA, USA: Citeseer, 2009.

[156] R. Bellman. *Dynamic Programming*. 6th. Princeton, New Jersey, USA: Princeton University Press, 1972.

[157] L. R. Jenkinson, P. Simpkin and D. Rhodes. *Civil Jet Aircraft Design*. 1st. AIAA, 1999.

[158] ESDU. *A framework relating the drag-rise characteristics of a finite wing/body combination to the those of its basic aerofoil*. Tech. rep. ESDU 78009. ESDU, May 1978.

Publications

Conference Proceedings

1. Hollom, J. and Qin, N. *"Robustness of Natural Laminar Flow Airfoil Drag Optimization to Transition Amplification Factor"*. In: 18th AIAA/ISSMO Multidisciplinary Analysis and Optimization Conference, AIAA AVIATION Forum. AIAA 2017-3144. Denver, Colorado, USA, June 2017. doi: 10.2514/6.2017- 3144.

2. Hollom, J. and Qin, N. *"Quantification and Multi-point Optimization of Natural Laminar Flow Airfoil Robustness to Transition Amplification Factor"*. In: AIAA SciTech Forum. AIAA. Kissimmee, FL, USA, Jan. 2018. doi: 10.2514/6.2018-1161.